



University of
Nottingham

UK | CHINA | MALAYSIA

A Study of Flame and Flow Development with Hydrous and Anhydrous Fuels in an Optical Spark Ignition Engine

Mohammadmohsen Moslemin Koupaie

Thesis submitted to The University of Nottingham for
the degree of Doctor of Philosophy

April 2019

Abstract

The work reported in this thesis was concerned with improving understanding of the in-cylinder flow and combustion with future fuels in a modern spark ignition engine, including hydrous ethanol as a potentially attractive solution in future dedicated ethanol IC engines.

The experiments were performed in a single cylinder optical research engine equipped with a modern central direct injection combustion chamber and Bowditch style optical piston. Results were obtained under “typical” part-load engine operating conditions with ethanol, iso-octane, B16I84, E10I90, E6B8I85, E85I10W5 and hydrous ethanol at 5%, 12% and 20% volume water.

High speed cross-correlated particle image velocimetry was undertaken at 1500rpm motoring conditions with the intake plenum pressure set to 0.5 bar absolute and the horizontal imaging plane fixed 10mm below the combustion chamber “fireface”. Comparisons were made to CFD computations of the flow. Complimentary flame images were obtained via natural light (chemiluminescence) over multiple engine cycles.

The flame images revealed the tendency of all fuels flame to migrate towards the hotter exhaust side of the combustion chamber, with no complimentary bulk air motion apparent in this area in the imaging plane. This exhaust migration phenomenon has been noted previously by others in optical pent-roofed engines but without both flow and flame imaging data being available.

The faster burning ethanol offset the tendency of the flame to migrate towards the hotter exhaust walls. The fastest combustion rate occurred with pure ethanol, with higher water content (>5%) generally slowing down the flame speed rate and offsetting the flame speed/migration benefit (in good agreement with recent laminar burning velocity correlations for hydrous ethanol).

Acknowledgements

I would like to thank my dearest parents for their love and unconditional support during my entire life especially for the past few years of my PhD study.

Thank you to my special wife and best friend, Ghazaleh, who has supported me for the past 15 years and put up with long distance relationship for a few years to complete my undergraduate and postgraduate studies.

I would like to thank my Ph.D. supervisors; Prof. Alasdair Cairns and Prof. Hua Zhao. Prof. Alasdair Cairns, thank you for all the support that you've given me during the project, for the hundreds of email replies and your invaluable guidance during my study.

I would like to thank everyone I've worked within the School of Engineering and Design in Brunel and Nottingham University. I am also thankful for my colleagues, Hassan Vafamehr, Thompson Lanzanova, Quan Liu and Jun Ma for their advice and help especially at the beginning.

Publications

The following papers have been derived in part from this thesis.

Moslemin Koupaie, M., Cairns, A., Vafamehr, H., and Lanzanova, T., "Cyclically Resolved Flame and Flow Imaging in an SI Engine Operating with Future Ethanol Fuels," SAE Technical Paper 2017-01-0655, 2017, <https://doi.org/10.4271/2017-01-0655>.

Moslemin Koupaie, M., Cairns, A., Vafamehr, H., and Lanzanova, "A Study of Hydrous Ethanol Combustion in an Optical Central Direct Injection Spark Ignition Engine", Applied Energy Journal, Volume 237, 1 March 2019, Pages 258-269, <https://doi.org/10.1016/j.apenergy.2018.12.093>.

Mohammadmohsen Moslemin Koupaie; Alasdair Cairns; Steve Simplay; Jun Xia; Hassan Vafamehr; Thompson MetzkaLanzanova, "Cyclically resolved flame and flow imaging in an alcohol fuelled SI engine" Fuel Journal, Volume 237, 1 February 2019, Pages 874-887, <https://doi.org/10.1016/j.fuel.2018.10.075>.

Table of Contents

ABSTRACT.....	I
ACKNOWLEDGEMENTS.....	II
PUBLICATIONS	III
TABLE OF CONTENTS.....	I
LIST OF FIGURES	V
LIST OF TABLES	XIV
NOMENCLATURE	XV
1. INTRODUCTION	1
1.1 GENERAL BACKGROUND AND INCENTIVE	1
1.2 THESIS OUTLINE.....	3
2. FLOW & COMBUSTION IN SPARK IGNITION ENGINES	4
2.1 INTRODUCTION	4
2.1.1 SPARK-IGNITION ENGINE OPERATION	8
2.1.1.1 SPARK RETARD DUE TO KNOCK LIMITED OPERATION	10
2.1.1.2 FUEL ENRICHMENT DUE TO TEMPERATURE LIMITED OPERATION.....	11
2.1.1.3 INCREASED ENGINE FRICTION	11
2.1.1.4 PUMPING LOSSES	12
2.1.1.5 INCREASED HEAT TRANSFER	13
2.1.1.6 OTHER LOSSES.....	14
2.2 REDUCING LOSSES IN SI ENGINES	16
2.2.1 ENGINE DOWNSIZING	16
2.2.2 ENGINE DOWN-SPEEDING	18
2.3 TURBULENT COMBUSTION	19
2.3.1 BASICS OF TURBULENT COMBUSTION	20
2.3.2 TURBULENT FLOW	21
2.4 CHARGE MOTION EFFECTS.....	23
2.4.1 SWIRL.....	23
2.4.2 SQUISH AND TUMBLE	24
2.5 IGNITION.....	25
2.6 PROCESS OF LAMINAR AND TURBULENT COMBUSTION	27

2.6.1	LAMINAR PRE-MIXED COMBUSTION	27
2.6.2	TURBULENT COMBUSTION	28
2.7	ALCOHOL FUELS	31
2.7.1	IMPACT ON SI ENGINES AND ALCOHOL TYPES.....	31
2.7.2	SOCIAL, ECONOMIC AND ENVIRONMENTAL ASPECTS	35
2.7.3	HYDROUS ETHANOL	37
2.7.4	HYDROUS ETHANOL APPLICATION IN SI ENGINES	39
2.8	SUMMARY OF LITERATURE.....	41
3.	EXPERIMENTAL ENGINE AND INSTRUMENTATION.....	42
3.1	INTRODUCTION	42
3.2	ENGINE TEST BED	42
3.3	DYNAMOMETER	43
3.4	COOLANT AND OIL SYSTEMS.....	43
3.5	EXPERIMENTAL OPTICAL ENGINE	45
3.5.1	GENERAL DESCRIPTION	45
3.5.2	OPTICAL CYLINDER HEAD.....	46
3.6	IN-CYLINDER PRESSURE MEASUREMENT	48
3.7	INJECTOR AND IGNITION TIMING CONTROL SYSTEM.....	49
3.8	CAMSHAFT	52
3.9	COMPRESSION RATIO	53
3.10	FUEL PREPARATION.....	53
3.11	FUEL SUPPLY SYSTEM.....	54
3.12	DATA ACQUISITION AND SYNCHRONISATION	55
3.13	ENGINE MAINTENANCE AND OPERATION	57
3.14	SUMMARY	57
4.	THREE DIMENSIONAL CFD FLAME & FLOW INVESTIGATION	58
4.1	INTRODUCTION	58
4.2	COMPUTER MODELLING OF TURBULENCE.....	59
4.2.1	DIFFERENTIAL EQUATIONS.....	60
4.2.2	DIRECT NUMERICAL SIMULATION.....	62
4.2.3	REYNOLDS-AVERAGED NAVIER STOKES (RANS).....	63
4.2.3.1	PHYSICAL CONCEPT OF TURBULENCE.....	63
4.2.3.2	THE GOVERNING EQUATIONS	64
4.2.3.3	ONE-EQUATION MODELS.....	66
4.2.3.4	TWO-EQUATION MODELS	66
4.2.3.4.1	THE $k - \epsilon$ MODEL.....	67
4.2.3.4.2	THE MODIFIED $k - \epsilon$ MODEL (RNG).....	68
4.2.3.4.3	THE $k - \omega$ MODEL.....	68
4.2.4	LARGE EDDY SIMULATION (LES)	69
4.3	CFD SOFTWARE MODEL SET-UP	70
4.3.1	PRINCIPLE OF CALCULATIONS	71
4.3.2	BOUNDARY CONDITIONS	71
4.3.3	GRID AND MESH TYPE	72
4.3.4	3D CFD ENGINE MODEL.....	73

4.4	SUMMARY	76
5.	IMAGING TECHNIQUES & THERMODYNAMIC PROCESSING	77
5.1	INTRODUCTION	77
5.2	MIE SCATTERING PRINCIPLE.....	78
5.3	LASER LIGHT SOURCE	79
5.3.1	HIGH ENERGY PULSED LASERS.....	79
5.4	PARTICLE IMAGE VELOCIMETRY AND EXPERIMENTAL SETUP	80
5.4.1	SEEDING PARTICLES	82
5.4.2	PIV LASER	84
5.4.3	CAMERA AND OPTICS	85
5.4.4	PIV TEST SETUP	85
5.4.5	CROSS-CORRELATION ANALYSIS.....	88
5.4.6	PIV ANALYSIS LIMITATIONS & ADVANCED INTERROGATION TECHNIQUES.....	91
5.4.6.1	LOSS OF PARTICLE PAIRS.....	91
5.4.6.2	PEAK LOCKING EFFECT	92
5.4.6.3	PARTICLE IMAGE DEFORMATION	92
5.4.6.4	WINDOW SHIFT METHOD.....	92
5.4.6.5	MULTIGRID ANALYSIS	92
5.4.6.6	LOCAL CORRELATION AVERAGING	93
5.4.6.7	CORRELATION MULTIPLICATION	93
5.5	HIGH-SPEED NATURAL LIGHT (CHEMILUMINESCENCE).....	93
5.5.1	HIGH-SPEED CAMERA AND SYNCHRONISATION	95
5.5.2	INTENSIFIER SWEEP	98
5.5.3	COMPARISON OF IMAGING METHODS	101
5.5.4	IMAGE ANALYSIS AND PROCESSING TECHNIQUES.....	105
5.5.4.1	FLAME IMAGE INITIAL PROCESSING AND BINARISATION.....	105
5.5.4.2	NOISE SUPPRESSION.....	106
5.5.4.3	FLAME IMAGE READ AND POST PROCESSING	107
5.5.4.4	FLAME RADIUS	108
5.5.4.5	FLAME SPEED AND SHAPE FACTOR	111
5.6	THERMODYNAMIC ANALYSIS AND TECHNIQUES.....	112
5.6.1	SAMPLE SIZE AND CYCLE SELECTION.....	112
5.6.2	MBT SPARK TIMING	115
5.6.3	IMEP CALCULATION	115
5.6.4	INDICES OF POLYTROPIC COMPRESSION AND EXPANSION.....	116
5.6.5	HEAT RELEASE CALCULATION	117
5.6.5.1	SIGNAL FILTERING	118
5.6.6	TWO-ZONE HEAT RELEASE & TEMPERATURE ANALYSIS	119
5.6.6.1	ITERATIVE PROCESS	120
5.6.7	LAMINAR BURNING VELOCITY CALCULATION	121
5.7	SUMMARY	122
6.	RESULTS AND ANALYSIS.....	124
6.1	INTRODUCTION	124
6.2	COLD FLOW.....	126

6.2.1	MOTORED ENGINE DATA	126
6.2.2	PIV THROUGHOUT THE COMPRESSION STROKE	127
6.2.3	PIV ON HORIZONTAL PLANE	129
6.2.4	3-D COMPUTATIONAL FLUID DYNAMICS	133
6.2.4.1	K-EPSILON RNG	133
6.2.4.2	K-EPSILON PREDICTIONS	140
6.2.4.3	A COMPARISON BETWEEN K-E AND K-E RNG	145
6.2.5	A COMPARISON BETWEEN PIV AND CFD.....	150
6.2.5.1	CFD ON THE TUMBLE PLANE	153
6.3	COMBUSTION.....	157
6.3.1	THERMODYNAMIC DATA.....	158
6.3.2	FLAME IMAGING.....	169
6.3.2.1	FLAME RADIUS	169
6.3.2.2	FLAME SPEED	173
6.3.2.3	CENTROID DISPLACEMENT	176
6.3.2.4	SHAPE FACTOR	179
6.3.3	BURNED AND UNBURNED GAS TEMPERATURE.....	182
6.3.4	LAMINAR BURNING VELOCITY.....	190
7.	CONCLUSION & RECOMMENDATIONS.....	191
7.1	SUMMARY OF RESULTS	191
7.2	CLAIMS FOR ORIGINALITY.....	195
7.3	RECOMMENDATIONS FOR FUTURE WORK.....	196
8.	REFERENCES.....	198
	APPENDICES.....	218
APPENDIX A	ORBITAL CYLINDER HEAD.....	218
APPENDIX B	PIV MATLAB CODE.....	219
APPENDIX C	GASKETING.....	222

List of Figures

FIGURE 2.1. TRANSPORTATION SECTOR ENERGY CONSUMPTION ESTIMATIVE (ADAPTED FROM [27]).	5
FIGURE 2.2. COMPARISON OF GLOBAL REGULATIONS FOR PASSENGER CARS [29].	6
FIGURE 2.3. RICARDO VIEW OF THE 2030 PASSENGER CAR ELECTRIFIED POWERTRAIN MIX IN EUROPE. ADAPTED FROM RICARDO [4].	7
FIGURE 2.4. COMPARISON OF THEORETICAL AND ACTUAL PV DIAGRAMS FOR FOUR-STROKE OTTO CYCLE ENGINE.	9
FIGURE 2.5. BSFC MAP FOR A NATURALLY-ASPIRATED SPARK-IGNITION ENGINE, WITH NUMBERS SHOWING THE TYPICAL LOSSES IN AN SI ENGINE. (1) KNOCK LIMITED, SPARK RETARD (2) COMPONENT TEMPERATURE LIMITED, FUEL ENRICHMENT (3) INCREASED FRICTIONAL LOSSES (4) INCREASED PUMPING LOSSES (5) INCREASED RELATIVE HEAT TRANSFER LOSSES. EACH ARROW SIGNIFICANCE IS BRIEFLY DESCRIBED BELOW.	10
FIGURE 2.6. TOTAL FRICTION MEAN EFFECTIVE PRESSURE (TFMEP), RUBBING FRICTION MEP (RFMEP) AND PUMPING MEP (PMEP) AS A FUNCTION OF LOAD FOR FOUR-CYLINDER SPARK IGNITION ENGINE, ADAPTED FROM [31].	12
FIGURE 2.7. GRAPHICAL ILLUSTRATION OF PUMPING LOSSES IN CONVENTIONAL AND LOGARITHMIC SCALED IN-CYLINDER PRESSURE-VOLUME DIAGRAMS.	13
FIGURE 2.8. COMBUSTION DURATION IN MILLISECONDS AGAINST ENGINE SPEED. FIGURE CREATED FROM DATA PUBLISHED BY HIRES [38].	14
FIGURE 2.9. DIAGRAM SHOWING THE ENERGY SPLIT FOR TYPICAL GASOLINE SI ENGINE AT 5BAR NET IMEP AND 2000 RPM, DATA ADAPTED FROM [39].	15
FIGURE 2.10. COMBUSTION PHASING LOSS REDUCES THE COMPRESSION RATIO IN THE IDEAL CONSTANT VOLUME PROCESS. ADAPTED FROM [39].	16
FIGURE 2.11. CONCEPTUAL BSFC MAPS FOR A 2.5L NATURALLY-ASPIRATED ENGINE (A) AND A 1.6L BOOSTED (B). ADAPTED FROM ZHAO [46] AND STONE [30].	19
FIGURE 2.12. THE LAMINAR BURNING VELOCITY AS A FUNCTION OF THE EQUIVALENCE RATIO, ADAPTED FROM METGHALCHI & KECK [49,50].	20
FIGURE 2.13. A) CYLINDER PRESSURE VS CRANK ANGLE FOR THREE DISTINCT SPARK TIMINGS (OVER ADVANCED, MBT AND RETARDED); B) EFFECT OF SPARK ADVANCE ON	

THE BRAKE TORQUE HIGHLIGHTING MBT FOR A GIVEN ENGINE. ADAPTED FROM AMANN [58].	26
FIGURE 2.14. GENERAL CORRELATION OF TURBULENT BURNING VELOCITIES IN TERMS OF DIMENSIONLESS GROUPS. ADAPTED FROM ABDEL-GAYED, AL-KHISHALI, AND BRADLEY [62].	30
FIGURE 2.15. BORGHI DIAGRAM SHOWING THE DIFFERENT REGIMES OF TURBULENT PREMIXED FLAMES, ADAPTED FROM PETERS [63]; BORGHI [64].	31
FIGURE 2.16. THE VOLUMETRIC ENERGY CONTENT OF ETHANOL GASOLINE BLENDS DISPLAYING THE FACT THAT AS THE ETHANOL CONTENT RISES, THE ENERGY CONTENT FALLS IN A LINEAR FASHION [66].	33
FIGURE 2.17. GLOBAL ETHANOL PRODUCTION BY COUNTRY/REGION AND YEAR. ADAPTED FROM [84,85].	36
FIGURE 2.18. ETHANOL DISTILLATION ENERGY PER LITRE. NUMBER OF DISTILLATION STAGES: * 8 STAGES; ** 12 STAGES; *** 19 STAGES. ADAPTED FROM [5,6,8].	38
FIGURE 2.19. COMPARISON OF NET ENERGY BALANCE FOR ANHYDROUS AND WET ETHANOL (E65W35) TAKING INTO ACCOUNT ALL ETHANOL PRODUCTION STEPS [7].	39
FIGURE 3.1. ENGINE TEST BED.	44
FIGURE 3.2. COOLANT SETUP SCHEMATIC.	44
FIGURE 3.3. ENGINE SETUP SCHEMATIC.	46
FIGURE 3.4. COMBUSTION CHAMBER AND PISTON CROWN.	47
FIGURE 3.5. EXTENDED PISTON ASSEMBLY.	47
FIGURE 3.6. MANUFACTURER GUIDELINES FOR INJECTOR LOCATION. (PROVIDED COURTESY OF MAHLE POWERTRAIN).	50
FIGURE 3.7. CLAMPING METHOD FOR PIEZO INJECTOR.	50
FIGURE 3.8. PLANAR MIE IMAGES SHOWING THE LIQUID FUEL DISTRIBUTION AT FOUR TIME POINTS DURING A SINGLE INJECTION OF 10 MG FUEL AT 200BAR [112].	51
FIGURE 3.9. SPARK IGNITION CONTROL SYSTEM	52
FIGURE 3.10. CAMSHAFT PULLEY AND TDC INDICATOR.	52
FIGURE 3.11. PISTON WINDOW ASSEMBLY.	53
FIGURE 3.12. FUEL SUPPLY SYSTEM.	54
FIGURE 3.13. TIMING SEQUENCE FOR FUEL INJECTION AND IMAGE ACQUISITION.	55
FIGURE 3.14. DATA ACQUISITION SYSTEM.	56
FIGURE 4.1. ANSYS MESH STRUCTURES.	72

FIGURE 4.2. ANSYS MESH GENERATED AT 450° ATDC WITH INLET AND EXHAUST BOUNDARIES.	73
FIGURE 4.3. ENGINE SOLID PARTS IN 2-D.	74
FIGURE 4.4. INITIAL FULL SOLID MODEL.	75
FIGURE 4.5. 3-D SOLID MODEL INCLUDING VALVES, PORTS, SPARK PLUG, AND INJECTOR.	75
FIGURE 5.1. LIGHT SCATTERING PRINCIPLE [161].	79
FIGURE 5.2. PRINCIPLE OF LASER EXPLAINING STIMULATED EMISSION AND AMPLIFICATION [55].	79
FIGURE 5.3. PIV EXPERIMENTAL SETUP.	81
FIGURE 5.4. PRINCIPLE OF FRAME STRADDLING TECHNIQUE.	81
FIGURE 5.5. SEEDING GENERATOR.	83
FIGURE 5.6. LASER SHEET THICKNESS,	86
FIGURE 5.7. PIV LASER, MIRROR, CAMERA, AND OPTICAL APPARATUS.	87
FIGURE 5.8. CROSS-CORRELATION ANALYSIS.	88
FIGURE 5.9. MOLECULE EXCITATION AND PHOTONS PRODUCTION.	94
FIGURE 5.10. HIGH SPEED CAMERA MOUNTED WITH NIKON LENS.	96
FIGURE 5.11. LED LAMP INDICATING 40° BTDC.	97
FIGURE 5.12. NOISE IN INITIAL RECORDED IMAGE WITHOUT INTENSIFIER.	98
FIGURE 5.13. APPARENT FLAME SPEED AT 50% AND 80% GAINING LEVEL, (1500 RPM, 0.5 BAR INLET PRESSURE, ETHANOL MBT FOR ALL THE FUELS).	100
FIGURE 5.14. FLAME RADIUS COMPARED TO OPTICAL PISTON BORE RADIUS FOR ETHANOL (MBT).	101
FIGURE 5.15. ELLIPSE USED TO MARK THE EDGE OF OPTICAL CROWN.	108
FIGURE 5.16. ILLUSTRATION OF THE FLAME IMAGE PROCESSING PROCEDURE. CYCLE CLOSEST TO THE ARITHMETIC MEAN OF ETHANOL FLAME RADIUS, MEASURED AT 27 CAD AIT.	110
FIGURE 5.17. THE CUMULATIVE PERCENTAGE ERROR INDICATING THE REDUCING OF COV OF IMEP OVER 300 CYCLES.	113
FIGURE 5.18. ALL 300 COMBUSTION CYCLES DISPLAYED WITH THE NUMERICAL MEAN, FASTEST AND SLOWEST CYCLES SUPERIMPOSED (1500 RPM, ETHANOL MBT SPARK TIMING).	114
FIGURE 5.19. IN CYLINDER PRESSURE AND VOLUME DURING THE COMPRESSION STROKE.	116

FIGURE 5.20. IN CYLINDER PRESSURE AND VOLUME DURING THE EXPANSION STROKE.	117
FIGURE 5.21. INTERVAL SIZE EFFECT ON MFB RESULTS,	118
FIGURE 5.22. MFB GRAPH PRESENTED IN 4 BOXES AVERAGING SIZE.....	119
FIGURE 5.23. FLOWCHART OF THE TWO-ZONE HEAT RELEASE MODEL.....	121
FIGURE 6.1. THE MOTORED IN-CYLINDER PRESSURE OF AN INDIVIDUAL CYCLES (1500 RPM).....	126
FIGURE 6.2. ZOOMED VIEW OF MOTORING SHOWING CYCLIC VARIATION FOR INDIVIDUAL CYCLES (1500 RPM).....	127
FIGURE 6.3. EFFECT OF A NUMBER OF BATCHES (100 CYCLES EACH) ON MEASURED VELOCITIES WITH THE ERROR BARS (100-1500 CYCLES AT 1500 RPM).....	128
FIGURE 6.4. PIV IMAGE DIVISION IN 4 ZONES.....	130
FIGURE 6.5. PIV MEAN VELOCITY FIELD AT 180° BTDC AT 1500 RPM.	130
FIGURE 6.6. VARIATION OF TURBULENCE INTENSITY AGAINST CRANK ANGLE AT 1500 RPM.	131
FIGURE 6.7. PIV MEAN VELOCITY FIELD AT 90° BTDC AT 1500 RPM.	132
FIGURE 6.8. PIV MEAN VELOCITY FIELD AT 40° BTDC AT 1500RPM.	132
FIGURE 6.9. PIV MEAN VELOCITY FIELD AT 30° BTDC AT 1500 RPM.	133
FIGURE 6.10. PIV MEASUREMENT OF THE VARIATION OF AVERAGE VELOCITY AGAINST CRANK ANGLE DEGREE. MEASURED AT 10MM BELOW THE SPARK PLUG WHERE THE LASER SHEET WAS LOCATED.....	135
FIGURE 6.11. NUMBER OF ITERATIONS PER TIME STEP IS SHOWN AT EACH CRANK ANGLE DEGREES.	135
FIGURE 6.12. VELOCITY FIELDS ON THE HORIZONTAL PLANE USING K-E RNG AT 180° CA BTDC. MEASURED AT 10MM BELOW THE SPARK PLUG WHERE THE LASER SHEET WAS LOCATED FOR PIV MEASUREMENTS.	136
FIGURE 6.13. VELOCITY FIELDS ON THE HORIZONTAL PLANE USING K-E RNG AT 90° CA BTDC. MEASURED AT 10MM BELOW THE SPARK PLUG WHERE THE LASER SHEET WAS LOCATED FOR PIV MEASUREMENTS.	137
FIGURE 6.14. VELOCITY FIELDS ON THE HORIZONTAL PLANE USING K-E RNG AT 40° CA BTDC. MEASURED AT 10MM BELOW THE SPARK PLUG WHERE THE LASER SHEET WAS LOCATED FOR PIV MEASUREMENTS.	138

FIGURE 6.15. VELOCITY FIELDS ON THE HORIZONTAL PLANE USING K-E RNG AT 30° CA BTDC. MEASURED AT 10MM BELOW THE SPARK PLUG WHERE THE LASER SHEET WAS LOCATED FOR PIV MEASUREMENTS.	139
FIGURE 6.16. VELOCITY FIELDS ON THE HORIZONTAL PLANE USING K-E AT 180° CA BTDC.	141
FIGURE 6.17. VELOCITY FIELDS ON THE HORIZONTAL PLANE USING K-E AT 90° CA BTDC	142
FIGURE 6.18. VELOCITY FIELDS ON THE HORIZONTAL PLANE USING K-E AT 40° CA BTDC.	143
FIGURE 6.19. VELOCITY FIELDS ON THE HORIZONTAL PLANE USING K-E AT 30° CA BTDC.	144
FIGURE 6.20. K-E AND K-E RNG (ON THE LEFT) CFD AT 180° CA BTDC.	146
FIGURE 6.21. K-E AND K-E RNG (ON THE LEFT) CFD AT 90° CA BTDC.	146
FIGURE 6.22. K-E AND K-E RNG (ON THE LEFT) CFD AT 40° CA BTDC.	147
FIGURE 6.23. K-E AND K-E RNG (ON THE LEFT) CFD AT 30° CA BTDC.	147
FIGURE 6.24. CFD K-E AND K-E RNG MEAN VELOCITY FIELD DIVIDED INTO 25 ZONES. A) CFD K-E RNG MEAN VELOCITY FIELD AT 40° BTDC, B) CFD K-E MEAN VELOCITY FIELD AT 40° BTDC, C) CFD K-E RNG MEAN VELOCITY FIELD AT 30° BTDC, AND D) CFD K-E MEAN VELOCITY FIELD AT 30° BTDC.	148
FIGURE 6.25. COMPARISON BETWEEN TWO TURBULENCE METHODS CFD (K-EPSILON RNG) AND CFD (K-EPSILON), SHOWING MAGNITUDE VELOCITY FOR 30° (LEFT) AND 40° BTDC (RIGHT).	149
FIGURE 6.26. MEAN VELOCITY FIELDS ON THE HORIZONTAL PLANE FOR CFD AND PIV IMAGES.	151
FIGURE 6.27. CFD AND PIV MEAN VELOCITY FIELD DIVIDED INTO 25 ZONES. A) PIV MEAN VELOCITY FIELD AT 40° BTDC, B) CFD MEAN VELOCITY FIELD AT 40° BTDC, C) PIV MEAN VELOCITY FIELD AT 30° BTDC, AND D) CFD MEAN VELOCITY FIELD AT 30° BTDC.	152
FIGURE 6.28. COMPARISON BETWEEN CFD (K-EPSILON RNG) AND PIV, SHOWING MAGNITUDE VELOCITY FOR 30° (LEFT) AND 40° BTDC (RIGHT).	153
FIGURE 6.29. MEAN VELOCITY FIELD ON THE TUMBLE PLANE AT 40° CA BTDC. ..	154
FIGURE 6.30. MEAN VELOCITY FIELD IN THE TUMBLE PLANE AT 90° CA BTDC.	155
FIGURE 6.31. MEAN VELOCITY FIELD IN THE TUMBLE PLANE AT 180° CA BTDC.	156

FIGURE 6.32. NET IMEP AND COMBUSTION STABILITY VALUES FROM THE CYCLES CLOSEST TO THE OPTICAL MEAN (300 CYCLES) OF BASE FUELS AND WET ETHANOL. (1500 RPM, 0.5 BAR INLET PRESSURE, ETHANOL MBT).....	159
FIGURE 6.33. NET IMEP AND COMBUSTION STABILITY VALUES FROM THE CYCLES CLOSEST TO THE OPTICAL MEAN (300 CYCLES) OF B16I84, E10I90, E6B8I85 AND E85I10W5. (1500 RPM, 0.5 BAR INLET PRESSURE, ETHANOL MBT).....	159
FIGURE 6.34. NET IMEP AND COMBUSTION STABILITY VALUES FROM THE CYCLES CLOSEST TO THE AVERAGE CYCLE (1500 RPM, 0.5 BAR INLET, ETHANOL MBT).....	160
FIGURE 6.35. POSITION OF MAXIMUM PRESSURE FOR ALL THE FUELS. CLOSEST CYCLE TO THE ARITHMETIC SLOW CYCLE. (1500 RPM, 0.5 BAR INLET PRESSURE, ETHANOL MBT).	161
FIGURE 6.36. POSITION OF MAXIMUM PRESSURE FOR ALL THE FUELS. CLOSEST CYCLE TO ARITHMETIC MEAN CYCLE. (1500 RPM, 0.5 BAR INLET PRESSURE, ETHANOL MBT). .	162
FIGURE 6.37. POSITION OF MAXIMUM PRESSURE FOR ALL THE FUELS. CLOSEST CYCLE TO ARITHMETIC FAST CYCLE. (1500 RPM, 0.5 BAR INLET PRESSURE, ETHANOL MBT)....	162
FIGURE 6.38. 300 COMBUSTION CYCLES OF BASE FUELS AND WET ETHANOL UNDER MBT FIX SPARK TIMING DISPLAYED WITH THE CYCLES CLOSEST TO NUMERICAL MEAN (1500 RPM, 0.5 BAR INLET PRESSURE, ETHANOL MBT).	163
FIGURE 6.39. 300 COMBUSTION CYCLES OF B16I84, E10I90, E6B8I85 AND E85I10W5 UNDER MBT FIXED SPARK TIMING FOR ETHANOL CONDITION DISPLAYED WITH THE CYCLES CLOSEST TO NUMERICAL MEAN. (1500 RPM, 0.5 BAR INLET PRESSURE, ETHANOL MBT).....	164
FIGURE 6.40. EXPERIMENTAL IN-CYLINDER PRESSURE DATA (60 CYCLES) FOR THE RELEVANT FASTEST AND SLOWEST CYCLES; TAKEN FROM COMBUSTION UNDER STOICHIOMETRIC CONDITIONS, (1500 RPM, 0.5 BAR INLET PRESSURE, ETHANOL MBT).	164
FIGURE 6.41. 300 COMBUSTION CYCLES DISPLAYED WITH THE CYCLES CLOSEST TO NUMERICAL MEAN (1500 RPM, 0.5 BAR INLET PRESSURE, ETHANOL MBT FOR ALL THE FUELS).....	165
FIGURE 6.42. MAXIMUM PRESSURE RISE RATE FOR ALL THE FUELS. 1500 RPM, ETHANOL MBT OPERATION. CYCLE CLOSEST TO THE ARITHMETIC MEAN.....	166
FIGURE 6.43. 300 CYCLES AVERAGE APPARENT HEAT RELEASE RATE FOR BASE FUELS AND WET ETHANOL FUELS (1500 RPM, 0.5 BAR INLET PRESSURE, ETHANOL MBT FOR ALL THE FUELS).....	167

FIGURE 6.44. 300 CYCLES AVERAGE APPARENT HEAT RELEASE RATE FOR B16I84, E10I90, E6B8I85 AND E85I10W5 (1500 RPM, 0.5 BAR INLET PRESSURE, ETHANOL MBT FOR ALL THE FUELS).	167
FIGURE 6.45. 300 CYCLES AVERAGE APPARENT HEAT RELEASE RATE FOR ALL FUELS (1500 RPM, 0.5 BAR INLET PRESSURE, ETHANOL MBT FOR ALL THE FUELS).....	168
FIGURE 6.46. COMPUTED FLAME RADIUS CLOSEST DATA TO 60 AVERAGED CYCLES FOR BASE FUELS AND WET ETHANOL FUELS (1500 RPM, 0.5 BAR INLET PRESSURE, ETHANOL MBT FOR ALL THE FUELS).	170
FIGURE 6.47. COMPUTED FLAME RADIUS CLOSEST DATA TO 60 AVERAGED CYCLES FOR B16I84, E10I90, E6B8I85 AND E85I10W5 (1500 RPM, 0.5 BAR INLET PRESSURE, ETHANOL MBT FOR ALL THE FUELS). HIGHLIGHTED SECTION WAS CHOSEN AT 15 CAD AIT TO SHOW THE VALUES IN LARGER SCALES.....	170
FIGURE 6.48. COMPUTED FLAME RADIUS CLOSEST DATA TO 60 AVERAGED CYCLES FOR ALL FUELS (1500 RPM, 0.5 BAR INLET PRESSURE, ETHANOL MBT FOR ALL THE FUELS). HIGHLIGHTED SECTION WAS CHOSEN AT 15 CAD AIT TO SHOW THE VALUES IN LARGER SCALES WITH THE ERROR BARS.....	171
FIGURE 6.49 ERROR BARS FOR COMPUTED FLAME RADIUS CLOSEST DATA TO 60 AVERAGED CYCLES FOR ALL FUELS (1500 RPM, ETHANOL MBT FOR ALL THE FUELS). THE ERROR BARS ARE MULTIPLIED BY 100 (NOT THE ERROR VALUES ABOVE) IN ORDER TO COMPARE ERRORS IN THE SAME GRAPH.	172
FIGURE 6.50. APPARENT FLAME SPEED CLOSEST DATA TO 60 AVERAGED CYCLES FOR BASE FUELS AND WET ETHANOL FUELS (1500 RPM, 0.5 BAR INLET PRESSURE, ETHANOL MBT FOR ALL THE FUELS).	173
FIGURE 6.51. APPARENT FLAME SPEED CLOSEST DATA TO 60 AVERAGED CYCLES FOR B16I84, E10I90, E6B8I85 AND E85I10W5. (1500 RPM, 0.5 BAR INLET PRESSURE, ETHANOL MBT).....	174
FIGURE 6.52. APPARENT FLAME SPEED CLOSEST DATA TO 60 AVERAGED CYCLES FOR ALL THE STUDIED FUELS (1500 RPM, 0.5 BAR INLET PRESSURE, ETHANOL MBT FOR ALL THE FUELS).....	175
FIGURE 6.53. INDIVIDUAL FLAME CONTOURS OF FASTEST SLOWEST AND MEAN CYCLES, STARTING FROM IGNITION UNTIL ONE CONTOUR BEFORE THE OPTICAL WINDOW WAS APPROACHED IN EVERY 3 INTERVALS. (1500 RPM, 0.5 BAR INLET PRESSURE, ETHANOL MBT FOR ALL THE FUELS).	177

FIGURE 6.54. A) FLAME CONTOUR FOR ETHANOL, W5E95, W12E88, W20E80, ISO-OCTANE AND B16I84 CLOSEST TO 60 AVERAGED FLAMES. B) EUCLIDEAN CENTROID DISPLACEMENT MEASUREMENT FOR ALL 4 FUELS CLOSEST TO 60 AVERAGED FLAMES. (1500 RPM, 0.5 BAR INLET PRESSURE, ETHANOL MBT FOR ALL THE FUELS)..... 178

FIGURE 6.55. COMPUTED SHAPE FACTOR SPEED CLOSEST DATA TO 60 AVERAGED CYCLES FOR BASE FUELS AND WET ETHANOL FUELS (1500 RPM, 0.5 BAR INLET PRESSURE, ETHANOL MBT FOR ALL THE FUELS). HIGHLIGHTED SECTION WAS CHOSEN AT 15 CAD AIT TO SHOW THE VALUES IN LARGER SCALES..... 180

FIGURE 6.56. COMPUTED SHAPE FACTOR CLOSEST DATA TO 60 AVERAGED CYCLES FOR B16I84, E10I90, E6B8I85 AND E85I10W5 (1500 RPM, 0.5 BAR INLET PRESSURE, ETHANOL MBT FOR ALL THE FUELS). HIGHLIGHTED SECTION WAS CHOSEN AT 15 CAD AIT TO SHOW THE VALUES IN LARGER SCALES..... 180

FIGURE 6.57. COMPUTED SHAPE FACTOR CLOSEST DATA TO 60 AVERAGED CYCLES FOR ALL FUELS (1500 RPM, 0.5 BAR INLET PRESSURE, ETHANOL MBT FOR ALL THE FUELS). HIGHLIGHTED SECTION WAS CHOSEN AT 15 CAD AIT TO SHOW THE VALUES IN LARGER SCALES..... 181

FIGURE 6.58. COMPUTED VALUES OF UNBURNT GAS TEMPERATURES FOR THE TWO BASE FUELS AND ISO-OCTANE BLENDS. OBTAINED FROM THE TWO-ZONE HEAT RELEASE MODEL. (1500 RPM, 0.5 BAR INLET PRESSURE, ETHANOL MBT FOR ALL THE FUELS). 182

FIGURE 6.59. COMPUTED VALUES OF BURNT GAS TEMPERATURES FOR THE TWO BASE FUELS AND ISO-OCTANE BLENDS. OBTAINED FROM THE TWO-ZONE HEAT RELEASE MODEL. (1500 RPM, 0.5 BAR INLET PRESSURE, ETHANOL MBT FOR ALL THE FUELS). 183

FIGURE 6.60. COMPUTED VALUES OF AVERAGE GAS TEMPERATURE SCALED WITH MASS FRACTION BURNED (AT MASS FRACTION BURNED=0, AVERAGE TEMPERATURE= UNBURNT GAS TEMPERATURE AND AT MASS FRACTION BURNED=1, AVERAGE TEMPERATURE= BURNT GAS TEMPERATURE), THE TWO BASE FUELS AND ISO-OCTANE BLENDS. OBTAINED FROM THE TWO-ZONE HEAT RELEASE MODEL. (1500 RPM, 0.5 BAR INLET PRESSURE, ETHANOL MBT FOR ALL THE FUELS). 184

FIGURE 6.61. COMPUTED VALUES OF UNBURNT GAS TEMPERATURES FOR ETHANOL AND HYDROUS BLENDS. OBTAINED FROM THE TWO-ZONE HEAT RELEASE MODEL. (1500 RPM, 0.5 BAR INLET PRESSURE, ETHANOL MBT FOR ALL THE FUELS). 185

FIGURE 6.62. COMPUTED VALUES OF BURNT GAS TEMPERATURES FOR ETHANOL AND HYDROUS BLENDS. OBTAINED FROM THE TWO-ZONE HEAT RELEASE MODEL. (1500 RPM, 0.5 BAR INLET PRESSURE, ETHANOL MBT FOR ALL THE FUELS). 185

FIGURE 6.63. COMPUTED VALUES OF AVERAGE GAS TEMPERATURE SCALED WITH MASS FRACTION BURNED (AT MASS FRACTION BURNED=0, AVERAGE TEMPERATURE= UNBURNED GAS TEMPERATURE AND AT MASS FRACTION BURNED=1, AVERAGE TEMPERATURE= BURNED GAS TEMPERATURE), FOR ETHANOL AND HYDROUS BLENDS. OBTAINED FROM THE TWO-ZONE HEAT RELEASE MODEL. (1500 RPM, 0.5 BAR INLET PRESSURE, ETHANOL MBT FOR ALL THE FUELS).	186
FIGURE 6.64. COMPUTED VALUES OF UNBURNT GAS TEMPERATURES FOR ALL THE FUELS TESTED. OBTAINED FROM THE TWO-ZONE HEAT RELEASE MODEL. (1500 RPM, 0.5 BAR INLET PRESSURE, ETHANOL MBT FOR ALL THE FUELS).	187
FIGURE 6.65. COMPUTED VALUES OF BURNT GAS TEMPERATURES FOR ALL THE FUELS TESTED. OBTAINED FROM THE TWO-ZONE HEAT RELEASE MODEL. (1500 RPM, 0.5 BAR INLET PRESSURE, ETHANOL MBT FOR ALL THE FUELS).	188
FIGURE 6.66. COMPUTED VALUES OF AVERAGE GAS TEMPERATURE SCALED WITH MASS FRACTION BURNED (AT MASS FRACTION BURNED=0, AVERAGE TEMPERATURE= UNBURNED GAS TEMPERATURE AND AT MASS FRACTION BURNED=1, AVERAGE TEMPERATURE= BURNED GAS TEMPERATURE), FOR ALL THE FUELS TESTED. OBTAINED FROM THE TWO-ZONE HEAT RELEASE MODEL. (1500 RPM, 0.5 BAR INLET PRESSURE, ETHANOL MBT FOR ALL THE FUELS).....	189
FIGURE 6.67. COMPUTED VALUES OF LAMINAR BURNING VELOCITY FOR THE ETHANOL, ISO-OCTANE, AND E10Iso90. (1500 RPM, 0.5 BAR INLET PRESSURE, ETHANOL MBT FOR ALL THE FUELS).....	190

List of Tables

TABLE 2.1. PROPERTIES OF ISO-OCTANE AND GASOLINE COMPARED WITH TWO ALCOHOL FUELS (ETHANOL AND BUTANOL). ADAPTED FROM HEYWOOD, TURNER, ZHAO, AND BROUZOS [29,63,74].	34
TABLE 2.2. WTT, WTW, AND TTW GHG EMISSIONS (CO ₂ EQUIVALENTS) FOR A SELECTION DIFFERENT BIOFUEL FOR 2010. ADAPTED FROM [91].	37
TABLE 3.1. KEY ENGINE SPECIFICATIONS.	45
TABLE 5.1. LENS CONFIGURATION.	85
TABLE 5.2. EMISSION PEAKS OF KEY COMBUSTION SPECIES IN IC ENGINE [YANG, ZHAO AND MEGARITIS, 2009]	94
TABLE 5.3. COMPARISON OF THE MAJOR TECHNIQUES OF CAPTURING FLAME PROPAGATION IN THE CYLINDER [178,180,181].	102
TABLE 6.1. FUEL PROPERTIES OF THE THREE BASELINE FUELS.	125
TABLE 6.2. ENGINE OPERATING PARAMETERS.	126
TABLE 6.3. TURBULENCE INTENSITY MEASURED AT 30°,40°,90°, AND 180° CA BTDC IN 4 ZONES.	129

Nomenclature

Abbreviations

AFR	Air- Fuel Ratio	aTDC	After top dead centre.
AV	Average velocity	B16I84	16% n-butanol in iso-octane
BDC	Bottom dead centre	BMEP	Brake Mean Effective Pressure
BSFC	Brake Specific Fuel Consumption	bTDC	Before top dead centre.
CA	Crank angle	CA_Pmax	Crank angle location of maximum pressure
CA50	Crank angle location of 50% mass fraction burned	CAD	Computer Aided Design
CAD AIT	Crank angle degree after ignition timing	CFD	Computational fluid dynamics
CMOS	Complementary Metal Oxide Semiconductor	CO	Carbon monoxide
COV	Coefficient of variation	DAQ	Data Acquisition
DI	Direct Injection	DISI	Direct injection spark ignition
DNS	Direct Numerical Simulation	EMOP	Exhaust maximum opening point
EU	European Union	EGR	Exhaust Gas Recirculation

FPS	Frame per second	FDA	Flame Development Angle
I	Intensity	ICCD	Intensifier charged-couple device
ICE	Internal combustion engine	IMOP	Intake maximum opening point
LES	Large Eddy Simulation	MBT	Maximum Brake torque
MFB	Mass Fraction Burned	NBR	Nitrile Butadiene Rubber
NEDC	New European Drive Cycle	NOx	Nitrogen Oxide
OH	Hydroxyl Radical	PC	Personal Computer
PFI	Port Fuel Injection	PIV	Particle image velocimetry
PLIF	Planar Laser-Induced Fluorescence	Pmax	Maximum in-cylinder pressure
RANS	Reynolds-Averaged Navier-Stokes	RMS	Root mean square
RNG	Re-Normalisation group theory	RON	Research octane number
ROHR	Rate of Heat Release	RPM	Revolution per minute
SI	Spark Ignition	SOI	Start of Injection
TDC	Top dead centre.	THC	Tetrahydrocannabinol
TI	Turbulence intensity	WTT	Well to Tank
WOT	Wide Open Throttle	WTW	Well to Wheel
TTW	Tank to Wheel	TTL	Transistor-Transistor Logic

Symbols

Δ	-	Difference
\dot{m}_e	Kg/s	Entrained mass flow rate
\bar{u}_i	m/s	Mean velocity
u'_{kr}	m/s	Local effective r.m.s. turbulence velocity
Γ_φ	-	Exchange coefficient
$\bar{\Delta}$	-	Filter width
$\bar{\phi}'$	-	Filter function
A_s	m^2	Squish area
C_D	-	Drag coefficient
D_L	mm^2/s	Molecular diffusivity
I'	-	Intensity distribution
K_t	$W.m^{-1}.K^{-1}$	Thermal conductivity
N_d	-	Number of data
P_C	mm	Length of contour perimeter
P_C	mm	Length of circle perimeter
Q_{HV}	MJ/kg	Heating value
R_s	m/s	Swirl ratio
R_t	-	Coefficient of the fluctuating velocity (time)
R_x	-	Coefficient of the fluctuating velocity (distance)
S_p	m/s	Instantaneous piston speed
S_l	m/s	Unstretched laminar burning velocity
S_n	m/s	Stretched laminar burning velocity
\bar{U}	m/s	Mean flow velocity

c_p	kJ/kg.K	Specific heat capacity (constant pressure)
c_v	kJ/kg.K	Specific heat capacity (constant volume)
f_μ	-	Damping function
l_I	mm	Integral length scale
l_k	mm	Kolmogorov length scale
u'	m/s	r.m.s. Turbulence velocity
u_{te}	m/s	Turbulent entrainment velocity
v_{sq}	m/s	Squish velocity
δ_l	mm	Laminar flame thickness
η_f	-	fuel conversion efficiency
τ_I	sec	Integral time scale
ω_n	Rad/s	Rotating crankshaft angular speed
ω_s	m/s	Solid body angular speed
$\bar{\phi}$	-	Time- mean
$\acute{\phi}$	-	Fluctuation
A	mm ²	Area
B	mm	Bore
C	mm	Conrod length
\hat{C}	-	Mean number of particles per unit volume
d	-	Constant displacement
D	mm	Engine displacement
K	-	Karlovitz stretch factor
k	kJ/kg	Turbulence kinetic energy
ℓ_1	mm	Proportionality constant

M	-	Magnification factor
NPI	-	Number of pixels
p	bar	Pressure
Q	kJ/s	Heat Transfer
r	mm	Radius
Re	-	Reynolds number
Re_T	-	Turbulent Reynolds Number
U	m/s	Velocity
V	m ³	Volume
Z	mm	Distance between the piston crown top and the cylinder head
Ψ	-	state of the particle ensemble
Le_l	-	Lewis number
Ma_l	-	Markstein number
S	-	Strain rate
U	m/s	Instantaneous local fluid velocity
t_l	sec	Time
ν	m ² /s	kinematic viscosity
γ	-	Ratio of specific heats
ε	m ² /s ³	Turbulent kinetic energy dissipation rate
ρ	kg/m ³	Density
τ	-	Kolmogorov micro-scale
φ	-	Fluid property
ω	m ² /s ³	Specific dissipation rate
ϕ	-	Instantaneous scalar quantity

μ	kg/m.s	Dynamic viscosity
φ	-	System size
Δz_0	m	Laser sheet thickness
Δx^2	m ²	Interrogation area

1. Introduction

1.1 General Background and Incentive

The Spark Ignition (SI) engine remains the major source of propulsion for passenger cars on a global scale. Within Europe, the diesel remains dominant, however recent advancements in gasoline engine downsizing together [1,2] with the recent “dieselgate” emissions scandal has resulted in considerable uncertainties around the dominance of this powertrain platform. As a result, there is now elevated focus upon powertrain electrification, where the “cleaner” gasoline is well suited to hybrid and electric range extender concepts foreseen to attract significant market share in the medium term [3,4].

The adoption of ethanol has attracted considerable interest in recent years, especially when produced from renewable sources. During the ethanol production process, irrespective of the crop used, the resulting mixture from the fermentation process contains more than 85% volume of water [5]. Distillation can be used to separate this water until the mixture reaches the azeotropic point (approximately 94% ethanol-in-water v/v, so-called hydrous ethanol). Subsequently, diverse dehydration techniques can be used to obtain anhydrous ethanol (99% ethanol, or purer). Thus, a large quantity of energy is expended during the distillation and dehydration processes in order to remove the water excess, especially after the mixture reaches around 80% of ethanol-in-water [6]. For this reason, several researchers have studied the best compromise between net energy gain during the ethanol production process and water-in-ethanol content from different crops and production processes [7–10]. From such studies it can be deduced that the best compromise is between 80% and 90% of ethanol-in-water (v/v) based upon net gain.

It follows that the direct use of “wet” ethanol (ethanol-in-water mixtures with less than 95% ethanol v/v) in spark ignition engines have attracted recent interest. In general, the higher water content acts as a diluent and requires more advanced spark timing to reach MBT (Minimum spark advance for Best Torque) [6,7]. The Flame Development

Angle (FDA), combustion duration and heat release rates also deteriorate as a result of lower combustion temperatures [11–13]. As a result, the unburned fuel fraction, aldehyde emissions and other hydrocarbon emissions can be increased with increased water content [14]. In addition to increased emissions, the application of high water-in-ethanol content mixtures in vehicles may have the energy and environmental impact benefits counterbalanced by worse specific fuel consumption with the issues of water separation in flex-fuel gasoline blends [15]. In practical terms, hydrous ethanol may be more suitable for future dedicated ethanol SI engines, where modern central direct injection systems can overcome the challenges associated with the cold start of E100 [16,17].

Despite the relative apparent maturity of the SI engine, many of the interactions that occur during combustion are complex, with cycle to cycle variations in the in-cylinder flow (bulk and smaller scale), spark energy, charge homogeneity (with some stratification in fuel and/or EGR unavoidable) and flame-wall interactions and arising heat transfer [18,19]. During combustion, the spark initiates a flame kernel between the electrodes that is initially laminar in nature, with local turbulence quickly serving to convect and distort the flame [20,21]. As the flame grows progressively larger scales of turbulence are encroached, which beneficially wrinkle the flame surface, leading to a larger entrainment area provided excessive stretch rates are not incurred [22]. Conversely, the flame development slows as the walls are approached, with progressively smaller scales left available ahead of the flame and wall heat transfer affecting the rate of mass burning. By the time the flame reaches the periphery, a considerable proportion of mass has been entrained but remains in unburned pockets behind the kernel [22]. Overall the flame propagation therefore, involves complex physical and chemical interactions, which remain difficult to reliably simulate by any means. Experimental methods to simultaneously image the flow and flame have previously been attempted but usually involve compromise in spatial or temporal resolution. For example, Ruess [23] employed PIV with simultaneous planar flame imaging via Mie scattering, but significant compromises were necessary for the seeding density which led to lack of clarity in the definition of the flame front. Elsewhere, Cairns and Sheppard [22] adapted a dual seeding approach, where planar flame images were captured at high resolution via Mie scattering (with fine particles of Titanium dioxide adapted) while larger particles (culinary white pepper) were simultaneously

injected through the cylinder wall and tracked via Particle Tracking Velocimetry. The work uncovered some useful flame-flow interactions (such as the flame “pinching” the flow and accelerating existing bulk air motions), but flow tracking was sparse and not suitable to define spatial and temporal variance in turbulence (with the method also highly laborious to employ over multiple cycles).

The currently reported work has been concerned with improving understanding of the behaviour of the combustion events with such potential future fuels on both an individual and averaged basis, with PIV flow information also available. In particular, the effects of bulk flame migration were studied to understand the sensitivity of such events in the presence of varying in-cylinder turbulence with differing fuels. In addition, several flame related parameters, such as shape factor and apparent flame speed, are discussed and compared with the flow and heat release analysis.

1.2 Thesis Outline

The work reported in this thesis was concerned with improving understanding of the interaction of bulk air motions with the flame propagation when using potential future fuels on combustion characteristics in a spark ignition research engine. In Chapter 2, a literature review is presented which includes descriptions of the common efficiency losses in gasoline spark ignition engines. This is followed by an overview of basic theory and techniques for defining turbulent in-cylinder flow and combustion with hydrous and anhydrous fuels. Provided in Chapter 3 are descriptions of the optically accessed research engine and associated auxiliary equipment. Set out in Chapter 4 are details of computational fluid dynamic techniques and a review of essential principles required to predict the in-cylinder flow. Presented in Chapter 5 are details of imaging techniques for the flow and the flame alongside thermodynamic analysis of each imaged cycle. In Chapter 6, the imaging and analysis results of the currently reported study are presented and discussed. Finally, reported in Chapter 7 are the conclusions of this research, with recommendations for future work.

2. Flow & Combustion in Spark Ignition Engines

2.1 Introduction

Climate change is clearly linked to human-generated greenhouse gas emissions such as carbon dioxide, methane, and nitrous oxide [24], even though these changes are part of a natural cyclic phenomenon as well. The majority of these perturbations primarily result from emissions associated with energy use and are produced in order to support population and economic growth. For these reasons global greenhouse gas (GHG) emissions are indispensable and must be reduced in order to hold the global average temperature to well below 2°C above pre-industrial levels, with efforts underway to limit the temperature increase to 1.5°C above pre-industrial levels by 2030 through the adoption of the Paris Protocol agreement, Article 2 [25]. Recently, the EU legislation set CO₂ emission target for sales-weighted new cars rose for the first time on record in 2017, up 0.8% from 120.1g/km to 121.0g/km. This was primarily associated with decreasing diesel sales following adverse media attention. The industry target is to reduce fleet greenhouse gas emissions by 20% by 2020 (from 1990 levels) to an average of 95g/km. A financial penalty of €95 for each gram of CO₂ emission exceeding the limit multiplied by the EU-wide registration will be applied if in any case the CO₂ emission target cannot be reached [26].

The transport sector is responsible for about 25% of the total carbon dioxide emissions in the European Union and roughly 30% in the USA. Presented in Figure 2.1 is the World transportation sector delivered energy consumption by energy source from 2010 to 2040 in quadrillion Btu units. It can be seen gasoline and diesel engines are responsible for around 75% of consumed energy, summing up to approximately 80 quadrillion BTU, which is expected to increase by 50% to 120 quadrillions BTU in 2040. Motor gasoline including ethanol blends remains the largest transportation fuel, but its share of total transportation energy consumption is expected to decline from

39% in 2012 to 33% in 2040 [27]. It is imperative to consider that the data presented in Figure 2.1 were published before dieselgate and this resulted in more restrictions toward diesel. The scandal also has turned attention to more electrification which will be discussed further later in this chapter.

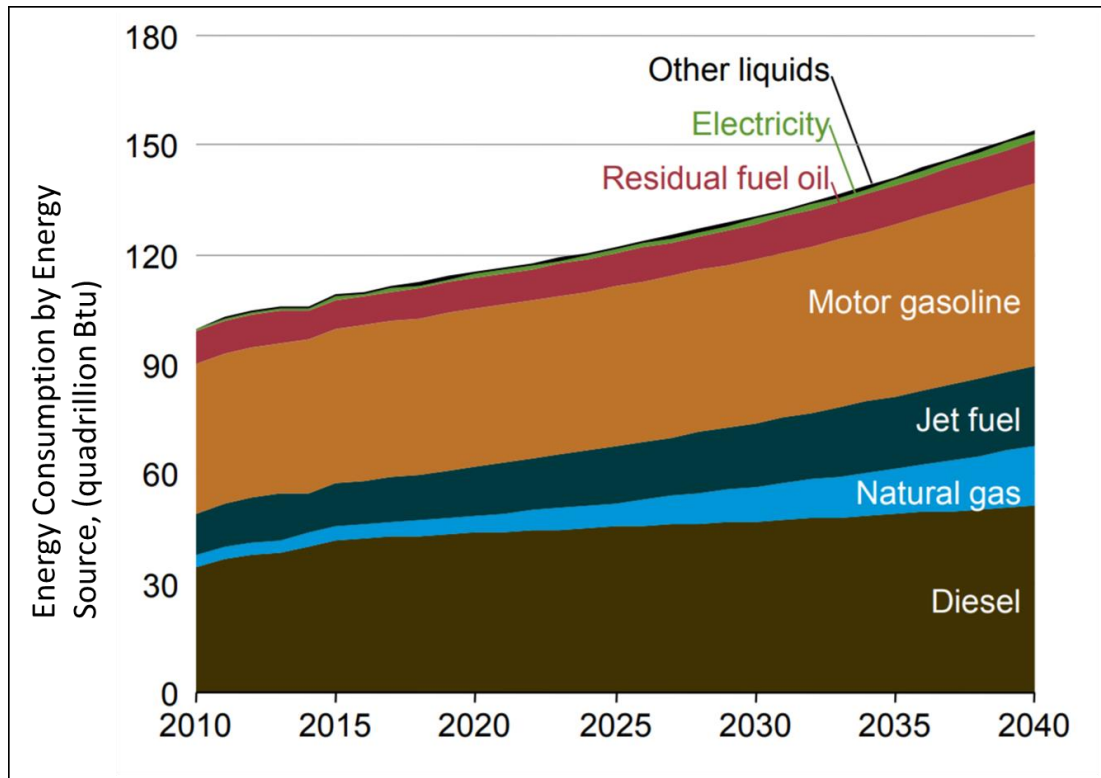


Figure 2.1. Transportation sector energy consumption estimative (adapted from [27]). More stringent legislation limits can be considered as the main reason for the lower share of road vehicles energy demand to reduce fuel consumption and CO₂ emissions per kilometer. A clear comparison of fuel consumption from this legislation for passenger cars is EU 2015 legislation set average manufacturers' fleet target limits on fuel consumption of 5.6 l/100 km for gasoline cars and 4.9 l/100 km for diesel in comparison this will expected to reduce to 4.1 l/100 km of gasoline and 3.6 l/100 km of diesel in 2021 [28].

More g CO₂/km emissions can be expected for heavier vehicles. It is a necessity to have different size vehicles to be fit within these limits, a g CO₂/km to vehicle weight curve has been proposed to consider the new European driving cycle (NEDC). Nevertheless, extremely low emission vehicles (below 50 g CO₂/km) have a higher weight in the average fleet count. These reasons pushed manufacturers to produce hybrid and fully electrified vehicles to offset “dirtier” vehicles and reduced rates of

technology application in conventional vehicles. Other countries have similar regulations, as shown in Figure 2.2.

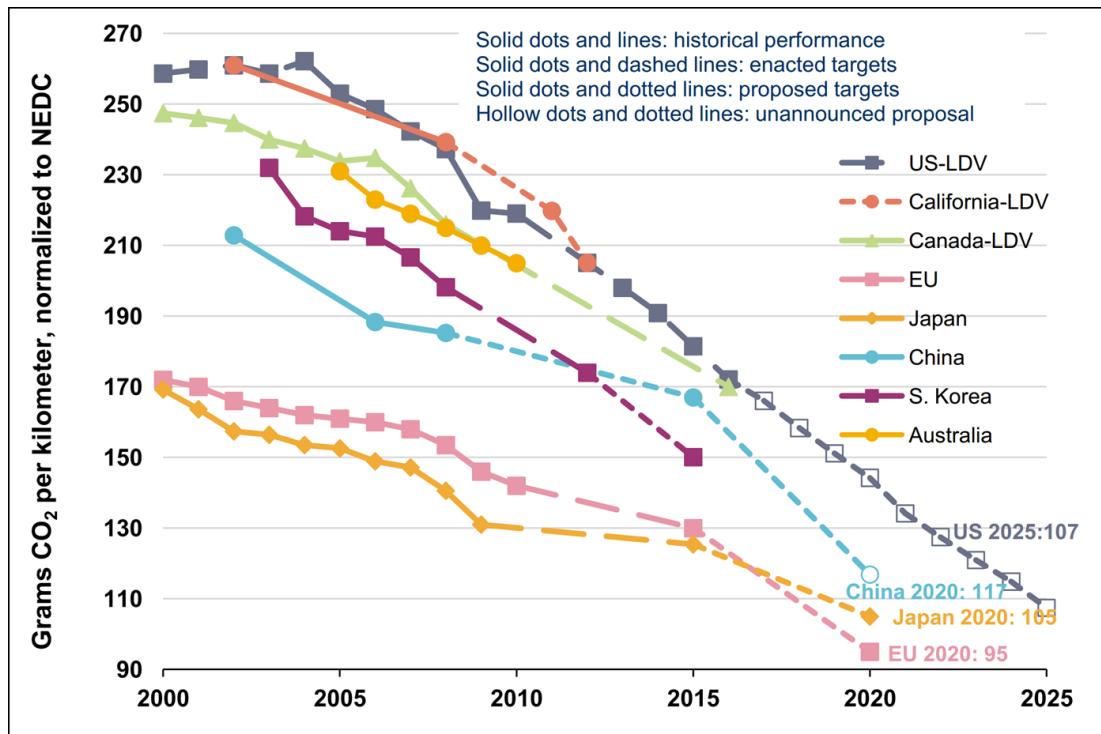


Figure 2.2. Comparison of global regulations for passenger cars [29].

The recent “Dieselgate” scandal has turned attention to regulations against the pollutant emissions from both diesel light and heavy-duty passenger vehicles. Moreover, many cities around the globe have shown the intent to encourage a diesel engines ban in urbanized centres. This will eventually lead to heavier vehicle electrification and most importantly more gasoline vehicles. Considering how the electricity is generated, there will be only local emissions improvements with the possibility of an increase in total CO₂ emissions, especially if coal is used. A rise of electrification of passenger car powertrains – whether through hybridization or substitution with pure battery-electric architectures is unavoidable especially if US 2025 CAFE, EU targets for 2021 and China Phase 4/5 are to be met [4]. However, this requires substantial market penetration of hybrid electric vehicles (HEVs) and battery electric vehicles (BEVs). A recent “white paper” report from Ricardo [4] shows passenger car powertrain options currently available, together with a broad estimate of CO₂ emissions savings and relative increase in costs. It can be seen that fuel cell and Battery Electric Vehicles (BEV) are among those technologies with the highest carbon reduction potential. However, the cost impact is significantly higher in comparison to

conventional gasoline internal combustion engines (ICE) [4]. The future of electrified powertrains is difficult to predict due to current market complexity and politics. Reliable market projections must necessarily be based on a scenario comprising assumptions on the development of government policies, legislation, incentives, customer preferences, the availability of attractive vehicles with an electrified powertrain, the likely investment in charging infrastructure, and future battery costs. Presented in Figure 2.3 is the Ricardo view as to how the powertrain mix of 2030 could be influenced by the level of charging infrastructure investment between now and then. It can be seen that if limited investment in charging infrastructure is considered then it leads to focus of BEV use in the smaller-size vehicles. Instead, a noticeable increase in Plug-in Hybrid Electric Vehicle (PHEV) usage can be seen as consumers find the benefits of city-based Zero Emission Vehicle (ZEV) use while using the combustion engine for extra-urban and long-distance journeys. If a policy of more aggressive investment in charging infrastructure is followed, then the PHEV market is tremendously reduced, and BEV application will be spread across a much broader range of vehicle segments. Ricardo [4] believes with car manufacturers moving toward attractive vehicles with more spacious interior concepts, high penetration rates for BEV are very much possible. For instance, the Volkswagen group has mentioned that it expects its battery electric vehicle (BEV) share to increase to 25 percent in 2019 and subsequently 50 percent by 2030. However major challenges in charging infrastructure to solve the problem of range and queuing anxiety of both private and fleet buyers must be considered.

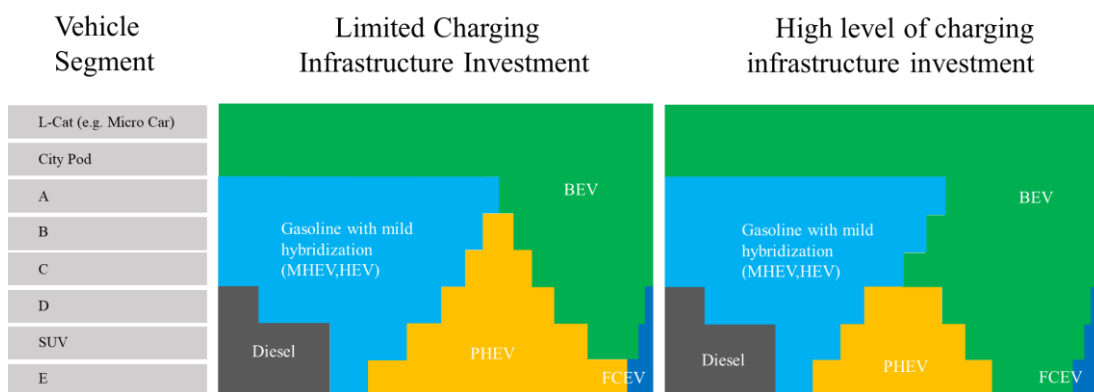


Figure 2.3. Ricardo view of the 2030 passenger car electrified powertrain mix in Europe. Adapted from Ricardo [4].

This report also emphasizes the fact that by 2030, a good 70% of all cars sold worldwide will still have an ICE with a minimum powertrain electrification level of

mild hybrids. Continuing advances in the internal combustion engine are expected to decrease gasoline energy consumption, the key technologies are explained later on in the Spark Ignition Engine Operation section.

2.1.1 Spark-Ignition Engine Operation

To convey more in depth understanding of the fundamentals four-stroke engine operating principle can be described by four phases (induction, compression, expansion, exhaust) of 180 crank angle degrees (CAD) each, taking two crank revolutions to complete a thermodynamic cycle. One way to study the performance of four-stroke SI engine is by analyzing its theoretical cycle. The theoretical cycle is an approximation to the real cycle with many simplifications such as [30,31]

1. Constant pressure induction of mass of air.
2. Reversible adiabatic (isentropic) compression of the charge as the piston moves from bottom dead centre (BDC) to top dead centre (TDC).
3. Reversible constant-volume heat transfer to the working gas from an external source while the piston is at top dead centre. This process is intended to represent the ignition of the fuel-air mixture and the subsequent rapid burning.
4. Reversible adiabatic (isentropic) expansion (power stroke)
5. Reversible constant-volume process in which heat is rejected from the air while the piston is at bottom dead centre.
6. Mass of air is released to the atmosphere in a constant pressure process.
7. Considering instantaneous valve events.

In the real cycle, there are many losses such as pumping losses, heat transfers, combustion losses, blowby losses, and blowdown losses. Also, the valve events do not

occur instantaneously and start at the TDC or BDC. Presented in Figure 2.4 is a comparison of theoretical and actual PV diagrams for four-stroke Otto Cycle engine, indicating losses mentioned before.

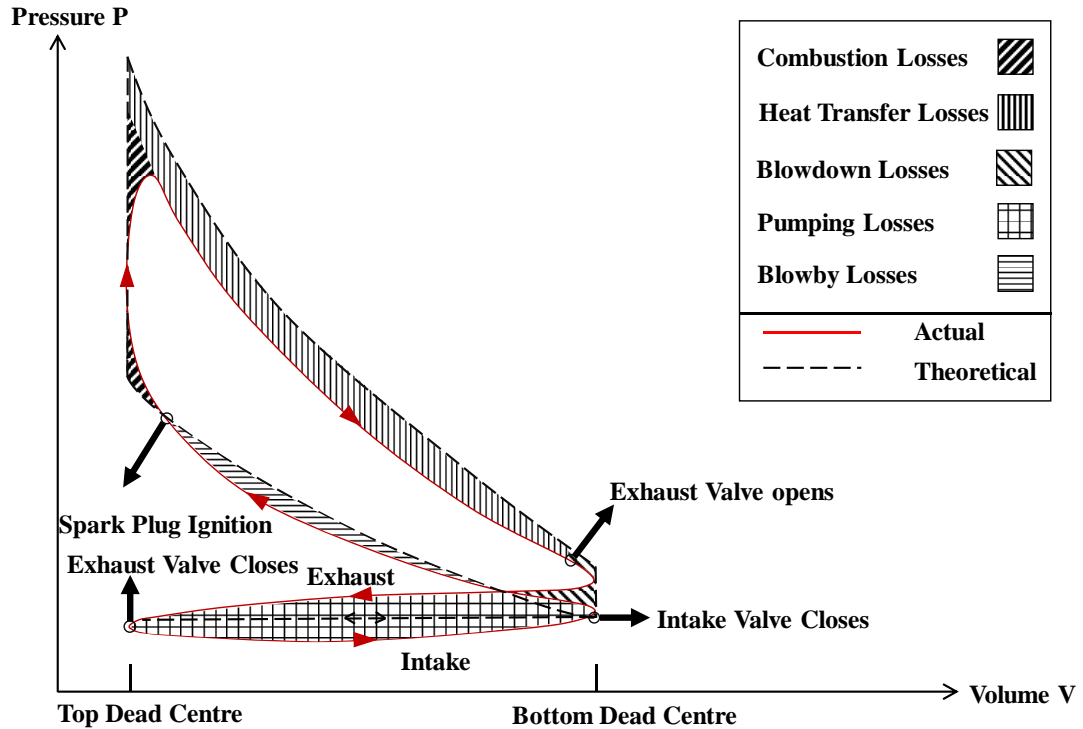


Figure 2.4. Comparison of theoretical and actual PV diagrams for four-stroke Otto Cycle engine.

A BSFC map indicates the rate of fuel consumption over the entire operating range of an ICE and is a convenient tool to understand the magnitude of the relative losses of particular engine design. A modern naturally-aspirated Spark-Ignition (SI) engine has minimum Brake Specific Fuel Consumption (BSFC) somewhere near the centre of the engine speed-load map. There is normally a slight bias towards higher loads and lower speeds [32]. The BSFC can be used to compute the engine efficiency also known as fuel conversion efficiency of an engine using the following formula:

$$\eta_f = 1/BSFC \cdot Q_{HV} \quad (2.1)$$

Where Q_{HV} (Lower Heating Value) for regular gasoline = 12.06 kW·h/kg, any engine has a different efficiency at different load and speed as the BSFC value is changing in respect with the lowest BSFC value at full load (when the intake air is unthrottled) and maximum torque. For SI engines typical best values of brake specific fuel consumption

are about 270 g/kW.h which is equivalent to a fuel conversion efficiency of 30% [31]. The actual efficiency can be lower or higher than the engine's average due to varying operating conditions.

There are 5 dominant losses behind the BSFC map that reduce efficiency as the operation is moved away from the "sweet spot" of minimum BSFC. These mechanisms are labelled in Figure 2.5 each of these parameters plays a significant role in reducing engine efficiency.

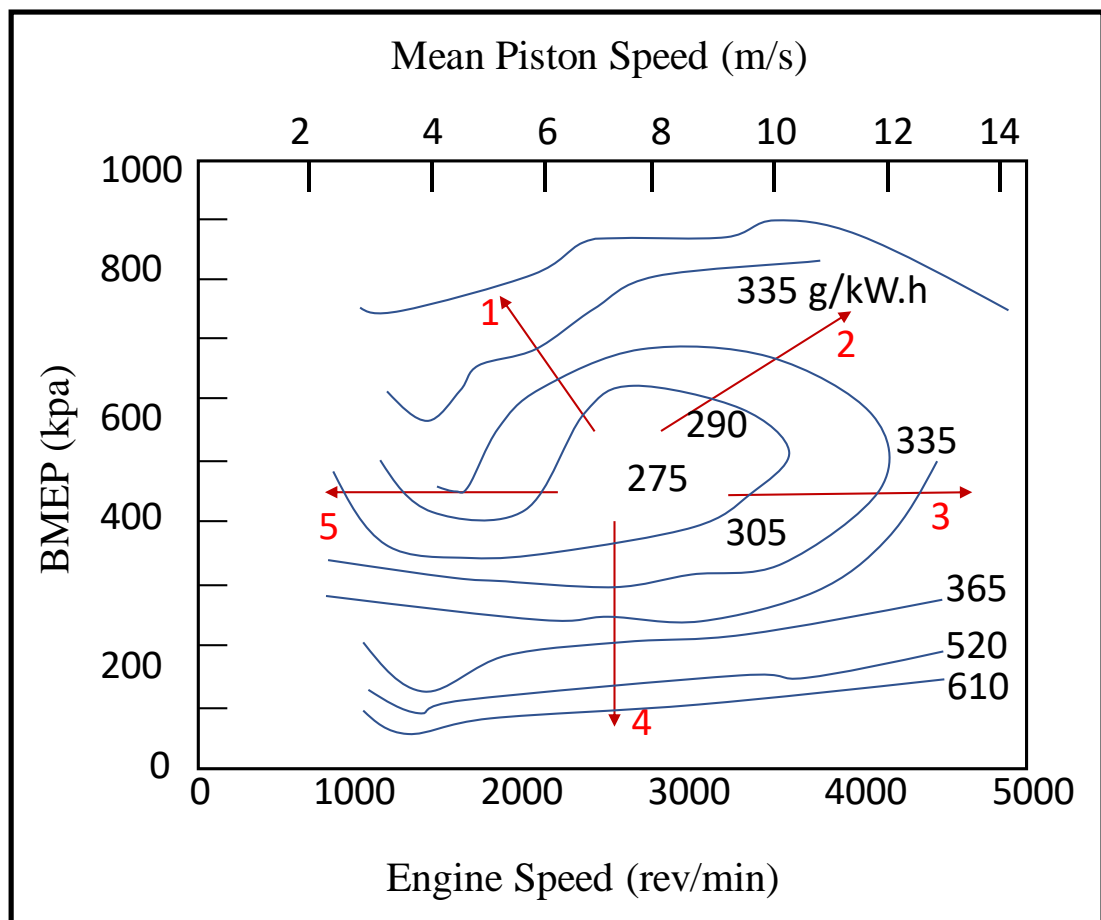


Figure 2.5. BSFC map for a naturally-aspirated spark-ignition engine, with numbers showing the typical losses in an SI engine. (1) Knock limited, spark retard (2) Component temperature limited, fuel enrichment (3) Increased frictional losses (4) Increased pumping losses (5) Increased relative heat transfer losses. Each arrow significance is briefly described below.

2.1.1.1 Spark Retard due to Knock Limited Operation

The thermal efficiency of an SI engine is increased in direct relation with compression (and hence expansion) ratio. A limitation arises as gas temperature also increases in

direct relation with compression ratio and efficiency. Therefore, to maximise engine efficiency the compression ratio is increased to a point when end gas knock occurs at high load and low speed, where the knock is then deemed to excessively limit low speed performance and/or the fuel economy. The problem is exacerbated in modern downsized SI engines due to the Low Speed Pre Ignition (LSPI) and Super Knock phenomenon associated with suspended lubricant [33]. Otherwise, to avoid “conventional” knocking combustion a retarded spark timing is required to move away combustion phasing from the Maximum Brake Torque (MBT) location. Through this design process, the engine efficiency is increased in areas where the engine is most commonly operated in exchange for decreased efficiency in an area of the speed-load map where the engine has previously been rarely operated [30,31]. This is more problematic an approach in aggressively downsized and down-speed IC engines, where alternative knock reduction strategies must be sought such as water injection or cooled EGR [34,35].

2.1.1.2 Fuel Enrichment due to Temperature Limited Operation

Achieving maximum performance of an engine is possible at high speed and high load. However, as a result, the total heat transferred to the walls is also increased to its maximum value. At such high temperatures, the exhaust and in-cylinder components of an engine are vulnerable to thermal load related failures. Alternatively, sustained high temperatures can lead to pre-ignition. The most common failures occur in the following components: spark plugs, sharp combustion chamber edges, exhaust valves, pistons, emissions after-treatment systems and turbochargers (where applicable). In order to reduce this high temperature, over-fueling can be used [36,37]. This over-fueling leads to rich combustion and eventually reduces the in-cylinder temperature prior to combustion albeit at the expense of three-way catalyst efficiency.

2.1.1.3 Increased Engine Friction

Engine frictional losses increase as a function of engine speed squared [31]. This friction also increases at higher engine load due to higher pressure from combustion and ultimately increasing rubbing friction between the cylinder liner and piston rings.

Therefore, the energy required to compensate these losses also increases and leads to lower engine efficiency. It can be seen from Figure 2.6 that rubbing friction mean effective pressure is increased as the load increases under firing, whereas it is roughly constant in motoring conditions. It can be concluded that this difference is due to higher temperatures at higher loads but it is widely agreed that the speed effect dominates the frictional losses [31].

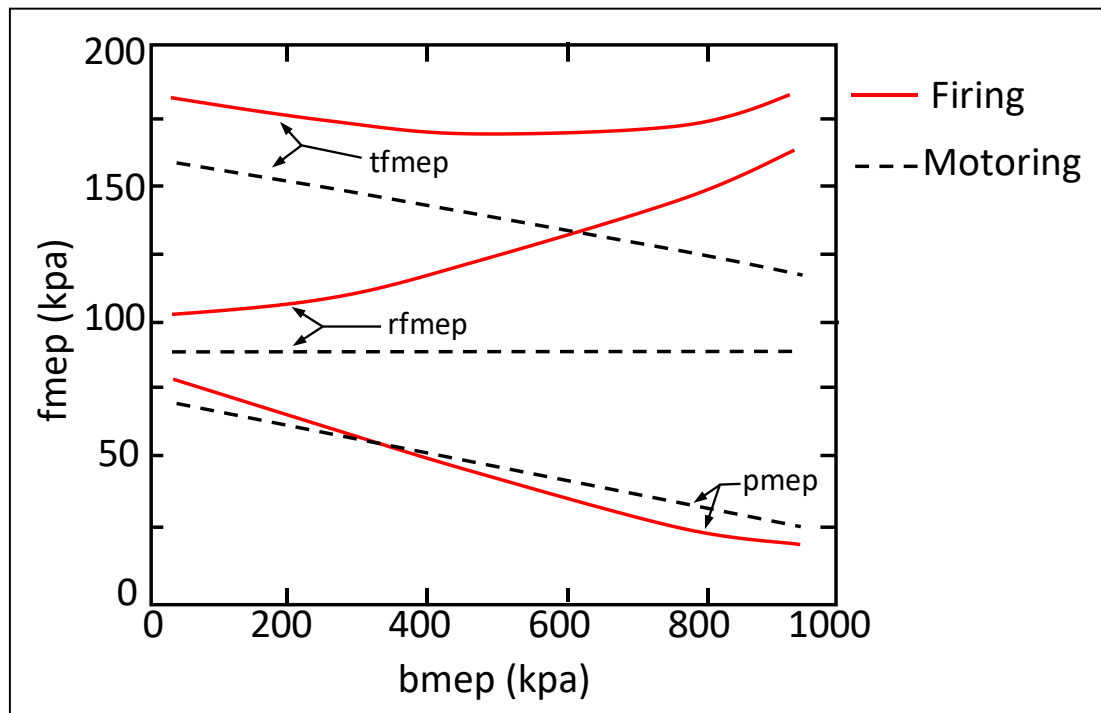


Figure 2.6. Total friction mean effective pressure (tfmep), rubbing friction mep (rfmep) and pumping mep (pmep) as a function of load for four-cylinder spark ignition engine, adapted from [31].

2.1.1.4 Pumping Losses

A stoichiometric air-to-fuel ratio is commonly used in an SI engine, primarily due to the synergy with a lower cost three-way catalyst and acceptable trade-offs with combustion and thermal efficiencies [31]. In the case of rich combustion, the efficiency is decreased with the following benefits, producing a faster burn (when slightly rich) and reducing dissociation effects lead to more power with lower exhaust gas temperatures. Under stoichiometric conditions, the air mass flow into the engine must be reduced in direct proportion to the load and hence fuel mass. This is typically achieved by fitting the intake air gas path with a throttle mechanism, which reduces

the intake air pressure below atmospheric pressure at part load. As the engine must still expel the gas at atmospheric pressure (or higher) this results in negative pumping work that must be overcome using a proportion of the induced energy. The pumping work is therefore defined as the net work required per cycle to charge the air into and exhaust gasses out of the cylinder. The relative influence of the pumping loss of the engine used within this work is illustrated in Figure 2.7.

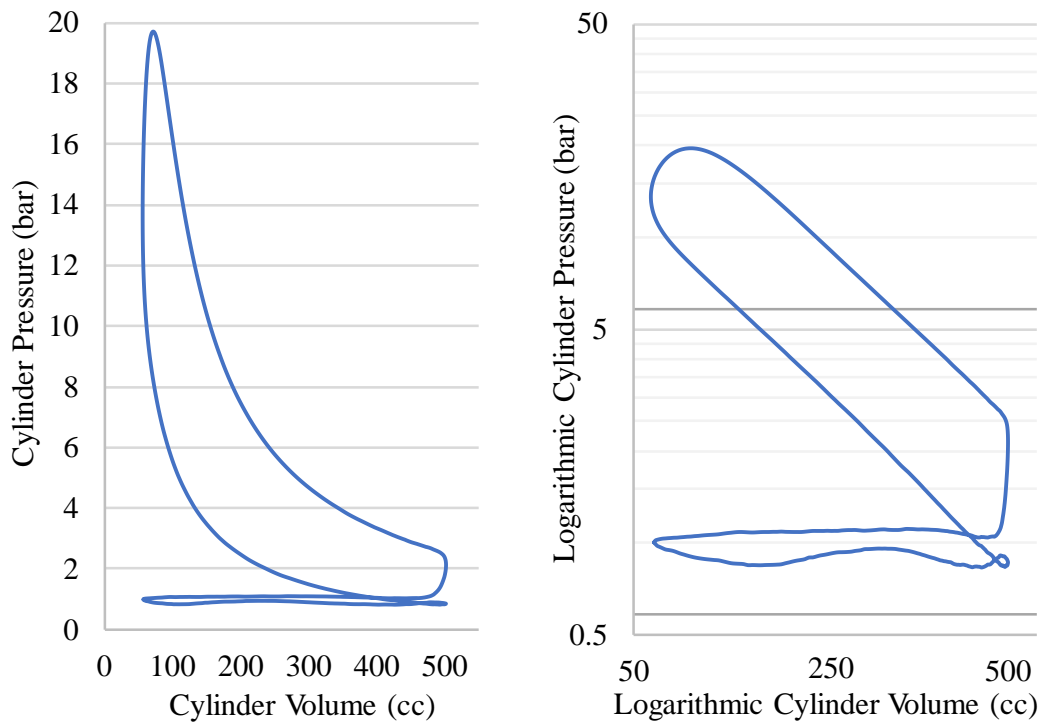


Figure 2.7. Graphical illustration of pumping losses in conventional and logarithmic scaled in-cylinder pressure-volume diagrams.

2.1.1.5 Increased Heat Transfer

Engine efficiency is limited by heat transfer from the working fluid into the engine components such as the cylinder head, valves, piston crown, and cylinder liner. Heat transfer and combustion duration are directly related, so an increase in one eventually increases the other. This may happen as the engine speed is reduced to less than the area of minimum BSFC (when there is an increase in heat transfer due to longer time available during combustion for heat transfer at low engine speeds, as displayed in Figure 2.8).

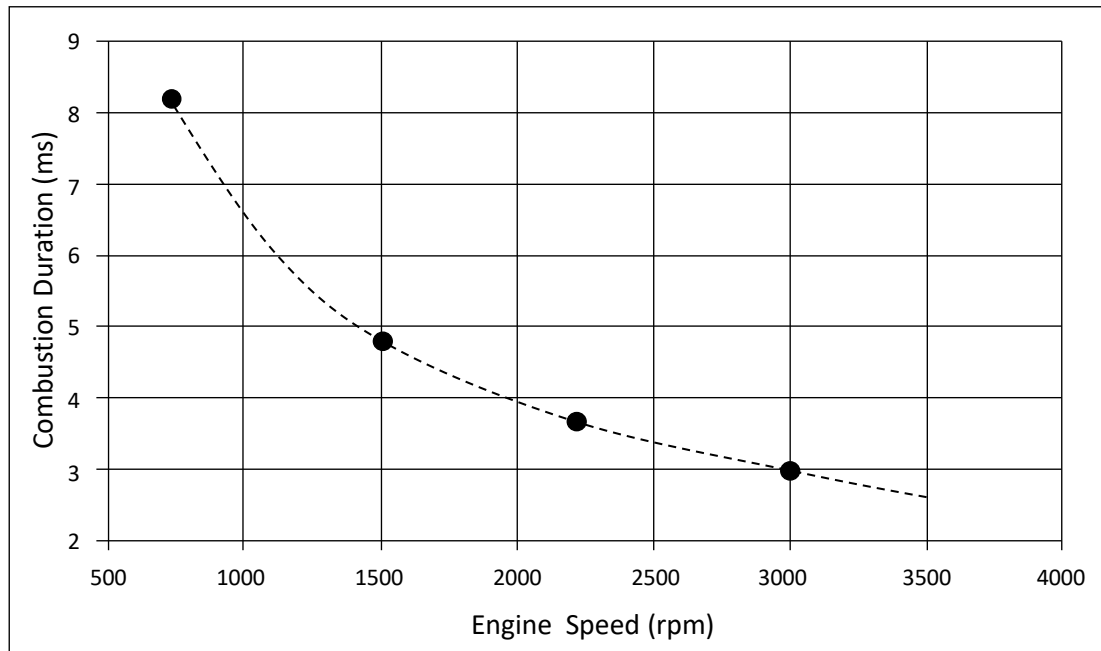


Figure 2.8. Combustion duration in milliseconds against engine speed. Figure created from data published by Hires [38].

2.1.1.6 Other Losses

Five main specific losses have been outlined thus far, however, some other sources of energy losses exist. Presented in Figure 2.9 is a typical thermodynamic “split of losses” for an automotive SI engine under the following operating conditions: 5bar net Indicated Mean Effective Pressure (IMEP_{net}) and 2000rpm. It can be seen that the pumping losses discussed in Section 2.1.1.4 have been included in this split (labelled “gas exchange”), this can be used as a reference value to compare the contribution of the other losses. While these pumping losses are a noticeable proportion, it is clear that the other losses are by no means negligible. Figure 2.9 illustrates that a tremendous amount of work is lost due to the heat that is transferred through the combustion chamber walls (almost twice the pumping losses). Additionally, if the compression stroke and combustion were assumed adiabatic (no heat transfer across walls), the combustion phasing losses could also be excluded as advancing the crank angle location of 50% mass fraction burned (CA₅₀) to Top Dead Centre (TDC) would eliminate this loss. This, of course, neglects the onset of knock in real engines at higher loads. The magnitude of heat loss can be described as the combination of these two losses through the combustion chamber and liner walls. Real charge is already oriented very closely to the engine and operating point under analysis, and therefore consider

whether a full-load or partial-load operating point is analyzed. Incomplete combustion takes in to account no complete combustion, as a result of which its theoretically attainable chemical equilibrium is not reached. It is important to note losses for $\lambda < 1$ is considered in Real charge. The loss resulting from the real combustion characteristics should be taken into consideration including duration and shape of the real combustion characteristic. Loss resulting from real gas behavior is considered with thermodynamic properties of the cylinder content as a function of pressure and temperature.

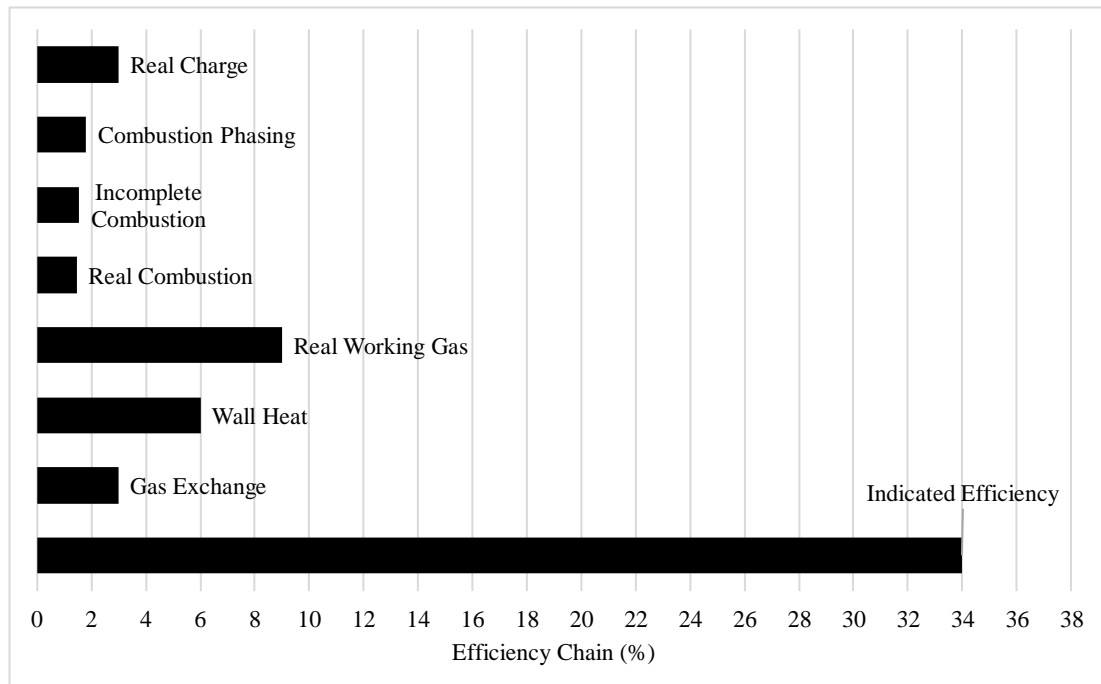


Figure 2.9. Diagram showing the energy split for typical gasoline SI engine at 5bar net IMEP and 2000 rpm, data adapted from [39].

Combustion phasing can be described with a constant-volume process with heat release at the combustion centre of gravity to quantify the difference to the ideal constant volume combustion at top centre. This is shown in Figure 2.10 by defining a modified compression ratio CR^* that is the outcome of phasing of the 50% mass fraction burned location of $TC \rightarrow TC^*$ [39].

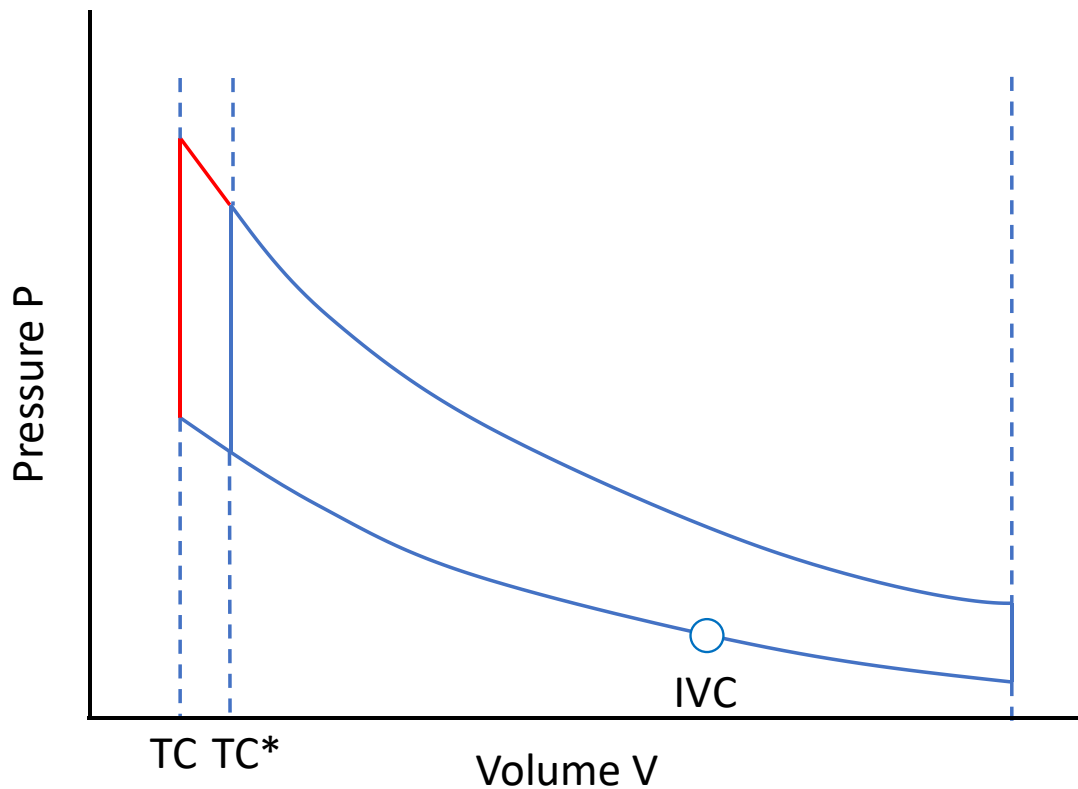


Figure 2.10. Combustion phasing loss reduces the compression ratio in the ideal constant volume process. Adapted from [39].

2.2 Reducing Losses in SI Engines

2.2.1 Engine Downsizing

Two common approaches have arisen to reducing engine pumping losses:

- 1 Load point shifting (essential avoidance of mapped areas of high pumping work via techniques such as downsizing or cylinder deactivation)
- 2 Reduced intake throttling via variable valve actuation (to either increase charge dilution or redirect the throttling to the valve itself as part of a more efficient part load breathing strategy i.e. very early or late intake closing).

Controlled Auto-Ignition (CAI) combustion was a trending research topic in the years between 2000 and 2005, with many researchers intending to eliminate part load pumping losses via negative valve overlap operation (high residual charge dilution). The arising combustion mode was seen by many as a long-term solution to improving gasoline engine efficiency with ultra low NO_x [40,41]. However, some significant

challenges were found to limit this long-term solution, particularly limited operating window compared to homogenous spark ignition combustion, with low load limited by insufficient residual gas temperature and poor combustion stability and high load limited by breathing [42]. Moreover, the production of such an engine with adequate control over the timing and rate of auto-ignition would seem difficult with current fuel blends and on-board combustion diagnostics [30]. Another method proposed to reduce part load pumping loss was spray-guided stratified SI combustion that is currently considered to be a potential replacement for homogenous SI combustion in the long-term [43]. However, some disadvantages of this method reduced its potential, including remaining issues with operational robustness and relatively high NO_x and particulate after-treatment costs.

Considering the downsides of earlier methods, another method to reduce part-load pumping losses would be to operate the engine nearer the region of maximum BSFC for more of its operating time. This can be achieved through “engine downsizing” [44], where the capacity of the engine is reduced but maximum engine performance is maintained with higher intake pressure, or so-called “boosting”. This reduces pumping losses under part-load, as the reduction in engine capacity means that for a fixed low load (in terms of brake torque), the inlet manifold pressure must be higher [30]. This was particularly attractive for the limited load range covered by the NEDC [45].

Additional benefits of downsizing other than reduced part-load pumping losses is downsized engines typically have reduced net frictional losses as the number of cylinders are reduced. In order to be near the optimum [30] the displacement per cylinder is often maintained, hence the total number of cylinders is reduced. Nonetheless, the reduction in the number of cylinders by a certain amount may not be equal to the same reduction in frictional losses due to the higher in-cylinder pressures that occur. Increased pressure in downsized engines is provided by a turbocharger to boost the intake manifold pressures; in this procedure, some of the heat in the exhaust gasses can be recovered that would otherwise be lost. Therefore, turbo-charging can be used to increase engine efficiency and reduce CO₂ emissions. There are some drawbacks to using turbochargers such as a delay between load demand and the boosted inlet manifold pressure that is required, especially at low load where the turbocharger is not at an efficient rotational speed. This delay is often called “turbo-lag”. The transient response increases in respect to power demand, leading to

insufficient torque and increased in-vehicle acceleration times. Two-stage turbochargers have been proposed to improve the transient response by providing a larger speed-load operating window. The benefit of having two turbochargers is that the smaller turbocharger is engaged in a lower engine speed where the air-flow rate demands are complimentary, while the larger turbocharger is engaged at higher engine speeds (and the small unit is bypassed to avoid over-speeding). Despite the benefits from two-stage turbo charging, cost and transient response still remain key issues for downsized engines and the degree of downsizing that can be practically achieved [1].

2.2.2 Engine Down-Speeding

Maximum low-speed engine load greatly increases by using turbochargers or superchargers [45] (solving the problem of transient delay, however causing a minor loss due to the parasitic mechanical drive of a supercharger). This has the effect of decreasing the engine speed required for given power output. Through longer gearing, the frictional and pumping losses of a downsized engine can be noticeably reduced by using a technique known as engine down-speeding. The cumulative effect of engine downsizing and engine down-speeding is presented in terms of the two BSFC maps in Figure 2.11.

The BSFC maps for both engines have similar maximum power and engine speed range. It can be concluded from these maps that, for a given gear ratio, engine downsizing alone enhances BSFC at motorway cruising speeds. Lean burn is more efficient because of the increased ratio of specific heats, the value of γ is increased because of the excess air. In terms of emissions, the unburned hydrocarbons and CO are improved provided the combustion efficiency is maintained and that the combustion is not limited due to excessive flame stretch, however, emissions of NO_x will be worst unless the ultra-lean operation is achieved [31]. It can also be seen that down-speeding by increasing the gear ratio can also improve BSFC even more. However how much this amount can be implemented is mainly dependent on the head-room in low-speed torque and this can vary from engine to engine. Regardless, by using this technique, improvements in fuel consumption over the NEDC have been recently reported [45].

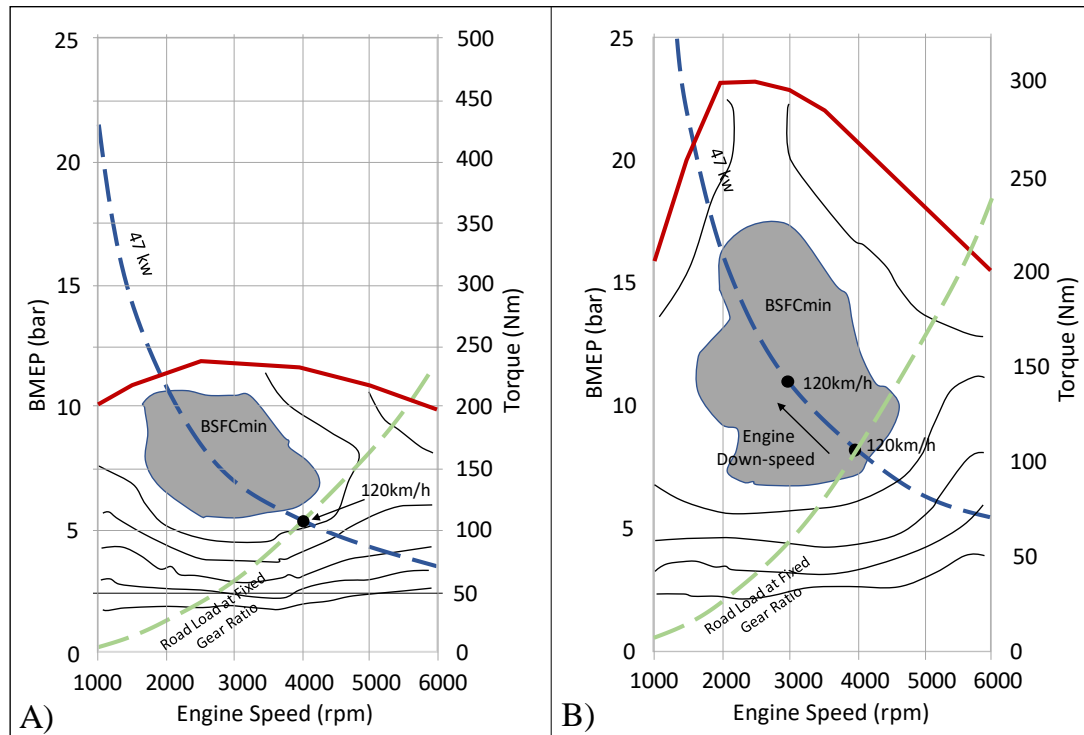


Figure 2.11. Conceptual BSFC maps for a 2.5L naturally-aspirated engine (A) and a 1.6L boosted (B). Adapted from Zhao [46] and Stone [30].

2.3 Turbulent Combustion

An appropriate understanding of combustion can highly increase engine efficiency and power output, it is important to characterise the features of turbulent in-cylinder flow as the flow has a significant effect on the flame and its propagation. Moreover, knowledge and understanding of turbulent flow can provide efficient lean-burn or high residual rate combustion, leading to improving fuel economy and lower emissions when implemented along with high energy ignition. Different types of fluid motion within an engine exist such as axial swirl, also referred as swirl (bulk air motions introduced into the cylinder with a degree of tangential momentum so as to rotate around the cylinder axis). Such bulk motion has been previously shown to persist throughout the cycle, with high turbulence generated locally at the walls [31]. The term tumble (also referred to as barrel swirl) denotes bulk air motions introduced to the cylinder with a degree of rotation perpendicular to the cylinder axis [47]. Most modern four-valve production engines are designed to impose such tumbling motions (often together with a degree of axial swirl) through the adoption of angled inlets and a pent roof cylinder head geometry to manipulate the turbulence [48].

2.3.1 Basics of Turbulent Combustion

Pre-mixed combustion requires both atomized fuel and air to operate, this is valid for both spark ignition and compression ignition internal combustion engines. The quantity of fuel is controlled so that the ratio of the mass of air to the mass of fuel is balanced between a range of 12:1 and 18:1 for a homogeneous spark-ignition engine. However, the AFR ratio can be misleading under some conditions as it does not account for when the charge is liquefied. For example, cold-start or alcohol fuels could cause this misleading if the desired temperature or pressure to vaporize the fuel could not be met. This issue can be avoided by heating the charge prior to ignition but this is a challenge to effectively implement in a practical and affordable manner. The flame development rate could also be affected by colder temperature, on the contrary, if the unburned gas temperature rises, the turbulent flame speed experienced after the spark also increases, which can have a direct knock-on effect on the subsequent flame development. Metghalchi & Keck [49,50] presented in, Figure 2.12 the variable nature of the burning velocity rate and its dependency on AFR for differing fuels.

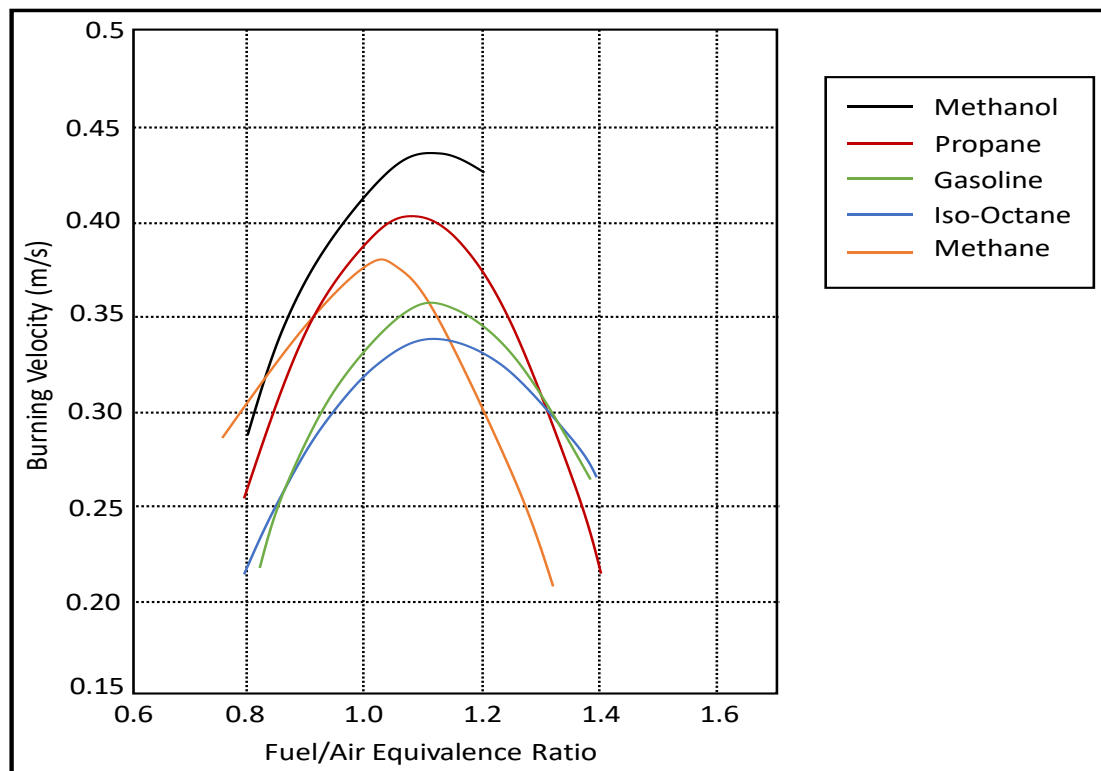


Figure 2.12. The laminar burning velocity as a function of the equivalence ratio, adapted from Metghalchi & Keck [49,50].

The maximum velocity shown in the above figure occurs at a slightly rich equivalence

ratio. Due to dissociation at high temperatures, molecular oxygen can be found in the burned gases when operating under stoichiometric fuelling, thus some additional fuel can be added and burned and a higher Indicated Mean Effective Pressure (IMEP) is provided due to the increased temperature and pressure [51]. It's important to mention, at either side of this optimum there is a very steep drop-off in the speeds recorded because under yet richer conditions, the lack of available oxygen (extra fuel) and a low ratio of specific heats causing a vast reduction in combustion (and three-way catalyst) efficiency and, ultimately, misfire even though at first causing charge cooling and knock reduction. However, some caution is required when considering such data obtained under laminar like conditions due to considerable spread amongst the data, as both differences in measurement or calculation techniques or whether or not the influence of flame distortion, stretch and cellularity have been considered [20,51].

2.3.2 Turbulent Flow

Many advantages of turbulent flow exist such as accelerating burn rate, more complete combustion and better mixing of the charge. Without turbulence, there would be not enough time for efficient combustion in typical automotive internal combustion engines. In addition, deliberately increased rates can assist with charge mixture preparation and ensure thorough mixing with any residual gases so as to help ensure high dilution tolerance. Ultimately improved thermal efficiency and increased output may be achieved. However, the limits of turbulence have to be taken into consideration. Excessive turbulence can cause flame quenching and increased combustion duration, hence reducing combustion efficiency that leads to increased pollutant emissions. Turbulence can be described as a large and small-scale eddies co-existing in a chaotic manner, cycle to cycle variations are the nature of turbulence as it is unsteady. However statistical analysis with enough accurate data can be used to calculate instantaneous local fluid velocity under steady conditions as [31].

$$U(t) = \bar{U} + u(t) \quad (2.2)$$

where \bar{U} is the mean flow velocity and is defined as the time average of $U(t)$. The universal fluctuating velocity component u can be defined by its root mean square value u' to give the turbulence intensity:

$$u' = \lim_{\tau \rightarrow \infty} \left[\frac{1}{\tau} \int_{t_0}^{t_0 + \tau} (U^2 - \bar{U}^2) dt \right]^{1/2} \quad (2.3)$$

Because a number of different length scales exist in the flow, so the flame front shape is wrinkled, the eddy size and pattern are affected by the engine geometry; the largest eddy can be as large as the cylinder height and/or bore and the smallest one is governed by the molecular diffusion. integral length scale l_I , can be used to define turbulence that can be considered as an average intensity of the average sized eddies. Experimentally l_I is defined as the integral of the coefficient of the fluctuating velocity R_x (number of data points taken) at two points in the flow with respect to the distance between them [20,31].

$$l_I = \int_0^{\infty} R_x dx \quad (2.4)$$

Where R_x can be defined as

$$R_x = \frac{1}{N_d - 1} \sum_{i=1}^{N_d} \frac{u(x_0)u(x_0 + x)}{u'(x_0)u'(x_0 + x)} \quad (2.5)$$

This application has a restriction that requires a vast amount of information in order to statistically minimise cyclic variation effects. Hence many researchers considered length scale calculation by finding a correlation between the integral time scale τ_I (much easier to measure) and length scale. This can be defined as the correlation between two velocities but at a fixed point in space with differing times instead of trying to follow the flow around the bore [31].

$$\tau_I = \int_0^{\infty} R_t dt \quad (2.6)$$

$$R_t = \frac{1}{N_d - 1} \sum_{i=1}^{N_d} \frac{u(t_0)u(t_0 + t)}{u'(t_0)u'(t_0 + t)} \quad (2.7)$$

Based on this Tabaczynski [52] was able to correlate a link between the scales when the turbulence is relatively weak:

$$l_I = \bar{U} \tau_I \quad (2.8)$$

Equation (2.8) provides a method of calculating the largest length scales a method must be found for calculating the smallest and therefore first scales a flame encounters (Kolmogorov length scale l_k). At smallest scale the molecular viscosity will dominate any kinetic energy, hence dissipating it to thermal energy. Kolmogorov length and time scales can be defined by assuming ε represents the dissipation per unit mass and ν kinematic viscosity [31,52].

$$l_k = \left(\frac{\nu^3}{\varepsilon} \right)^{\frac{1}{4}} \quad (2.9)$$

$$\tau_k = \left(\frac{\nu}{\varepsilon} \right)^{\frac{1}{2}} \quad (2.10)$$

The size of the smaller eddies (Kolmogorov length scale) is shown in Equation (2.9) while the Kolmogorov time scale (Equation(2.10)) characterizes the momentum-diffusion of the structures. Everything that is dissipated at the smallest scales, has to be present at larger scale first. Since the dissipation rate is equal to the kinetic energy production rate, an approximation for the rate at which kinetic energy is supplied to the small scales can be obtained. The kinetic energy of the flow is proportional to φ^2 . Where φ is the system size. The time scale of the large eddies can be estimated as L/φ where L is the length of large eddy, that can also be assumed as system length, and φ can be defined as system size. Assuming that the kinetic energy supply rate will be related to the inverse of this time scale. The dissipation rate can now be estimated by the following relation:

$$\varepsilon = \frac{\varphi\varphi}{L/\varphi} = \frac{\varphi^3}{L} \quad (2.11)$$

2.4 Charge Motion Effects

2.4.1 Swirl

As already mentioned previously, swirl can be defined as the rotation of the charge in the cylinder around a central axis. It can be generated by inclining the inlet pipes in the radial direction in ported engines. In four stroke engines, swirl may be produced

by the induction system; e.g. helical or tangential inlet ports, shrouded valves and valve deactivation. The intensity of the imposed swirl can be quantified by the swirl ratio, R_s (Heywood, [31]) where ω_n is the angular speed of the rotating crank shaft and ω_s is the angular velocity of a solid body swirl, measured by swirl meter or by laser velocimetry techniques.

$$R_s = \frac{\omega_s}{\omega_n} \quad (2.12)$$

The swirl improves the mixing of air and fuel in the charge to encourage a homogenous mixture. In 1977 early attempts to measure swirl was made by Nagayama, Araki, and Iioka [53], that involved using a tracking paddle wheel that pivoted about the cylinder axis. A more modern method, image velocimetry techniques such as PIV (Particle Image Velocimetry) and LDV (Laser Doppler Velocimetry) has been used to measure the in-cylinder flow [54,55]. The comparison between old fashioned way of measuring swirl and using velocimetry techniques (PIV) with CFD (Computation Fluid Dynamic) were performed by Nordgren and coworkers [56] and they proved that the old fashioned wheel could not correct for, or predict, the swirl centre migrating away from the cylinder axis, whereas CFD and PIV could. Also, average angular momentum should be used in Equation (2.12), as the value is much lower nearer the walls than in the centre due to viscous drag and friction, average value considers flow to be uniform throughout the flow field. In the modern engine R_s is constantly changing and can be as high as 5 or 10 [47]. Much of the angular momentum induced is then lost as the mixture is compressed but swirl is not completely dissipated; creating another type of motion when it is compressed called Squish.

2.4.2 Squish and Tumble

Squish happens as the piston arrives at TDC (Top Dead Centre); at the end of the compression stroke to be more precise where the mixture on the outer edges of the cylinder is caused by a reduction in volume at the outer edges forces the mixture towards the cylinder axis in a radial inward motion. The amount of squish depends on the engine geometry in a way that an engine with a pent-roofed, flat-bottomed combustion chamber has a different squish than a flat-topped or a bowl piston crown. Squish can be defined as the percentage squish area – the percentage of the cross-

sectional area of the piston crown ($A_s = \pi B^2/4$) that is nearest to the cylinder head as the piston approaches TDC [31]. The instantaneous displacement of the charge over the outer section of the piston crown of the squish region, especially in bowl crowns must satisfy the mass conservation. This velocity for a simple pent-roof design is:

$$\frac{v_{sq}}{S_p} = \frac{A_s}{b(Z+c)} \left[1 - \frac{Z+c}{C+Z} \right] \quad (2.13)$$

where A_s is the squish area, b is the width of the squish region (usually the bore), Z is the distance between the piston crown top and the cylinder head and C is the conrod length. Even though these models neglect blow-by and friction losses, a very good estimate for the squish velocity can be achieved [31].

2.5 Ignition

Combustion can be divided into three phases when analysing the burn duration [30]:

- 1 Initial laminar burn – usually 1-10% MFB where the flame kernel is small enough, so the turbulence influence is negligible.
- 2 Turbulent burning – The main part of the combustion that includes, wide flame front and pockets of unburnt mixture entrained behind the flame front. This is usually referred to as 10-90% MFB
- 3 Final burn – The final burn phase (90-100% MFB) is much slower since by now the flame front area will be progressively reduced because of contact with the combustion chamber surfaces.

For the propagation of a spherical laminar flame, with a radius of r , the geometrical stretch rate can be described as [57]:

$$\frac{1}{A} \left(\frac{dA}{dt} \right) = \frac{2}{r} \left(\frac{dr}{dt} \right) \quad (2.14)$$

A = flame surface area

The highest stretch rate happens at the early phase because the kernel can buckle and extinguish with only the high temperature plasma between the two spark electrodes able to counteract the stretch rate's desire to quench the flame. In this condition spark timing plays a significant role as it will massively influence the work extracted from

the charge in a way that too early a spark in the compression stroke (also known as advanced from TDC) and the work from initial flame will be lost as it will be count as negative work against the rising piston. Conversely, too late spark ignition (also known as retarded) leads to reduced temperature, slower burn rate and ultimately reduced thermal and combustion efficiencies, due to the expanding volume. The optimum spark ignition timing then is in between, Figure 2.13 extracted from Amann [58] shows three ignition timings, retarded, advanced and in between where the maximum torque can be achieved (MBT). It can be seen that the advanced spark (blue) has the highest pressure however the torque output will be low as shown in same figure section b), this indicates the negative work against the rising piston. MBT timing is shortly after 30° spark timing employed here, shown in red color and via an arrow in Section b).

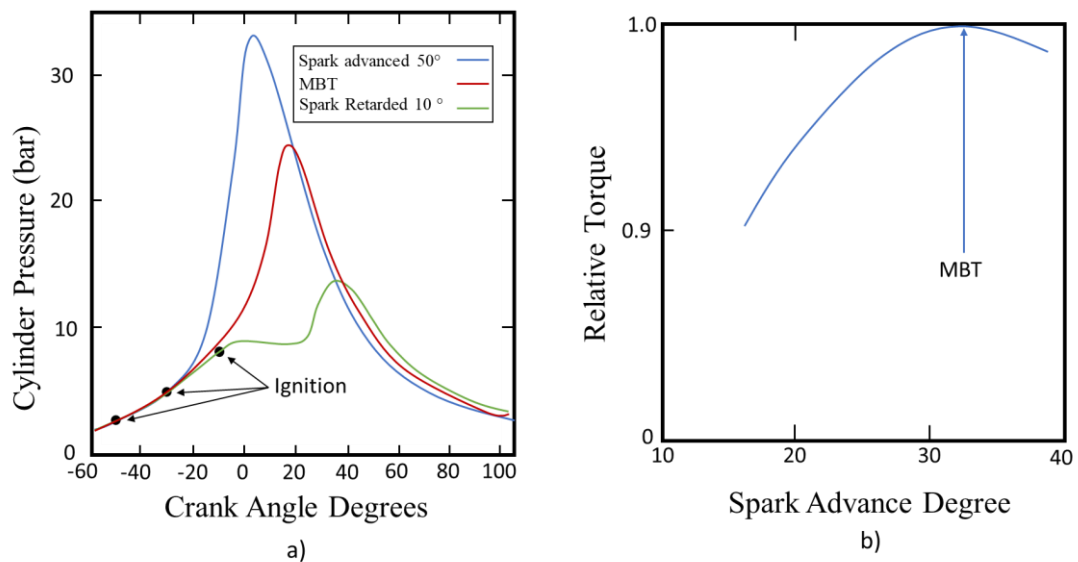


Figure 2.13. a) Cylinder Pressure vs crank angle for three distinct spark timings (over advanced, MBT and retarded); b) Effect of spark advance on the brake torque highlighting MBT for a given engine. Adapted from Amann [58].

The majority of SI engines have an MBT that relates to 50% of the mass burned occurring (CA50) between 8° and 10° after top dead centre with an APM_{ax} at about 16° aTDC. As Heywood [31] mentioned there are many ways of inciting spark ignition and combustion in a cylinder that is primed with combustible material. As early as 1999 the use of multi-spark discharge was investigated by Davis, Bouboulis, and Heil [17] to reduce the issue of poor cold starting in FFVs. These experiments were tested with a variety of spark geometry configurations and ethanol blended fuels and showed that a multiple spark discharge improved the start-ability response time of ethanol blended fuels [17].

2.6 Process of Laminar and Turbulent Combustion

The bulk motion of mixtures around the spark have a drastic impact and is an important source of cyclic variation. At the spark moment, the electrical potential rises until the mixture between electrodes ignites. Spark arc that is formed from ionizing streams propagate from one electrode to another, the created arc is a plasma which expands due to exothermic reactions between the species in the mixture.

Considering laminar combustion, the spark kernel will propagate outwards in a near-spherical manner. However, in reality, the IC engine is subject to turbulent conditions, but it is still necessary to understand laminar burning condition to further understand turbulent combustion.

If the initial flame develops more quickly (primarily due to faster chemistry) it follows that more of the turbulent spectrum will become available more quickly to aid flame wrinkling and improve the rate of unburned mass entrainment into the flame. Such physical effects have been shown to be brought about by the faster initial chemical reaction rates with high ethanol content fuels in SI engines, but become amplified as the turbulent spectrum is faster encroached.

2.6.1 Laminar Pre-Mixed Combustion

Mixtures ahead (quiescent) and behind (entrained, unburnt) the flame can both be defined with laminar combustion. The threshold velocity at which the flame initiates combustion and has a massive influence on the remainder of combustion is the unstretched laminar burning velocity (S_L). This laminar burning velocity is defined as the global rate of chemical reaction in the mixture and is dependent on flow mixture, induction temperature and in-cylinder pressure. Many researchers, for example, Metaghalchi, Keck and Gülder [49,59], have studied laminar burning velocities under typical internal combustion engine conditions that provide a good basis of study given the degree of experimental correlation. However accurate data for laminar burning velocity under these engine conditions is still insufficient and it should be noted effects of flame cellularity and wall friction were not considered due to experiment limitations.

Two regimes are typically used to define laminar burning velocity: stretched (S_n) (m/s) and unstretched (S_l) (m/s) which are correlated by

$$(S_l) - (S_n) = \ell \frac{1}{A} \left(\frac{dA}{dt} \right) \quad (2.15)$$

Where ℓ is the proportionality constant, which defines the effect of the stretch and is often referred to as the ‘Markstein length’. This length defines the amount of stretch the flame will experience and can be defined in dimensionless form:

$$\begin{aligned} \frac{(S_l) - (S_n)}{(S_l)} &= \frac{1}{A} \left(\frac{dA}{dt} \right) \left(\frac{\delta_l}{S_l} \right) \left(\frac{\ell}{\delta_l} \right) \\ &= KMa \end{aligned} \quad (2.16)$$

Where δ_l is the laminar flame thickness and Ma represents Markstein length as a dimensionless group, while the Karlovitz stretch factor (K) is representing the first three terms of Equation (2.16). Laminar flames propagating through any fuel, air and residual gas mixed charge are identified by the laminar flame speed S_l and thickness δ_l . Molecular diffusivity can be used to define laminar thickness δ_l (mm) [31]:

$$\delta_l = \frac{D_L}{S_l} \quad (2.17)$$

The Lewis number can be used instead of Ma as it is more reliable even though significant work by Bradley, Lawes and Sheppard has been done to achieve consistent values of Ma . The Lewis number increases in the linear proportion of Ma , so it can be used as a measurable reference as showed by Harper [60] .

$$Le = \frac{K_t}{\rho c_p D_L} \quad (2.18)$$

Where K_t is the thermal conductivity, ρ is the density of the mixture and c_p is the specific heat capacity of a constant pressure system.

2.6.2 Turbulent Combustion

Fluid dynamic strain can be applicable during turbulent flame propagation as the turbulence can distort and stretch the flamelet; this can be expressed by the turbulent Karlovitz stretch factor (K) as the ratio of chemical to eddy lifetime as below:

$$K = \frac{u' \delta_L}{l_I S_L} \quad (2.19)$$

Where u' is the r.m.s turbulence velocity, l_I is integral length scale, δ_L is laminar flame thickness, and S_L is unstretched laminar burning velocity. Damköhler number (inverse of the Karlovitz stretch factor) was used by Abraham, Williams, and Bracco [61] in order to construct a map showing the differing flame regime areas in pre-mixed SI engines assuming weak turbulence, reaction sheets and distributed regions. From investigations by AbdelGayed, Al-Khishali, and Bradley [62] a correlation was found between the Karlovitz factor and the turbulent Reynolds number, Re_T :

$$K = 0.157 \left(\frac{u'}{S_L} \right) Re_T^{-0.5} \quad (2.20)$$

To find turbulent entrainment velocity it is necessary to define laminar burning velocity as the initial laminar flame propagates from the kernel and it becomes stretched, so the velocity can be calculated based on the rate of entrained mixture into the flame front's reaction zone, so the turbulent entrainment velocity can be found using the stretched laminar burning velocity:

$$u_{te} = \frac{\dot{m}_e}{\rho_u A_i} \quad (2.21)$$

Where A_i is the area of a circle whose radius is equal to that of the flame and \dot{m}_e is entrained mass flow rate. Based on u_{te} , Abdel-Gayed published correlations of flame regions shown in Figure 2.14. The dotted lines across the graph are measured using the constant stretch factor Equation (2.16) which is a product of KLe . The structure of the flame can be determined from the magnitude of this stretch factor, where $KLe < 0.15$ is consider to be continuous laminar flame sheet burning regime. This sheet begins to break-up when $0.15 < KLe < 0.3$, localised quenching happens when this magnitude is between 0.3 and 1.5 and any value over 1.5 considered to be total quenching.

Equation (2.20) and Figure 2.14 can be merged to demonstrate a more compact form over the entire range of displayed results:

$$\frac{u_{te}}{S_L} = 0.88 \left(\frac{u'_k}{S_L} \right) (KLe)^{-0.3} \quad (2.22)$$

In 1988 Borghi confirmed that all flames in ICEs begin with laminar flames and that depending on the turbulent field to which they were subjected could be divided into different regimes based on the length and velocity scales of the flame and the turbulence. Shown in Figure 2.15 is the Borghi diagram which is very similar to the Abdel-Gayed diagram, detailing the differing regions of combustion, based on two non-dimensional parameters: $\frac{u'}{S_L}$ and $\frac{l_f}{\delta_l}$. Laminar flames are in 'Laminar' area of the Borghi diagram where $Re_T < 1$, as the flame propagate and interacts with turbulence then the flame fall into region labelled 'A', at this region the turbulence intensity is so small that the flame thickness is only able to wrinkle the flame front as Taylor microscale is higher than flame thickness. The next region identified by Label 'B' is where velocity fluctuations become larger with respect to laminar burning velocity in a way that $(u'/S_L = 1)$. This area was further explored by Peters [63].

Ultimately the ratio between the turbulent and laminar burning velocity indicates the flame speed ratio, which can be used for comparing the ability of the flow field to increase the rate of unburned mass entrainment.

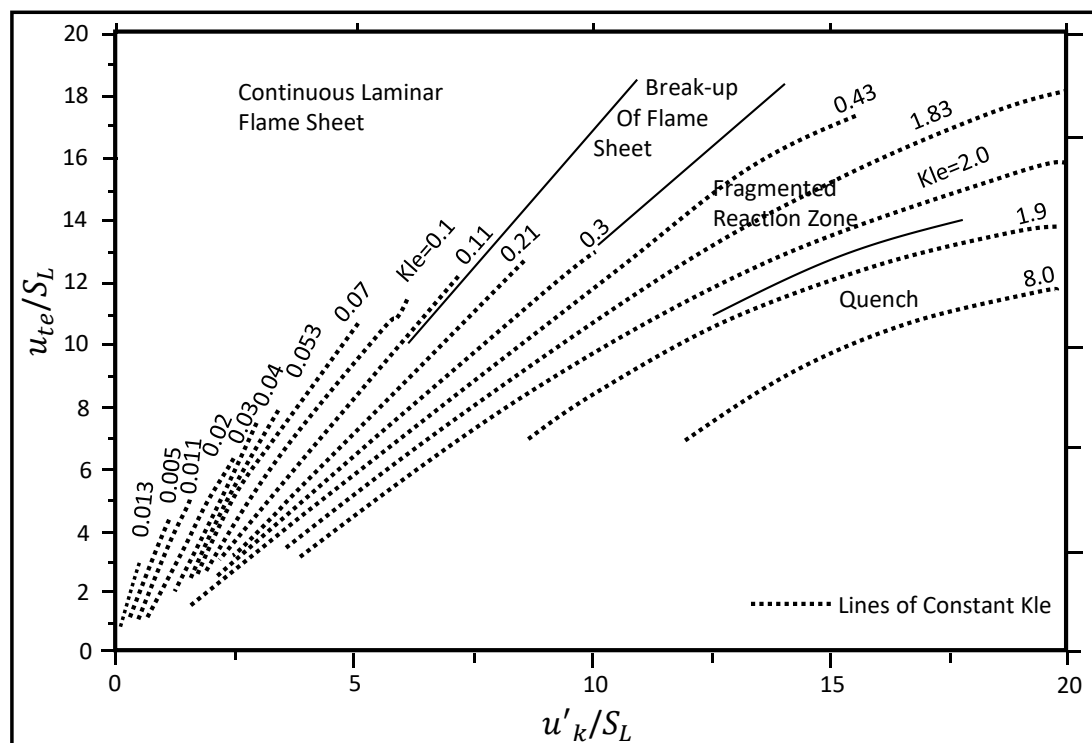


Figure 2.14. General correlation of turbulent burning velocities in terms of dimensionless groups. Adapted from Abdel-Gayed, Al-Khishali, and Bradley [62].

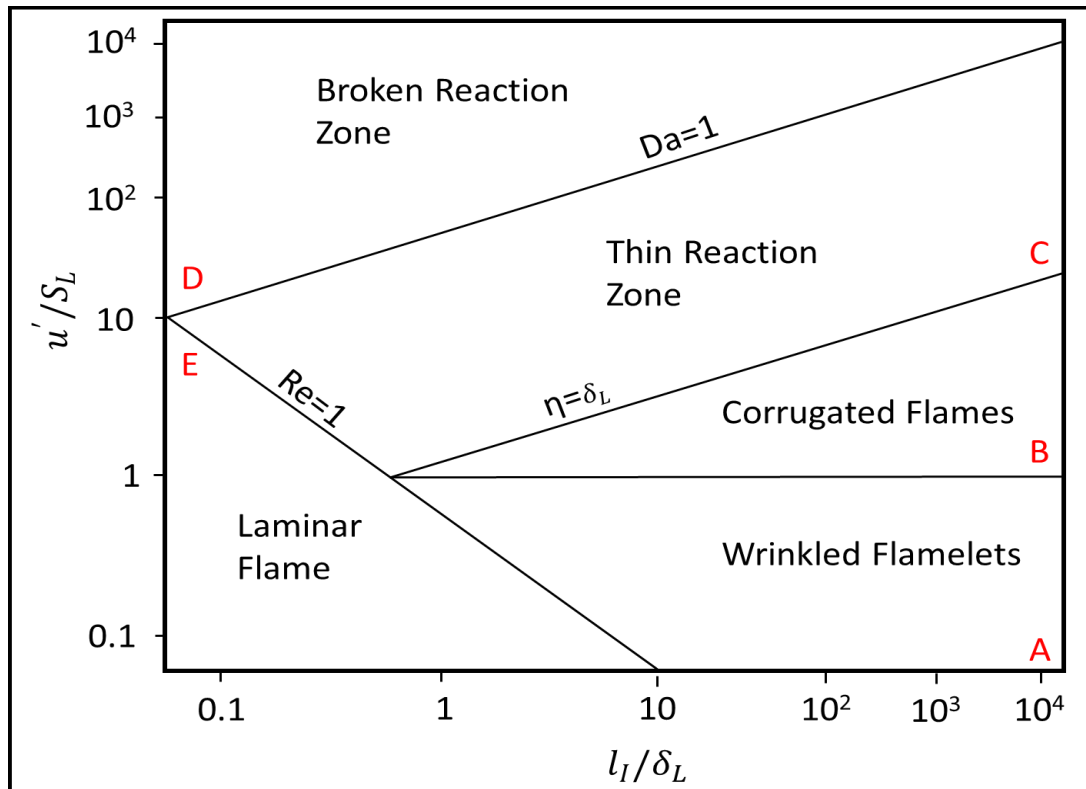


Figure 2.15. Borghi diagram showing the different regimes of turbulent premixed flames, Adapted from Peters [63]; Borghi [64].

2.7 Alcohol Fuels

2.7.1 Impact on SI engines and Alcohol Types

Higher latent heat of vaporisation, lower unburned gas temperatures and improved knock resistance [65,66] are some benefits of the lower carbon alcohols (ethanol and methanol) to increase engine performance and efficiency over gasoline fueled engines. As mentioned before one of the major problems of downsized SI engines is knocking phenomena due to the increased in-cylinder temperature and pressure. Alcohol fuel with the higher latent heat of vaporisation mainly leads to improved knock resistance in modern SI engines [66] and is an attractive prospect for current downsized SI engines. It is important to mention that the unique properties of alcohol require careful consideration in the engine design. In 2007 Turner [65] showed that engine output can be increased by 10-15% with possible additional benefits for dedicated ethanol operation in the future if the engine power cell and compression ratio can be optimized accordingly. It is important to consider the low volumetric energy content of the

alcohol in comparison to other fuels, as shown in Table 2.1. Moreover, in 2008 Kar [67] investigated the effects of gasoline-ethanol blends on vaporisation and thermodynamic properties, showing the blended ethanol fuels exhibit azeotropic and evaporation characteristics tendencies with the quicker evaporation of blends with lower ethanol concentrations (0-30%) than those with higher ethanol content. Furthermore, fuel blending with higher ethanol concentration than 85% would cause cold start problems due to ethanol's higher latent heat of vaporization, which causes charge induction to occur with a partly liquidised fuel-air mixture. This has convinced many researchers to use direct injection to help alleviate cold start performance. For instance, in 1987 Siewart and Groff [16] concluded that an engine with low carbon alcohols could be started at -29°C by late injection of a high a high-pressure stratified charge in the cycle. Moreover, in 2007 Nakajima, Saiki and Goryozono [68] demonstrated that an engine running port fuel injection can be started as low as -10°C by deactivating one intake valve (with also the compression ratio increased from 10.5 to 11.5). In addition to such drive-ability issues, alcohol corrosion and other detergent effects must be taken into consideration through mechanical engine upgrades such as material changes to the fueling system and valve seats [68–71].

While many studies have investigated the “lower” carbon alcohols, “higher” carbon alcohols such as butanol, pentanol, and propanol have also been suggested and considered for automotive use. These fuels are expected to have better resistance to water contamination, lower Reid Vapour Pressure, and a higher calorific value making the related fuel consumption better than ethanol-based counterparts. In addition, in 1998 Yacoub, Bata and Gautam [73] investigated adoption of much higher carbon alcohol-gasoline fuel blends in a single-cylinder research engine and indicated that these fuels showed a much higher resistance to knock when compared to gasoline. However, Aldehyde emissions were higher for all alcohol blends, with formaldehyde as the main constituent regardless of the type of alcohol in the blend [66].

In 2009 Cairns [66] studied ethanol and butanol gasoline blends in a way that both fuels had comparable oxygen mass weighting; ethanol 10% versus butanol 16% both with 3.35% O_2 weighting. It was concluded that higher carbon alcohol (butanol) and lower carbon alcohol (ethanol) had similar fuel consumption rate and similar spark timing for MBT combustion at part-load. Other studies comparing the same fuels were undertaken in a single-cylinder optical research engine with fixed spark timing by

Malcolm in 2007 [74]. This study reported no major difference between the three tested fuels, E25, Bu25 and neat iso-octane (in terms of combustion characteristics). Shown in Table 2.1 is a direct comparison of lower carbon alcohol fuels to traditional fuels (both typical gasoline and iso-octane). In many automotive applications, alcohol fuels are used to dilute and blend in a way to enhance performance and reduce emissions without fundamental changes to the power plant. Elsewhere, Bata [75] calculated the performance of various gasoline/butanol splash blends in a 2.2 litre naturally aspirated research engine. These workers found an increase in specific fuel consumption of 6.5% when using 20% butanol. However, the relative production cost and emissions of butanol must be taken into consideration as well and it has currently limited global uptake.

The clear fact can be observed from Figure 2.16 that ethanol has a lower volumetric energy content. This observation is further explained in Figure 2.16 showing volumetric energy content of ethanol-gasoline blends is linearly reduced as the ethanol content rises.

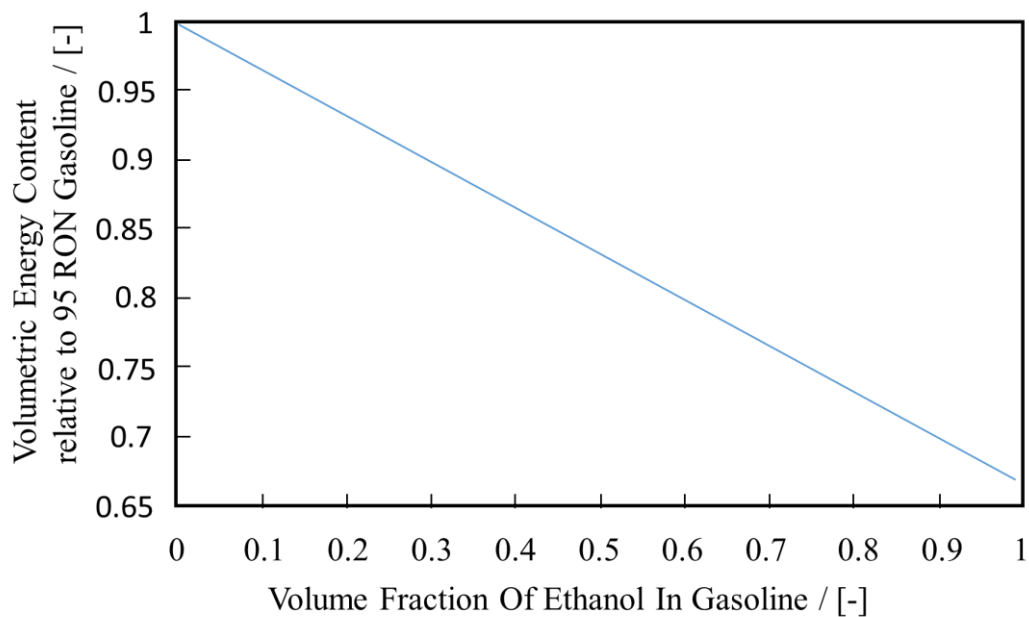


Figure 2.16. The volumetric energy content of ethanol gasoline blends displaying the fact that as the ethanol content rises, the energy content falls in a linear fashion [66].

Table 2.1. Properties of iso-octane and gasoline compared with two alcohol fuels (ethanol and butanol). Adapted from Heywood, Turner, Zhao, and Brouzos [29,63,74].

Property	Iso-octane	Gasoline	Ethanol	Butanol
Chemical Formula	C ₈ H ₁₈	C ₄ -C ₁₂	C ₂ H ₅ OH	C ₄ H ₉ OH
Density at atmospheric pressure and temperature (kg/m ³)	0.692	0.72-0.78	0.792	0.81
Lower Heating Value (MJ/kg)	44.3	43.4	26.9	32
Stoichiometric AFR	15.13	14.6	9	11.1
Molecular Weight	114.23	110	46.07	74.12
Volumetric Energy Content (MJ/litre)	30.6	31.6	21.2	31.6
RON	100	95	109	98
Sensitivity (RON minus MON)	0	8-12	18	10
Reid Vapour Pressure (bar)	0.52	1.03	0.18	0.03
Latent Heat of Vaporisation (kJ/kg)	308	305	840	430
Auto-ignition Temperature (°C)	NA	260-460	360	314
Oxygen Content by Weight (%)	0	0	34.8	21.6

2.7.2 Social, economic and environmental aspects

Ethanol production from cereals requires several steps including milling, saccharification, fermentation, distillation, and dehydration. However, if the ethanol is to be produced from sugar syrups (molasses), a by-product from the sugar refining process, milling and saccharification are no longer needed. Ethanol production cost has been reduced by half compared to 1980 [77]. For example, the residual cane bagasse can be burned in furnaces to generate steam in sugar-cane ethanol production; this can be used to generate electricity using steam turbines that not only provides enough electricity for the ethanol power plant but also commercial uses. Moreover, power plant efficiency has been steadily increased since 1980.

Various oil crisis and international sugar price fluctuations [78] in the 1970s demanded a solution in Brazil. The Pro-Álcool program arose, promoting internal energy security and incentives to agricultural and industrial sectors connected to the sugarcane market in the 1970s to address this issue. Nowadays, flexible fuel (FF) SI engines are available in the vast majority of Brazilian cars including hydrous ethanol (E95W05) and gasohol (E27) [79]. Despite the vast majority usage of any mixture of gasoline and ethanol in the FF SI engines, some can also operate using “natural” gas (gasoline/ethanol mixtures) [80]. In the 1970s the USA introduced tax credits for ethanol production as a solution to overcome international oil dependency [81] due to the mentioned oil and sugar price fluctuations and to support the corn agricultural sector; also due to environmental concerns regarding gasoline anti-knock additives (leaded gasoline). After 2005 USA government policies developed a huge ethanol production growth [82] that enabled the USA to be the largest ethanol producer globally in the following years, as shown in Figure 2.17. Nowadays a minimum of 10% ethanol in US gasoline is mandated through policy, with 15% ethanol also available in 28 US states and 85% ethanol expected by the end of 2017 [83]. It can be seen that global ethanol production has doubled in the last decade and this has been promoted by more countries to tackle emissions from GHG and replace fossil fuels. European countries have committed to adopting 10% ethanol (E10) by 2020 [84], with E5 currently being the most common ethanol gasoline blend in the EU but with E10 already available in Belgium, Finland, France, and Germany. More widely, China and India also plan to promote E10 mandates by 2020 [84,85].

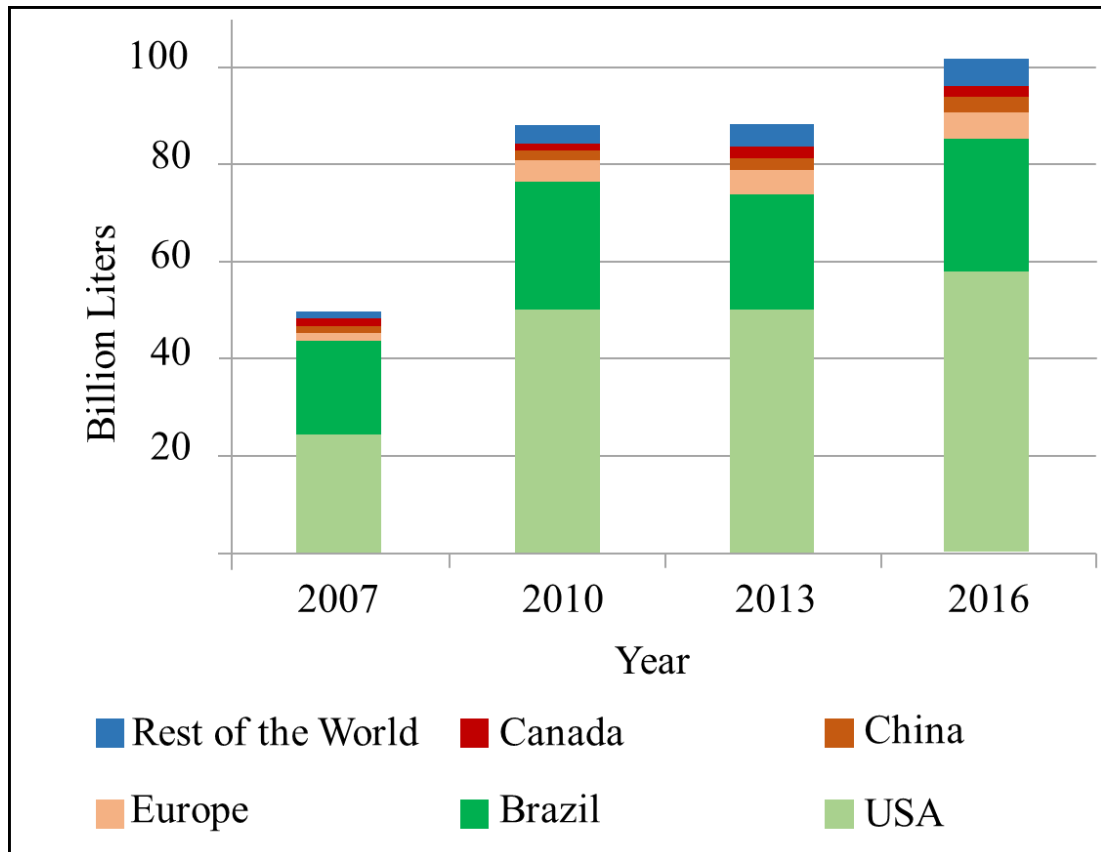


Figure 2.17. Global ethanol production by country/region and year. Adapted from [84,85].

Caution must be taken in the land usage for ethanol production as if the land used for food is to be replaced by the one for ethanol crop production and by considering water and biodiversity then the overall greenhouse gas emissions from this crop source would be even greater than those of gasoline [86–88]. Emissions of ethanol and fossil fuels have been studied based on life cycle with a focus on CO₂. These studies generally claim that ethanol life cycle pollutant gaseous emissions from specific feedstock are reduced compared to fossil fuels, as shown in global reports presented in [89–91]. Presented in Table 2.2 is the CO₂ emission for ethanol-gasoline blends and diesel in the following categories, well to tank (WTT), tank to wheel (TTW) and well to wheel (WTW). Diesel WTT is reasonably good because diesel engines have a higher brake thermal efficiency, also most diesel is a straight cut in the crude oil distillation process which means naturally about one-third in the distillation column is diesel [92]. It can be seen that the emissions differences of (TTW) between pure ethanol and gasoline are similar, so the main benefits are from fuel production pathways in a way that when comparing (WTW) with worst production pathway of ethanol to conventional gasoline emissions, still fossil fuel results in higher GHG emissions.

Nevertheless, ethanol usage is still dependent on its production price, which is directly linked to the energy consumption during the whole biofuel production cycle. Other production pathways using nonfood crops would be able to provide more benefits regarding GHG emissions, no food competition, land usage change, between others. However, problems exist such as within the enzyme-based lignocellulose-to- ethanol process which leads to more expensive production methods in comparison to first-generation ethanol production [82,93].

Table 2.2. WTT, WTW, and TTW GHG emissions (CO₂ equivalents) for a selection different biofuel for 2010. Adapted from [91].

Fuel	WTT g CO ₂ /km	TTW g CO ₂ /km	WTW g CO ₂ /km
E100	-127 to 30	146	19 to 176
E85	-82 to 29	143	61 to 171
E20	6 to 28	148	154 to 176
E10	17 to 28	150	166 to 178
Gasoline	29	156	185
Diesel	25	120	145

2.7.3 Hydrous ethanol

A five stage process is required to mass produce ethanol fuel according to Quintero and Montoya [94] These steps include: pre-treatment of the raw material, hydrolysis, fermentation, separation and dehydration, and wastewater treatment. After the fermentation phase, the residual water content varies from 6% to 12% [5]. Further distillation can be used to separate ethanol from water up to 96% (v/v) ethanol purity, the processed product is then generally referred to as hydrous ethanol. Another step can be implemented to increase the purity of ethanol via further dehydration. Conventionally, extractive distillation using ternary azeotropic mixtures are used by the addition of benzene, heptane, cyclohexane, or other hydrocarbons to the ethanol/water mixture. The produced azeotrope boils at a lower temperature than the ethanol/water azeotrope, hence separating the hydrocarbon and water from ethanol albeit at high energy cost [95]. Moreover, a more modern method that has a higher

capital cost but lower energy demand in comparison to the extractive method can be implemented. This method uses molecular sieves with a zeolite material [96] which is based on a hydrophilic zeolite material that contains big enough pores to absorb water molecules (2.8 \AA) but not the smaller ethanol molecules (4.46 \AA), which then leads to mixture separation.

Energy expense during distillation after 80% ethanol-in-water content increases exponentially [5–7,97,98]. Hence it can be concluded that most energy intensive process is ethanol-water separation processes (distillation and dehydration) after 80% ethanol-in-water content. Presented in Figure 2.18 is the ethanol distillation energy per litre versus a number of distillation stages, which clearly shows this exponential trend. So, many researchers studied and considered the use of wet ethanol with higher water content rather than that of hydrous ethanol to reduce overall fuel production cost. It is clearly shown in Figure 2.19 that, for USA corn ethanol, for example, significant energy can be saved (WTT) by using wet ethanol instead of anhydrous ethanol (pure ethanol). Despite the possible benefits of using wet ethanol and good indications for the distillation processes in Figure 2.18 and Figure 2.19 respectively, the increases in process optimization and new technologies must be taken into consideration. Previous work [6] showed distillation would result in more benefit for higher water content wet ethanol, even though another modelling study showed economical distillation of until 90% of water-in- ethanol [8].

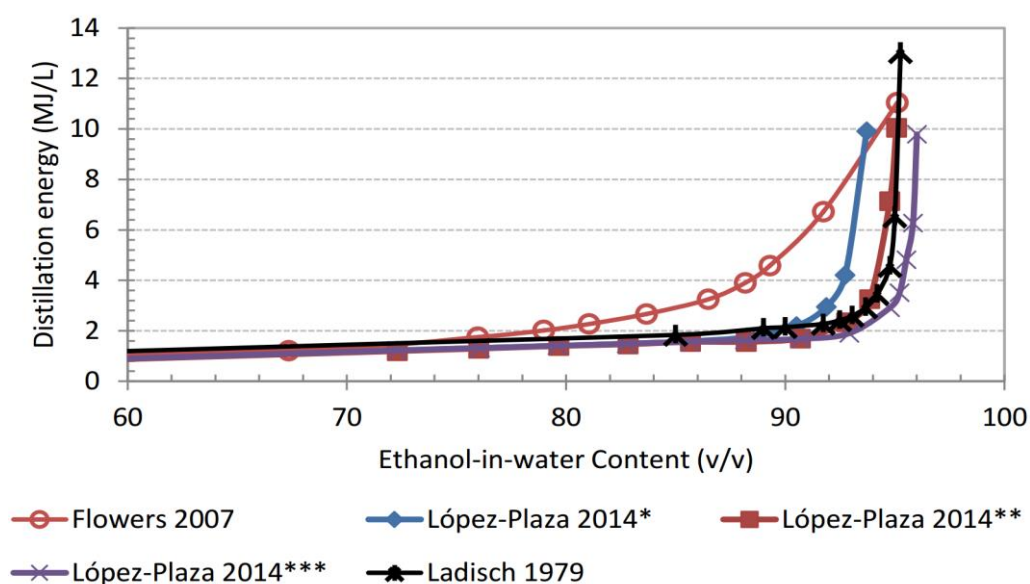


Figure 2.18. Ethanol distillation energy per litre. Number of Distillation Stages: * 8 stages; ** 12 stages; *** 19 stages. Adapted from [5,6,8].

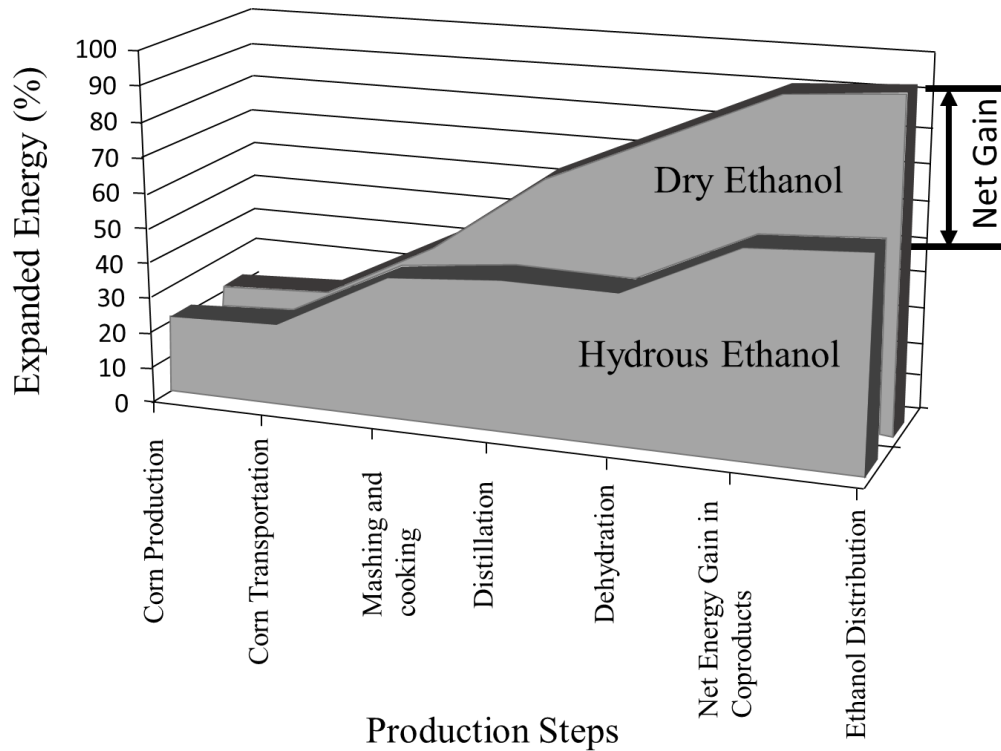


Figure 2.19. Comparison of net energy balance for anhydrous and wet ethanol (E65W35) taking into account all ethanol production steps [7].

2.7.4 Hydrous ethanol application in SI engines

The application of hydrous ethanol has been reported since before the Second World War as described by Wiebe and Porter's report of 1949 in the US scenario [99]. The main reason for this application was to increase the power of aircraft engines during takeoffs. Low octane gasoline was used to power those engines; hence, hydrous ethanol was injected into the intake system of these aircraft engines to reduce charge temperature and decrease knocking. Reports from the 1980s in the US [100,101] present results from an unpublished report of Deardorff (1979) that shows a water-in-ethanol content of 10% provide the best engine thermal efficiency, however, a decrease in generated power per unit of fuel volume was unavoidable due to the lower heating value of ethanol-water mixtures. In this experiment a six-cylinder inline engine gasoline engine was used, running on different wet ethanol mixtures. Carburettor jet nozzles were modified to enable operation with ethanol (as well as spark timing adjustments). Later in 2002, a catalytic igniter technology was used to enable combustion of 30% water in ethanol content [102], further study in 2005 [103]. The catalytic igniter was installed inside a pre-chamber in a way to propagate a torch

ignition like combustion through the combustion chamber. This was used to solve the problem of engine cold start and avoid costly high energy spark systems. Both NO_x and CO emissions were reduced significantly during the experiments; around 90% reduction in NO_x was also reported at some tested points. The reported CO reduction was mainly due to the CO water-gas shift mechanism. To the contrary, hydrocarbon emissions increased substantially.

In 2007 Brewster [11] investigated the application of hydrous ethanol of up to 20% water on a mass basis, in four-cylinder air-assisted direct injection (DI) turbo-charged engine at high loads (from 10 to 20 bar BMEP). More advanced spark timing was reported for hydrous ethanol MBT. Moreover, higher exhaust gas temperatures were reported due to longer combustion durations that were the outcome of delayed spark timing for hydrous ethanol. Longer flame development angle and combustion duration were noted as the amount of water in ethanol content increased, resulting in a reduction of BMEP. It was also reported that water in ethanol reduced in-cylinder pressure and temperature gradients that showed the potential of water in knock mitigation. NO_x was reduced, and THC emissions increased with water in-ethanol content increase due to a lower temperature.

In 2008 Dal Bem [104] studied the use of E75W25 (wet ethanol) and E99W1 (anhydrous ethanol) in a modified four cylinder in-line 1.0 litre flex fuel PFI engine under both compression ratios of 13.6:1 and 16.2:1 at full throttle. The increased water content in the lower compression ratio (13.6:1) reduced power and torque considerably and increased specific fuel consumption noticeably. Spark timing advance was required, and exhaust temperatures were reduced. Engine thermal efficiency was slightly lower. CO and NO_x emissions were considerably reduced while THC emissions increased to almost double the amount. The higher compression ratio (16.2:1) resulted in higher peak torque and power and THC significantly increased while NO_x was reduced, there was no comment about knock and in-cylinder pressure sensors were not used. Anhydrous fuel could not be run at 16.1:1 compression ratio.

Munsin and Laonual [15,105] studied hydrous ethanol fuel in small SI engine generator set. These workers operating at an engine load of 3.8 bar BMEP, concluded that the brake efficiency for E95W5 (wet ethanol containing 5% of water) was near 20% [14] and stated the engine running hydrous ethanol could satisfy 2011 emissions

regulations when using a three-way catalytic converter. Moreover, it has been shown that an increase in water content reduced the overall engine efficiency and increased unburned hydrocarbon and aldehyde emissions. The serious engine part wear and oil lubricant contamination were reported. No combustion analysis was presented.

More recently, research by Aleiferis and co-workers [106] reported that hydrous ethanol of 10% water content resulted in a faster flame propagation combustion with a constant intake air pressure compared to gasoline and iso-octane base-fuels. In addition, this study compared PFI (port fuel injection) and DI (direct injection) result in single cylinder optical SI engine at very low load (nearly 1.5 bar IMEP). Increase in combustion duration was reported for water-in-ethanol fractions above 10% and shortened under PFI operation. A higher level of droplet diffusion burn in the flame development images was observed in direct injection when compared to PFI operation.

Overall most prior studies of hydrous ethanol fuel showed that the water added to the fuel will reduce the combustion temperature due to both dilution and revised chemical kinetic mechanisms, leading to longer combustion duration with a higher fraction of unburned hydrocarbons and intermediate species but lower NO_x formation.

2.8 Summary of Literature

The currently reported work is generally concerned with the optical study of future fuels for next generation SI engines. The literature reviewed has uncovered the key fundamental combustion parameters and main trends towards clean high efficiency spark ignition engines, with ethanol blended fuels being progressively more widely adopted in key areas. Such fuels offer good synergy with modern downsized direct injection SI engines, where the high anti knock rating of the ethanol may be leveraged. When produced via sustainable means, such fuels offer inherent CO₂ reductions, which may be maximized if residual water content can be tolerated. However, a lack of understanding of the influence of such residual water on the fundamentals of the combustion remains apparent. Prior studies have lacked flow and flame imaging, with the potential influence of the flow insufficiently quantified to allow observations to be largely attributed to the fuels alone.

3. Experimental Engine and Instrumentation

3.1 Introduction

The experimental test facilities used during this work are described in this chapter. This includes the engine test bed, single cylinder optical research engine with its component and control units, air inlet and exhaust systems, ignition and injection systems, data acquisition system and fuel supply system. The optical engine operation and maintenance schedule including a pressure sensor and injector calibration procedures are also briefly explained. The engine has been used extensively for several years, as reported previously by prior researchers including Tongroon, Attar, Ma, and Liu [107–110].

3.2 Engine Test Bed

The engine test bed comprises a bespoke Ricardo Hydra optical single cylinder DISI research engine, mounted on a Cussons single cylinder test bed with an integrated dynamometer, oil and coolant module control systems. As is usually the case with single cylinder optical research engines, cyclic variations in speed were reduced using an oversized flywheel directly coupled to the engine crankshaft. In addition, the Cussons rig included an appropriately heavy base plate to help dampen the vertical vibrations (essential in optical work, with acceptable low vibrations verified by a crude “penny test” i.e. placing a penny on the optical head and physically observing no penny movement during motoring or firing).

3.3 Dynamometer

The Dynamometer was manufactured by McClure as an electric DC machine capable of a maximum speed of 6000 rpm rated at 400volts and 70 amps with a continuous power rating of 30 kW. The assembly is operated through a KTK thyristor converter unit (type 6P4Q30) so could be used as a DC motor to drive the engine for starting and motoring operations (i.e. when the engine was operated as an air compressor with non-firing operations) and/or as a DC generator during engine braking operations (i.e. when the engine was operated as an air expander with firing operations). Whilst performing the engine braking operations, the DC power generated by the dynamometer was converted to three-phase AC power by the converter unit and fed back into the mains supply. A speed signal was provided by a tacho-generator mounted on the dynamometer shaft so that the speed selected at the control console by the operator was maintained within an accuracy of $< \pm 5$ rpm by automatic adjustments to the motoring or loading torque. The cooling method for the dynamometer was via an electrically driven force ventilation fan mounted on the base frame.

3.4 Coolant and oil systems

The lubrication and coolant pump circulation were integrated into the test bed base frame. The engine coolant was a mixture of de-mineralised water and commercial anti-freeze with a mixing ratio of 2:1. The coolant was drawn from the bottom of the header tank and pumped through the heat exchanger before entering into a three-way valve which separated and controlled the flow for both the engine block and cylinder head as shown in Figure 3.1 with the engine setup schematic presented in Figure 3.2, which operated on fully separated flow paths. Upon exiting the engine, the coolant returned to the top of the header tank via separate return pipes. An electric heater was in place within the system in order to achieve a desired operating temperature prior to and during starting and motoring operations. The coolant temperature was measured and controlled via a closed loop system by a Spirax Sarco probe sensor mounted in the vertical subframe of the header tank. The lubrication system included a pump driven with an AC motor and a heat exchanger that controlled and monitored the oil temperature by another Spirax Sarco sensor with a closed loop control system. Both the coolant temperature (with an accuracy of $< \pm 2^{\circ}\text{C}$) and oil temperature ($< \pm 4^{\circ}\text{C}$) were adjustable by the control panel to have different operating conditions.

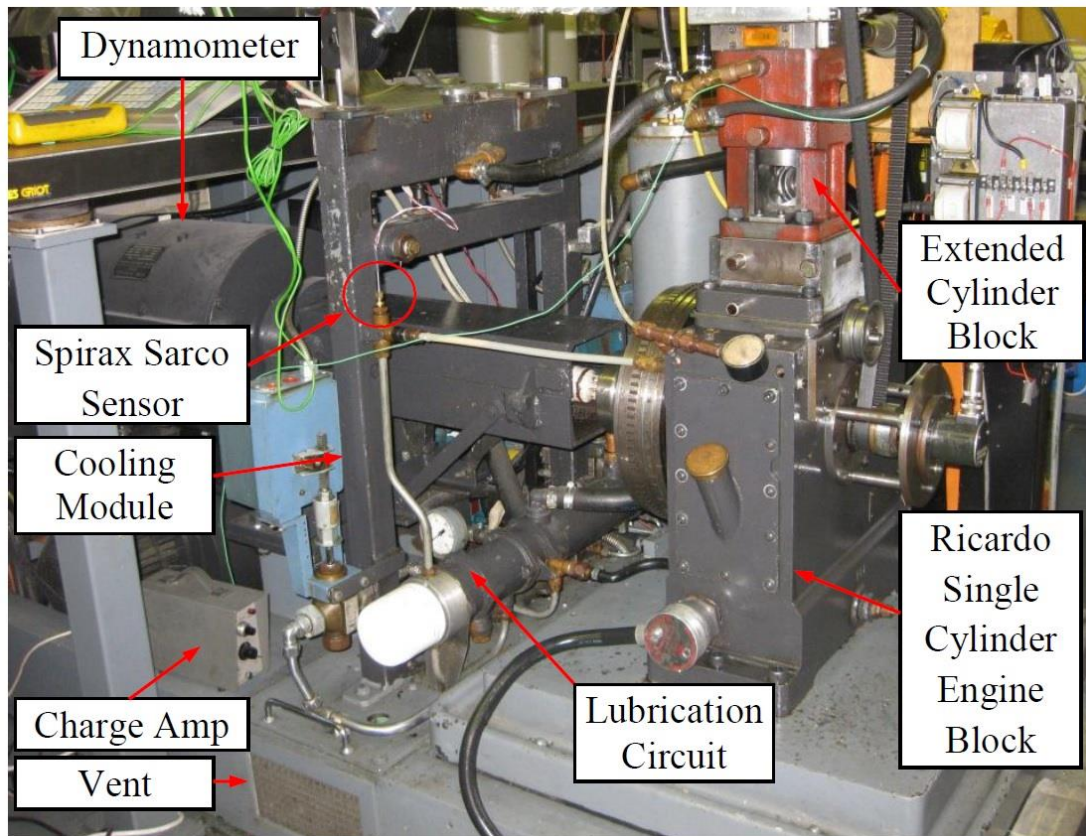


Figure 3.1. Engine Test Bed.

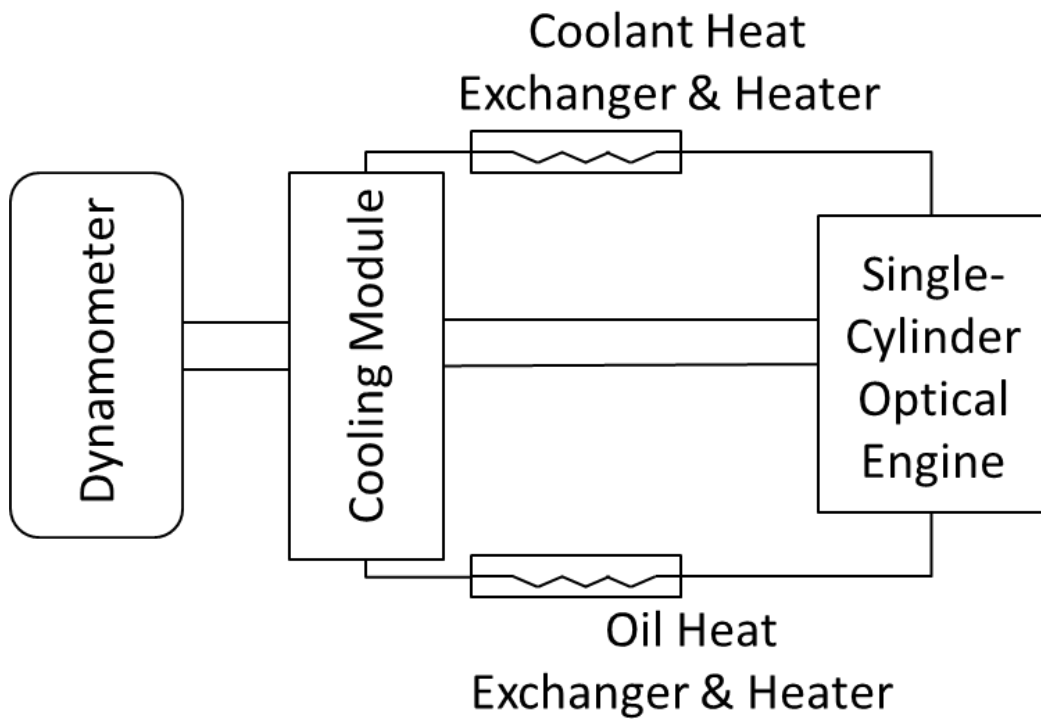


Figure 3.2. Coolant Setup Schematic.

3.5 Experimental Optical Engine

3.5.1 General description

A customized single cylinder DISI optical engine was used in this study. The basic engine specifications are presented in Figure 3.3 and the optical engine schematics are presented in Table 3.1. The cylinder head had a pent-roof combustion chamber design with a centrally mounted spray-guided direct injection as presented in Figure 3.3. The engine was fitted with a "neutral" intake port, without the sharp inner corner radius associated with high tumble engine designs and the four valves were operated by double overhead camshafts housed in an aluminum casing. The bottom-end was based on a Ricardo Hydra, mounted on a 30kW Cussons test bed with integrated oil and coolant control. The Hydra was fitted with a customized cast iron block, wet liner, and a Bowditch piston as indicated. The Bowditch type piston allowed for a 45° mirror to be placed inside the hollow core providing optical access to the combustion chamber through a quartz piston crown. A sandwich plate was designed to join the cylinder head and the extended block with two additional side windows (21mm height) providing additional optical access to the combustion chamber. There was no optical access to the pent-roof area.

Table 3.1. Key Engine Specifications.

Displaced volume	447 cc
Stroke	89 mm
Bore	80 mm
Compression ratio	8.67:1
Inlet valves diameters	29.5 mm
Exhaust valves diameters	21 mm
Valve lift	9 mm
Cam duration (Exhaust, Intake)	220° c.a. (end of ramp)
EMOP	265° aTDC (compression)
IMOP	455° aTDC (compression)
Engine Coolant temperature	90°C
Start of Injection	270° bTDC

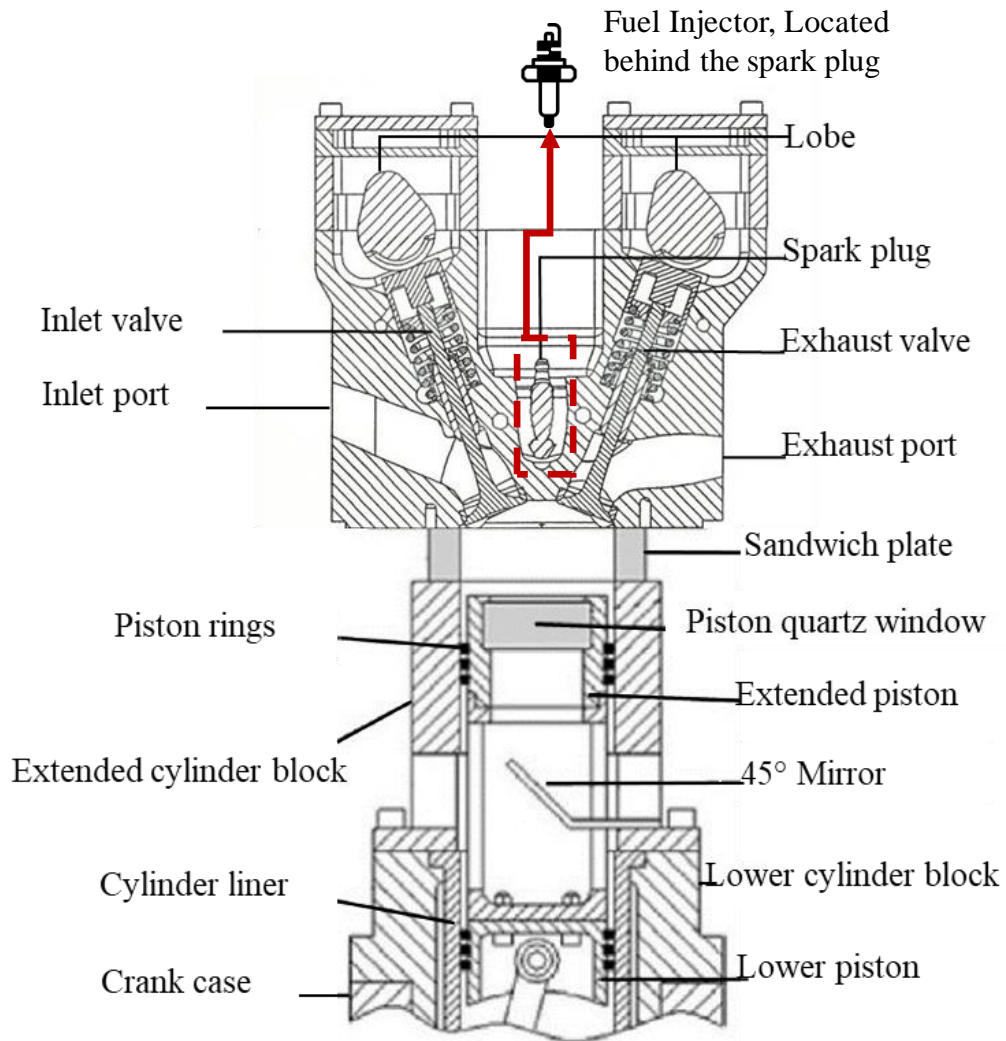


Figure 3.3. Engine Setup Schematic.

3.5.2 Optical Cylinder Head

The extended piston was made of aluminium. It was mounted on a lower cylinder block attached directly to the engine crankcase. The extended piston mounted on the lower piston ran in the lower block utilizing two compression rings and one oil control ring (PTFE compression rings lubricated with grease). The flat-topped piston crown quartz window had 55 mm diameter, allowing 50% of the horizontal bore area to be imaged. Figure 3.4 shows the visible area provided and the positioning of the valves. The blow-by effect was a concern in this design as the piston top-land was abnormally longer than standard piston design as compression rings had to be in a safe distance at top dead centre from side windows extended piston is presented in Figure 3.5.

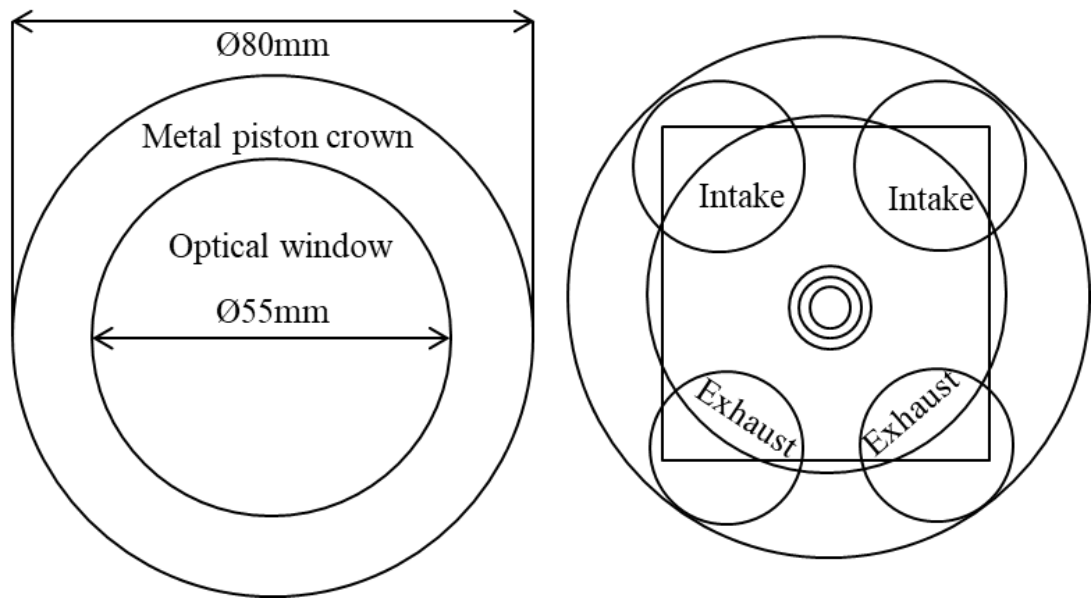


Figure 3.4. Combustion Chamber and Piston Crown.

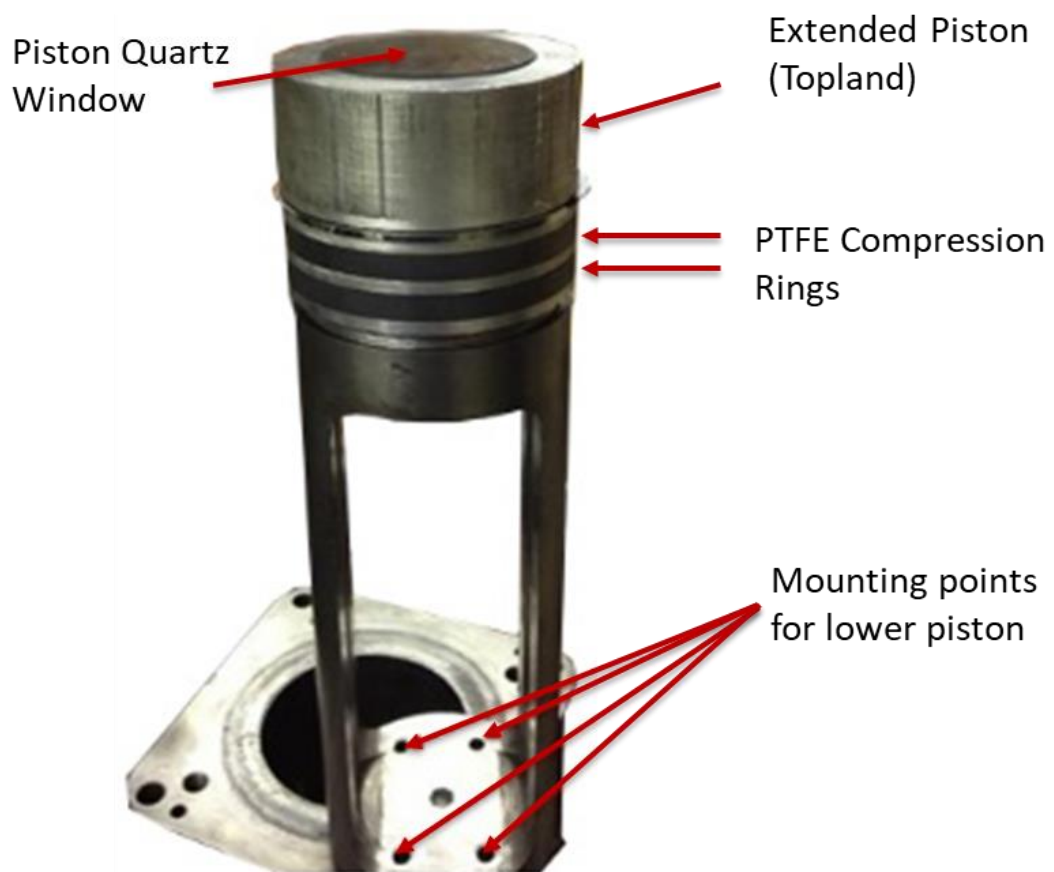


Figure 3.5. Extended Piston Assembly.

3.6 In-Cylinder Pressure Measurement

Cylinder pressure variation is mainly due to volume change and combustion, the effect of volume change on pressure can be accounted for; thus, the combustion characteristics can be obtained from accurate pressure data. In addition, pressure measurement can indicate cyclic variation and can clearly show any misfiring or knocking combustion. Pressure can be used for the engine performance analysis such as engine load measurement or for heat release analysis such as mass fraction burned analysis. In order to measure the in-cylinder pressure, a Kistler type 6055B80 piezoelectric pressure transducer, connected to a charge amplifier Kistler type model 568 via a high impedance cable, was used in this experiment. The sensor was installed flush with the chamber wall. The pressure transducer was calibrated with a dead weight pressure gauge apparatus to provide accurate measurement; this was done by assigning the voltage signal outputs from the transducer to the correct pressure readings. To achieve accurate calibration, the face of the transducer was cleaned in an ultrasonic bath followed by attaching it to the hydraulic circuit of a “dead weight” testing rig. A pressure sensor in the inlet was used to input in the LabView program the intake pressure of 0.5 bar to offset the in-cylinder pressure. The hydraulic circuit was then pressurised by adding known loads (precision weights) to the balancing piston of the tester, the corresponding voltage signal outputs provided by the transducer could then be linearly correlated by applying a range of different weights within the full measuring range of the pressure transducer. The transducer was calibrated within a maximum range of 100 bar as the maximum in-cylinder pressure during the experiment was not intended to exceed this limit (associated with the optical components). The time constant of the charge amplifier was set to ‘long’ for calibration purposes, this would be switched to ‘short’ throughout the actual experiments to account for the rapid change in pressure during in-cylinder pressure measurements. The corresponding pressure-to-voltage ratio was 10.03bar/V, which was entered in the data acquisition software for the relevant pressure calculations. Thermodynamic loss angle, which is the measure of the angle before TDC at which the peak motoring in-cylinder pressure arises due to thermodynamic irreversibilities including heat transfer and mass blow-by, was selected based on the previous researcher. A prior worker at Brunel [111] has concluded that the use of a capacitive probe allows the most accurate determination of the loss angle, where the engine may be motored under warmed up

conditions and the loss angle directly measured in a dynamic testing condition (albeit without combustion present). Unfortunately, no such probe was available at Brunel at the time of the tests. Therefore, a loss angle of 1.0 was selected based on prior experience of optical SI engines and the general recommendation of the pressure measurement manufacturer, AVL. One percent error in thermodynamic loss angle calculation could lead to 10% error in IMEP calculations. The in-cylinder pressure data acquisition system was capable of measuring pressure up to 100 bar with a sensitivity of 19.4 pC/bar and uncertainty of $\pm 0.1\%$.

3.7 Injector and ignition timing control system

The injector used in the experiment was a Siemens Piezo production part (MAHLE Part Number: NGM00084766), which sprayed a 90° fuel cone directly in front of the spark plug. Design information in terms of the external packaging of the injector and recommended the location of the spark plug relative to the plume were provided by MAHLE powertrain, however moderate modification to the cylinder head and the injector were carried out by a previous colleague [110] researching on the same engine. To achieve the precise requirements for the spray pattern, moderate modifications to the cylinder head and the injector was carried out to comply with these manufacturer guidelines, as illustrated in Figure 3.6. The clamping method adapted replicated that used in the MAHLE DI3 engine assembly, which was previously developed by MAHLE in collaboration with the injector suppliers. Set out in Figure 3.7 is the clamping method for the Piezo injector, which was used throughout the experiments with parts included, Forked clamp (Yellow), Clamp supporter (Blue block), Threaded bar (Green) and Injector tip washer (Red). The recommended peak operating pressure of the injector was 200 bar, the burst pressure of the injector was informally confirmed with Continental (formerly Siemens) to be 275 bar. Researcher at Chalmers University of Technology Gothenburg [112] have experimentally investigated the spray formation and consequent atomisation of such outward opening piezoelectric gasoline DI injector mentioned above using a constant pressure spray chamber. The sizes and velocities of the droplets and the resulting spray shapes were evaluated by adopting Planar Mie scattering and PLIF techniques (with the same fuel and tracer configurations used throughout the currently reported thesis) combined with Phase Doppler Anemometry (PDA) analysis and high-speed imaging. Figure 3.8 shows the

spray formation via Planar Mie images illustrating the shapes and movements of the spray generated by a single injection of 10mg fuel under 200bar rail pressure at four different time points.

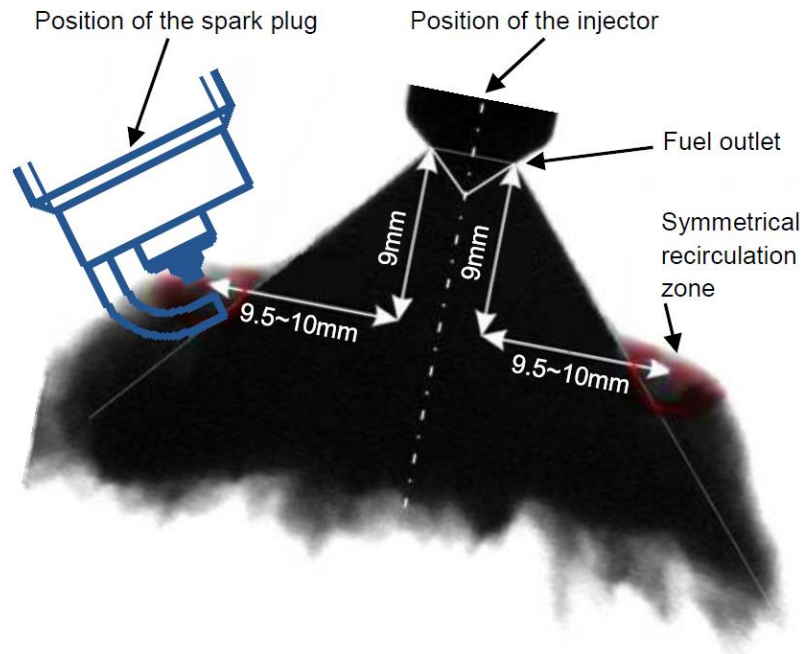


Figure 3.6. Manufacturer guidelines for injector location. (provided courtesy of MAHLE powertrain).

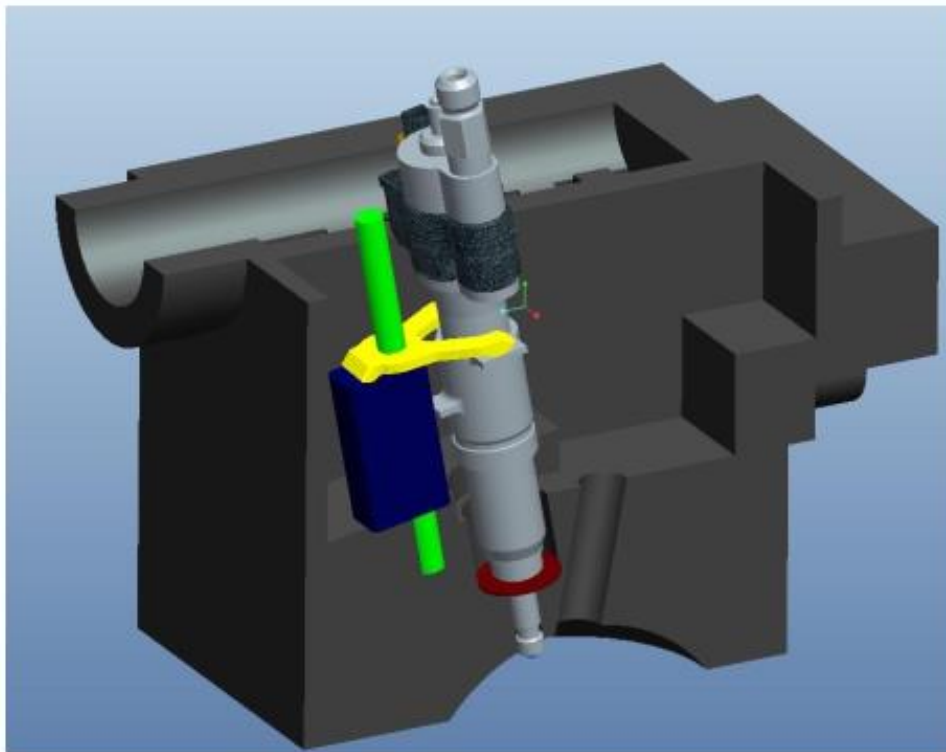


Figure 3.7. Clamping method for Piezo injector.

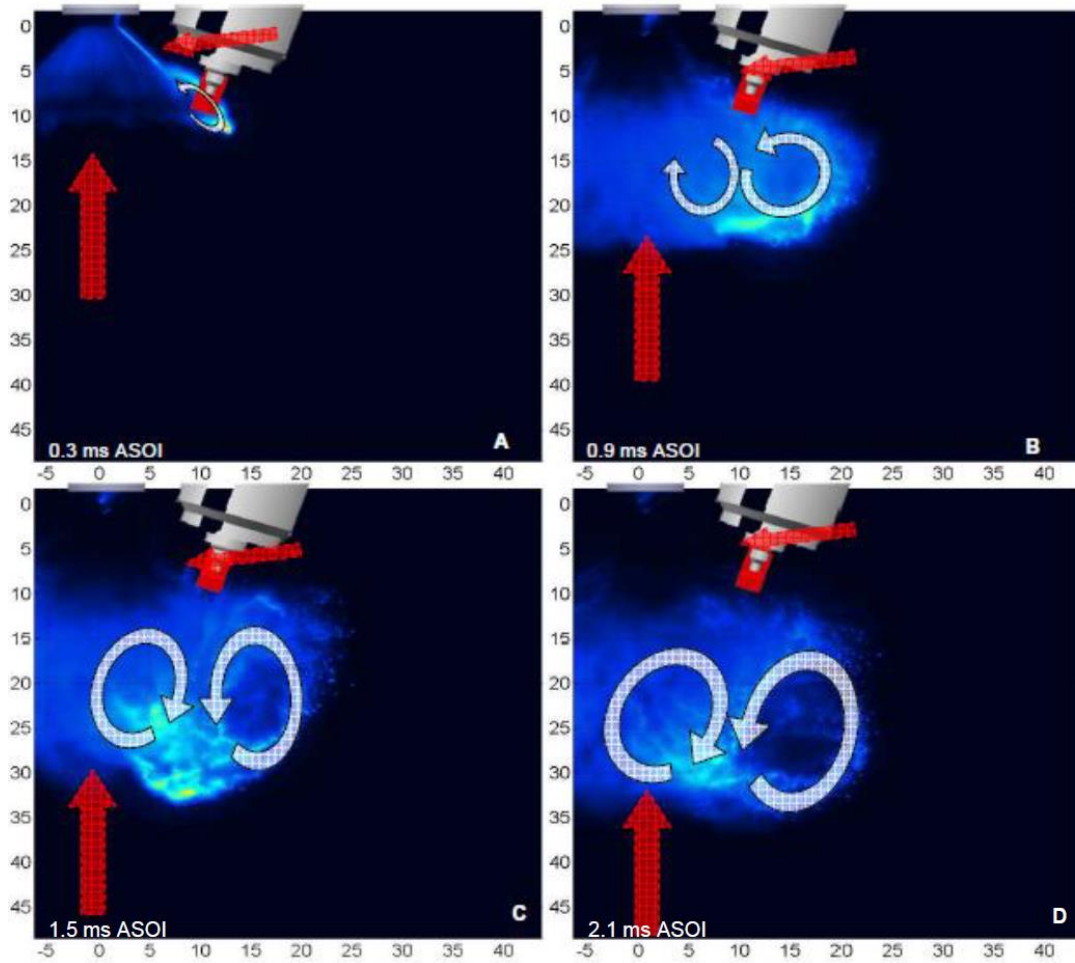


Figure 3.8. Planar Mie images showing the liquid fuel distribution at four time points during a single injection of 10 mg fuel at 200bar [112].

The spark ignition timing was controlled by an in-house built control system shown in Figure 3.9 that picks up a reference signal and generates a spark ignition trigger with an adjustable time offset and signal width. For this unit to work a reference signal and a clock signal to set the timing and width of the spark ignition was required. The signal was provided by a shaft encoder mounted onto the end of the crankshaft. The encoder generated a Transistor-Transistor Logic (TTL) signal for each crankshaft revolution and crank angle based clock signals of a resolution of 1°CA . The clock signal was used to set spark timing in crank angle. This spark ignition system was designed for a 4-stroke engine by taking two revolutions per engine cycle. The reference signal was generated by an “AND” gate logic unit which picked up signals from the crankshaft encoder and a signal generated by a cam sensor on the exhaust valve camshaft pulley wheel.

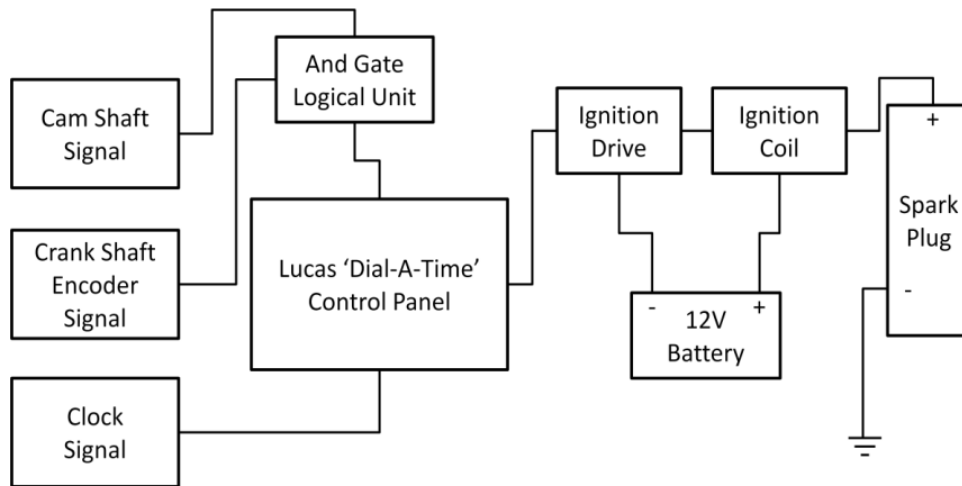


Figure 3.9. Spark Ignition Control System

3.8 Camshaft

The camshafts used throughout this research provided 9 mm valve lift with 220 °CA duration (end-of-ramp) operating with normal valve timing. The overhead camshafts were driven from the crankshaft using a synchronous belt drive with an adjustable jockey tensioner. The valve timing was adjustable by using slotted holes in the camshaft pulley wheel presented in Figure 3.10. Firing top dead centre was marked on the camshaft pulley (TDC is where two marker lines have the minimum distance from each other).

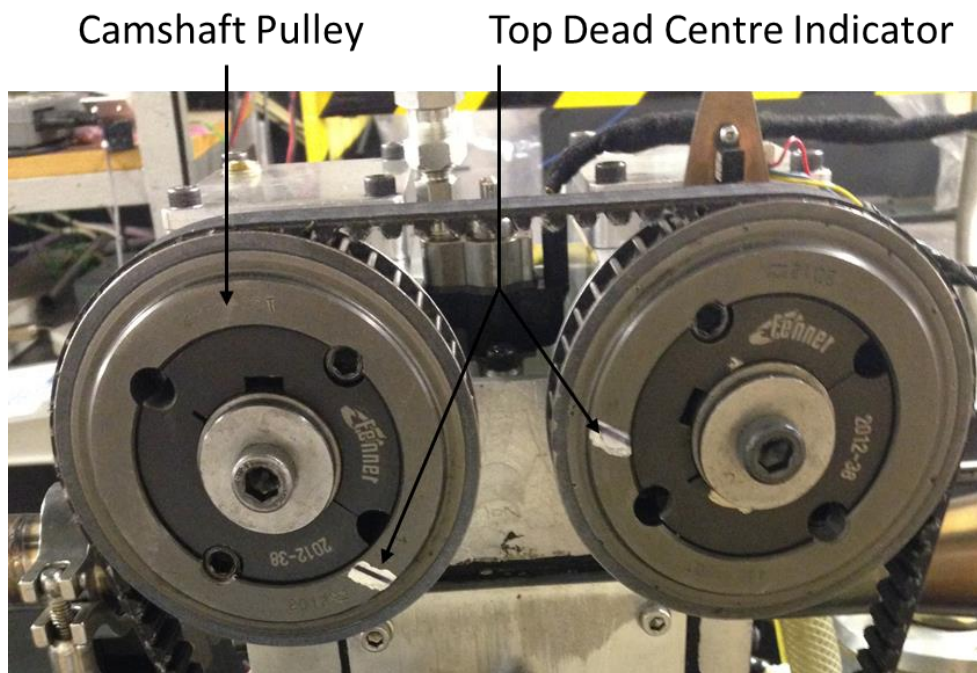


Figure 3.10. Camshaft pulley and TDC indicator.

3.9 Compression Ratio

A quartz piston crown with a diameter of 55mm was used in this research with a spacer and threaded lock ring attach the window in its place from below shown in Figure 3.11. A compression ratio of 8.67:1 was calculated by taking into account the actual Bowditch piston dimensions after assembly. During the optical measurements, a soft gasket (Chieftain Gasket Jointing 1 mm thick) was inserted on either side of the window of the quartz piston which improved the strength and stability of the piston crown. The material used was a Nitrile Butadiene Rubber (NBR) binder. In addition, an anti-stick finish on both surfaces was required during experiments. The copper spacer was placed after the soft gasket and cushioned the window from the threaded screw. A list of engine components' gaskets and sealants that should be replaced for each engine build up is presented in Appendix C.

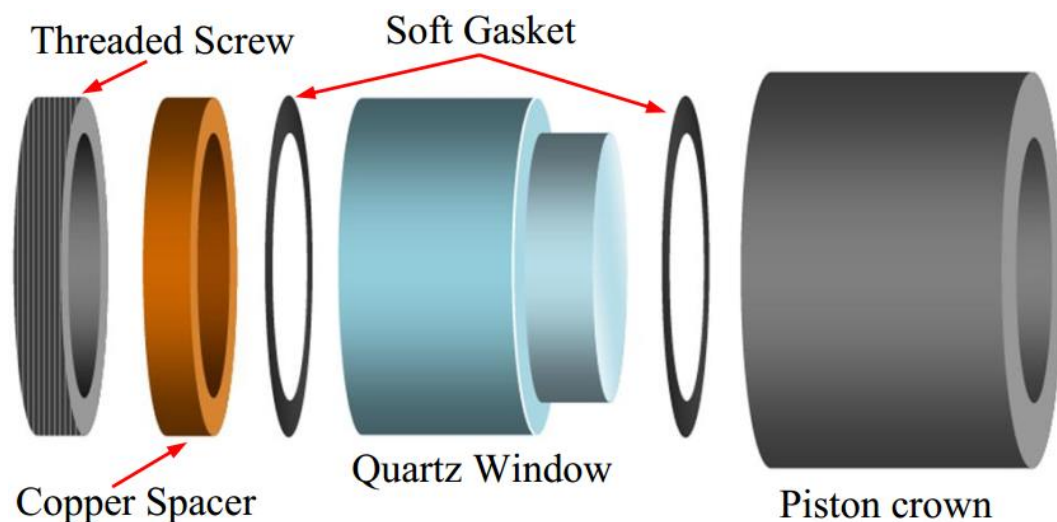


Figure 3.11. Piston Window Assembly.

3.10 Fuel Preparation

The following hydrous and anhydrous fuels were used during this research, ethanol, iso-octane, B16I84, E10I90, E6B8I85, E85I10W5 and hydrous ethanol at 5%, 12% and 20% volume water. Ethanol and iso-octane were used as a benchmark for comparison with other fuels. The fuel supply system was flushed for each fuel, which was necessary to have certainty about the fuel used in the experiment. All the blended fuels used in the test were mixed based on their volume measured with a graduated

cylinder, W5E95 (95% volume ethanol and 5% volume water) and based on the fuel lambda sensor (Horiba Mexa-110 AFR) was adjusted in respect to each fuel H/C and O/C ratio.

3.11 Fuel Supply System

Fuel was pressurized from a fuel tank by a compressed air pump (PowerStar4 (S64 P4S64)) with an amplification ratio of 64:1. Fuel pressure was adjusted by controlling the air pressure and is determined by the ratio between the area of the air drive piston, the area of the liquid drive piston and the applied driving air pressure. The fuel was supplied to a common rail with the regulated air inlet pressure at ~ 5.5 bar this pump could generate rail pressures of up to ~ 340 bar, the 100 bar pressure was adjusted with a pressure gauge installed to monitor and set the rail pressure injector. Figure 3.12 lays out the schematic of this fuel supply system. The pressure variation in the fuel rail was measured by the previous researcher [110] at ± 4 bar at 200 bar fuel pressure with 0.5 ms injection duration using iso-octane.

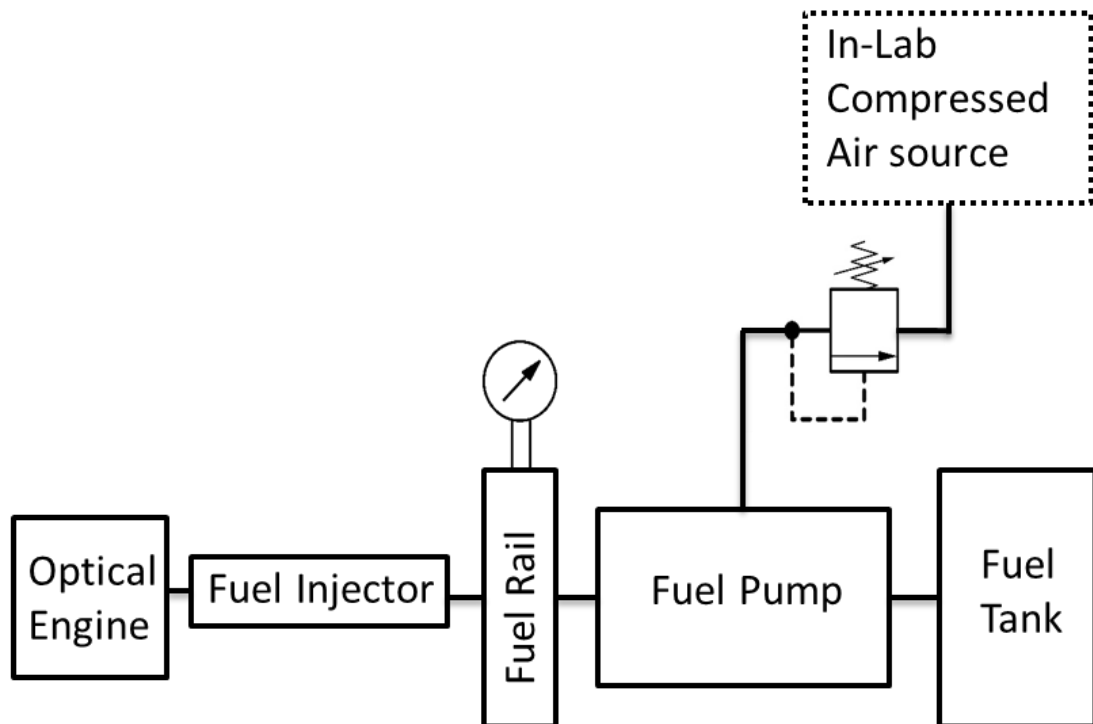


Figure 3.12. Fuel Supply System.

3.12 Data acquisition and synchronisation

National Instrument board type NI USB-6251 was used in this research as a Data Acquisition System (DAQ) with a host computer and a LabView based program capable of real time data and averaging acquisition to calculate IMEP and COV of IMEP. The board (type NI USB-6251) is a multifunction data acquisition card with 16-bit resolution and a sampling rate of 1.25 MS/s. Three inputs which receive the pressure charge amplifier output signal, the engine clock signal and engine reference signal were used in this DAQ. The card was connected with a USB cable to the host computer which was used to store the data and perform the calculations based on user-specified cycles. A reference signal provided by an And Gate Logic unit was set to 80° CA bTDC to synchronise the data acquisition system. This unit received a signal from a shaft encoder (clock signal) with 1° CA resolution and a signal from the hall-effect cam sensor. The hall-effect sensor was attached to the exhaust camshaft pulley and provided a signal for each cycle at 80° CA bTDC, as illustrated in Figure 3.14 next page. As shown in Figure 3.13, in addition to the spark timing, the reference signal generated at 80° BTDC was also used via a multi-channel signal generator to initiate the fuel injection and the image acquisition process, as to be detailed in the next chapter.

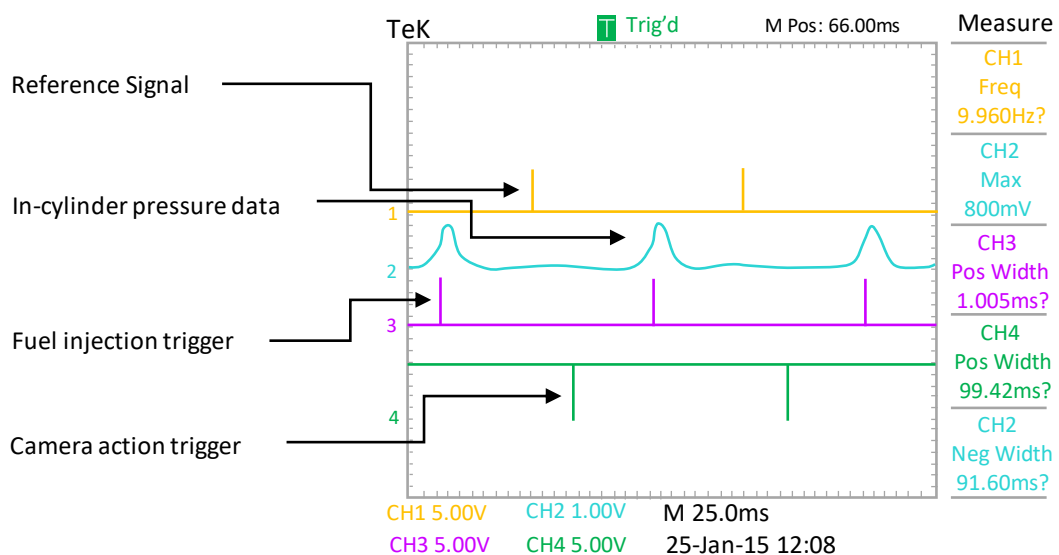


Figure 3.13. Timing sequence for fuel injection and image acquisition.

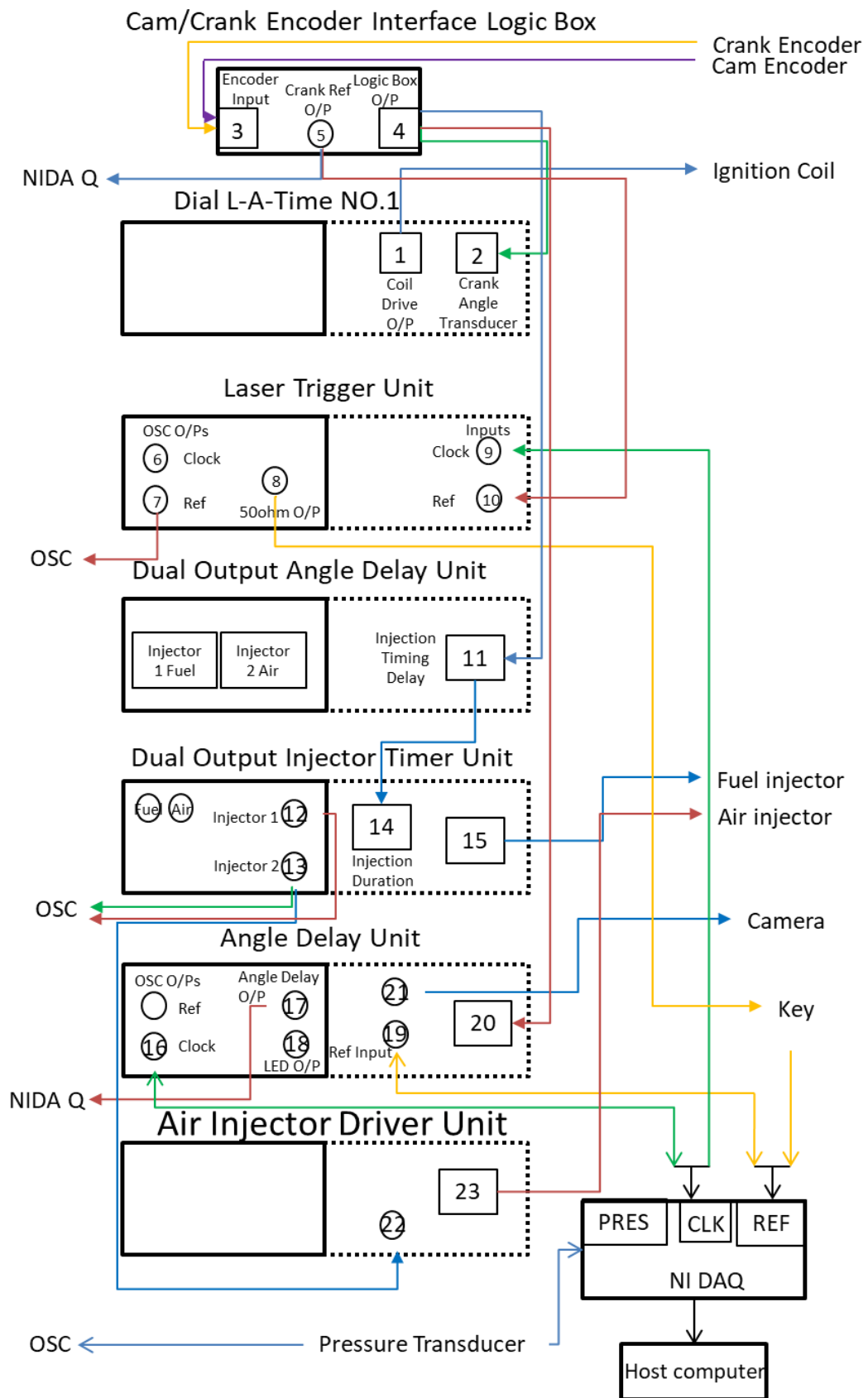


Figure 3.14. Data Acquisition System.

3.13 Engine Maintenance and Operation

Commercial non-fluorescing lubricating paste was used to lubricate the extended piston and cylinder block. This was required due to optical window fouling and fluorescence emission observed in previous tests when using conventional engine lubricant. As the extended piston was lubricated with a paste and not a conventional lubricant, the test duration was minimized. The lubrication was changed after each set of tests to avoid any damage as part of a robust testing procedure required given that optical engines are delicate and may only run for short firing periods, (up to 2 minutes combustion). Coolant and engine oil levels were checked before starting the engine for each test. The fuel tank was filled with fresh fuel as discussed in the fuel preparation section, as the fuel spectroscopic behavior could change over time [113].

The fuel injector and spark plug were powered using a commercial 12-volt battery. The state of charge was checked before running the engine to ensure accurate operation. The water pump and water heater were switched on half an hour before switching on the oil pump. When the water temperature was about 60-70 °C then the oil pump was switched on to reach a temperature of 40°C. The pressure transducer, fuel injectors, and spark plug were inspected regularly and controlled during each experiment via the engine control unit. The calculated major half order torsional speed for the engine was 700 rpm (11.8 rev/s) [114] and hence the engine must not be run at or near to this speed. During testing the engine was motored to around 1000 rpm as quickly as possible using the rpm dial on the Hydra control system.

3.14 Summary

The engine test cell facilities such as dynamometer, fuel supply system, oil system, and engine control system were demonstrated. The experimental optical engine was presented containing optical cylinder head, compression ratio, and camshaft. The data acquisition and synchronisation, Injector and ignition timing control system and in-cylinder pressure measurement were also presented in this chapter, finally, test procedure maintenance was explained

4. Three Dimensional CFD Flame & Flow Investigation

4.1 Introduction

Over the past decade, numerical analysis has been extensively used and validated for engineering design and optimisation. Computational Fluid Dynamics (CFD) has also contributed a vital part in the research development of the IC engine and is increasingly used for the analysis of in-cylinder flow to understand turbulence behavior, mixture formation, and combustion. In the currently reported study, the 1-D CFD method was used to validate initial values (intake and exhaust thermodynamic data) for 3-D boundary conditions whereas 3-D CFD was used to investigate the in-cylinder flow pattern.

Conventional research methods for engine development demonstrate the importance of numerical analysis. Numerical engine studies and analysis plays a vital role in the development of engines as it helps analyse various engine configurations without physically building an engine. Thus, engine simulation helps to reduce the cost and time involved in developing a new engine [115]. In the early 1950s and 1960s ICE modelling studies were used to model simple mathematical formulae because computers were only capable of simple calculations. For example, one well known empirical engine model is the Wiebe function [116] which has been used to predict the burned mass rate and a fraction. The Wiebe function and its derivatives, such as double Wiebe functions, have since been widely applied in zero-dimensional engine modeling tools [116,117]. The infancy of Computational Fluid Dynamics (CFD) in-cylinder engine modeling started as early as the 1970s. However, until the 1980s engine CFD modeling was not generally used in engine development due to the following two facts: limited capacity of computers and general engine CFD code or software was not available at the time. Instead, engine modeling with phenomenological models was mainly applied in this period. For instance, coupling of phenomenological quasi-steady

spray models [118] and soot and NO formation models [32,119] tremendously extended the potential of engine modeling compared to zero-dimensional simulations. The rapid increase of computational power of personal computers and flexible mesh generation techniques in many commercial engine CFD justifies the engine simulation. In addition, demands for more optimized simulating advances in engine combustion techniques, detailed fuel chemistry solvers have also become a standard part of many engine CFD tools since 2001 [120]. Despite the fact that state-of-the-art engine modeling tools normally have larger quantitative uncertainties than engine experiments, engine simulations have some significant benefits over experimental measurements in engine development and optimization. These advantages include low cost, the ability to study a wide range of conditions, separated physical and chemical processes and precise in-cylinder information which is normally not available or is inaccessible in experiments [121]. Recent efforts in the fields of mesh generation techniques, numerical methods, heat transfer, turbulence, chemical kinetics, and multi-phase flows further enhanced the predictability of IC engine modeling tools. Hence, the quantitative prediction capability of the next generation of IC modeling tools should be even better [122].

4.2 Computer Modelling of Turbulence

Turbulence can be described as follows, “three dimensional, rotational, intermittent, highly disordered, diffusive and dissipative” [123] that is known for the most complicated kind of fluid motion.

In CFD software the choice of turbulence model depends on considerations such as the physics encompassed in the flow, the established practice for a specific class of problem, the level of accuracy required, the available computational resources and the amount of time available for the simulation. Four CFD methods have been considered to select the most appropriate solution to investigate flow field inside the engine cylinder. Reynolds-Averaged Navier-Stokes (RANS) and Large-Eddy Simulation (LES) are the two most popular modelling methods of IC engine applications. Both methods use similar equations and are based on the same principle. However, in terms of physical meanings of parameters in the equations, the difference is identified and will be explained. The differential solution solves the motion of a fluid in three

dimensions as described by a system of partial differential equations that represent mathematical statements of the conservation laws of physics (mass, momentum, energy and concentration conservation). Direct Numerical Simulation (DNS) has made a significant contribution in turbulence research over the last decades [124], this method involves the numerical solution of the full three-dimensional, time-dependent Navier–Stokes equations without the need for any turbulence model.

4.2.1 Differential Equations

Mass, momentum, energy and concentration conservation are representing mathematical statements of the conservation laws of physics which can be used to describe the motion of a fluid in three dimensions by a system of partial differential equations. The momentum conservation equations are called the Navier–Stokes equations. The equations are presented in the most general form of multi-phase flows [125,126], as the single-phase ones are easily derived by just setting the volume fraction, r_i equal to unity. A convenient assumption for deriving partial differential equations is based on the concepts of time and space averaging; that describes more than one phase can exist at the same location at the same time. If so then, any small volume of the domain of interest can be imagined as containing, at any time, a volume fraction r_i of the i th phase. Consequently, if there are n phases in total then:

$$\sum_{i=1}^n r_i = 1 \quad (4.1)$$

Assuming the above notation, following balance equations can be derived:

Conservation of phase mass

$$\frac{\partial}{\partial t}(\rho_i r_i) + \text{div}(\rho_i r_i \vec{V}_i) = \dot{m}_i \quad (4.2)$$

Where ρ_i is the density, \vec{V}_i is the velocity vector, r_i is the volume fraction of phase i and \dot{m}_i is the mass per unit volume entering the phase i from all sources per unit time, and div is the divergence operator meaning the limit of the outflow divided by the volume as the volume tends to zero.

Overall mass conservation equation

$$\sum_{i=1}^n \left[\frac{\partial}{\partial t} (\rho_i r_i) + \text{div}(\rho_i r_i \vec{V}_i) \right] = 0 \quad (4.3)$$

Conservation of phase momentum

$$\frac{\partial}{\partial t} (\rho_i r_i u_{ik}) + \text{div}(\rho_i r_i \vec{V}_i u_{ik}) = r_i (-\vec{k} \cdot \text{grad } p + B_{ik}) + F_{ik} + l_{ik} \quad (4.4)$$

Where u_{ik} is the velocity component in the direction k of phase i ; p is pressure, assumed to be shared between the phases; \vec{k} is a unit vector in the k -direction; B_{ik} is the k -direction body force per unit volume of phase i ; F_{ik} is the friction force exerted on phase i by viscous action within that phase; and l_{ik} is the momentum transfer to phase i from interactions with other phases occupying the same space.

Conservation of species-in-phase mass:

Conservation of phase energy

$$\frac{\partial}{\partial t} (r_i (\rho_i h_i - p)) + \text{div}(\rho_i r_i \vec{V}_i h_i) = r_i Q_i + H_i + J_i \quad (4.5)$$

Where h_i is stagnation enthalpy of phase i per unit mass meaning the thermodynamic enthalpy plus the kinetic energy of the phase plus any potential energy; Q_i is the heat transfer to phase i per unit volume; H_i is heat transfer within the same phase, e.g. by thermal conduction and viscous action; and J_i is the effect of interactions with other phases.

Conservation of species-in-phase mass

$$\frac{\partial}{\partial t} (\rho_i r_i m_{il}) + \text{div}(\rho_i r_i \vec{V}_i m_{il}) = \text{div}(r_i \Gamma_{il} \text{grad } m_{il}) + r_i R_{il} + \dot{m}_i M_{il} \quad (4.6)$$

Where m_{il} is the mass fraction of chemical species l present in phase i ; R_{il} is the rate of production of species l , by chemical reaction, per unit volume of phase i present; Γ_{il} is the exchange coefficient of species l (diffusion); and M_{il} is the l - fraction of the mass crossing phase boundary, i.e. it represents the effect of interactions with other phases.

All of the above equations can be expressed in a single form as follows:

$$\frac{\partial}{\partial t}(\rho_i r_i \varphi_i) + \text{div}(\rho_i r_i \vec{V}_i \varphi_i) = \text{div}(r_i \Gamma_{\varphi_i} \text{grad } \varphi_i) + r_i s_{\varphi_i} + \dot{m}_i \Phi_i \quad (4.7)$$

$$\equiv \text{Total } (\varphi_i)$$

Where φ_i is any extensive fluid property; the first term on the right-hand side expresses the whole of that part of the source term which can be so expressed, with Γ_{φ_i} being the exchange coefficient for φ_i ; s_{φ_i} is the source/sink term for φ_i , per unit phase volume; and $\dot{m}_i \Phi_i$ represents the contribution to the total source of any interactions between the phases, such as any phase change with Φ_i being the value of φ_i in the material crossing the phase boundary, during phase change. For turbulent flow, averaging over times which are large compared with the fluctuation time leads to similar equations for time-average values of φ_i with fluctuating-velocity effects usually represented by enlargement of Γ_{φ_i} [123]. More details on the above concepts and equations may be found in [127].

4.2.2 Direct Numerical Simulation

DNS solves the numerical solutions of (mass, momentum, energy and concentration conservation) full three-dimensional, time-dependent Navier–Stokes equations without the need for any turbulence model. Solving spatial and temporal scales of turbulence numerically makes DNS very informative in comparison to other competing modelling methods. Amongst all of the available approaches, Direct Numerical Simulation (DNS) has made a significant contribution in turbulence research over the last few decades [124]. However, solving flow inside an SI engine cylinder numerically requires a tremendous amount of computational power which is currently either impossible or it is not cost effective. Another important issue with DNS applications for SI engine modelling is the validation of the obtained results. According to Sandham [128] and Coleman and Sandberg [129], the following are the criteria for such validation:

- Validation of the obtained numerical data against analytical solutions, experimental data, and different numerical codes.
- Parametric studies with different grid resolutions, domain sizes, and time steps.

- The time step (Δt) should be comparable with the Kolmogorov time-scale and the grid spacing, (Δx_i), with the Kolmogorov micro-scale (τ), while the ratios of $\Delta t/\tau$ and $\Delta x_i/\tau$ should be of the order of unity.
- Evaluation of the statistical quantities budgets.

4.2.3 Reynolds-Averaged Navier Stokes (RANS)

As discussed earlier in this chapter, the study of flow inside an SI engine requires a tremendous amount of computational power to be solved numerically, therefore engineers have been researching since 1985 [130] the Reynolds-Averaged Navier Stokes (RANS) approach. In this method all of the unsteadiness is averaged out meaning unsteadiness is effectively considered as part of the turbulence itself. The RANS equations govern the transport of the averaged flow quantities, with the whole range of the scales of turbulence being modelled and can be used to approximate turbulent flow quantities. This approximation is based on knowledge of the properties of the flow turbulence to give approximate time-averaged solutions to the Navier–Stokes equations. The RANS-based modelling approach therefore greatly reduces the required computational effort and resources so widely adopted for practical engineering applications.

4.2.3.1 Physical Concept of Turbulence

Transfer of energy to smaller spatial scales across a continuous wave-number spectrum (3D nonlinear process) can be described as the main characteristics of turbulence. An Eddy is a useful concept for discussing the main mechanisms of turbulence [131,132]. An eddy can be expressed as a typical turbulence pattern, covering a range of wavelengths, with large and small eddies co-existing in the same volume of fluid. The actual modes of turbulence are eddies and high-vorticity regions [133,134]. The kinetic energy from the mean motion is extracted from the largest eddies because eddies of comparable size can only exchange energy with one another [123]. This energy is then transferred to neighbouring eddies of smaller scales continuing to smaller and smaller scales (larger and larger velocity gradients), the smallest scale being reached when

eddies lose their energy by the direct action of viscous stresses that converts into internal thermal energy on the smallest-sized eddies [135].

The amount of energy dissipated and the stretching process cannot be affected by viscosity; however, the smallest scale at which dissipation takes place is determined by viscosity. The large eddies that characterise the large-scale motion play a vital role in determining the rate at which the mean-flow kinetic energy is fed into turbulent motion and can be passed on to smaller scales and be finally dissipated. It is very important to accurately model large eddies as they are mainly responsible for the transport of momentum and heat. Larger-scale eddies which are primarily responsible for turbulent mixing usually cannot be affected by viscosity with the exception of a ‘viscous sublayer’ which fluid will have zero velocity relative to the boundary [123]. Furthermore, the effects of density fluctuations on turbulence are small. Therefore, simulations usually neglect the direct effect of viscosity and compressibility on turbulence. It is also important to note that it is the fluctuating velocity field that drives the fluctuating scalar field (hence why the effect of the latter on the former usually being taken as negligible).

4.2.3.2 The Governing Equations

The assumptions are that the turbulent fluid is a continuum, Newtonian in nature and that the flow can be described by the Navier–Stokes equations. The equations for turbulence fluctuations are derived by Reynolds de-composition describing the turbulent motion as a random variation about a mean value.

$$\phi = \bar{\phi} + \phi' \quad (4.8)$$

Where ϕ is the instantaneous scalar quantity, $\bar{\phi}$ is its time- mean value and ϕ' is the fluctuating part of the turbulence. The time-average of the fluctuating value is zero $\overline{\phi'} = 0$, and the mean value $\bar{\phi}$ can be defined as:

$$\bar{\phi(x)} = \lim_{t \rightarrow \infty} \frac{1}{\Delta t} \int_{t_1}^{t_1 + \Delta t} \phi(x, t) dt, t_1 \ll \Delta t \ll t_2, \quad (4.9)$$

Where t_1 is the time scale of the rapid fluctuations and t_2 is the time scale of the slow

motion for non-stationary turbulence. By mathematical substitution of Equation (4.8) into conservation equations mentioned earlier for single-phase, incompressible flows and then taking the time-mean of the resulting equations, derives the following continuity and NS equations:

$$\frac{\partial \bar{u}_i}{\partial x} = 0 \quad (4.10)$$

$$\frac{\partial \bar{u}_i}{\partial t} + \frac{\partial}{\partial x_j} (\bar{u}_i \bar{u}_j) = -\frac{1}{\rho} \frac{\partial \bar{p}}{\partial x_i} + \nu \frac{\partial^2 \bar{u}_i}{\partial x_j \partial x_j} - \frac{\partial}{\partial x_j} (\overline{u'_i u'_j}) \quad (4.11)$$

Where \bar{u}_i is the mean velocity, u'_i the fluctuating velocity, ρ is the fluid density and ν the kinematic viscosity. Equation (4.11) is known as the Reynolds-Averaged Navier–Stokes (RANS) equation, while the term $(\overline{u'_i u'_j})$ is the Reynolds-stress tensor:

$$\tau_{ij} = \overline{u'_i u'_j} \quad (4.12)$$

In order to correlate Reynolds stresses to the rate of strain of the mean motion, the turbulence eddies are thought of as parcels of fluid, which like molecules, collide and exchange momentum, obeying the kinetic theory of gases. Thus, in analogy with the molecular viscous stress, the Reynolds (turbulence) stresses are modelled as follows:

$$\tau_{ij} = \overline{u'_i u'_j} = \frac{2}{3} k \delta_{ij} - \nu_t \left(\frac{\partial \bar{u}_i}{\partial x_j} + \frac{\partial \bar{u}_j}{\partial x_i} \right), \quad (4.13)$$

$$k = \frac{1}{2} \overline{u'_i u'_i} = \frac{1}{2} (\overline{u'^2_1} + \overline{u'^2_2} + \overline{u'^2_3}) \quad (4.14)$$

where k is the turbulence kinetic energy and $\nu_t = \mu_t/\rho$ is the turbulence or eddy (kinematic) viscosity which, in contrast to the molecular (kinematic) viscosity is not constant; and may vary significantly from flow to flow and from point to point [127]; and δ_{ij} is the Kronecker delta.

Two-equation models, such as $k - \varepsilon$ and $k - \omega$ [127], described below in this subsection, use differential equations to compute both the characteristic velocity and length scale and then estimate the value of ν_t by the following equations:

$$v_t = \begin{cases} c_\mu f_\mu \frac{k^2}{\varepsilon} & (k - \varepsilon \text{ model}) \\ \alpha^* \frac{k}{\omega} & (k - \omega \text{ model}) \end{cases} \quad (4.15)$$

Where f_μ is a damping function, c_μ and α^* are constants, ε is the turbulence energy dissipation rate and ω the dissipation per unit turbulence kinetic energy. These models will be explained thoroughly in separate sections later.

4.2.3.3 One-Equation Models

In the simplest form, one-equation models are defined as formulating one additional transport equation for the computation of a turbulence quantity, usually the turbulence kinetic energy (k). Length-scale distribution (L) is still needed for one-equation modelling, which is defined algebraically and is usually based on available experimental data. Most researchers decided to add additional equations as a one-equation model is difficult to use without experimental data [127].

4.2.3.4 Two-Equation Models

Two-equation models use two transport equations for two turbulence properties in addition to the mean-flow Navier–Stokes equations. The first one is usually that for the turbulence kinetic energy (k) and the same as the one-equation model. The second can be any of the following quantities, depending on the modeling purpose and availability of experimental data [127]:

- The dissipation rate of turbulence kinetic energy (ε)
- The specific dissipation rate (ω)
- The length scale (L)
- The product of ($k \sim l$)
- The time scale τ
- The product of k and τ

For the foreseeable future, this type of modelling is the most preferred by the industry as shown by Hanjalic [136]. In the next section, the $k - \varepsilon$ and $k - \omega$ models are presented, as being representative of the two-equation models, along with their improvements (k- ε , RNG).

4.2.3.4.1 The $k - \varepsilon$ Model

The most commonly used and verified two-equation model, with many improvements covered over the years, is the so-called $k - \varepsilon$ model. In its standard form as reported by Launder and Sharma [137], this model can be specified as following the kinematic eddy viscosity ν_t equation:

$$\nu_t = C_\mu \frac{k^2}{\varepsilon} \quad (4.16)$$

The turbulence kinetic energy (k) equation is expressed as:

$$\frac{\partial k}{\partial t} + \bar{u}_j \frac{\partial k}{\partial x_j} = \frac{\partial}{\partial x_j} \left[\frac{(v + \nu_t)}{\sigma_k} \frac{\partial k}{\partial x_j} \right] - \varepsilon + \tau_{ij} \frac{\partial \bar{u}_i}{\partial x_j} \quad (4.17)$$

The turbulence dissipate rate (ε) equation is:

$$\frac{\partial \varepsilon}{\partial t} + \bar{u}_j \frac{\partial \varepsilon}{\partial x_j} = \frac{\partial}{\partial x_j} \left[\frac{(v + \nu_t)}{\sigma_\varepsilon} \frac{\partial \varepsilon}{\partial x_j} \right] - c_{\varepsilon 1} \frac{\varepsilon}{k} \tau_{ij} \frac{\partial \bar{u}_i}{\partial x_j} - c_{\varepsilon 2} \frac{\varepsilon^2}{k} \quad (4.18)$$

Where $\sigma_k = 1.0$ and $\sigma_\varepsilon = 1.3$ are the Prandtl numbers for k and ε , respectively. The other model constants are:

- $C_\mu = 0.09$
- $c_{\varepsilon 1} = 1.44$
- $c_{\varepsilon 2} = 1.92$

Despite being unable to predict flows with adverse pressure gradients (static pressure increases in the direction of the flow) [138], the k- ε model is recommended for gross

estimation of the flow field and for cases such as combustion, multiphase flows and flows with chemical reactions [139].

4.2.3.4.2 The Modified $k - \varepsilon$ Model (RNG)

Modifications and improvements of the standard $k - \varepsilon$ model are in many forms two most commonly used are, flows with strong buoyancy and the Renormalization Group (RNG) $k - \varepsilon$ model [140] The RNG $k - \varepsilon$ model is a modification of the standard $k - \varepsilon$ model with a better indication of the recirculation length in separating flows. The model can be expressed by the same equations (4.16)(4.17)(4.18) of the standard $k - \varepsilon$ model but with a modified coefficient that attempts to take into consideration different scales of motion through changes to the production term $c_{\varepsilon 2}$; this term is computed via the following equation:

$$c_{\varepsilon 2} \equiv c_{\varepsilon 2} + \frac{C_{\mu} \eta^3 (1 - \eta / \eta_0)}{1 + \beta_1 \eta^3} \quad (4.19)$$

$$\eta = \frac{sk}{\varepsilon}, \quad S = \sqrt{2s_{ij}s_{ij}}, \quad S = \frac{1}{2} \left(\frac{\partial \bar{u}_i}{\partial x_j} + \frac{\partial \bar{u}_j}{\partial x_i} \right) \quad (4.20)$$

Where S shows the mean strain-rate of the flow and s_{ij} is the deformation tensor. The model constants are:

$$\begin{aligned} C_{\mu} &= 0.085 & c_{\varepsilon 1} &= 1.68 & \beta &= 0.012 \\ c_{\varepsilon 1} &= 1.42 & \sigma_k &= \sigma_{\varepsilon} = 0.72 & \eta_0 &= 4.38 \end{aligned}$$

Many researchers found that this model gives better results than the standard $k - \varepsilon$ model for separating flows [138,140]. More details for the study can be found in the work of Karabelas [142].

4.2.3.4.3 The $k - \omega$ Model

A second type of the two-equation model is another ‘successful’ model and also widely used by researchers. It was initially proposed by Kolmogorov in 1942 [143]. Spalding [144] developed an improved version of this model in 1972. This model was also

developed further by numerous scientists and engineers, but the most important development was by Wilcox [145]. In the currently reported study, the most recent version of the model (Wilcox (2006 $k - \omega$ model) is presented below [138,145]:

Kinematic eddy viscosity (ν_t) equation:

$$\nu_t = \frac{k}{\tilde{\omega}}, \quad \tilde{\omega} = \max \left[\omega, C_{lim} \sqrt{\frac{2S_{ij}S_{ij}}{\beta^*}} \right], \quad C_{lim} = \frac{7}{8} \quad (4.21)$$

Turbulence kinetic energy (k) equation:

$$\frac{\partial k}{\partial t} + \bar{u}_j \frac{\partial k}{\partial x_j} = \frac{\partial}{\partial x_j} \left[\left(\nu + \sigma^* \frac{k}{\omega} \right) \frac{\partial k}{\partial x_j} \right] - \beta^* k \omega + \tau_{ij} \frac{\partial \bar{u}_i}{\partial x_j} \quad (4.22)$$

Specific dissipation rate (ω) equation:

$$\frac{\partial \omega}{\partial t} + \bar{u}_j \frac{\partial \omega}{\partial x_j} = \frac{\partial}{\partial x_j} \left[\left(\nu + \sigma \frac{k}{\omega} \right) \frac{\partial \omega}{\partial x_j} \right] - \beta \omega^2 + \frac{\sigma_d}{\omega} \frac{\partial k}{\partial x_j} \frac{\partial \omega}{\partial x_j} + a \frac{\omega}{k} \tau_{ij} \frac{\partial \bar{u}_i}{\partial x_j} \quad (4.23)$$

The auxiliary relations and closure coefficients of the model are specified as follows:

$$\begin{aligned} a &= 0.52 & \beta_0 &= 0.0708 & \beta &= \beta_0 f_\beta & \beta^* &= 0.09 & \sigma &= 0.5 & \sigma^* &= 0.6 & \sigma_{d0} &= 0.125 \end{aligned} \quad (4.24)$$

Where C_{lim} is the stress-limiter strength.

The $k - \omega$ model is argued to be more appropriate compared to the standard $k - \epsilon$ model in the case of adverse pressure gradient and can this model can be easily integrated into the viscous sub-layer without any additional damping functions [138]. However, this model can be very sensitive to mesh density in the vicinity of the wall.

4.2.4 Large Eddy Simulation (LES)

The most important disadvantage of the DNS model is a computational expense, with

RANS being less accurate than DNS due to averaging turbulence quantities. The Large Eddy Simulation modelling approach is more suitable to understand bulk air motions and its interactions and of wider applicability than RANS and less computationally demanding than DNS. In LES modelling for turbulence, the important large scales are fully resolved whilst the small sub-grid scales are modelled. The main advantage of LES compared to RANS models is that in the former only the small, isotropic turbulent scales are modelled and not the entire spectrum as is the case in the latter. The LES approach is extremely useful for the prediction of complex flows where other turbulence models may prove inadequate [146].

The first attempts of LES in engineering by Deardorff [147] was in 1970. Since then, LES has been widely applied for the modelling of turbulent flows. Instead of time-averaging (RANS), a spatial filtering approach is adopted in order to separate the resolved (large-eddy) field from the small-eddy (sub-grid) field. This filter defines the computational point where time-averaging should be implemented (small-eddies) a filter operation is defined by the convolution demonstrated below [148].

$$\bar{\phi}'(x) = \int \phi'(x')G(x, x'; \bar{\Delta})dx' \quad (4.25)$$

Where G is the specified filter function and $\bar{\Delta}$ is the filter width. The filter function $\bar{\phi}'(x)$ is responsible for determining the structure and size of the small scales to be simulated [149]. More details about spatial filtering techniques are presented in Aldama [150], Pope [151] and Sagaut [152].

4.3 CFD Software Model Set-up

The ANSYS ICE Engine simulation was undertaken in FLUENT for cold flow simulation. In early work, a comparison was made between ANSYS and similar software including CONVERGE, COMSOL, OpenFOAM, Star-CCM+, and KIVA. ANSYS ICE was preferred over similar software due to many benefits such as readily available software licensing, a wide variety of turbulent models being available and customizability of the software with access to each part of the model. The model was integrated with other engineering software on the desktop by adding CAD and FEA connection modules. Single interface and ICE (Internal Combustion Engine) is

specifically developed for Cold-flow, port flow, and combustion simulation types. Fluent also has a powerful pre-processor to import geometry files from CAD and provides high quality mesh creating ability with flexibility. It has advanced physical models for the description of turbulence, heat and energy transfer, multi-phase/species etc. Two types of solver are available for both steady and transient flow calculations.

4.3.1 Principle of Calculations

ANSYS FLUENT uses the conservation equations of mass and momentum for all flow calculations in case that heat transfer is also involved. The principle of these equations was explained in the previous section; Equation (4.1) to (4.8). The RANS calculation method was used for the flow structure simulation and the modified turbulence model used was the Re-Normalisation Group (RNG) model. Some benefits of the modified $k - \varepsilon$ model (RNG) are listed below:

- 1 The RNG model has an additional strains rate term that significantly improves the accuracy for rapidly strained flows.
- 2 The RNG theory provides an analytical formula for turbulent Prandtl numbers, while the standard model uses user-specified, constant values.
- 3 Swirl modification is undertaken in the ANSYS RNG model.

4.3.2 Boundary Conditions

Almost every computational fluid dynamics problem is defined by its boundary condition initial values, hence the boundary conditions are as important as the physical equations. The boundary conditions include mechanical structure conditions, engine breathing inlet/outlet pressure and temperature, piston movement profile, valve lift profiles, and minimum valve lift. For the mechanical structure, the basic engine parameters are connection rod length and crank radius, the intake port geometry configuration, exhaust valves dimensions etc. The 3D engine mechanical structure was constructed using the 3D CAD software “SolidWorks”, and then imported into the CFD tools as a Parasolid Model Part file format (.x_t). All engine mechanical structures including the valves, valve seats, and inlet faces were defined prior to CFD

calculations. The other boundary conditions can be generated after the mechanical code is imported into the CFD tools and meshed. The inlet and outlet boundary conditions are defined in boundary condition tab in the solver setting.

4.3.3 Grid and Mesh Type

The mesh dynamics was handled by ANSYS mesh. The model consisted of approximately 1,200,000 elements including 4 Node Linear Tetrahedron, 8 Node Linear Hexahedron, 6 Node Linear Wedge (Prism) and 5 Node Linear Pyramid. Figure 4.1 shows typical mesh type used for the currently reported modelling. The global cell size was of the order of 0.5 mm. The model domain started at the intake port/manifold interface and extended to the exhaust port outlet. The grid dependency study was examined with testing the solution in finer mesh size and very similar results with less than 3% difference were achieved, so the global cell size was of the order of 0.5 mm was considered mesh independent. A time-step of 1° CA was used throughout the analysis, except at valve opening events where 0.5° was necessary. Ideal gas properties for air were used throughout the simulation. Shown in Figure 4.2 is the Ansys mesh generated piston at bottom dead centre.

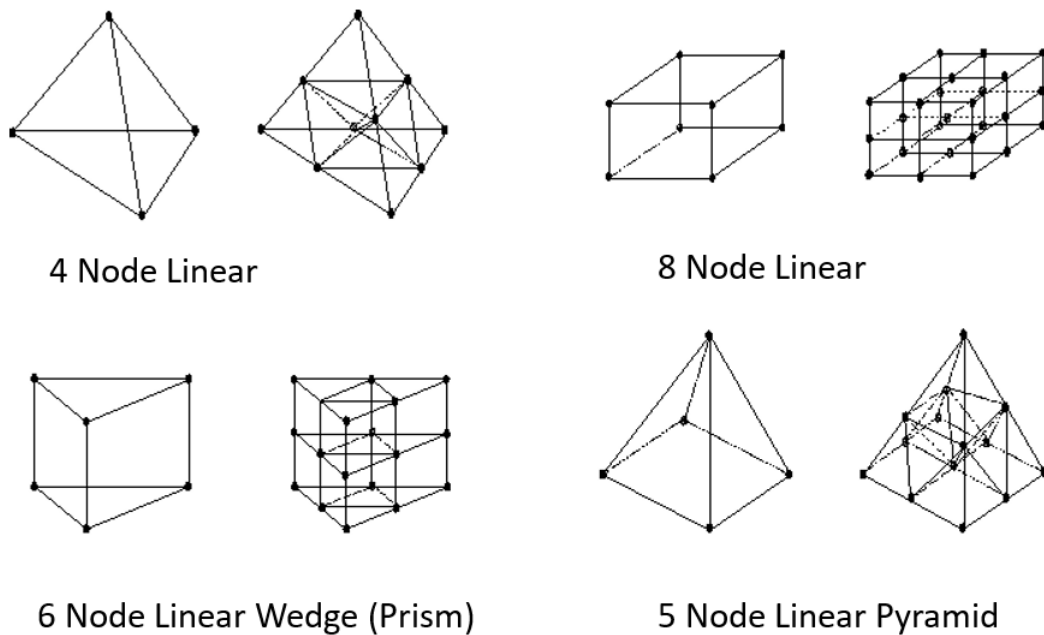


Figure 4.1. Ansys Mesh Structures.

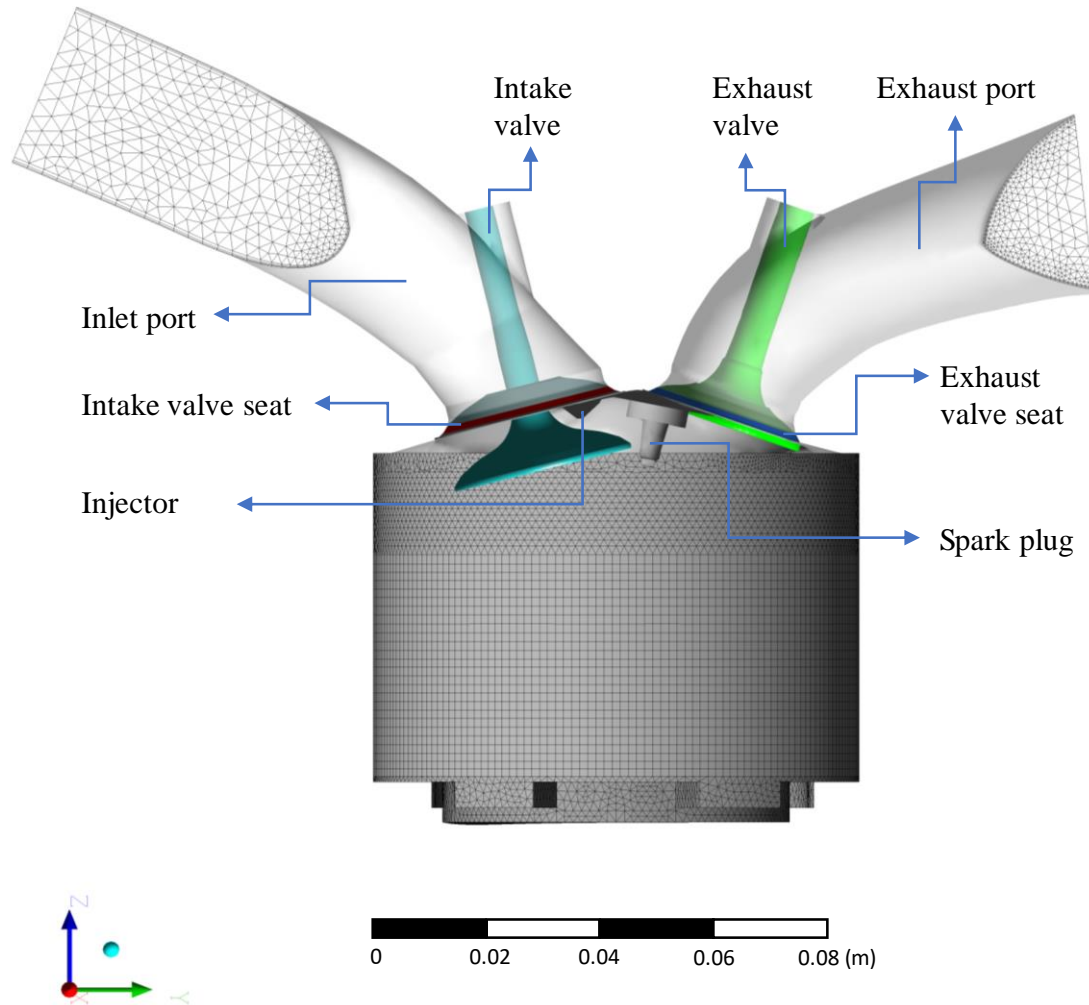


Figure 4.2. Ansys Mesh Generated at 450° aTDC with inlet and exhaust boundaries.

4.3.4 3D CFD Engine Model

Initially, an attempt was made to model the engine in 2-D using the Ansys fluent section function. Shown in Figure 4.3 is the engine piston and valves in 2-D. All of the engine solid parts including the cylinder, injector, inlet, and exhaust valves were modeled in SolidWorks using available drawings or measurements scaled with verified data that are set out in Appendix A. Despite the simplicity of the model, significant time was spent to generate the dynamic mesh. After many attempts in 2-D mesh generation, it was concluded that 3-D ICE engine in Ansys was more sensible as this module has been designed specifically for the study of cold flow and port flow. The 3-D model was generated and validated with real world engine data, this can be seen in Figure 4.4 showing the inlet port, inlet valve seat on the left-hand side and exhaust

port, exhaust valve seat on the right-hand side. The inlet and exhaust valves had to be extruded from the port geometry. The spark plug and injector were modeled based on data provided by previous researchers [108–110]. A 3-D Solid model was initially created with 4 valves and full-size cylinder as displayed in Figure 4.4. However, due to the symmetrical nature of the real engine, a half model was considered acceptable because there was no swirl inclination in the intake port. In half model CFD, symmetrical boundary conditions are used to reduce computation time, as a full model would potentially be very expensive to solve and as the mentioned earlier result would ideally be same due to symmetrical nature of the real engine, considering RANS method. In order to account for any flow initialisation effects, the model was run for 2 complete cycles until cycle to-cycle convergence was achieved for the in-cylinder quantities (e.g. pressure, velocity field, turbulent kinetic energy, etc.). Ideal gas properties for air were used throughout the simulation.

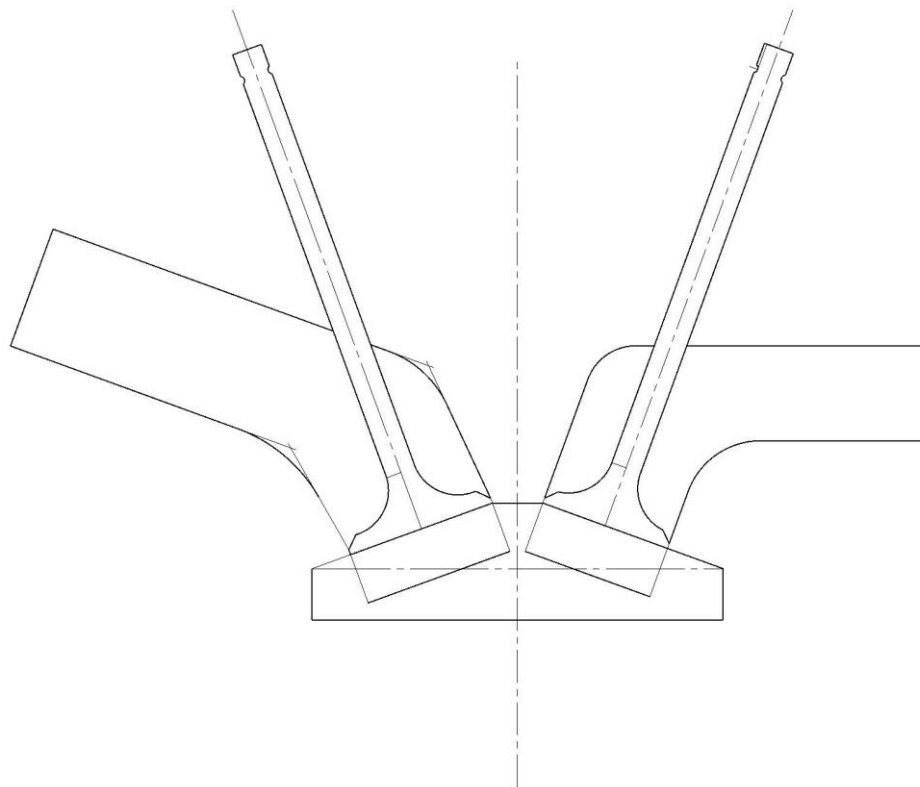


Figure 4.3. Engine Solid Parts in 2-D.

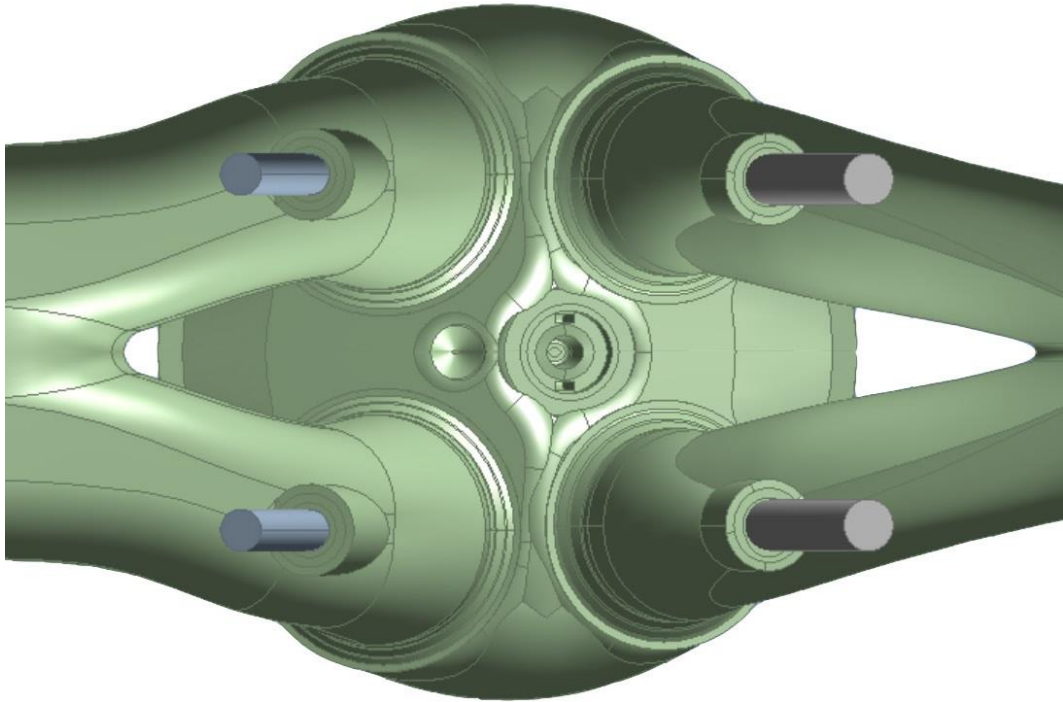


Figure 4.4. Initial Full Solid Model.

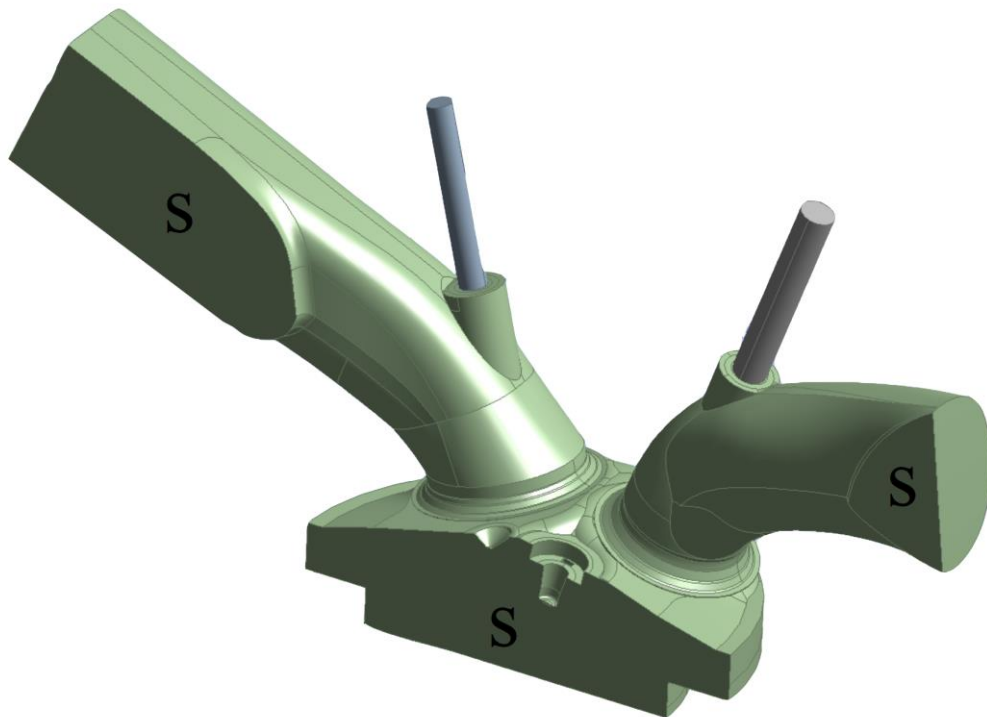


Figure 4.5. 3-D Solid Model including valves, ports, spark plug, and injector.

4.4 Summary

Many types of three-dimensional fluid dynamic codes were discussed in this chapter. This section briefly explains the benefits of each method for the in-cylinder flow structure analysis. The modified $k - \varepsilon$ model (RNG) was selected as the most efficient model with respect to its accuracy and computational demands.

- DNS is obviously the method that provides the most precise and detailed description of turbulence, however, it is still out of reach of 3D flow field engine studies primarily due to remaining constraints in computational power
- The one-equation RANS model is highly dependent on experimental data making it difficult to prescribe algebraically the length scale.
- The two-equation eddy viscosity models are still the most commonly used turbulence modelling methods due to improvements, with recent demonstrations in engine flow field investigations [18].
- The $k - \varepsilon$ model has been widely used and verified over the years and it is highly recommended for initial estimation and understanding of varying flow fields.
- The $k - \omega$ model is superior to the classic $k - \varepsilon$ model for several reasons and is capable of accurate calculation of near-wall situations. However, its refined mesh near those areas makes this model more sensitive compare to the $k - \varepsilon$ model.
- The modified $k - \varepsilon$ model (RNG) uses an extra term dependent on the strain invariant, thus considers the influence of additional strains rates. It can capture flow effects that the standard $k - \varepsilon$ may not capture. In addition, it is highly recommended and verified to understand turbulence flow field properties.
- LES can be considered as one of the most accurate methods available for practical computations. However, LES computations are several times more power demanding than RANS.

5. Imaging Techniques & Thermodynamic Processing

5.1 Introduction

Presented in this chapter are descriptions of the flame and flow imaging techniques used to measure and visualize the turbulent flame development and flow structures in the customized single cylinder DISI optical engine.

Early investigations of flame imaging used natural light [153,154] and the schlieren technique [51,155,156] to obtain high-speed ciné photography images. These techniques proved useful to understand the main features of flame propagation, despite not providing enough insight into the turbulent structure of the flames. In the 1980s and 90s developments in laser diagnostics allowed images of “slices” through the flame with laser induced fluorescence (PLIF) and Mie scattered light images of flames [157]. This method applied to the OH molecule provides a good definition of the flame front. However, this was limited by the repetition rate of the high power lasers so restricting images to one per cycle and has often limited imaging to a restricted area of the cross section of the bore. The repetition rate of the laser could be reduced by using the alternative Mie scatter method, in which it is essential to introduce particles that burn or change scattering characteristics within the flame, this has been widely adopted for flame imaging and resulted in cyclically resolved images of flame development in a single combustion event [158–160]. More recently high-speed natural light (chemiluminescence) capable of non-intrusive and continuous monitoring of flames has been used to understand the fundamentals of flame propagation with more insight into the turbulent structure of the flames. Imaging systems via endoscopic access are also now being used to maintain the thermodynamics, heat transfer and speed/load range as close as possible to that of an all-metal engine.

The flow within the cylinders of internal combustion engines is known to affect engine

performance and emissions significantly, with a number of prior investigations involving hot wire anemometry, laser Doppler velocimetry, and planar velocimetry techniques. Most of these methods have been used to define both the position of the flame front and to measure gas velocities. This, however, was limited by the attainable spatial resolution of the flame front. In the currently reported study, preliminary PIV images of the in-cylinder flow were obtained under motoring conditions at a horizontal imaging plane close to TDC (10 mm below the fire face) throughout the compression stroke ($30^\circ, 40^\circ, 90^\circ$ and 180° bTDC) for a low load engine operating condition at 1500rpm/0.5 bar inlet plenum pressure using planar laser sheet imaging and seeding particles. A series of high speed cyclically resolved flame images were then acquired at the same engine condition to understand flame propagation for a variety of baseline fuels and blended with either gasoline, iso-octane or Butanol.

5.2 Mie Scattering Principle

The interaction of electromagnetic radiation with matter through media illumination is called “scattering”. If there is no energy absorption between the light and incident medium, then all of the light is scattered and if the incident and scattered light frequencies are equal the term is called “elastic scattering” [48] So, Mie scattering is the elastic scattering of light with particles with similar or larger wavelength. The Mie signal is proportional to the square of the particle diameter. Mie scattering is much stronger than Rayleigh scattering which is an elastic scattering of light by particles much smaller than the wavelength of the light and, therefore, a potential source of interference for this weaker light. Scattering processes are demonstrated graphically in Figure 5.1 alongside Mie scattering for larger particles [161]. Angular dependence of the scattered intensity especially for smaller particles must be considered carefully for successful Mie imaging experiments. The scattered light intensity is clearly dependent upon the angle of viewing, which is generally set to 90° during planar laser sheet imaging. Mie scattering is often used to measure flow velocities applying Particle Image Velocimetry (PIV).

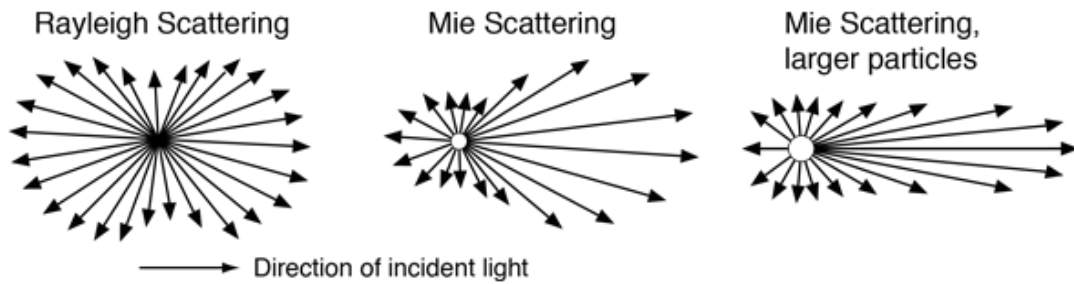


Figure 5.1. Light Scattering Principle [161].

5.3 Laser Light Source

The word laser is an acronym for light amplification by stimulated emission of radiation, which defines the operating principle of a laser as shown in Figure 5.2. Excited electrons in an active medium gain a higher energy level by an external source of energy leading to photon generation in the active medium. Eventually arriving light waves will stimulate more emission than absorption. The emitted photons are in phase and have the same polarization state and propagate in the same direction. Emitted photons numbers will be amplified in the medium through the optical feedback provided by reflecting surfaces.

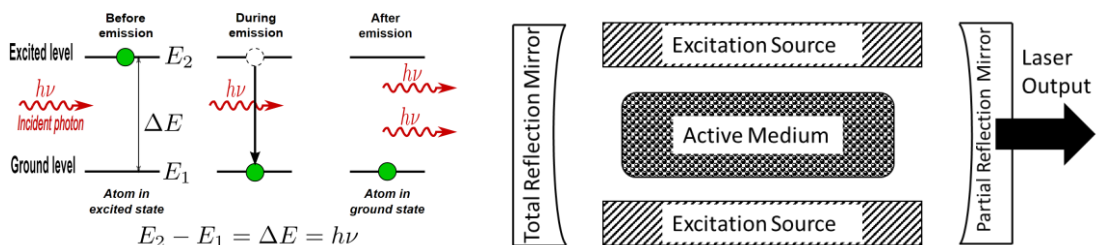


Figure 5.2. Principle of Laser explaining stimulated emission and amplification [55].

5.3.1 High Energy Pulsed Lasers

A high energy pulsed laser is commonly used in light scattering, particle image velocimetry (PIV) measurements. The signal to noise ratio is highly increased when gated detection is used because of their higher intensities. The most common types of high energy pulsed lasers used are flashlamp-pumped Nd:YAG lasers and excimer lasers. Nd:YAG lasers produce output at $1.06 \mu\text{m}$ and are used to produce beams in three wavelengths by frequency doubling or tripling in optical crystals. Out of three generated wavelength, the most common is 532 nm produced from a Q-switched Nd:YAG laser of 1 joule in a single pulse of 10 ns [55].

5.4 Particle Image Velocimetry and Experimental Setup

Particle image velocimetry is a non-intrusive technique that calculates velocity vectors from the displacement of the element of fluid in a known time interval. A thin slice of laser sheet is used to illuminate seeding particles in the flow, these seeding particles scatter the light that is detected by a charged coupled device camera as shown in Figure 5.3. In the currently reported work the laser sheet thickness was set to 2mm by using a laser burn and alignment paper. In order to calculate the flow velocity magnitude, the laser unit and the camera are synchronized so the double pulsed laser sheet produce two images with a known time delay that can be recorded into two separate frames by employing the so-called frame straddling technique as presented in Figure 5.4. The pair of images is then divided into a matrix of interrogation areas (IA) of pixels, in which the cross-correlation analysis is performed to determine the average particle displacement vector and then the velocity vector magnitude. The PIV technique then can be considered to result in the Eulerian “mean” velocity comparing to the Lagrangian value obtained by particle tracking velocimetry. At the onset of analysis, each PIV image is divided into a series of small interrogation areas, this will be further explained in cross-correlation analysis later in this chapter.

Many researchers have worked on two-dimensional PIV measurements to characterise in-cylinder fluid motion under motoring conditions. Reuss [162] used the PIV technique to correlate CFD calculations of the swirling flow inside an overhead valve disc shaped single cylinder research engine which included the contributions of both the turbulence and cyclic variation. By comparing these measurements with CFD models, these studies were able to identify a number of modelling improvements including swirl in the residual gas, simulation of the gas exchange during valve overlap and improved numerical accuracy.

Double pulsed PIV measurement was previously used by Reeves [163] to investigate tumble for a flow field inside a production geometry four-stroke engine incorporating optical access through both the cylinder wall and piston crown. Mid-plane of the cylinder at different intervals in the compression stroke during different cycles were examined with the auto-correlation technique with a series of 1.12mm x 1.12mm interrogation areas with 50% overlap between neighboring regions.

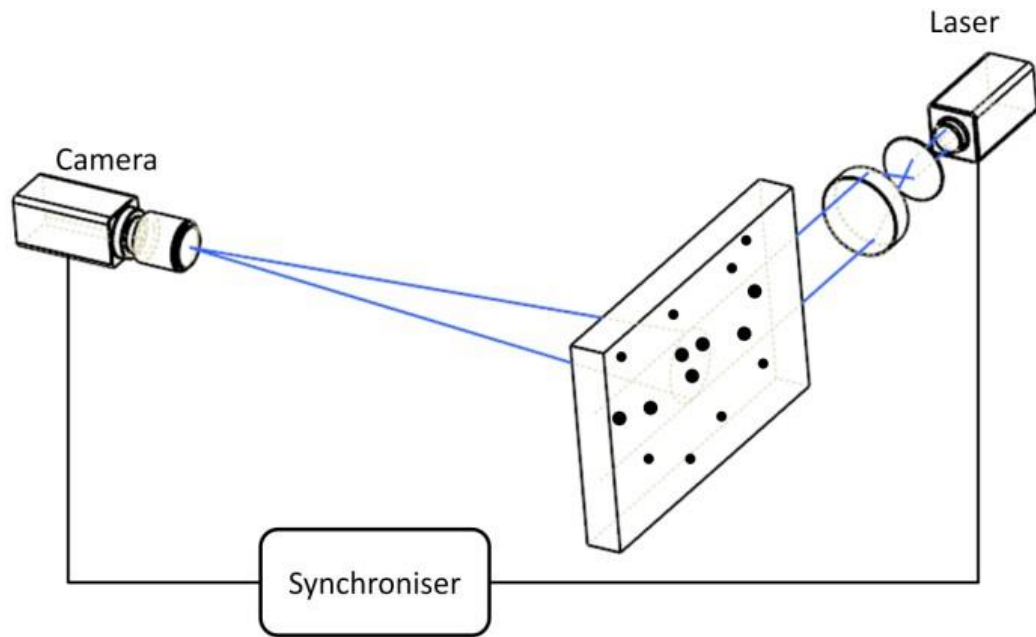


Figure 5.3. PIV Experimental Setup.

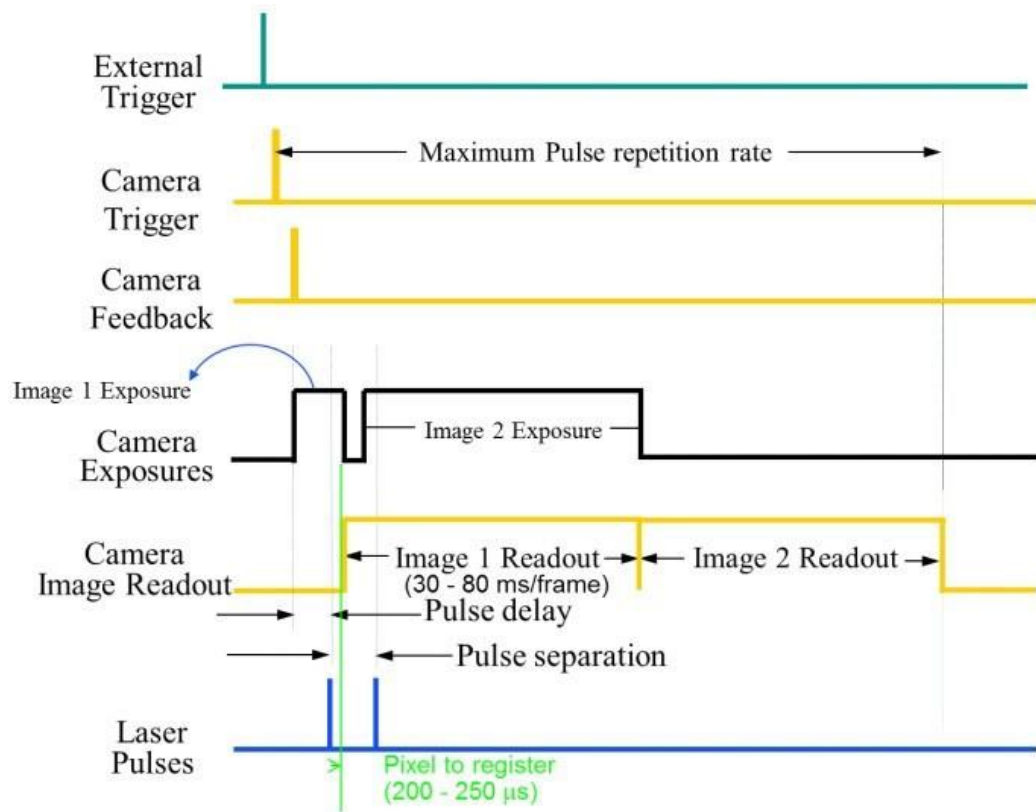


Figure 5.4. Principle of Frame Straddling Technique.

5.4.1 Seeding Particles

PIV measurements depend on light scattering by particles present in the fluid, particle seeding requirements can be summarized as:

- Particle flow tracking ability (appropriate size and mass with low drag)
- Particle light scattering characteristics
- Particle number density in the flow
- Particle tendency to foul optical windows
- Particle tendency to abrade or adhere to cylinder surfaces

So, it's crucial for seeding particles to be non-toxic, non-corrosive, non-abrasive, non-volatile and chemically inert. To meet these requirements vegetable oil was selected as the PIV seeding particle, with properties enabling minimum drag impact while yet scattering enough light for the PIV measurements. The seeding density was set to be sufficiently high through experimentation. As the more particle image pairs enter into the interrogation area the probability of valid displacement detection increases. Keane and Adrian [164] recommended that more than five particles pairs should be used in each interrogation area for a valid displacement calculation. The mean number of particles in a given interrogation area Δx^2 may be described by the dimensionless image density (N_i):

$$N_i = \frac{4\hat{C}\Delta z_0}{\pi} |\Delta x^2| \quad (5-1)$$

where \hat{C} is the mean number of particles per unit volume and Δz_0 is the thickness of the laser sheet. If the image density is large ($N_i > 1$), each interrogation area will contain many particle images and be capable of yielding a measurement of velocity.

A 10F03 seeding generator (as presented in Figure 5.5) supplied by Dantec Dynamics was used, which works according to Bernoulli's principle. Compressed air passes into the atomiser via the atomiser regulator to the air tube which caused a high flow velocity flow field at the exit of the compressed air tube. This operation causes a pressure drop near the tip of another tube partially immersed in the liquid. According to Bernoulli's principle, the arising vacuum sucks out the liquid, which is then dispersed into small droplets by the high speed air flow. The liquid droplets are then blown to the outlet of the seeding generator by the air flow in the chamber. The seeding generator 10F03 can

continuously supply seeding flow with an average droplet size of Sauter Mean Diameter (SMD) $2\mu\text{m}$ to $5\mu\text{m}$ up to a pressure of 3bar.

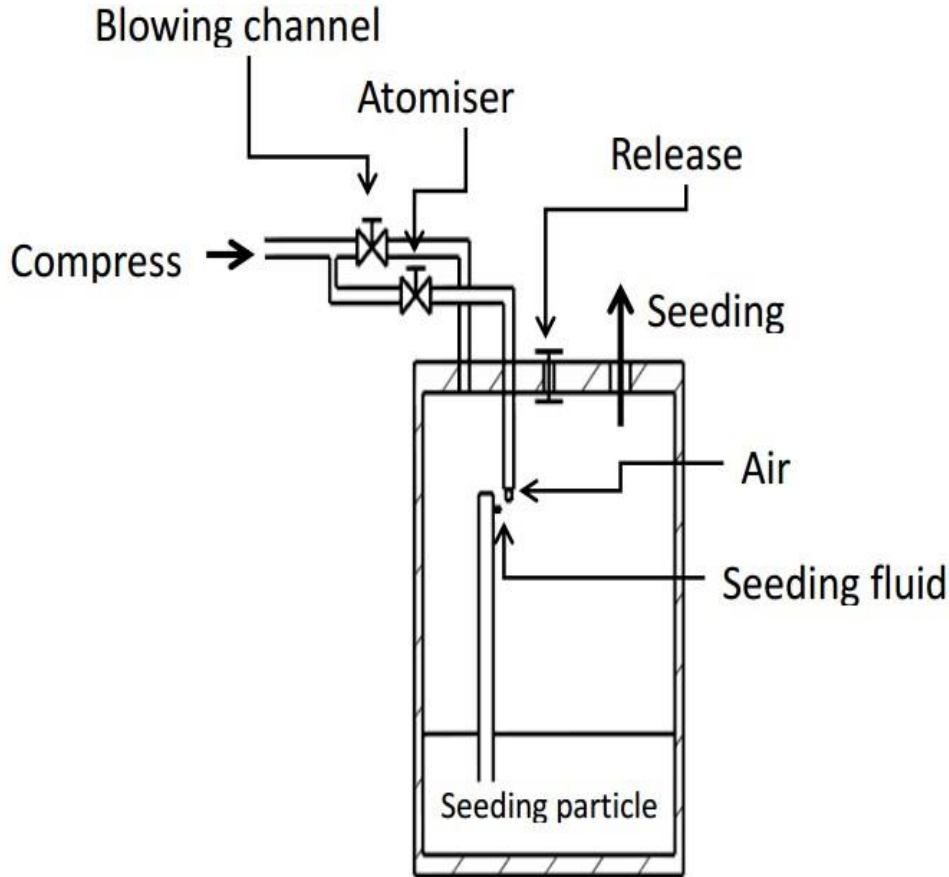


Figure 5.5. Seeding Generator.

Since turbulence flow are highly chaotic, seeding particles deviate to some degree to the motion of the true fluid. Ideally the particle will be a good approximation to a fluid element if its density is the same as that of the working fluid and a particle size is smaller than the smallest length scale, the Kolmogorov length scale (l_k Equation 2.9). The degree to which the tracer particle behaves as a fluid element is quantified by the Stokes number, defined as [172]:

$$St = \frac{1}{18} \frac{(\rho_p - \rho_g)}{\rho_g} \left(\frac{d}{l_k} \right)^2 \quad (5-2)$$

where ρ_p and ρ_g are the densities of the particle and the fluid, respectively, and d is the particle diameter.

The drag force is influenced by relative velocity, fluid particle properties, and particle shape. Drag force with the particle inertia governs the particle motion. The equation of motion describing the acceleration of a solid particle was considered [165] as described

below.

$$\frac{dU_p}{dt} = \frac{3}{4} C_D \frac{\rho_g}{D_p \rho_p} (U_g - U_p)^2 \quad (5-3)$$

where U_p and U_g are the respective gas and particle velocities, C_D is the drag coefficient, D_p is the particle diameter and ρ_p and ρ_g are the particle and gas densities. The drag coefficient C_D is dependent on the Reynolds number (Re_p) and can be described for a spherical solid particle as [48]:

$$C_D = \frac{24(1 + 0.15(Re_p^{0.687}))}{Re_p} \quad (5-4)$$

During the currently reported study Equation (5-4) was used for the analysis of the acceleration of the seeding particles. This was then compared with earlier investigations of the drag on the oil droplets with U_p/U_g of less than 1.

5.4.2 PIV Laser

A high pulsed energy Nd: YAG laser was used during the currently reported PIV experiments. The setup involved providing two laser pulses within a short time interval. This was done by using a single cavity Nd: YAG laser to illuminate the field of view. A gating arrangement of a single flash lamp discharge from the single cavity laser was used to provide two laser shots. This limited the time interval between the two laser pulses to a range of 20 μ s to 200 μ s (which eventually reduces the laser light intensity and laser pulse width). Hence using a twin-oscillator, twin-amplifier frequency doubled Nd: YA laser can allow infinite and independent control over the time interval, width, and intensity of the laser pulses. The laser unit used for the PIV experiments was a NANO L 135-15 PIV laser manufactured by Litron Lasers. This consisted of a laser head and laser arm that was used to guide the laser sheet towards the side window of the optical engine. The laser unit was powered by the LPU 550 power station configured to drive 2 laser units with a 550W combined throughput. The laser head consisted of two 1064 μ m laser units, half wave plates, mixing and steering polarisers and a harmonic 144 generator. The laser head supplies 532 μ m laser beams with up to 136mJ laser pulse energy under a 160 μ s optimised Q-switch delay. More advanced PIV systems (diode-pumped Nd: YLF) with lasers offering outputs of up to 10-40 mJ per pulse at 1-5 kHz

at 1053 nm, would resolve the limitation of repetition range of Nd:YAG-based systems in performing time-resolved experiments. However, due to availability Nd:YAG-based systems, NANO L 135-15 PIV was used.

5.4.3 Camera and Optics

A Dantec Dynamic FLOWSENSE 4M camera system was placed in front of the 45° mirror with negligible out of plane movement to capture seeding particles during currently reported study. The simplified one-camera system suffers from the restriction that the optical axis must be aligned in the direction normal to the light-sheet plane. Moreover, such systems only yield two velocity components within the measurement plane and are therefore only suitable for the investigation of flows with a negligible out-of-plane velocity component. The CCD camera was capable of a maximum resolution of 2048x2048 pixels, 20.4 fps at full resolution, 7.4 μm pixel size, peak quantum efficiency of 56% and with a minimum inter-frame time of 200ns. The lens used for the PIV test was an UV-Nikkor 60 mm lens attached with a 532nm narrow band filter to remove background light. The configuration of the lens is shown in Table 5.1.

Table 5.1. Lens Configuration.

Focal Length	60 mm
Aperture	f/32 to f/2.8
Reproduction ratio	1:10 to 1:2
No of lens Elements	8
Lens Group	7
Maximum angle of view	39°40'

5.4.4 PIV Test Setup

A Dantec Dynamic FLOWSENSE 4M camera system with a CCD camera and high pulsed energy Nd: YAG laser was used throughout currently reported PIV experiments. The measurements were achieved by providing two laser pulses within a short time

interval. This was done using a twin-oscillator, twin-amplifier frequency doubled Nd: YA laser for illumination of the PIV area with the single cavity Nd: YAG laser with gating of a single flash lamp discharge from the single cavity laser to provide two laser shots. The laser sheet was formed in a way that the sheet thickness did not exceed 2 mm. The sheet was placed in a way that it spread all over the horizontal imaging plane as shown in Figure 5.6. The laser sheet was aligned at 5 mm above the optical piston and 10 mm below the spark plug, as close as possible to TDC (at 30°bTDC as any closer was restricted by the piston intruding into the field of view of the side window). Presented in Figure 5.7 is the experimental arrangement of the PIV laser, mirror, camera, and optical apparatus. The ICCD camera was positioned in a way that images were captured through the 45° mirror via the Bowditch optical access and then was focused with a scaled paper in order to clearly capture images at 30°bTDC. The same scaled sheet was used to define the two points for PIV analysis software (Dantec Dynamicstudio version 3.00). This software uses the distance between these two points as a reference to be able to measure image dimensions.

In the currently reported study, PIV images were captured with a largest possible aperture and smallest f-number of 2.8 to provide shallow (small) depth of field. The maximum laser output was set to 100 mJ and verified by a laser measuring probe to produce sufficient scattering light from the vegetable oil droplets. The dropout rate of velocity vectors was kept minimized by adjusting the maximum time interval between the two laser pulses. This was done by sweeping time interval of the two laser pulses from 30 μ s to 200 μ s; 100 μ s was set as it was reasonably high enough to minimize dropout rate and low enough to trace the vector velocity changes within this period.

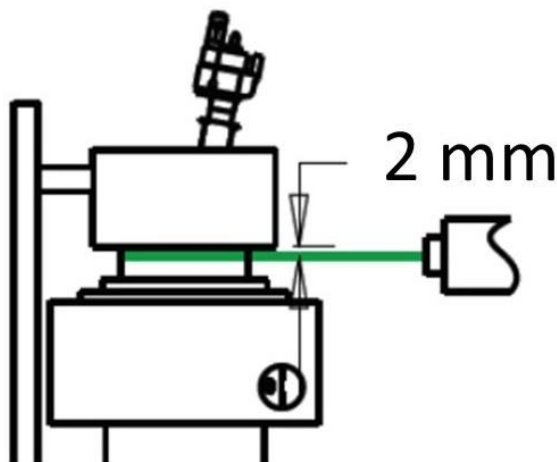


Figure 5.6. Laser Sheet Thickness,

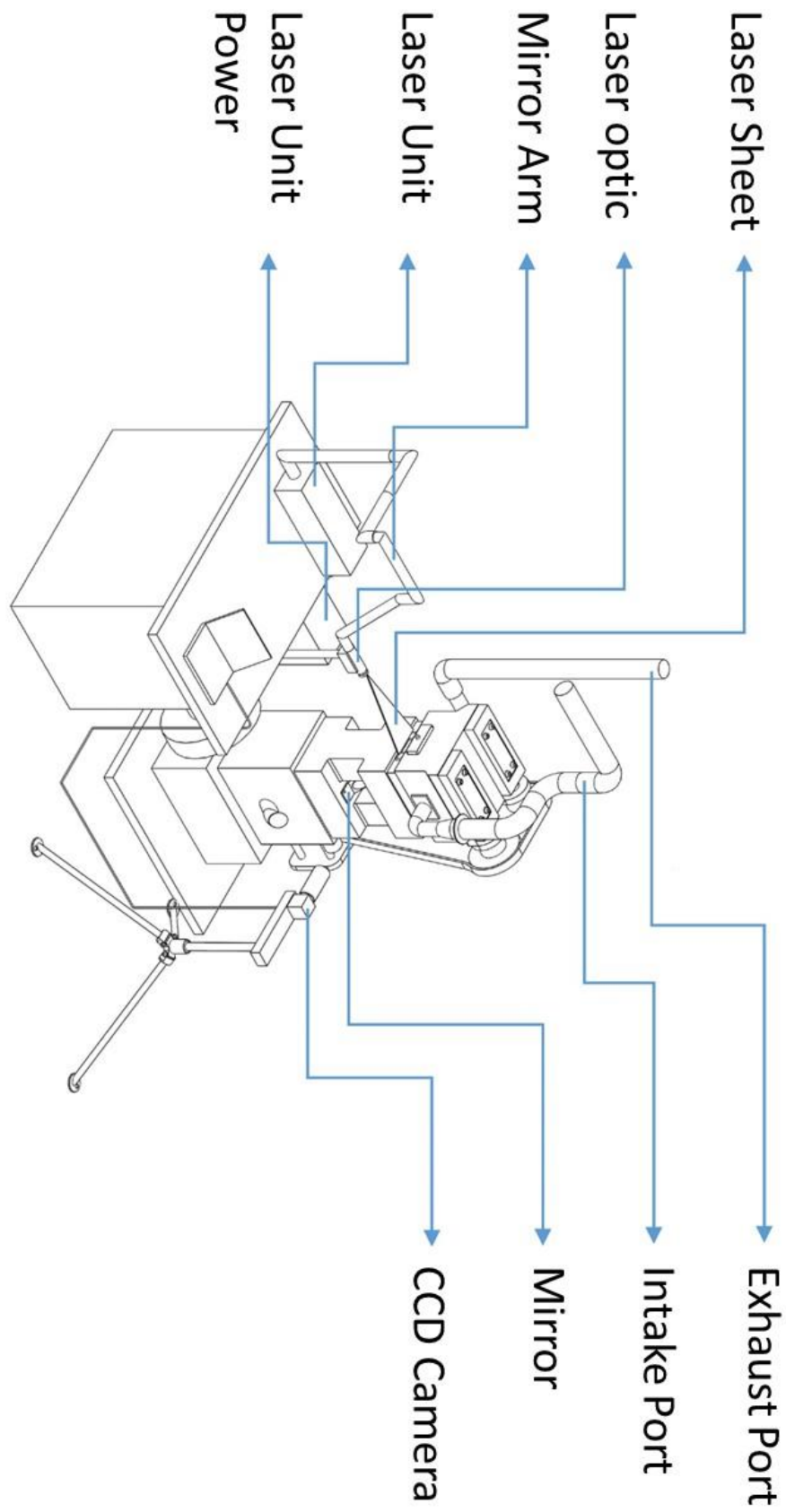


Figure 5.7. PIV laser, mirror, camera, and optical apparatus.

5.4.5 Cross-Correlation Analysis

Dantec Dynamics software (Dynamicstudio Version 3.00) was used to calculate the particle displacement vector and obtain velocity vector maps by using the cross-correlation method to locally correlate two images of particles on two separate frames. This method is based on dividing each PIV recorded image into a number of interrogation areas and evaluating the velocity vectors in that region. For this PIV experimental setup, a 32x32 pixels interrogation area was used combined with the Gaussian algorithm, which corresponds to a spatial resolution of 1.8mm x 1.8mm. Figure 5.8 shows a schematic representation of the evaluation process to determine the displacement vector.

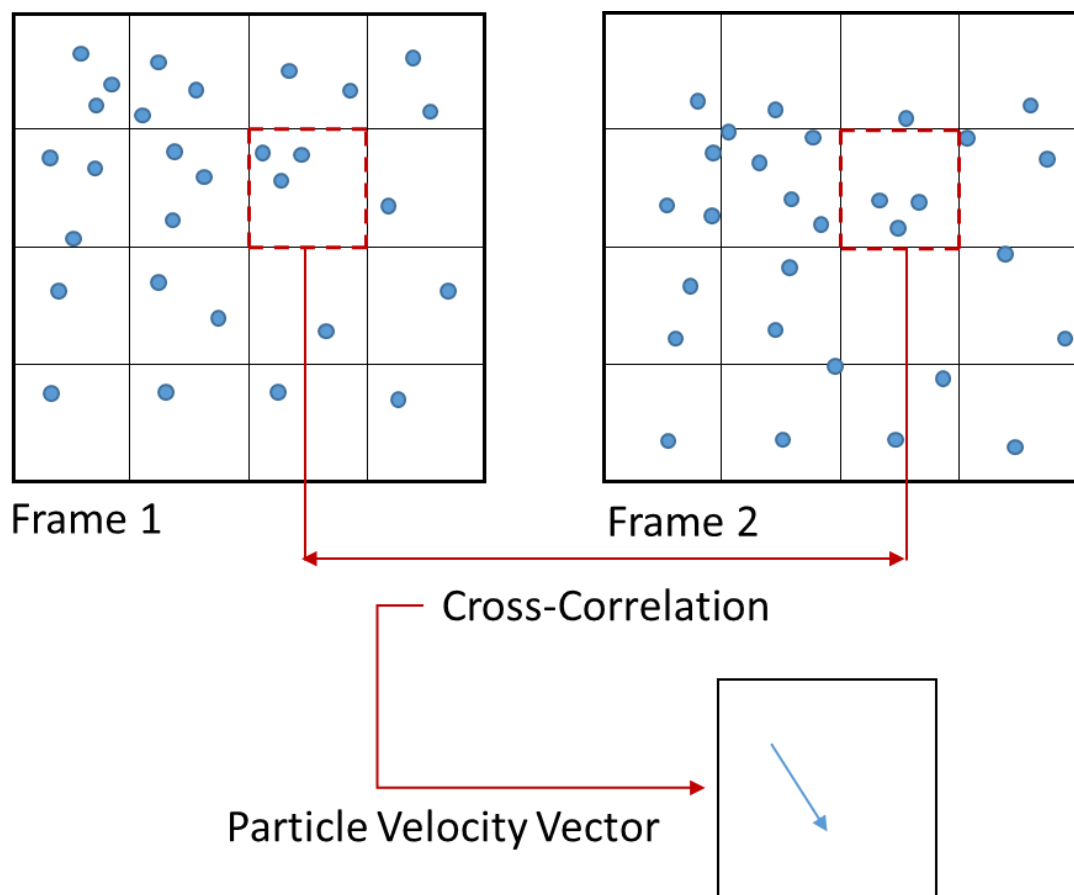


Figure 5.8. Cross-Correlation Analysis.

Interrogation regions in each recorded image of the PIV consist of a random distribution of particle images which a certain pattern of N particles can be formed in the flow as shown below [166]

$$\Psi = \begin{pmatrix} x_1 \\ x_2 \\ \cdot \\ \cdot \\ x_N \end{pmatrix} \quad (5-5)$$

$$\text{with } x_i = \begin{pmatrix} x_i \\ y_i \\ z_i \end{pmatrix}$$

Where Ψ represents the state of the particle ensemble at a given time t , and x_i is the position vector of the particle I at the time t , in the interrogation volume of the laser sheet. [166]

Capital letters representing coordinate in the image plane and lowercase letters are used to reference coordinates in the object plane.

$$X = \begin{pmatrix} X \\ Y \end{pmatrix}$$

Assuming the magnification factor is M then,

$$x = \frac{X}{M} \quad \text{and} \quad y = \frac{Y}{M}$$

The single exposure for each image intensity field can be written as the following equation [166],

$$I(X, \Psi) = a_0 + \sum_{i=1}^N P(x_i) \cdot \tau(X - x_i) \quad (5-6)$$

Where $\tau(X - x_i)$ is the point spread function of the imaging lens and characterizes the impulse response of the imaging lens and $P(x_i)$ indicates the system transfer function, giving the light energy of the image of an individual particle i inside the interrogation volume (IV) and its conversion into an electronic signal. To increase the fraction of matched to unmatched particle images, two interrogation areas are offset in response to an estimated mean particle displacement. This will increase the signal to noise ratio at the correlation peak. The cross-correlation function for each pair of interrogation areas is therefore evaluated and the peak displacement vector is calculated, which correlates to the particle image displacement vector. Assuming inside the interrogation volume there is a constant displacement of all particles called d , then the particle locations at the second exposure are found by [166].

$$x'_i = x_i + d = \begin{pmatrix} x_i + d_x \\ y_i + d_y \\ z_i + d_z \end{pmatrix} \quad (5-7)$$

The correlated particle image displacement is given by

$$D = \begin{pmatrix} M \cdot d_x \\ M \cdot d_y \end{pmatrix} \quad (5-8)$$

The second exposure from the intensity distribution of the interrogation area can be modeled as:

$$I'(X, \Gamma) = \sum_{j=1}^N P'(x_j + d) \cdot \tau(X - x_j - D) \quad (5-9)$$

The first exposure from the intensity distribution of the interrogation area can be modelled as:

$$I(X, \Gamma) = \sum_{i=1}^N P(x_i) \cdot \tau(X - x_i) \quad (5-10)$$

The cross- correlation function for two interrogation areas can be form as:

$$\begin{aligned} R_{II}(s, \Psi, d) &= \langle I(X, \Gamma) \cdot I'(X + s, \Gamma) \rangle \\ &= \frac{1}{A_I} \sum_{i,j}^N P(x_i) \cdot P(x_j + d) \int_{A_I} \tau(X - X_i) \cdot \tau(X - X_j + s - D) \cdot dX \end{aligned} \quad (5-11)$$

Where s is the separation vector in the correlation plane and by differentiating the $i \neq j$ terms, which represent the correlation of different particle images and therefore randomly distributed noise in the correlation plane, and the $i = j$ terms which contain the desired displacement value, the following equation can be formed by summation of both terms into:

$$\begin{aligned} R_{II}(s, \Psi, d) &= \frac{1}{A_I} \sum_{i \neq j}^N P(x_i) \cdot P(x_j + d) \int_{A_I} \tau(X - X_i) \cdot \tau(X - X_j + s \\ &\quad - D) \cdot dX \\ &\quad + \frac{1}{A_I} \sum_{i=j}^N P(x_i) \cdot P(x_j + d) \int_{A_I} \tau(X - X_i) \cdot \tau(X - X_j + s \\ &\quad - D) \cdot dX \end{aligned} \quad (5-12)$$

This can also be represented as:

$$R_{II}(s, \Psi, d) = \frac{1}{A_I} \sum_{i \neq j}^N P(x_i) \cdot P(x_j + d) \cdot R_\tau(X_i - X_j + s - D) + R_\tau(s - D) \sum_{i \neq j}^N P(x_i) \cdot P(x_i + d) \quad (5-13)$$

It is possible to calculate correlations directly from Equation (5-9) to (5-13) but to increase efficiency, fast Fourier transform (FFT) algorithms are used in the currently reported study by Dantecstudio software. The correlation theorem states that the cross-correlation of two functions is equivalent to a complex conjugate multiplication of their Fourier transforms [55]:

$$R_{II} \Leftrightarrow \hat{I} \cdot \hat{I}'^*$$

Where \hat{I} and \hat{I}' are the Fourier transforms of the functions I and I' respectively. Computing two 2-D fast Fourier transforms on equal sized samples of the image, followed by a complex conjugate multiplication of the resulting Fourier coefficients can be used for calculation of the cross-correlation functions.

5.4.6 PIV Analysis Limitations & Advanced Interrogation Techniques

Advanced techniques have been introduced in this section to overcome the limitations posed by the application of the cross-correlation operator to interrogate the images. These techniques allow the measurement dynamic range to be increased in relation to the in-plane particle motion and shows the possibility of enhancing the correlation peak. Some major difficulties encountered during the development of PIV analysis and part of the solutions proposed include [167]:

5.4.6.1 Loss of Particle Pairs

Adopting smaller size of interrogation window can be used to increase the resolution of image analysis. However, fewer particles are considered in a small interrogating window [167]. Moreover, this will cause the loss of particle pairing because of particles flow in, and out, of the interrogating window of sequential images. Miss-match of particle image pattern may occur, and false velocity vector may be produced, especially for a small interrogating window. The resolution of image analysis is thus limited by

the size of interrogating window.

5.4.6.2 Peak Locking Effect

A digital image is composed of an integer number of pixels, with light intensity recorded as an integer number on every pixel. Also, the correlation function computed from two consecutive images is distributed over integer coordinates. Thus, the sub-pixel displacement computed from the correlation function distribution will be closer to an integer, known as the peak locking effect, since integer number has larger weighting. The peak locking phenomenon is more obvious for particle diameters of less than 2 pixels. Evidently, peak locking significantly reduces the accuracy of PIV measurements [168]; however the effect on velocity flow statistics may be within acceptable limits, this effect can lead to strange results for instantaneous spatial derivative data such as vorticity [169].

5.4.6.3 Particle Image Deformation

Velocity gradient of the flow field can deform particle image pattern between sequential images. Direct cross correlation from the deformed sequential images can cause multiple peaks of the correlation function, which either reduce the measurement accuracy or even worse, produce false velocities. Distorting the particle image properly according to the velocity gradients will improve the measurement results [167,170].

5.4.6.4 Window Shift Method

First correlation analysis is used to estimate in-plane particle image displacement, then a relative shift between the correlation windows can be applied in order to compensate for the loss of pairs due to the average particle motion. Hence the number of particle image pairs is increased. Two-step analysis is implemented where the interrogation is repeated the second time with the window in the second exposure shifted by the value of the displacement obtained from the first interrogation [171].

5.4.6.5 Multigrid Analysis

A logical consequence of the window shift technique is the multigrid approach: when the interrogation process is repeated several times, with the interrogation window shifted after each interrogation. As a result, the dynamic range is amplified; when the

window-refinement multigrid window-shift technique is applied. This process allows the elimination of the 1/4-rule [172] constraint and is usually terminated when the required window size (the smallest) is applied.

5.4.6.6 Local Correlation Averaging

In several experimental conditions, a high source density cannot be obtained for technical reasons. Hence analysis performed at low image number becomes critical, with the appearance of many spurious correlation vectors. One approach is to increase the number of particle pairs without increasing the window size consists of accumulating the effect of several instantaneous particle image recordings. However, this method is only valid when the flow is strictly steady, also beyond a given point, individual particle images cannot be distinguished any more. A better solution is therefore to average the correlation maps from the analysis of the single recordings [173,174]. This way no upper limit is found on the number of recordings that can contribute to building the correlation signal.

5.4.6.7 Correlation Multiplication

Correlation signal from every single pixel produces correlation map at a given location. One way to enhance the correlation peak height and reduce the noisy peaks is to multiply many correlation maps for a correlated value of the velocity but uncorrelated particle image pattern [175]. Multiplying each correlation map by those obtained at the neighboring location is the most commonly used method with the benefits of unsteady flow application. It's important to note that flows with a significant velocity gradient might not benefit from this method.

5.5 High-Speed Natural Light (Chemiluminescence)

The type of visualization that only uses the light from combustion source is often referred to as natural light imaging. This method works on the principle that as the flame propagates specific molecules become raised to an excited energy state via exothermic reactions. These molecules decay back to equilibrium energy levels resulting in the emission of a photon as illustrated in Figure 5.9.

The released photon wavelength whose radiation is much stronger than normal thermal radiation and therefore easier to detect with a sensor depends on the chemical structure.

The capture and analysis of this is often referred to as Chemiluminescence.

Table 5.2 shows the photon emissions wavelength groupings that differing chemical compounds display.

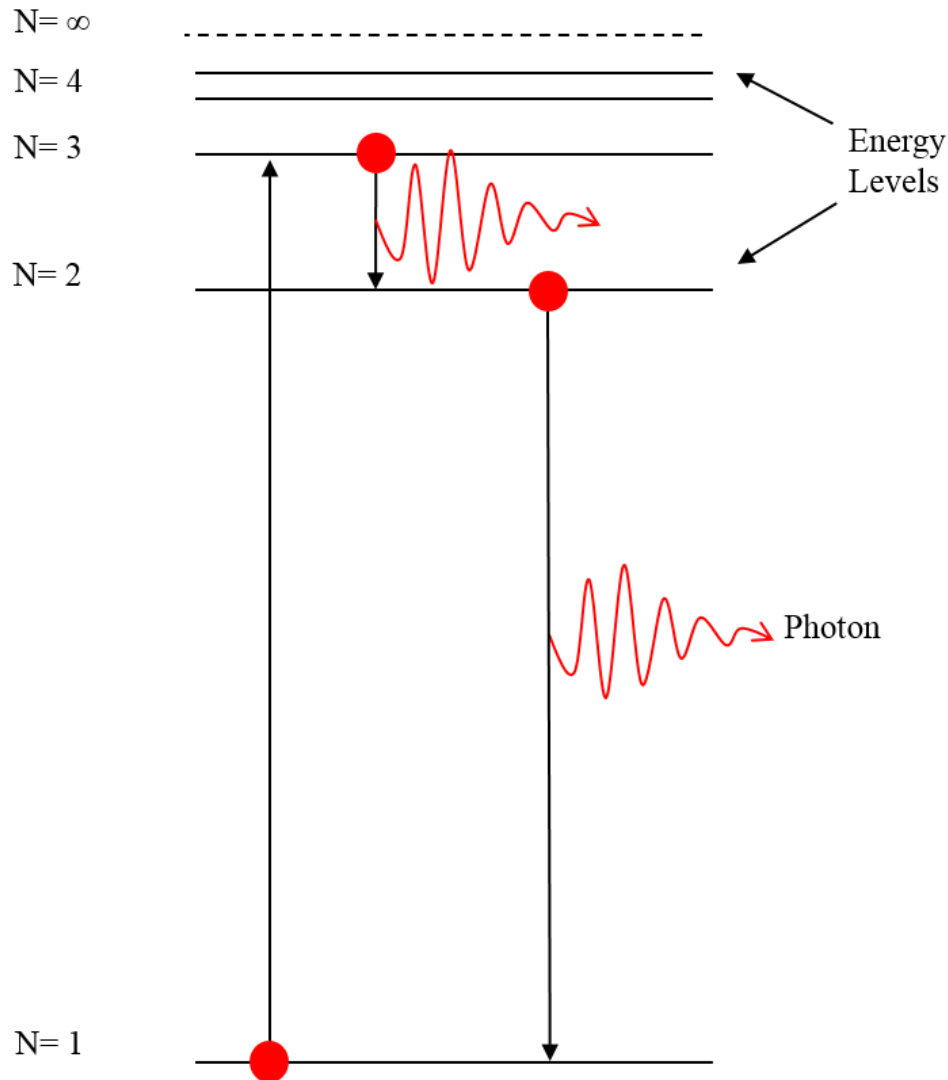


Figure 5.9. Molecule excitation and photons production.

Table 5.2. Emission peaks of key combustion species in IC engine [Yang, Zhao and Megaritis, 2009]

Methane CH (nm)	Hydroxide OH (nm)	Formaldehyde CH ₂ O (nm)	Carbon Dioxide CO ₂ (μm)	C ₂ (nm)	Aldehyde CHO (nm)
314 387-389 431	302-309	368 384 395 412-457	2.69-2.77 4.25-4.3	470- 474 516 558- 563	320, 330 330, 340 355, 360 380, 385

High speed natural light imaging has been used commonly since the creation of the optical engine. Previous work by Rassweiler and Withrow [154] was considered a milestone at the time, with image recording at a high-speed of 5000 frames per second (fps). The recording was resolved to a 2.4 crank angle degree per image to capture the flame propagation across the cylinder. Natural light imaging was later used to form a well-known formula to calculate the mass fraction burned. The same study also showed that a flame front released photons that indicated methane, C₂ and hydroxide combustion products. An attempt was made by Chomiak [176] to match the emissions rate from the flame front to the Kolmogorov scale from which a relationship with the turbulent flame scale could be found. The smallest highly luminous object inside the combustion area would have a size of 1.5mm as mentioned by Chomiak [176], which can be considered as the Kolmogorov scale in that region. Using the OH radical as a flame front marker in natural light imaging is one of the biggest challenges involved in this method. Therefore, to find the exact front of the flame is dependent on finding the UV light emitted from the hydroxide elements. However, this cannot be as evident in cool flame combustion. Srinivasan and Saravanan [177] have concluded that ethanol possesses low light intensity combustion because of much cooler combustion temperatures. In comparison to fuels like iso-octane, using a natural light method of measurement, the post process computer code analyzation is reliant on the emissions from combustion itself to indicate the flame front. With OH radicals being emitted as UV light the computer code will struggle to view the advancing flame using recorded images from a CMOS sensor camera. To improve the probability of detecting the flame front, the use of either an image intensifier or a suitable external light source of chamber illumination will help differentiate between the burnt and unburnt regions due to the difference in density. An image intensifier was used in the currently reported study to boost the available light from combustion and reduce noise significantly.

5.5.1 High-Speed Camera and Synchronisation

The MEMRECAM fx 6000 digital high-speed video camera, fitted with a metal-oxide semiconductor (CMOS) sensor, was used during the optical measurement. The camera presented in Figure 5.10 was placed in front of a 45-degree mirror as close as possible to increase resolution and avoid image distortion. When the camera was triggered, the

in-house LabView code would instantly start capturing data to allow the user to unify both the optical and thermodynamic results, cycle for cycle, at a later date via post-processing.

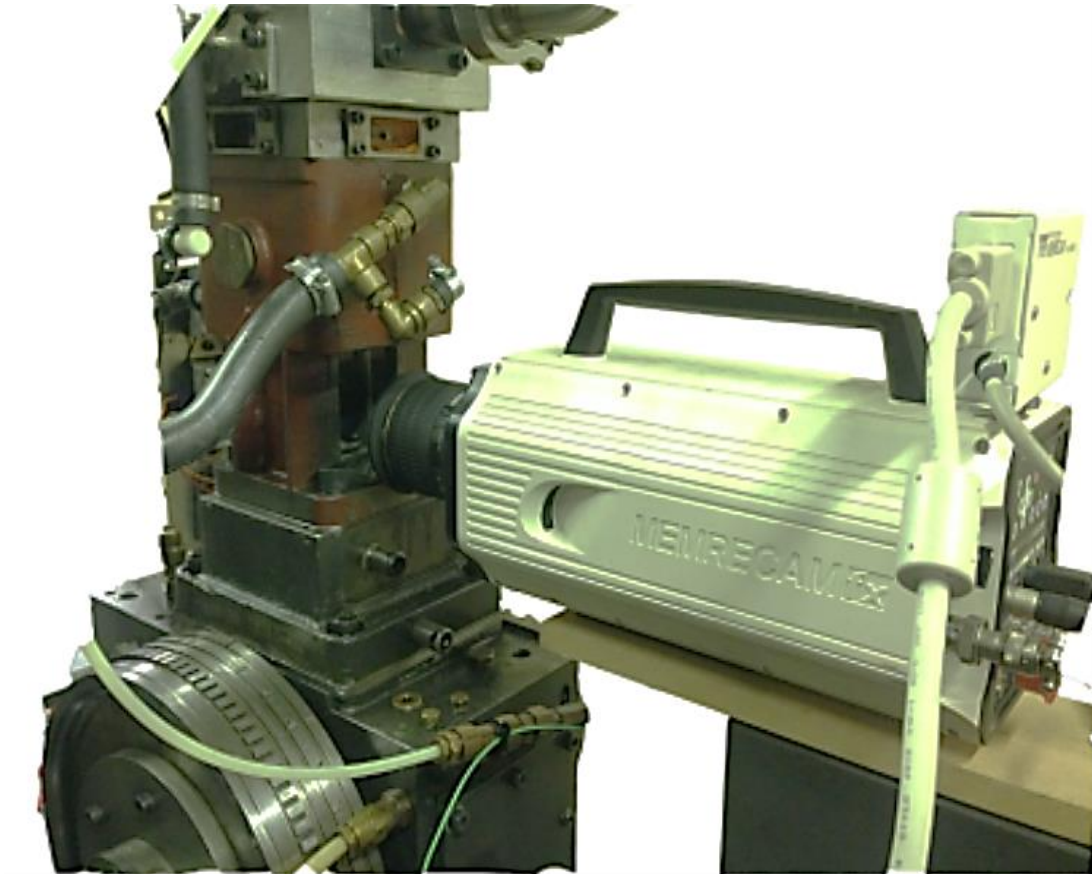


Figure 5.10. High Speed Camera mounted with Nikon Lens.

The camera was later coupled to a DRS Hadland Model ISL3-11 image intensifier, an electro-optical device that transfers low level light images into visible quantities of light in a single wavelength. This was necessary because initial tests without an intensifier incurred too much noise that could not be filtered and made image analysis impossible. DRS Hadland Model ISL3-11 imaging intensifier is characterised by a resolution that matches the (512 x 384) pixel camera at 6000 frame rate (fps) and not to limit camera's resolution. The laboratory lights were switched off before switching on the intensifier because intensifier principle of operation is boosting the available light from the exposed combustion region. Care had to be taken to protect the photocathode and phosphor screens inside the device. This ensured that only the combustion light would potentially enter the intensifier-camera coupling's aperture. After a sweep of intensity

settings (explained in more detail in the next section) from 40% gain to 85% gain, an intensifier gain was set to 80% for all imaging work. The lowest gain intensity was selected (80%) in a way that combustion light could be seen and analysed without having noise issues and avoided higher values to avoid damaging the intensifier.

Previous work [21] with the same intensifier but different engine considered 60% intensity. However, this prior study considered knocking combustion with full bore access, which provided more light for the CMOS camera. The camera was synchronized with a trigger-in signal from the high speed camera that was connected to the Data Acquisition System in a way that simultaneous flame images and pressure data could be recorded (later matched in post processing). The LED lamp illumination shown in Figure 5.11 was used to indicate spark ignition. It was set to blink once the engine was at 40°bTDC firing (set with a reference signal discussed in Chapter 3.12). This was then illuminated through the 45-degree mirror and as the camera and pressure data reached this point the LED blink could be recorded in the image. A post processing procedure was used to match this spark plug and LED illumination in GXlink (High Speed Camera Commercial Software) in the case that camera could not record spark ignition during recording. After accurately marking 40°bTDC each crank angle after or before that was set added or subtracted 1.5 CAD based on 6000 fps and 1500 rpm.

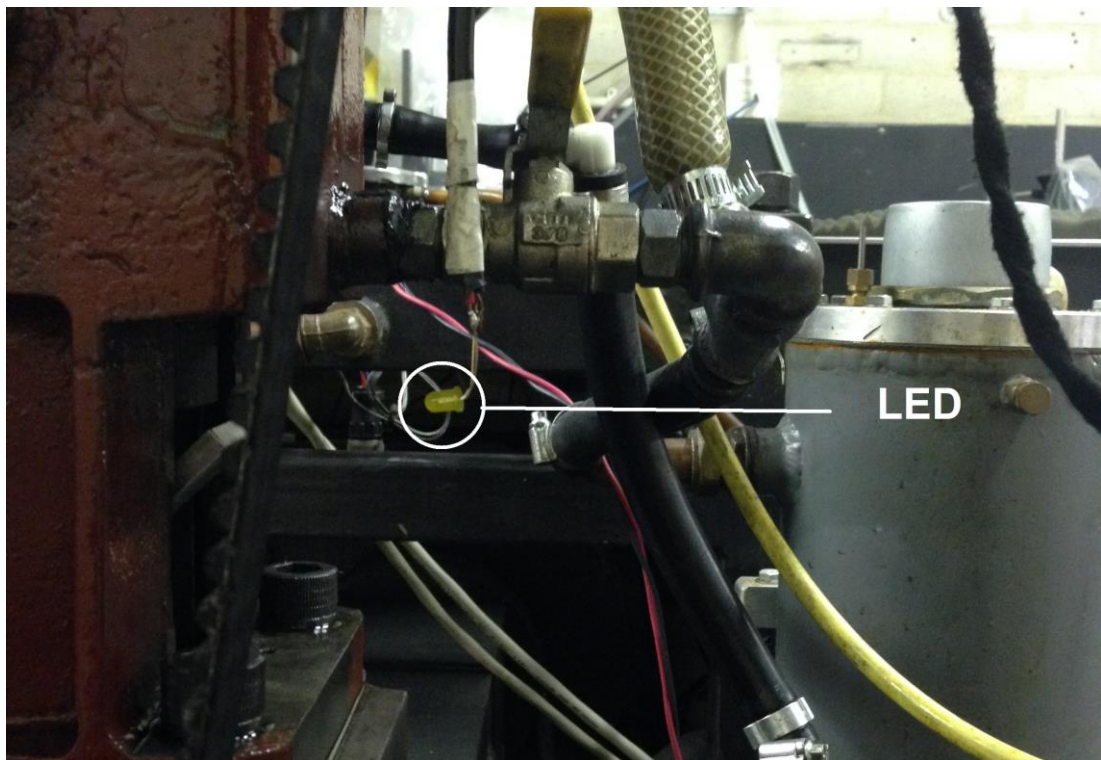


Figure 5.11. LED Lamp Indicating 40°bTDC .

5.5.2 Intensifier Sweep

An intensifier can be described as a device to increase the intensity of available light in an optical system for a low-light condition situation. An initial set of high speed recordings were done without an intensifier in use, this was done to qualify the light available only from combustion itself. Image analysis was undertaken on these recorded images without the intensifier in use. Despite using many noise filtration methods (discussed later in the image analysis section) image analysis of the recorded set, even in the case of rich combustion, was unable to provide accurate measurement of flame contours. Therefore, flame characteristics could not be evaluated due to the absence of enough light from the combustion. The CCD camera sensor sensitivity was increased automatically by the camera to be able to capture the flame as the exposure duration could not be changed during this experiment. Increasing sensor sensitivity potentially could capture flame images without the use of an intensifier but the noise also increased significantly and could not be filtered out in post-processing; this can be seen in Figure 5.12 where horizontal noise signals could not be filtered.

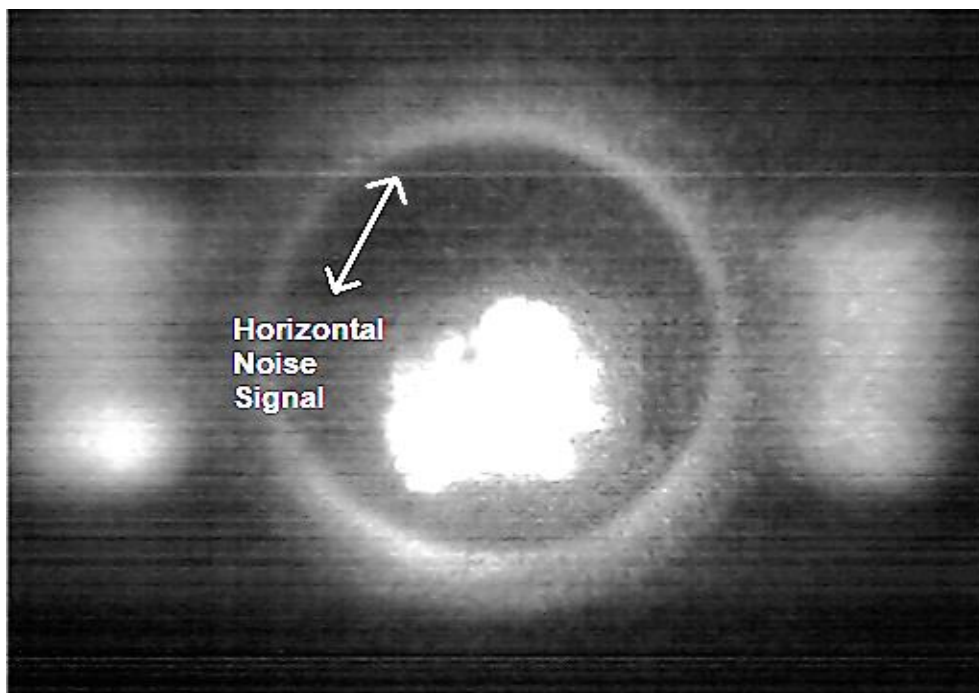


Figure 5.12. Noise in Initial Recorded Image Without Intensifier.

It was crucial to use an intensifier to capture flame images, so steps were taken to evaluate the sensitivity of the mean flame propagation parameters to the intensifier setting. The DRS intensifier (described in Chapter 5.5.1) was coupled to the camera. The intensifier's shutter opened when the camera's trigger was activated. This was done

to acquire the ideal light gain setting for the intensifier to be set at. Considering low gain on intensifier setting and the flame could have horizontal noise and still could not be clear enough; too high gain and the photocathode and phosphor screens in the device would be damaged due to excess light entering the shutter and effectively damaging the intensifier cells. It was decided that three gain intensity settings should be tested, as also tested by the previous researcher using the same intensifier [21]. An upper limit of intensifier gain was considered to be 90% as the bore radius was considerably smaller in comparison to previous experiments with full bore access and knocking combustion. Gain settings of 40%, 60%, 80%, and 85% were selected for the remaining test points. Engine test was carried out at 1500 RPM, using stoichiometric ethanol with MBT spark timing. In addition, the tests were repeated with lean and rich combustion. It was expected that, while stoichiometric fuelling would show little major distinction between cases, the imaging of lean combustion would be hampered due to the dimmer nature of lean burn flames thus demonstrating the lowest gain setting with which accurate results could be obtained and the imaging of rich combustion was brighter due to nature of rich flame combustion. Analysing the recorded flame data showed there are two parameters to observe and calculate. The first was to measure the maximum flame radius achieved. Due to the spark being situated at the centre of the cylinder, the ideal maximum radius should be full bore radius. However, there will be some fluctuations in the precision of this value due to sight lines from aligning the optical equipment and flame centroid displacement. These were later corrected in post-processing, as explained in the analysis section. The second parameter to affect image analysis is the early flame development and ignition that should be detected with the in-house Matlab code that will be discussed further in the analysis section. It is very important to record early flame behavior as in the early microseconds after the spark event contains the flame propagation. If this early flame propagation and light emission are not adequately captured by the camera right after the spark, then the true reasons for the resulting flame motion will not be available. In the stoichiometric intensifier sweep for ethanol, the flame radius analysis shows that Gain at 40% and 60 % were too low to capture the initial flame propagation. The flame radius measurements were unable to accurately match the actual radius of the bore. This inability to identify the early flame is also apparent from the flame speed trace at 50% gain level in Figure 5.13 (left) whereas shown in the same figure (right) is the apparent flame speed at 80% gain in comparison. The apparent flame speed is calculated using the change in distance (radius) over the

time step between images. It is equal to the sum of the turbulent entrainment velocity and the velocity at which the unburned gas is pushed away by compression due to piston motion and the expanding burned gas. Gain setting at 80% was tested and it was concluded that radius measurement is accurate enough to obtain less than 2% error, this error was measured by comparing maximum flame radius measured at each gain, and comparing to the maximum flame radius that is equal to optical piston radius of 27.5 mm. Flame radius fit at 80% gain for the closest cycle to average cycle ethanol is shown in Figure 5.16.

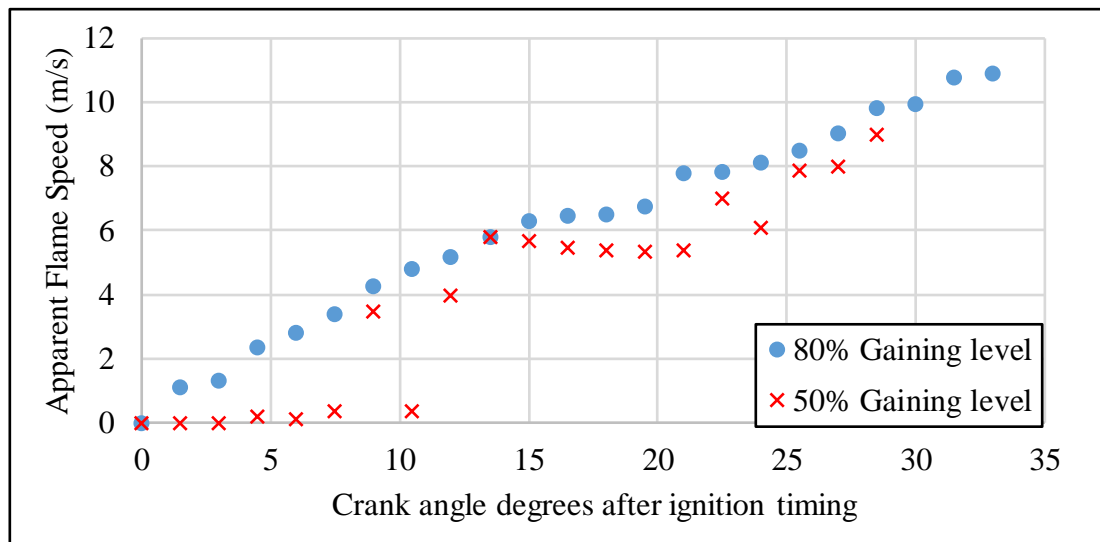


Figure 5.13. Apparent Flame Speed at 50% and 80% Gaining level, (1500 rpm, 0.5 bar inlet pressure, ethanol MBT for all the fuels).

Based on analysing the lean combustion results, it was concluded that a minimum of 90% gain should be selected, as with the dimmer combustion profile the CMOS can only detect a flame with a maximum radius of 12mm (under half the actual bore diameter). When the intensifier gain was increased to 90%, this identified radius was improved, but this was avoided as 90% gain could potentially damage the intensifier cells even though auto reset gaining was engaged. Even though different gain settings are essentially imaging the same combustion event and the flame profile and pattern should be roughly similar (allowing for minor cyclical variation), there is no flame at all in the 40% gain images. Inaccurate flame radius was also captured at 60% gain. As for the images taken at 80%, it was clearly improved analysis where flame radius matched actual bore radius, considering flame centroid displacement. The flame speeds were reasonable to 98%, visible bore radius mentioned earlier on Chapter 3.5.2 is 27.5 mm, As shown in Figure 5.14, ethanol radius reached 20 mm and was due to the flame

stretching toward exhaust side of the piston. Thus 80% was chosen to be the intensifier setting for all the recorded tests at stoichiometric, but it is important to note this was at the mercy of the 90% cap. Ideally, in the lean case, a higher setting would have been tested to confirm the satisfactory performance.

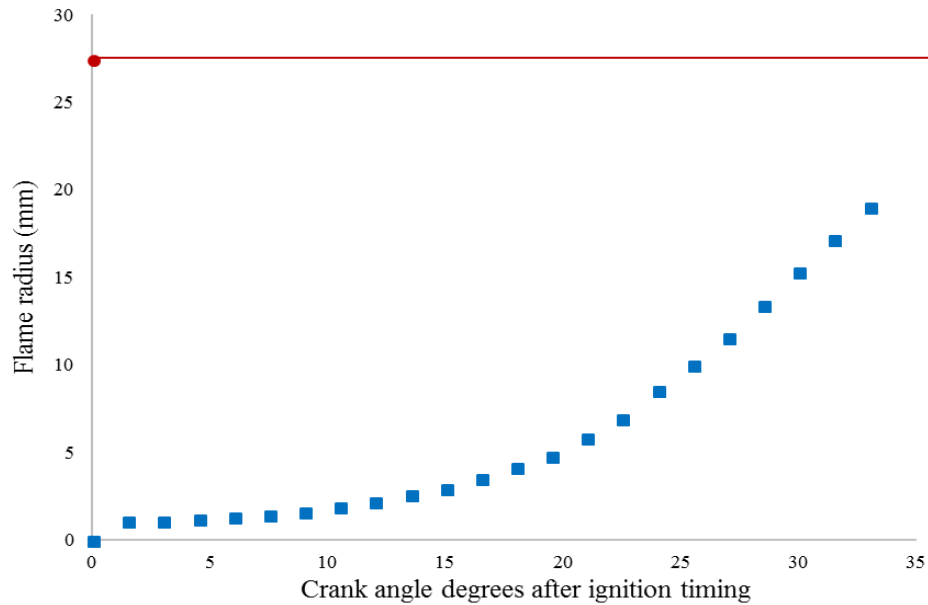


Figure 5.14. Flame Radius compared to optical piston bore radius for ethanol (MBT).

5.5.3 Comparison of Imaging Methods

A comparison of five imaging methods was used to determine the most suitable approach for the imaging required for this experiment. This was done by comparing all the positives and drawbacks of each method as described in Table 5.3. It was concluded that the most suitable method of flame imaging for the experiment was natural light imaging. This was based on technologies available in Brunel University at the time and the accuracy level required to compare different hydrous and anhydrous fuels. This method selection was also confirmed by a previous researcher [178]. Schlieren and natural light imaging were compared with the following two major outcomes [179].

1. The complex setup of Schlieren would eventually increase human error in the procedure in comparison to natural light imaging.
2. Metrics such as flame radius development and shape factor were unaffected by the choice of technique provided the natural light emission was sufficient, by using intensifier it was verified that natural light emission was sufficient.

Table 5.3. Comparison of the major techniques of capturing flame propagation in the cylinder [178,180,181].

Method	Advantages	Disadvantages
Natural Light/ Chemiluminescence	<ul style="list-style-type: none"> • Low in complexity to setup • Relatively inexpensive • Good measure of heat release fluctuations, both temporally and spatially • Alerts users to knocking regions • Allows user to spot species formation to analyse the chemical balance of the charge • Can visualise not only combustion but ‘cool-flame’ combustion due to the emergence of a CHO radical 	<ul style="list-style-type: none"> • Difficulties with identifying three dimensional structures • Signals must be interpreted carefully to ensure accuracy in the assessment of emissions spectra • May not detect the flame front of cooler flames – particularly ethanol • Can be hard to detect all species due to varying wavelengths and with the spectrum of emissions being beyond visible light • Requires an image intensifier or an artificially boosted image – especially for alcohol fuels with less luminous flames

Schlieren	<ul style="list-style-type: none"> • Very good contrast, especially compared to shadowgraph • Works with both laser and white visible light (like LEDs) • Due to its sensitivity to density changes, is suitable for detecting knock and for visualising the initiation and propagation of the flame • Provides an in-focus image, unlike shadowgraph 	<ul style="list-style-type: none"> • Can only generate information along the line of sight of the light source • Not able to see mixing clearly • If the flow is in three- dimensions the results can be misleading and the user is unable to integrate spatially throughout the flow • Requires the knife edge to be precisely placed • Requires a laser light source which could have a poor beam distribution • Double-pass can be very difficult to setup
Shadowgraph	<ul style="list-style-type: none"> • Lower quality equipment required compared to schlieren – therefore lowering expense • Works with both laser and white laser light • Due to its sensitivity to density changes, is great for detecting knock and visualising the initiation and propagation of the flame 	<ul style="list-style-type: none"> • Can only generate information integrated along the line of sight of the laser • Difficulties with identifying three-dimensional structures • Unable to integrate spatially throughout the flow • Double-pass can be difficult to setup • Requires a laser light source which could have a poor beam distribution • Sensitive to piston motion meaning lower accuracy around bore perimeter

Laser Sheet	Mie Scatter	<ul style="list-style-type: none"> • Can use any light source • Can use any type of camera (ICCD or high-speed) • Very strong signal • Clear distinction between the total burnt and unburnt gases • Good balance of spatially and temporal resolutions 	<ul style="list-style-type: none"> • Unable to function with droplets less than $0.5\mu\text{m}$ in size because of its second order size dependence • Usually restricted to two dimensional (though swinging sheet techniques can be used to increase complexity)
	PLIF	<ul style="list-style-type: none"> • Very simple to set-up • Very high contrast as it is able to ignore irrelevant light scatters • Good balance of spatial and temporal resolutions 	<ul style="list-style-type: none"> • Difficult to interpret signals • Must have an ICCD camera, thus raising costs • Requires a high-powered laser • Time-resolved images can take a long time to process, reducing the amount of optical work that can be completed in a day • Requires use of a dopant which may influence the in-cylinder mixture properties (such as the evaporation and the burn rates) • Requires a UV source to fluoresce the dopant

5.5.4 Image Analysis and Processing Techniques

In order to compare and analyse flame behaviors and characteristics for different fuels, each combustion image, and flame batches had to be analysed in a way that noise is removed. Flame characteristics should be measured with consistency and in a repeatable way. So, a variety of Matlab codes were written that are set out in Appendix C and compared to validate the repeatability and consistency of the measured factors. Some of the filtering methods are listed below and will be explained throughout this chapter.

- N-D filtering of multidimensional images
- Create predefined 2-D filter
- 2-D Gaussian filtering of images
- Normalized 2-D cross-correlation
- 2-D adaptive noise-removal filtering
- 2-D median filtering
- 2-D order-statistic filtering
- Local standard deviation of image
- Local range of image
- 2-D box filtering of images

5.5.4.1 Flame Image Initial Processing and Binarisation

Combustion cycles were captured using commercial software called GXlink as a concurrent set of images with default setting on the software. Then these images were downloaded in TIFF format with the mentioned commercial software. Each experiment incurred more than 16000 images that were including all four strokes (Intake, Compression, Combustion, and exhaust) for each cycle. An in-house MATLAB script was developed to batch process the files, initially, files were converted to binary images using `im2bw`. This function works in the following way: converting the grayscale image to a binary image. The output image Black and White (BW) replaces all pixels in the input image with luminance greater than the value of 1 (white) and replaces all

other pixels with the value 0 (black). Specify level in the range [0,1] this range is relative to the signal levels possible for the image's class. Therefore, a level value of 0.5 is midway between black and white, regardless of class. Initially, the Otsu's method was employed as a threshold finding technique, as it was offering an accurate distinction between the flame and the bore with the least processing time. However, in some conditions ideal result could be achieved with manually selecting threshold level in the Otsu's method due to the high noise.

$BW = \text{im2bw}(X, \text{map}, \text{level})$ converts the indexed image X with colormap map to a binary image. $BW = \text{im2bw}(\text{RGB}, \text{level})$ converts the true-color image RGB to a binary image. If the input image is not a grayscale image, im2bw converts the input image to grayscale and then converts this grayscale image to binary by thresholding [182].

5.5.4.2 Noise Suppression

Image noise was filtered using the “`bwareaopen`” function that works in a way that removes all connected components (objects) that have fewer than P pixels from the binary image BW , producing another binary image, $BW2$. The default connectivity is 8 for two dimensions [182]. This operation is known as an area opening and was used to filter out the noise and after the code started a counter to measure image pixels to separate images higher than 10 white pixels. Assuming black displayed 0 and white displayed 1, the start of ignition could be marked as the white pixels (fire) started to increase with an initial region of more than 30 pixels. An overlapping pixel counter function was integrated to stop recording firing images as the flame reached optical bore. Each set of images starting from ignition until reaching optical crown periphery (only combustion stroke) was extracted from the raw data and renamed in an appropriate format. Each firing test could be around 28-32 firing cycles depending on the start of recording. This was later modified with an extra 5-image buffer to make sure the start of ignition would be recorded, in a way that 5 extra images were recorded when code started to record any firing cycle (white pixels >30).

5.5.4.3 Flame Image Read and Post Processing

The next step of image processing deals with reading data from firing cycles separated as described above. Initially, each image was identified by its name. “Fuel”_”Image number”_”Image cycle” was then selected by the Matlab code. A dynamic masking process using $G = \text{fspecial}(\text{'gaussian'})$, $BGR = \text{imread}(\text{background})$ and $\text{imfilter}(BGR, G)$ were applied to remove any ‘halo’ from the bore by subtracting a black background image from each photo. Fspecial function returns a rotationally symmetric Gaussian lowpass filter of size $hsize$ with standard deviation σ (positive). Imfilter function filters the multidimensional array A with the multidimensional filter h . The array A can be logical or a non-sparse numeric array of any class and dimension. The result B has the same size and class as A imfilter computes each element of the output, B , using double-precision floating point. If A is an integer or logical array, imfilter truncates output elements that exceed the range of the given type and rounds fractional value.

Variable contrast method was adapted to adjust contrast in each image, this adjustment was done by setting a threshold and trial and error. Because many automatic adjustments such as imadjust failed to provide enough consistency with a different set of images and fuels. Imadjust automatically maps the intensity values in the grayscale image I to new values in J . By default, imadjust saturates the bottom 1% and the top 1% of all pixel values. This operation increases the contrast of the output image J automatically without being able to correct it. Gamma correction was also used to enhance flame detection and visibility for low light cycles and lean mixtures by setting the Correction property to Gamma. This property gives the desired gamma value of the output image. When set the Correction property to De-gamma, this property indicates the gamma value of the input image. This property was set to a numeric scalar value greater than to 1 and less than 1.2 depending on each image condition.

Subsequently, the image with the highest luminance was selected to identify the piston bore. An elliptical mask was plotted using “ imellipse ” around the flame, this function works with the interactive placement of an ellipse on the current axes. The function returns h , a handle to an imellipse object. The ellipse has a context menu associated with it that controls aspects of its appearance and behavior by right-clicking on the line to access this context menu. The ellipse position could be set manually in a way that creates a “draggable” ellipse on the object. Specified by $hparent$ position is a four-element vector that specifies the initial location of the ellipse in terms of a bounding

rectangle. The position has the form [xmin ymin width height]. Such positioning of the ellipse was tested many times to most accurately identify the piston window periphery as displayed in Figure 5.15.

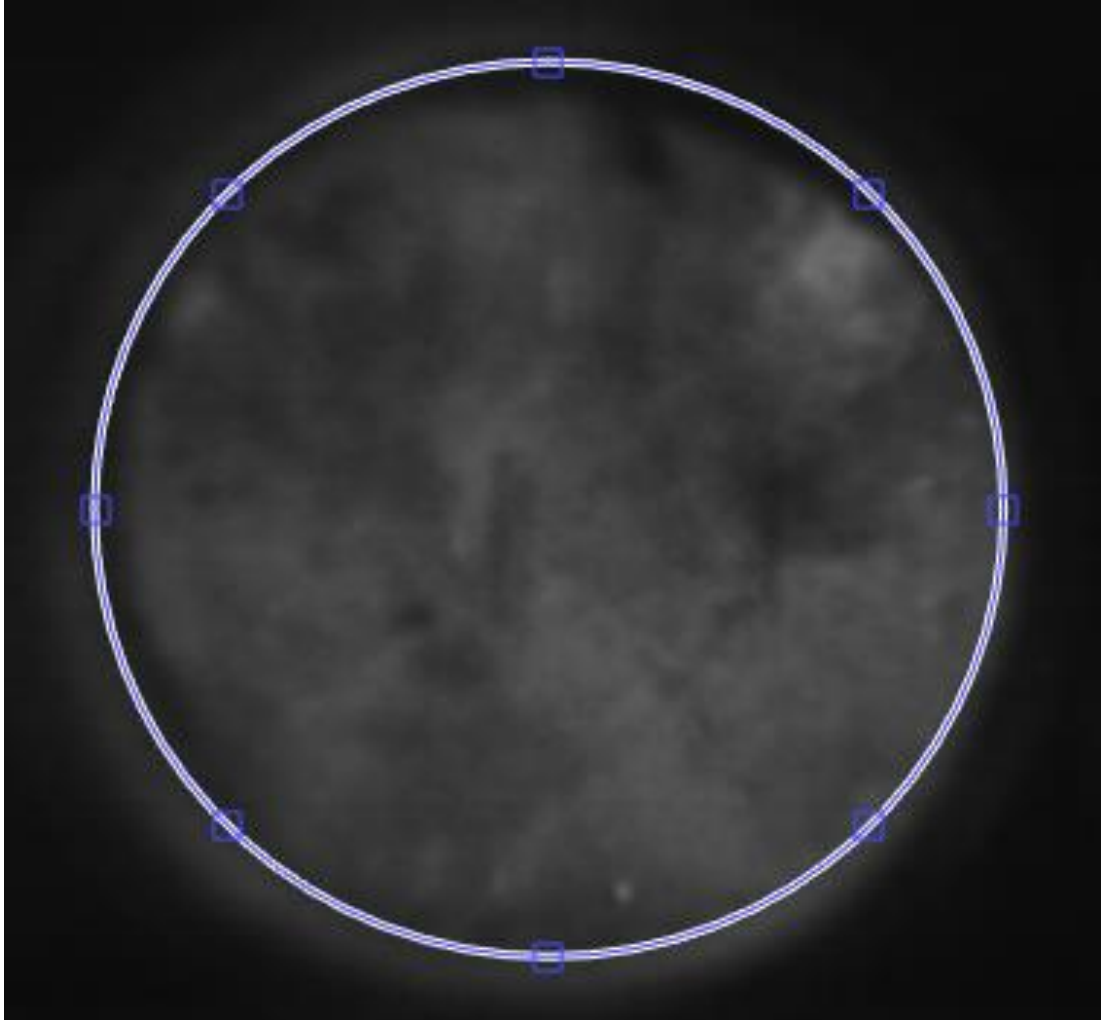


Figure 5.15. Ellipse used to mark the edge of optical crown.

It was also here that the ratio of the image to the real-world dimensions is created. This aided the correct calculation of the various analysis figures later (radius, area, etc.). Here the ratio was set as 1:2.71.

5.5.4.4 Flame Radius

Flame radius calculation is one of the most important initial values of the flame analysis as from this many other values can be derived. Therefore, obtaining the flame radius with the highest level of accuracy was considered and verified many times. The code used the best-fit circle method, an idea originally proposed by Keck [155], and used

numerous times in literature [20,62,183] to obtain the radius. This method seeks to find the flame's centre and radius by affixing a circle to the image. This is done so that the amount of unburnt charge encompassed by the circle is equal to the amount of burnt charge. This best-fit circle can be calculated by solving a non-linear, least-squares problem, in order to minimise the sum of the squares of the distances:

$$d_i^2 = (\|z - x_i\| - r)^2 \quad (5-14)$$

where d_i is the distance between a point x_i and the centre of the best-fit circle (z) which possesses a radius of r . If $u = (z_1, z_2, r)^T$, this means \tilde{u} needs to be determined so that:

$$\sum_{i=1}^m d_i(u)^2 = \min \quad (5-15)$$

Here the Jacobian, defined by the partial derivatives $\frac{\partial d_i(u)}{\partial u_j}$ is given by:

$$J(u) = \begin{pmatrix} \frac{u_1 - x_{11}}{\sqrt{(u_1 - x_{11})^2 + (u_2 - x_{12})^2}} & \frac{u_2 - x_{12}}{\sqrt{(u_1 - x_{11})^2 + (u_2 - x_{12})^2}} & -1 \\ \vdots & \vdots & \vdots \\ \frac{u_1 - x_{m1}}{\sqrt{(u_1 - x_{m1})^2 + (u_2 - x_{m2})^2}} & \frac{u_2 - x_{m2}}{\sqrt{(u_1 - x_{m1})^2 + (u_2 - x_{m2})^2}} & -1 \end{pmatrix} \quad (5-16)$$

From this, using the Gauss-Newton method, the best-fit circle could be iteratively computed around a set of given points [184]. If those points are the flame front data, then the calculated circle would equal one with a radius identical to that of the flame radius. Figure 5.16 at the bottom left shows the best-fit circle (Cyan), the flame perimeter (Black) and flame centre (Red).

Matlab calculations are further explained here by Richard Brown [185].

Regionprops function algorithm can be found below:

This function measures a variety of image quantities and features in a black and white image. Specifically, given a black and white image it automatically determines the properties of each contiguous white region that is 8-connected. One of these particular properties is the centroid. This is also the centre of mass. This would be the (x,y) locations of where the middle of each object is located. As such, the Centroid for regionprops works such that for each object that is seen in firing image, this would calculate the centre of mass for the object and the output of regionprops

would return a structure where each element of this structure would identify. Centroid of each object is in black and white image.

To calculate the inflated area of each image, the matrix that forms the binary image was simply summed to a single number that represented the area of the flame in square-pixels. Since the diameter of the imaging area was known (55mm) in terms of both the number of pixels in the image and the real diameter in millimeters, the area in square pixels could be easily converted into square-millimeters.

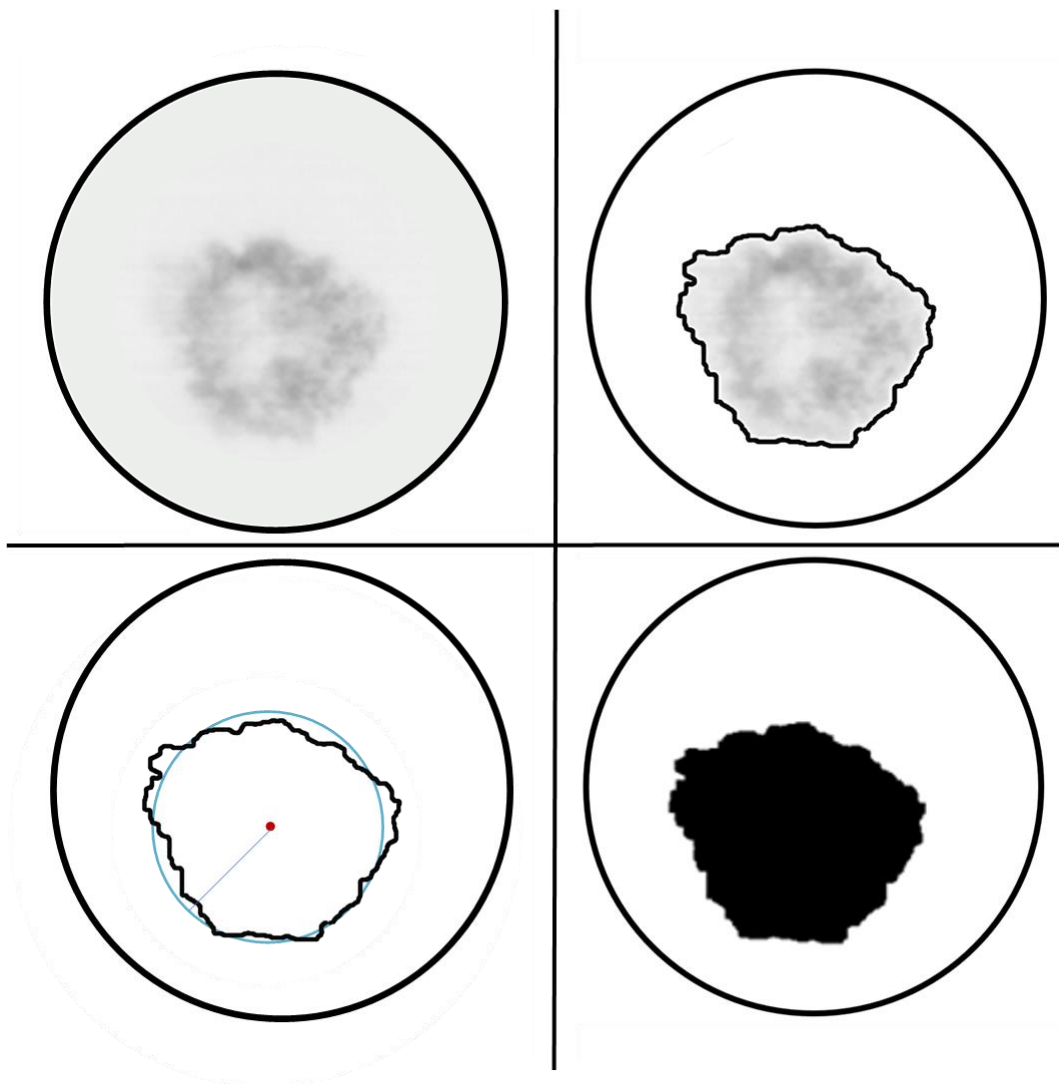


Figure 5.16. Illustration of the flame image processing procedure. Cycle closest to the arithmetic mean of ethanol flame radius, measured at 27 CAD AIT.

The flame centroid was identified by locating the point at which a centre of “mass” would be situated considering the inflated area as a solid object. For the finite set of pixels (p_x) centroid of the body is:

$$c = \sum \frac{p_x}{NPI} \quad (5-17)$$

where NPI is the number of pixels selected in the image and $p_x = (x_i, y_i)$ the Euclidean co-ordinates of the pixels.

5.5.4.5 Flame Speed and Shape Factor

The flame speed value is also important to the analysis of the flame development such as flame speed, flame radius, and shape factor and the effects that charge motion or residual gas levels can have on a combustion event. As stated earlier, the flame speed is the expansion rate of the flame's radius over a set time interval. In reality, it can be viewed as the radius growth rate. The time interval to analyse the two radii over was selected to be the interval between two flame images. As the camera was set to 6000 fps, this resulted in an interval of 166 μ s. The difference between the two best-fit circle's radii could then be used to determine the speed. So, the apparent flame speed was calculated using the changing distance (radius) over the time step between images and can be defined as sum of the turbulent entrainment velocity and the velocity at which the unburned gas is pushed away by compression due to any upward piston motion and the expanding burned gas.

The flame front analysis can be further enhanced by quantifying the developing flame front's distortion. This is referred to as the shape factor [48,153,186] and is defined as the ratio of the perimeter of the flame contour P_C to the perimeter of a circle whose radius is equal to that of the flame at a given crank angle (usually the radius of the best-fit circle, P_r):

$$SF = \frac{P_C}{P_r} \quad (5-18)$$

The perimeter of the flame contour was verified via the commercially available photo-editing software Photoshop. Batch processing of the black and white images would entail importing the TIFF file, selecting the flame area and using the Measure tool within Photoshop to produce a count of the perimeter pixels of the flame shape. Once this perimeter length had been converted to millimeters it became P_C and could be used in conjunction with the earlier calculated P_r . Comparing the Photoshop value to the radius of the a best-fit circle verified that values computed with the best-fit circle are

accurate to 99% comparing to Photoshop that could itself contain some error.

5.6 Thermodynamic Analysis and Techniques

A number of processes were devised to allow for accurate comparison between different fuels and for accurate analysis of the thermodynamic data being obtained in the lab. Set out below is the experimental characterisation of the engine's thermodynamic performance. For all tests, the decision was made to capture 300 thermodynamic cycles to consider a cycle-to-cycle variation to be accounted for in a manner in-line with standard industry practice for SI engines [187].

5.6.1 Sample Size and Cycle Selection

Cyclic variation can be defined as fluctuations in engine performance from one cycle to the next without changing engine control settings such as inlet pressure, load, spark timing etc. Young [188] concluded that if the cyclic variation was eliminated entirely, then the power output of an engine could be improved by ~10% and there would be a noticeable drop in emissions. Cyclic variation was studied further by Lyon [189] who identified a potential ~6% improvement in the fuel consumption rates if cyclic variations were eliminated. The causes of these cyclic variations are numerous and can be related to both flame and flow structure, each depending on other parameters. This includes phenomena such as the moment of induction the dissipation rate of turbulence or flow separation in the intake ports. Excessive bulk air motion or inlet pressure waves can impact on the turbulence intensity, which in turn can influence flame front wrinkling, increasing variation. In 1996 Ma and coworkers [190] found that increasing the inducted flow's turbulence intensity then the variation between cycles would increase as well. As the spark ignited formation of the mixture in the spark-gap plays an important role for the rest of the combustion process. Any variations in the state of the fuel (liquid or vapour), incomplete mixing of the charge or any excessive exhaust gas residuals present will affect the way the flame initially propagates from the spark plug [19]. The flame development rate can be altered by the duration and energy of the spark event. Moreover, the variation has been found to increase as a result of any factor that elongates the combustion duration as these factors result in a longer, slower flame meaning slower burning fuel being exposed to the turbulent spectrum for more time

and hence being more distorted. This will increase the chance of partial or complete misfires and will certainly increase the cyclic variations.

IMEP can be used to indicate cyclic variation as its relative performance measure for engine designers allows them to compare the output of engines of different sizes, as described in the equation below. Moreover, the rate of heat release (or mass fraction burned) and the in-cylinder pressure trace can be used to identify cyclical variation. The COV of IMEP should never exceed 5-10% [21] this has been considered for many experimental labs and in the currently reported study, the aim was to keep it below 5%.

$$COV_{IMEP} = \frac{IMEP_{STD}}{IMEP_{Average}} * 100 \quad (5-19)$$

Minimizing this variation is possible through repeated experiments and averaging to find the numerical mean and then to identify those cycles closest to that mean. This is an effective method when enough data are obtained to give accurate results that are indicative of the trend in data. In Figure 5.17 the decreasing trend indicates that as the amount of captured cycles grows until 50 cycles the percentage error between that cycle and those that have been previously recorded decreases and after 250 cycles it is less likely to skew results dramatically.

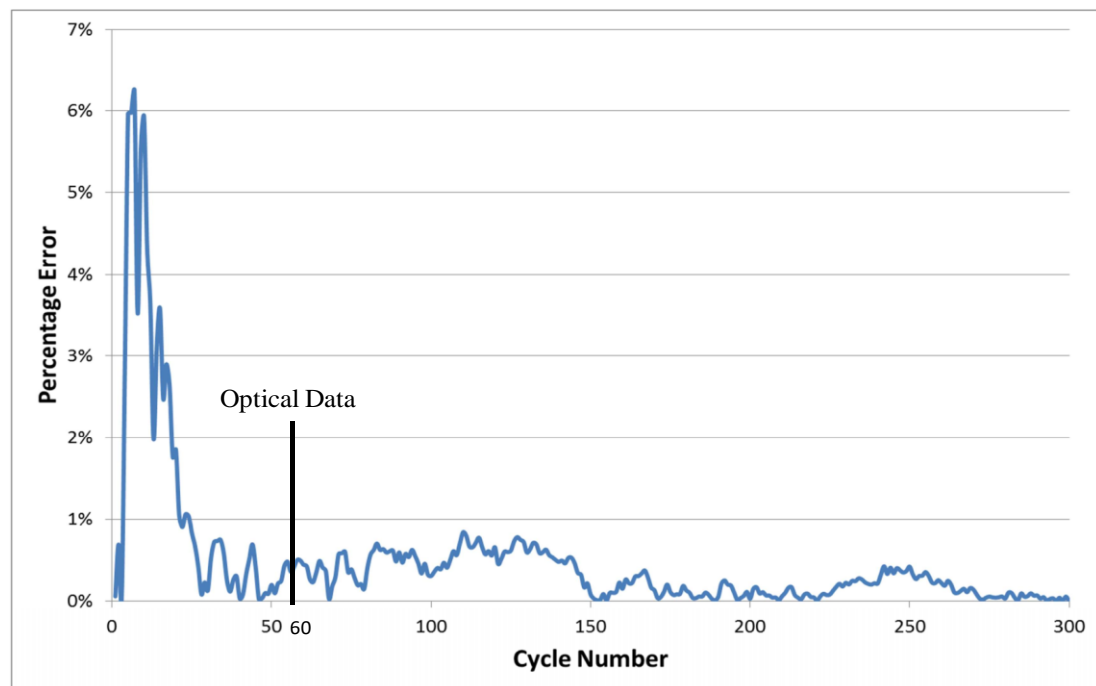


Figure 5.17. The cumulative percentage error indicating the reducing of COV of IMEP over 300 cycles.

Based on Brunt and Lancaster's [187,191] studies of the effects of SI engine cyclic

variation and sample size on the accuracy of in-cylinder pressure measurements, it was recommended that 150 cycles should be the minimum, while 300 cycles would still be ideal for SI engines as has become widely adopted in the powertrain industry. For thermodynamic analysis, 300 cycles were obtained for all the fuels and 60 cycles were obtained for optical measurements.

In order to compare the cyclic variation and combustion characteristics of the fuels, a procedure was adopted to allow for selection of real cycles representative of typical fast, mean and slow flame development events. When examining in-cylinder pressure data alone, with a sample size of 300 cycles it was generally observed that no single real cycle would exhibit in-cylinder pressure development identical to that of the arithmetic mean pressure profile computed over the data set. Hence it was crucial to manually select a real cycle whose pressure development was closest to the averaged cycles. Set out in Figure 5.18 is an example data set for the pure ethanol case (MBT spark timing at 40° bTDC, $\lambda=1.0$) with the mean case superimposed. The selected characteristic slow and fast cycle were those nearest the computed pressure data that was two standard deviations above or below the mean pressure profile, with the achieved upper and lower (or faster and slower) fits marked with the colored dashed lines in Figure 5.18. This was considered to be a robust method when comparing different fuels albeit still reliant on manual selection of the nearest cycles.

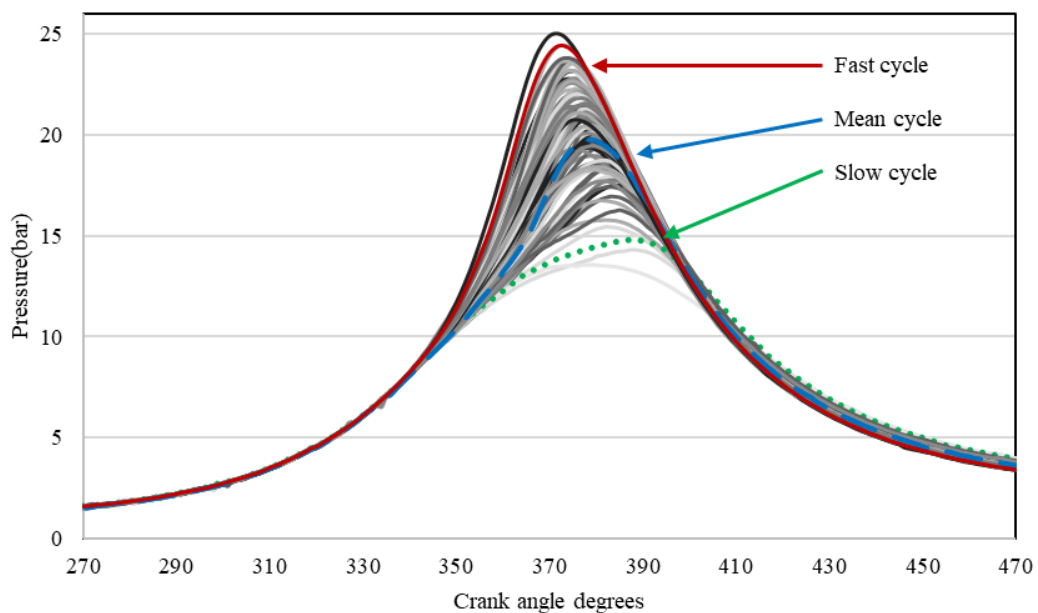


Figure 5.18. All 300 combustion cycles displayed with the numerical mean, fastest and slowest cycles superimposed (1500 rpm, ethanol MBT spark timing).

The above mentioned cycle selection method has been used to choose all mean cycles in the currently reported study. Further refinement of the model was necessary for optical data cycle selection, as 60 cycles of optical data were recorded for each fuel. To select a mean cycle it was necessary to compare the closest cycle to mean cycle and validate that cycle to another close imaged cycle to the mean. This cycle selection method was considered to be a robust method. The position of peak pressure is shown for slow, mean, and fast cycle for all the fuels, using the same cycle selection method. The maximum pressure rise rate was calculated correlating the pressure variation to the crank angle variation. Also, the position of the maximum pressure is presented for all the tested fuels in respect to their crank angle degree.

5.6.2 MBT Spark Timing

Spark timing sweeps were undertaken with pure ethanol starting from 50° bTDC to 20° bTDC, sweeping spark timing from 50° to 40° bTDC in 2° intervals showed increased IMEP and reduced COV of IMEP, on the contrary sweeping from 40° to 20° bTDC decreased IMEP and increased COV of IMEP. Therefore, 40° bTDC was identified as the optimal ignition timing where the minimum spark advance for best torque, maximum IMEP with 1.68% COV was achieved. The spark timing was kept constant for all the fuels and experiments in the currently reported study. This was to ensure that, nominally, the same flow field conditions existed on average at ignition timing for all tests, also mentioning, it is important to consider optimum ignition timing for the two primarily hydrocarbon fuels as there will be more heating of the unburned charge due to the combined expansion of the burned gas and the compression due to piston motion. This could potentially accelerate their flames and give different results. Ethanol crank angle that maximum pressure occurs (CA_Pmax) was 18° aTDC and 50 % mass fraction burned at 6° aTDC (CA50). This showed a good indication of MBT spark timing [31].

5.6.3 IMEP calculation

The IMEP net during combustion was calculated by the following formula, where p is the in-cylinder pressure, V is the cylinder volume and D is the engine displacement.

$$IMEP_{net} = \frac{\oint p dV}{D} \quad (5-20)$$

5.6.4 Indices of Polytropic Compression and Expansion

The polytropic indices (n) during compression and expansion were calculated by the following formula, where the terms are graphically defined in Figure 5.19 (compression) and Figure 5.20 (expansion).

$$n = \frac{\log(P_2/P_1)}{\log(V_2/V_1)} \quad (5-21)$$

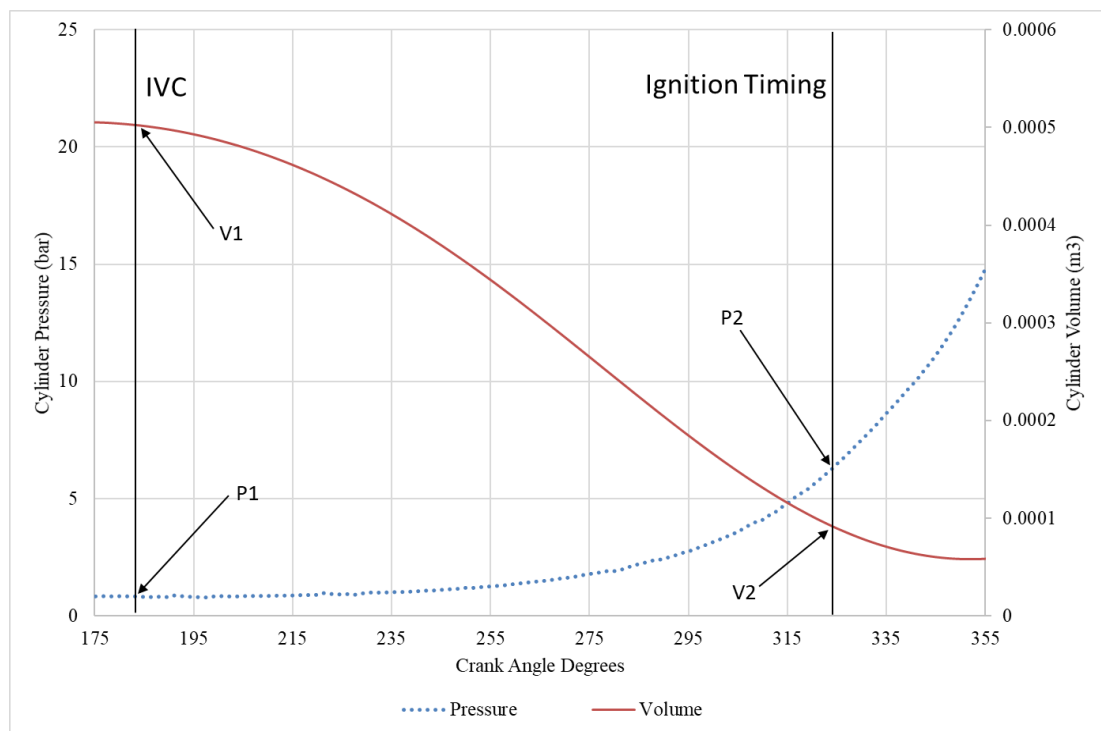


Figure 5.19. In Cylinder pressure and volume during the compression stroke.

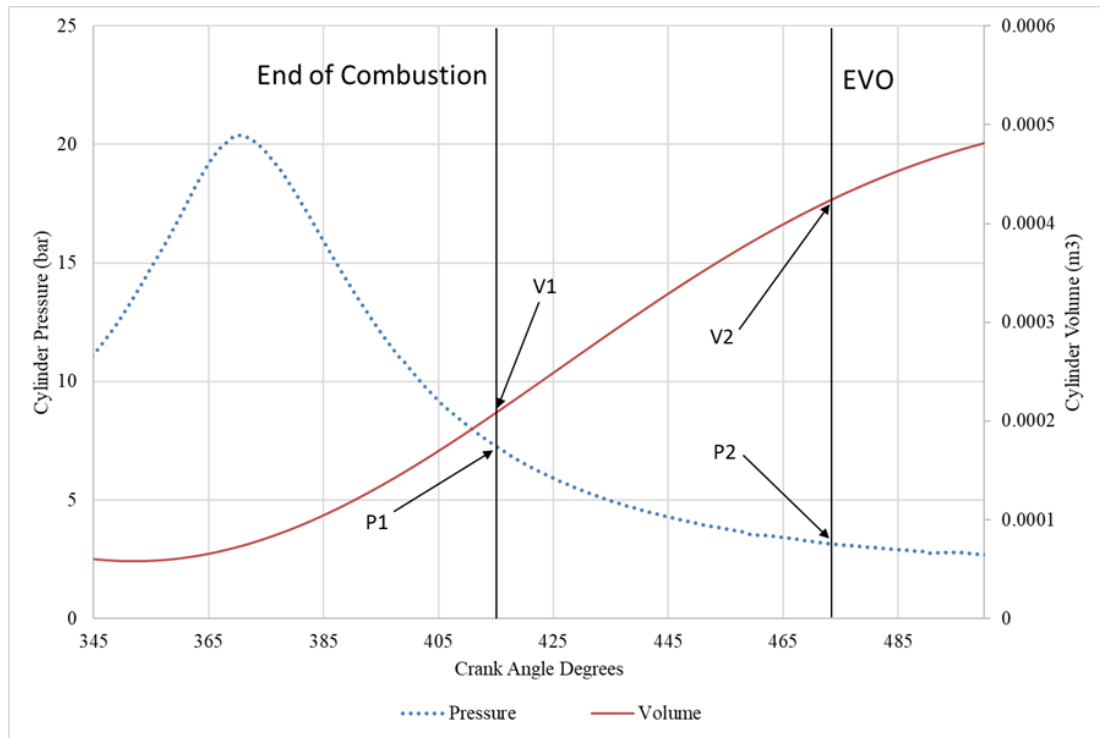


Figure 5.20. In Cylinder pressure and volume during the Expansion stroke.

The system is required to be closed with no mass or energy transferred for the polytropic condition during compression or expansion. Therefore, the calculation of the polytropic indices may only be made with points taken while all valves are closed and before/after combustion. The index of polytropic compression was calculated from a point taken just after Intake Valve Closure (IVC) and another immediately before the point of ignition (as ensured by examination of the pressure data). Noise caused by the intake valve closing can produce errors in the measurement of the index of polytropic expansion. Therefore, this region of noise was identified and avoided as mentioned by [192]. The impact of low-level noise across the whole pressure signal was reduced by averaging the measurement of P1 and P2 over 11 consecutive samples as described by [192]. The index of polytropic expansion was calculated from a point after the end of combustion and before Exhaust Valve Open (EVO). These points were clearly identified from the graph of cumulative heat release against crank angle.

5.6.5 Heat Release Calculation

The apparent heat release analysis was based on comparing the rate of change in

combustion chamber pressure and volume of a fired cycle to that predicted by polytropic compression and expansion. The variation of the fuel heat release and fluid to wall heat transfer were grouped in only one term, apparent heat release dQ_n , which means the variation of the fluid internal energy and boundary system work (piston work). The Rate of Heat Release (ROHR) for each cycle was found through the rate of change in volume and pressure at each measurement interval, as given by the following equation [30].

$$\frac{dQ_n}{d\theta} = \frac{\gamma}{\gamma - 1} p \frac{dV}{d\theta} + \frac{1}{\gamma - 1} V \frac{dp}{d\theta} \quad (5-22)$$

5.6.5.1 Signal Filtering

Signal filtering of apparent heat release data had to be used to reduce noise to accurately use the data from the heat release formula. To do so two methods were employed and tested to reduce some of the noise associated with data capture (electrical interference, vibration, and shock, etc.) without compromising the information. The first method is to increase the crank angle interval over which the pressure and volume are measured. Figure 5.21 shows that as the interval between crank angles is increased, the noise is reduced while the shape of the curve remains intact.

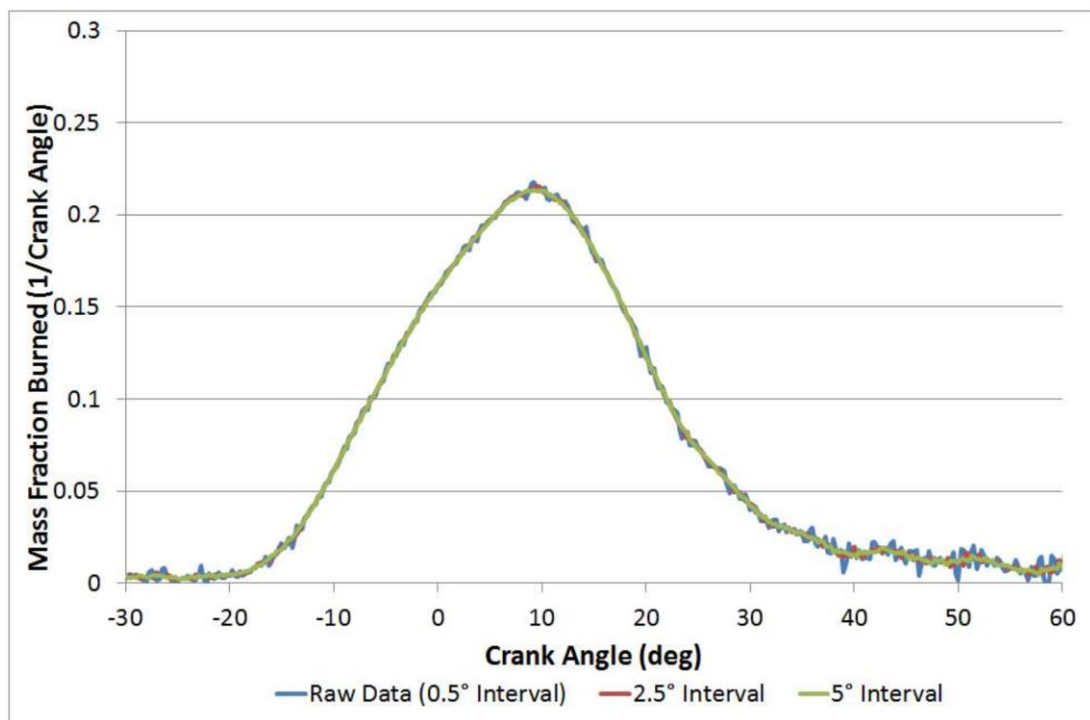


Figure 5.21. Interval size effect on MFB results,

It can be seen from this diagram that, there is a large amount of noise (vibration) occurring when the inlet valve closes. Even though this is not a key area of combustion analysis, any noise should be reduced where possible. Thus, the initial method to reduce noise, 5° interval filtering alone will not be sufficient. The next method uses a box filter. Instead of using each point as it is, an average number represents that point will be used. This average number contained from a set of other numbers, the box defines how many numbers will be averaged to represent that number. Indicated in Figure 5.22 are box filters used with 3, 5, 7 and 9 number averaging, it can be seen that as the box filter is increased the noise is reduced further with little deformation of the trace.

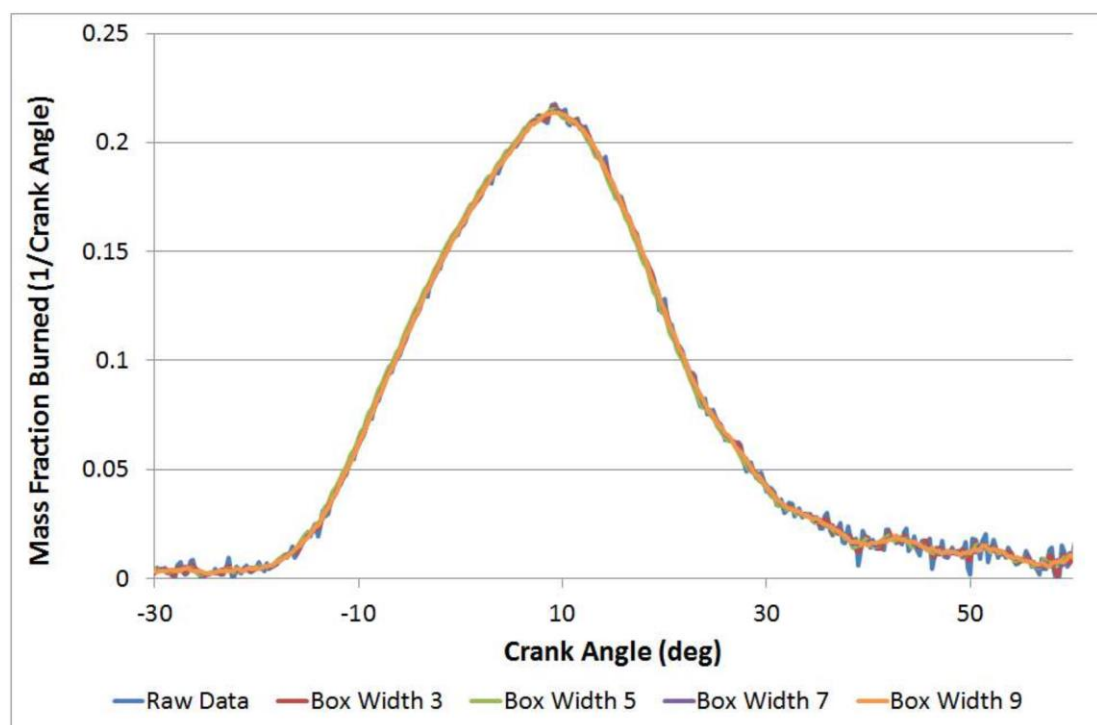


Figure 5.22. MFB Graph presented in 4 boxes averaging size.

Finally, it was decided to use both methods, box, and interval, to reduce noise without changing the shape of the MFB curve too much.

5.6.6 Two-zone Heat Release & Temperature Analysis

In-cylinder pressure data was used to analyse heat release with the two-zone method, in this method thermodynamic properties of the burned and unburned mixture fractions were measured. A few iterations required for convergence of this two-zone model (4-10) [193–195]. The two-zone method uses well-known subroutines of Ferguson [196]

that consider 10 species scheme for the combustion products, consisting of CO₂, H₂O, N₂, O₂, CO, H₂, H, O, OH, and NO. Fuel thermodynamic properties were calculated using a similar approach with polynomial curves as represented by Heywood [31]. Burned and unburned mixture temperature are separately calculated in the Ferguson method. Thermodynamic properties are calculated for mixture temperatures lower than 1000 K for the unburned zone by mixing fuel, air and residual gas. The unburned zone temperature is calculated as follows:

$$\frac{dT_u}{d\theta} = \frac{-\frac{dQ_{L,u}}{d\theta}}{m(1-\chi_b)C_{P,u}} + \frac{v_u}{C_{P,u}} \frac{\partial \ln v_u}{\partial \ln T_u} \frac{dP}{d\theta} \quad (5-23)$$

Combustion process in the burned zone at higher temperatures uses the equilibrium state of Olikara and Borman [197] to calculate speciation for the combustion products of H, O, N, H₂, OH, CO, NO, O₂, H₂O, CO₂, and N₂. Initial temperature value of the burned zone is calculated by adiabatic combustion assumption at the combustion start crank angle. Then at each time interval, the burned zone temperature differential depends on the burn rate $(\chi_b, \frac{d\chi_b}{d\theta})$, the measured cylinder pressure, and the heat losses of this zone, according to the following equation.

$$\frac{dT_b}{d\theta} = \frac{-\frac{dQ_{L,b}}{d\theta}}{m\chi_b C_{P,u}} + \frac{v_b}{C_{P,b}} \frac{\partial \ln v_b}{\partial \ln T_b} \frac{dP}{d\theta} + \frac{h_u - h_b}{\chi_b C_{P,b}} \left[\frac{d\chi_b}{d\theta} \right] \quad (5-24)$$

Heat losses are separately calculated for each zone by applying the Annand model [198], both heat convection and radiation are considered in this method [199]:

$$\frac{dQ_{L,j}}{d\theta} = A_{w,j} \left[a_{ht} \frac{k_j}{D} Re_j^{b_{ht}} (T_j - T_w) + \varepsilon_{ht} \sigma (T_j^4 - T_w^4) \right], j = u, b \quad (5-25)$$

Where

$$A_{w,u} = A_{cyl} (1 - \sqrt{\chi_b}) \quad A_{w,b} = A_{cyl} \left(\frac{1}{\sqrt{\chi_b}} \right) \quad A_{cyl} = \pi \frac{D^2}{2} + \pi D y_{cyl}$$

5.6.6.1 Iterative Process

The iterative process of the model is schematically outlined in Figure 5.23. Initially, the model reads all the data required such as the cylinder geometrical characteristics, the species thermodynamic coefficients, the fuel type data, and the mixture

characteristics (λ , f). The initial condition of the cylinder mixture is given by the single zone heat release equation. Hence the initial values for the start of combustion and the end of combustion are estimated with the single zone heat release analysis as well as a first indication of the burned fuel mass. Moreover, the initial value for air mass flow is estimated by assuming a volumetric efficiency while the fuel mass flow is calculated using the lambda index.

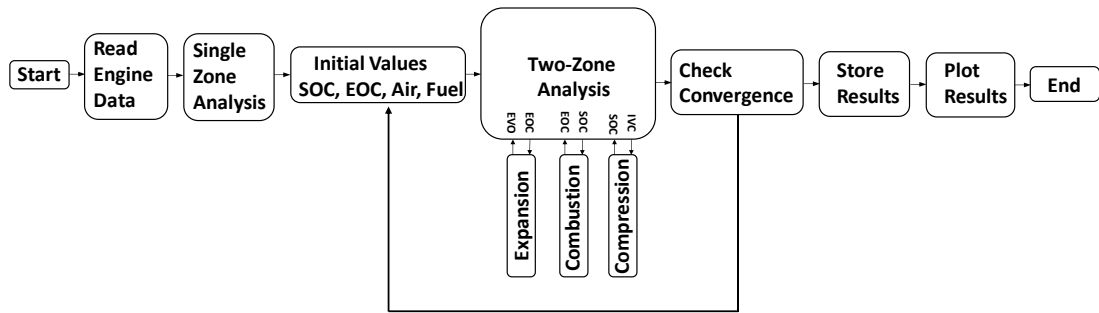


Figure 5.23. Flowchart of the two-zone heat release model.

5.6.7 Laminar Burning Velocity Calculation

A flame, at its core, is a self-sustaining chemical reaction that occurs in the flame front when an unburnt mixture is heated and converted to products. The flame front is actually made of two regions:

1. Preheat Zone: Unburnt mixture is heated via conduction. No energy release occurs here
2. Reaction Zone: Once the mixture is heated in the preheat zone, it transitions to the reaction zone where an exothermic reaction begins at T_{CRIT} . This temperature is dependent on the fuel composition and mixture ratios.

The rate of this transition is governed by the temperature, pressure and species concentration of the burning mixture thus the laminar burning velocity is defined as (where \dot{m}_r is the rate of production of burned gas) [31]:

$$S_L = \frac{\dot{m}_r}{A_f \rho_u} \quad (5-26)$$

Where A_f is the flame area, because the flame thickness is of order 0.2 mm, therefore in comparison to vessel dimensions the flame can be treated as negligibly thin [31]. In addition, Equation (5-27) can be used to calculate the laminar burning velocity of iso-octane, where $S_{L,0}$, α , and β vary with the fuel type and depend on the equivalence ratio.

$$S_L = S_{L,0} \left(\frac{T_u}{T_0} \right)^\alpha \left(\frac{P}{P_0} \right)^\beta \quad (5-27)$$

T_0 and P_0 are the reference temperature and pressure at the start of combustion, being available from the two-zone heat release model.

Subsequently, these predictions, along with the measured in-cylinder pressure data for the mean cycles, could be used to predict the laminar burning velocity for ethanol and E10Iso90 blend via empirical correlations produced previously by Gülder [200] and Heywood [31]. Some caution is required as these velocity correlations did not take into account any variation in exhaust gas residual quantity or quality. In addition, the correlations extrapolate a relatively limited original experimental data set to engine-like pressures and temperatures.

Ultimately the laminar burning velocity can be considered to provide an indication of the global rate of chemical reaction for a given mixture at a given temperature and pressure. Such a metric hence provides a useful method for describing potential differences in chemistry at differing pressures and temperatures with different fuels.

5.7 Summary

An introduction was conducted explaining imaging techniques for both flow and flame measurements, such as PIV, LDV, High-speed natural light (chemiluminescence) and their restrictions in the past studies. This was followed by Mie scattering and laser principles, PIV technique was then further explained and expanded as it was used to measure the flow alongside cross-correlation and PIV setup. Seeding particles were discussed to satisfy appropriate size and mass with low drag.

High-speed camera working principle and how the camera was synchronised with the reference signal was discussed. Use of intensifier was explained with a procedure to choose appropriate intensity. Table 5.3 compared the major techniques of capturing flame propagation in the cylinder. Flame analysis and processing techniques were discussed in section 5.5.4, containing initial processing followed by how to reduce noise in the image. Further flame characteristics such as flame radius, flame speed, and shape factor were explained and also the calculation was covered. Finally, thermodynamic analysis and techniques used during this research were explained, followed by a two-zone heat release model calculating unburned and burned gas temperature, and laminar burning velocity calculations. All the data processing were conducted using the mean cycle. This mean cycle was selected based on closest real cycle to the mathematical averaging of the data.

6. Results and Analysis

6.1 Introduction

Presented in this chapter is an in-depth analysis of the thermodynamic, flame and flow optical data obtained during this work. The main objective of the study was to improve understanding of the interaction of the bulk in-cylinder flow with turbulent premixed flame propagation when using base fuels including iso-octane, ethanol, butanol and the following blends, B16I84 (16% butanol, 84% iso-octane), E6B9I85 (6% ethanol, 9% butanol and 85% iso-octane), W5E95 (5% water, 95% ethanol), W12E88 (12% water, 88% ethanol) and W20E80 (20% water, 80% ethanol). The experiments were performed in a single cylinder research engine equipped with a modern central direct injection combustion chamber and Bowditch style optical piston. Results were obtained under typical part-load engine operating conditions. High speed cross-correlated particle image velocimetry was undertaken at 1500rpm motoring condition with the plenum pressure set to 0.5 bar absolute, with the horizontal imaging plane fixed 10mm below the combustion chamber “fireface”. Cyclically-resolved flame images were generated and after various processing methods allowed for quantification of the flame development. Data such as the mass fraction burned, in-cylinder pressure and the COV of IMEP could be extracted from the thermodynamic data; while the flame images were processed to calculate the mean flame radius, apparent flame speed, laminar burning velocity, and flame displacement, distortion.

Comparisons were made to CFD computations of the flow. The flame images revealed the tendency of the flame to migrate towards the hotter exhaust side of the combustion chamber, with no complimentary bulk air motion apparent in this area in the imaging plane. Presented in Table 6.1 is a list of some of the main properties of the three baseline fuels. The alcohol-based fuels have a lower stoichiometric air/fuel ratio due to the OH bond at the end of the alcohol chain, so alcohol-based fuels require a lower amount of inducted air to combust. Defining lower heating value as the amount of heat released from combusting a kilogram of each fuel and then returning those products to 150°C, the data in Table 6.1 shows that ethanol’s lower heating value is a little over

60% of the value of iso-octane, meaning that to produce an output equivalent to that of iso-octane, ~30% higher mass of fuel is required. This effect is indicated by the increased injection durations. The butanol was blended in a manner to represent a fuel with oxygen content equivalent to 10% ethanol fuel. It seems likely that butanol will only ever be adopted as a low volume blending agent (being of higher carbon count than ethanol, with increased production energy and arguably less advantage in terms of anti-knock additive in future boosted SI engines). The laminar burning velocities were taken from [141], being obtained at stoichiometric conditions at 423K and 5bar (considered to be representative of typical in-cylinder conditions under part load). It is apparent that differences amongst fuels at high pressure are quite small. Although experimental uncertainties of the order 1 cm/s typically exist, there is a decrease in burning velocity with decreasing pressure, increasing temperature, as well as generally with increasing carbon chain length for the alcohols.

Table 6.1. Fuel Properties of the three baseline fuels.

Fuel Parameters	Iso-octane	Ethanol	Butanol
Chemical Formula	C ₈ H ₁₈	C ₂ H ₅ OH	C ₄ H ₉ OH
Density 20 °C [g/cm ³]	0.69	0.79	0.81
Density 80 °C [g/cm ³]	0.64	0.73	0.76
Latent heat (at T boil [kJ/kg])	272	855	584
Latent heat (25 °C) [kJ/kg]	300	874	669
Heating value [MJ/kg], [MJ/l]	44.6, 30.8	26.9, 21.3	33.9, 27.5
Flash point [°C]	-12	12	30
Stoichiometric AFR	15.1	9	11.1
H/C, O/C	2.25, 0	3, 0.5	2.5, 0.25
Laminar burning velocity, [m/s]	0.36	0.42	0.42
RON	100	129	96
Injection duration, [ms]	0.52	0.78	NA

All tests were undertaken using the fixed test conditions listed in Table 6.2. The optimum ignition timing for ethanol was used and kept constant during all testing conditions.

Table 6.2. Engine Operating Parameters.

Parameter (Unit)	Value
Engine Speed (RPM)	1500
Relative AFR	1
Maximum COV of IMEP	5%
Inlet Pressure (bar)	0.5
Inlet Air temperature (°C)	35
Spark Timing (°BTDC), Constant	40

6.2 Cold Flow

6.2.1 Motored Engine Data

The following characterisation tests were performed in order to ensure robust mechanical operation of the optical engine to detect any leakage or fault prior to any advanced thermodynamic and optical testing. One thousand cycles of pressure data were recorded and analysed before each test. Shown in Figure 6.1 are one hundred pressure cycles recorded at the 1500rpm motoring condition with the plenum pressure set to 0.5 bar absolute. It can be seen that cyclic variations are minimal, with the difference between lowest peak pressure and highest peak pressure only 0.08 bar depicting the maximum pressure variation of less than 1% in the motoring test. Set out in Figure 6.2 is a zoomed-in view of the pressure data between 350 and 370 crank angle degrees, showing a pressure data range of 11 to 11.5 bar.

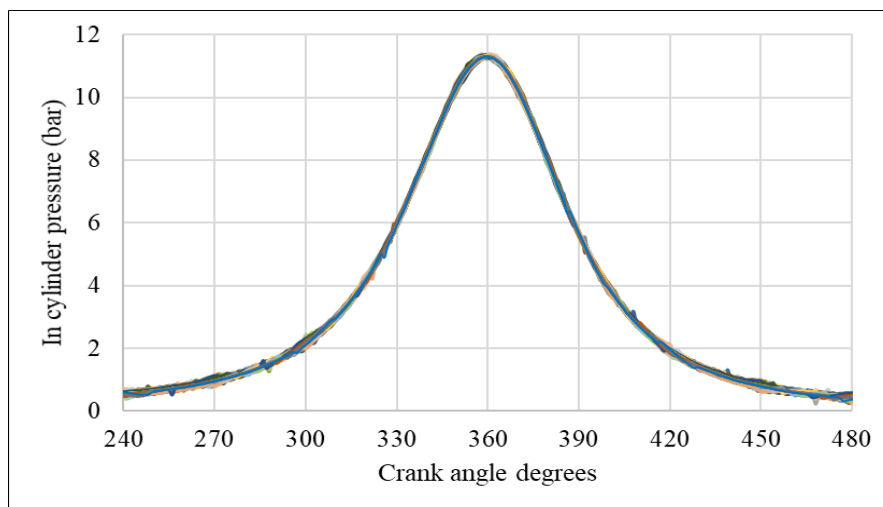


Figure 6.1. The motored in-cylinder pressure of an individual cycles (1500 rpm).

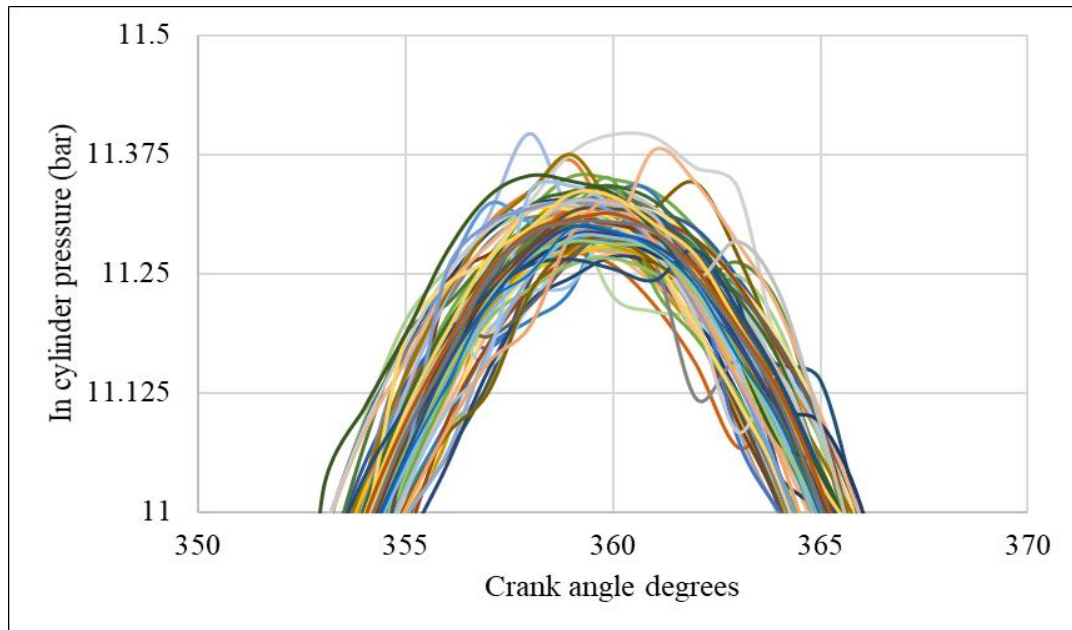


Figure 6.2. Zoomed view of motoring showing cyclic variation for individual cycles (1500 rpm).

6.2.2 PIV Throughout the Compression Stroke

It is crucial to have statistically robust calculations when considering a highly turbulent environment and the associated cyclic variations in the flow within an IC engine. In order to quantify the ‘ensemble mean’ flow field and turbulent flow parameters, 1500 cycles were selected at 30° CA BTDC and randomly (using MATLAB rand code) divided into 15 batches, with each batch containing 100 cycles. Figure 6.3 indicates the computed turbulence intensity and average velocity for these batches on a primary Y axis and secondary Y axis respectively.

It was concluded that the highest variation from 100-1500 cycles was 10% for turbulence intensity and 8.5 % for average velocity. Hence from Figure 6.3 and previous work [18] along with storage and time issues, 800 cycles were considered an appropriate total. These results were published in SAE [201]. The uncertainty for the calculated average velocity of 100 cycles was about 8.6% and reduced to 5.5% after average of 800 cycles. Similarly, maximum uncertainty for the turbulence intensity calculations was 10.1% for 100 cycles and gradually reduced to 3.5% at 800 cycles.

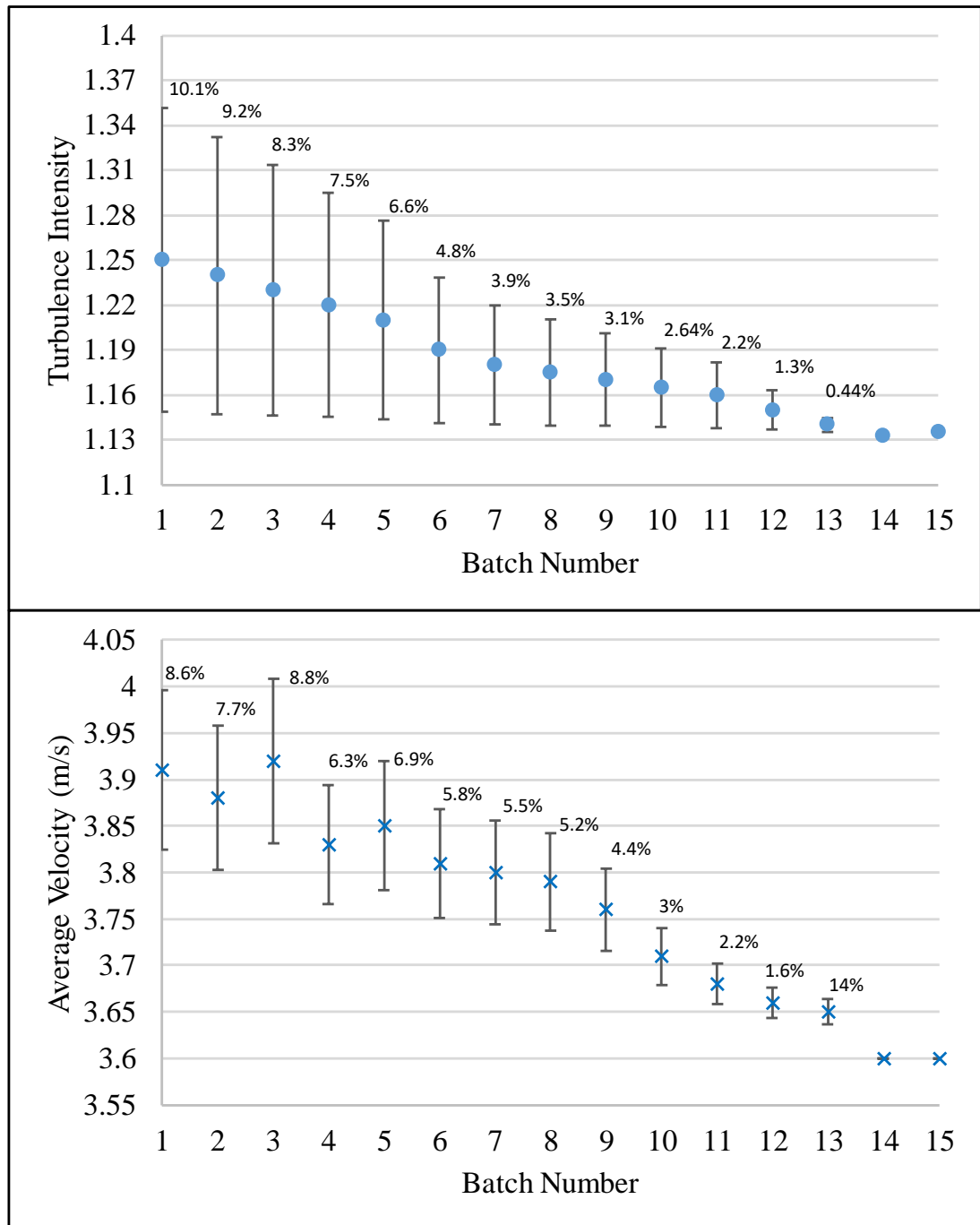


Figure 6.3. Effect of a number of batches (100 Cycles each) on measured velocities with the error bars (100-1500 cycles at 1500 rpm).

Turbulence intensity data presented herein are the RMS of the deviations measured from an average velocity at a 32x32 pixel “point” averaged over 800 cycles calculated in the MATLAB code that is set out in Appendix B. The points in each quadrant are averaged to produce one value representing that zone.

Understanding the flow fields between 180° CA BTDC and 30° CA BTDC under motoring conditions was considered important to try and understand the evolution of

the bulk air motions leading up to the ignition events. Caution is required, as the imaging plane was located somewhat below the spark plug. However, it was postulated that any residual bulk air motions could be as large as the chamber itself. If any such scales existed in the tumbling plane, then these should have also manifested as higher velocities in the horizontal plane (given the rotational nature of the tumble). Unfortunately, flow measurements were not possible at the very end of compression from 30° CA BTDC until TDC as at any crank angle after 30° CA BTDC the laser sheet was covered by the piston.

6.2.3 PIV on Horizontal Plane

To understand the behavior of the in-cylinder bulk flow, PIV images were divided into four zones (denoted I1, I2, E1, E2) with the inlet valves on the top and exhaust valves on the bottom side. Vector fields between 180° CA BTDC and 30° CA BTDC are from the period that the air is being compressed in the cylinder with both valves closed until top dead centre. The gas velocity range during this period was between 0-10 m/s.

The highest turbulence intensity in each zone presented in Table 6.3 was I1=1.24, I2=1.20, E1=1.22, and E2=1.18 these zones are displayed in Figure 6.4. It appears that the air flow was generally moving toward the centre of the cylinder. Furthermore, for this plane, it can be seen that two major vortices appear, albeit the centre of these structures were at the edges of the PIV plane. It's important to note the typical measurement accuracy of PIV is about 1% when modern processing is used and 10% uncertainty on vectors without using multi-pass algorithm [202]. Due to the limitations of dantecstudio software uncertainty on vectors for this study is $\pm 10\%$.

Table 6.3. Turbulence intensity measured at 30°,40°,90°, and 180° CA BTDC in 4 zones.

	180° BTDC	90° BTDC	40° BTDC	30° BTDC
Zone I ₁	1.24 ± 0.2	1.20 ± 0.2	1.17 ± 0.2	1.12 ± 0.2
Zone I ₂	1.19 ± 0.2	1.18 ± 0.2	1.20 ± 0.2	1.17 ± 0.2
Zone E ₁	1.22 ± 0.2	1.16 ± 0.2	1.21 ± 0.2	1.11 ± 0.2
Zone E ₂	1.13 ± 0.2	1.17 ± 0.2	1.18 ± 0.2	1.14 ± 0.2

Shown in Figure 6.5 is the flow field velocity at 180° CA BTDC, where the highest turbulence intensity was observed in the left inlet valve zone showed in Table 6.3, with the majority of the flow going toward the exhaust side and marginally shifted toward the centre of the piston.

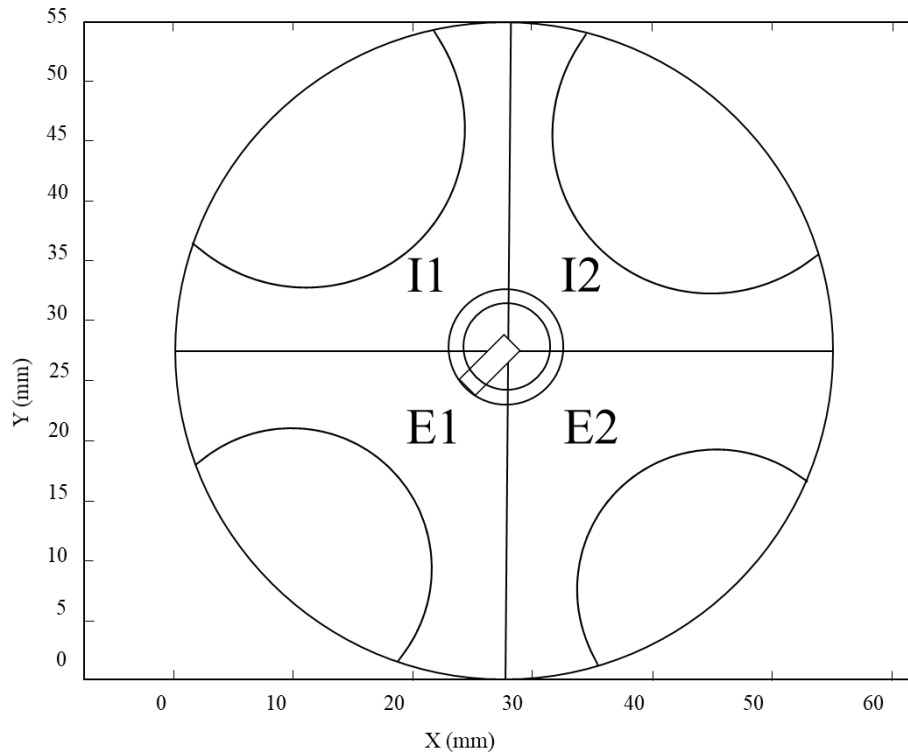


Figure 6.4. PIV image division in 4 zones.

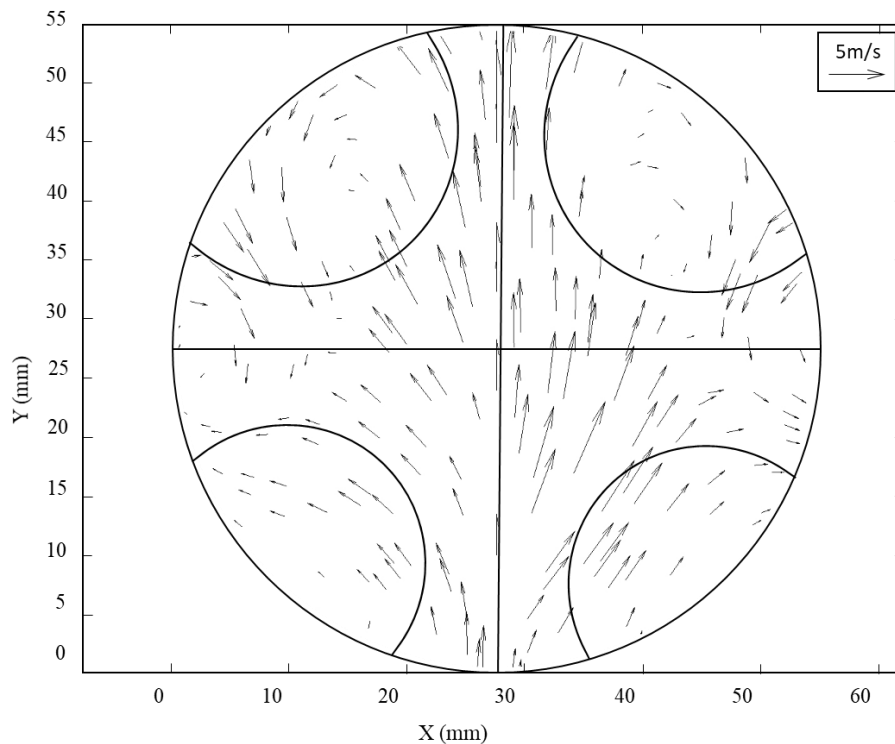


Figure 6.5. PIV Mean velocity field at 180° BTDC at 1500 rpm.

The velocity ranges for 30° CA BTDC were between 0-11 m/s with an average value of 3.6 m/s. The main overall visible structure is a large flow going toward the central point nominally below the spark plug. Figure 6.6 showing all four turbulence intensities from 180° CA BTDC to 30° CA BTDC with error bars. Error bars show presented data are statically identical due to the error of measurement explained above.

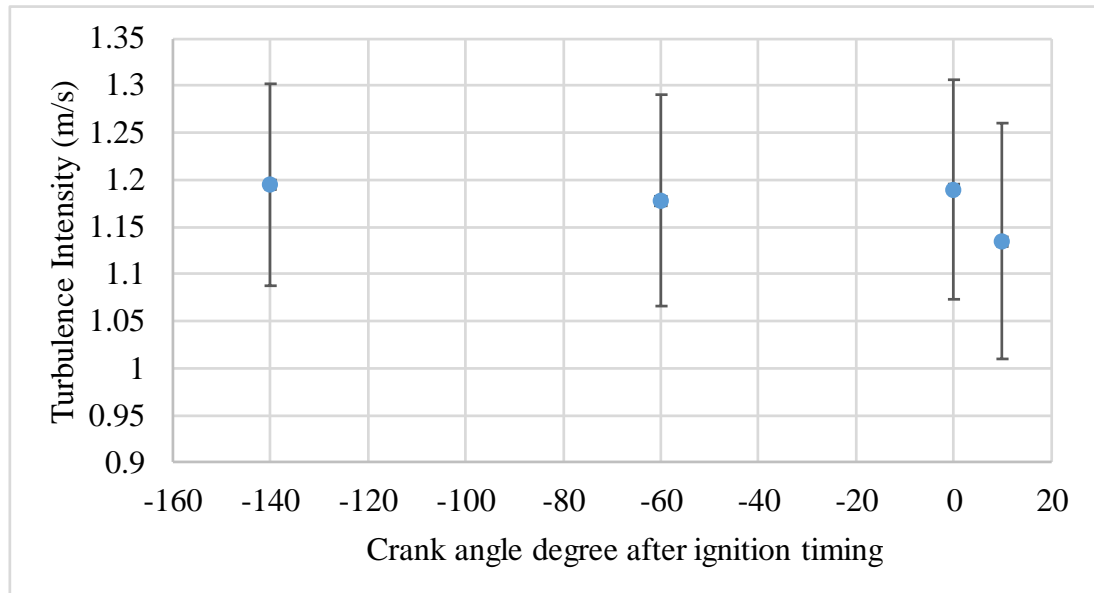


Figure 6.6. Variation of Turbulence intensity against Crank Angle at 1500 rpm.

Figure 6.7 displays the vector velocity fields at 90° CA BTDC, where all divided zones generally exhibited higher velocity when compared to 30° or 40° CA BTDC. Sparse vector was generated with Dantecstudio that used averaging of a sample over entire cycles, overall the image is good enough to pick up the bulk air motion which were of the concern of this study. Turbulence intensity data shows the highest value at Zone 1 (top left) whereas the lowest value is at the left exhaust valve zone (E1) with the dominant flow going toward the centre of the piston. Overall, the measured and predicted turbulence intensities computed in each zone were in good agreement. Shown in Figure 6.8 is the flow field velocity at 40° CA BTDC, which generally exhibited motion towards the centre of the piston below where the spark plug was located, with slightly higher overall turbulence intensity in comparison to 30° CA BTDC as shown in Figure 6.9. It was crucial to fully understand the flow at 40° CA BTDC because spark ignition happens at this crank angle. It can be seen that the PIV flow field showed no bulk motion toward the exhaust side of the piston and rather the flow was moving marginally toward the inlet valves. However, comparing turbulence intensities showed only a small noticeable difference in each studied field.

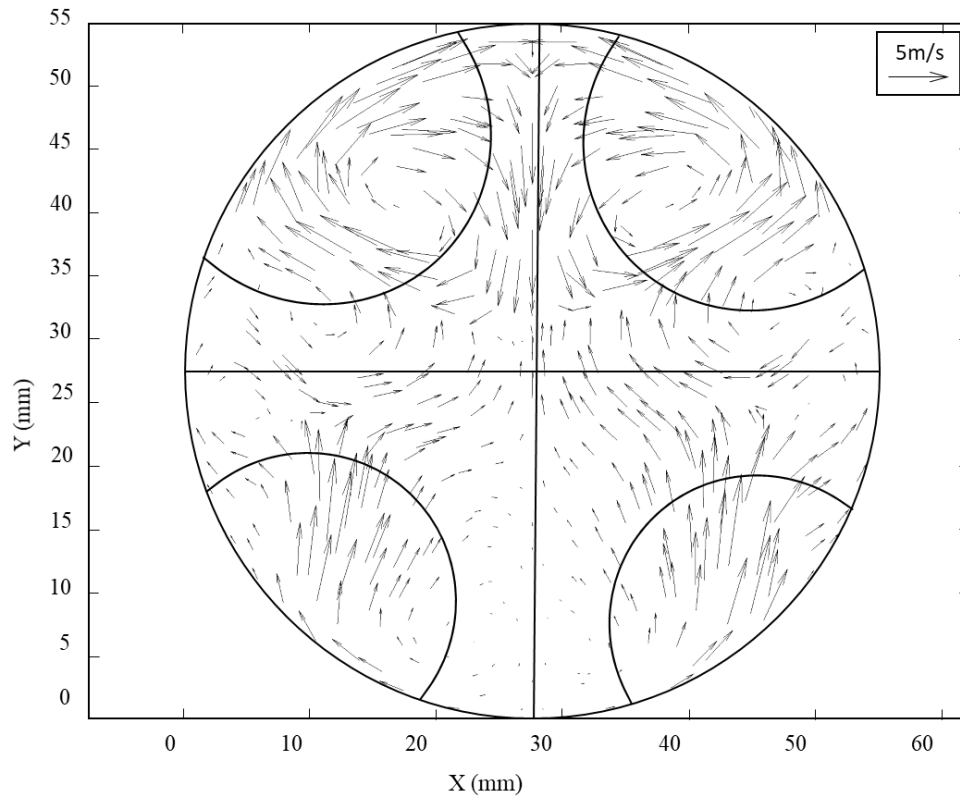


Figure 6.7. PIV Mean velocity field at 90° BTDC at 1500 rpm.

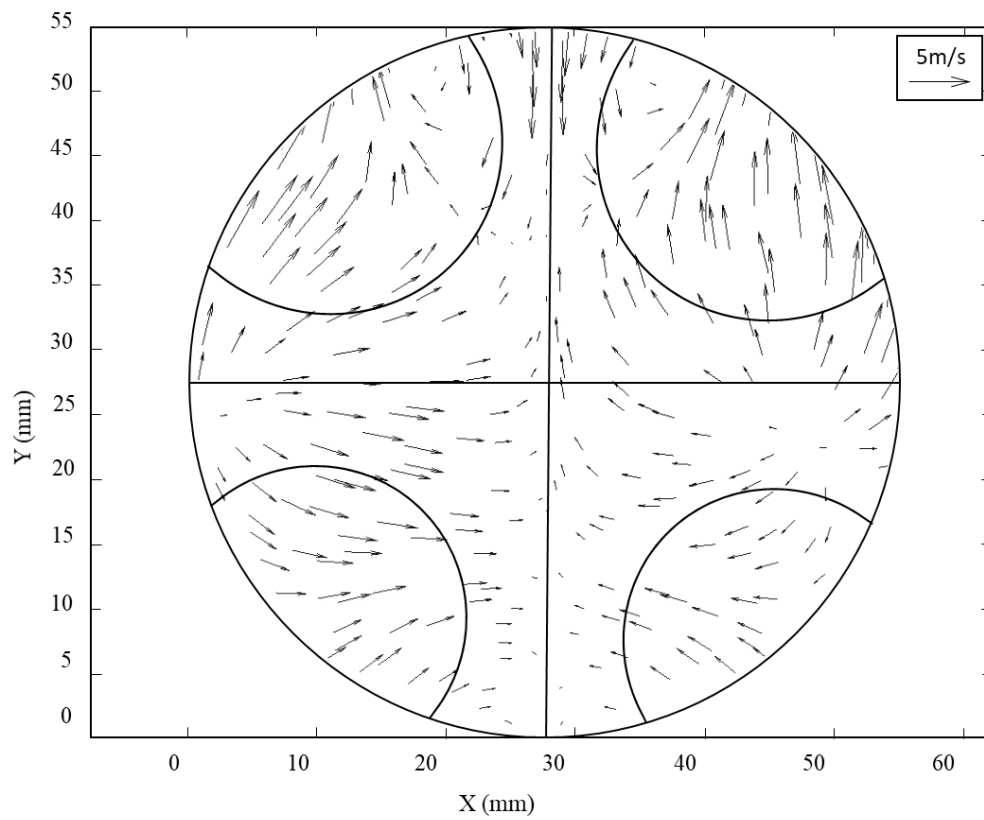


Figure 6.8. PIV Mean velocity field at 40° BTDC at 1500rpm.

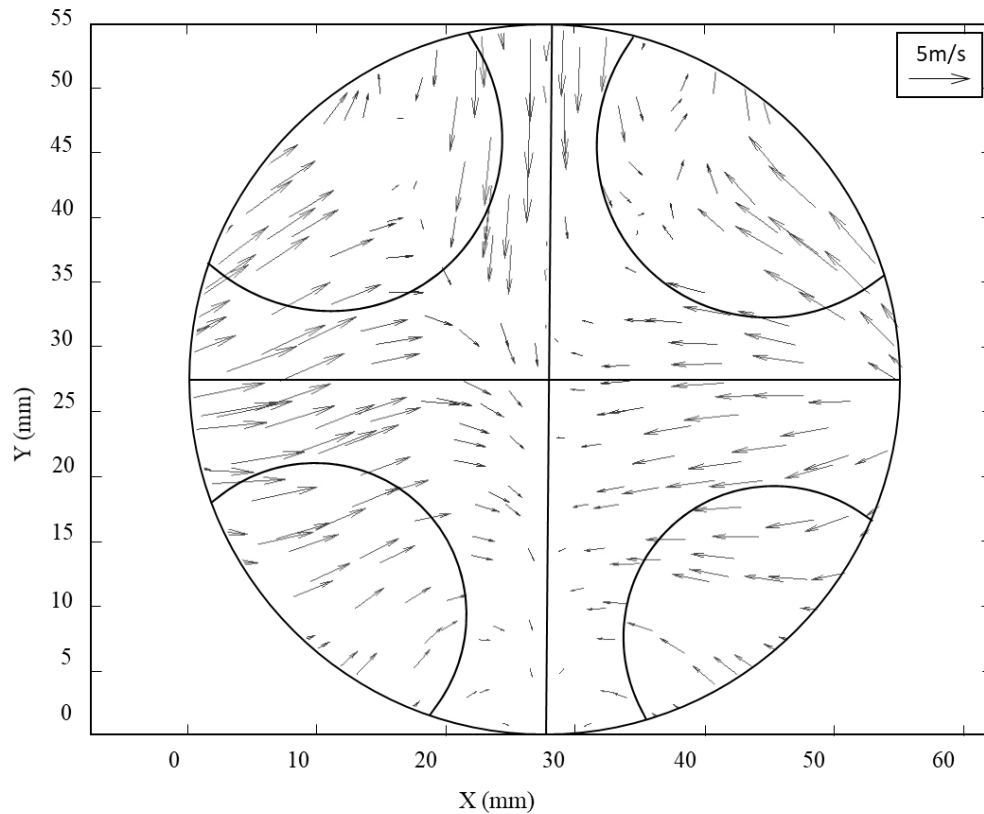


Figure 6.9. PIV Mean velocity field at 30° BTDC at 1500 rpm.

6.2.4 3-D Computational Fluid Dynamics

6.2.4.1 K-epsilon RNG

The calculations started from firing top dead, with inlet and exhaust valve lift motion profile were inputted in ICE engine inputs section alongside with engine connection rod length of 148mm, crank radius of 42mm, and engine speed of 1500 rpm. In order to account for any flow initialisation effects, the model was run for 4 complete cycles until cycle-to-cycle convergence was achieved for the in-cylinder quantities (e.g. pressure, velocity field, turbulent kinetic energy, etc.). Ideal gas properties for air were used throughout the simulation. Boundary conditions for inlet were as follows, inlet pressure were set to 0.5 bar gauge pressure, and inlet temperature was set to 300K. The maximum iterations per time step was set to 50 as showed in Figure 6.11, the number of time steps was set to 2960 calculated from the number of crank angles to run.

Shown in Figure 6.12 is the mean velocity vectors located at 180° CA BTDC measured at 10mm below the spark plug where the laser sheet was located for PIV measurements, it is evident that the overall flow is toward the inlet valves as indicated

in the figure. There seems to be a swirl flow on the top side of the piston, however, the modelling data was not sufficient to investigate flow entirely to see the effect of swirl on both sides. This was because the CFD model was only simulating one side of the piston (the other half was not modelled). The Mirror function was used to produce the other side of the piston for a better understanding of the piston geometry and to be comparable with the PIV flow mentioned in the previous section.

Mean velocity vectors at 90° CA BTDC shown in Figure 6.13 indicate flow heading toward the exhaust side of the piston with a swirl flow moving toward the side of the piston located near the inlet valves. Overall the main visible structure seems to have less velocity in comparison to flow at 180° CA BTDC.

Computational Fluid Dynamics analysis indicates the main visible structure of the flow at 40° CA BTDC (Spark Timing) is toward the centre of the piston. The bulk flow structure is stabilized and maintained for the rest of the intake stroke. This can be seen from Figure 6.14 and 90° CA BTDC. This would be expected as the mass flow rate should be stabilized around that point.

Flow structures after ignition were also important. Figure 6.15 shows the flow going toward the centre of the piston with an apparent swirl flow on the top. It can also be seen at the top section of the piston (where inlet valves are located) flow is apparently heading toward the side of the piston.

Overall the flow fields at 30° and 40° CA BTDC showed no bulk motion toward the exhaust. A prior researcher has indicated adequate charge homogeneity with the same engine [110] although some caution is required given the idealized nature of the modelling approach. Presented in Figure 6.10 is the average velocity data against crank angle degree before top dead centre, it can be seen that the highest velocity was achieved at 30° CA BTDC and the lowest was at bottom dead centre with the value of 3.62 and 3.12 m/s respectively.

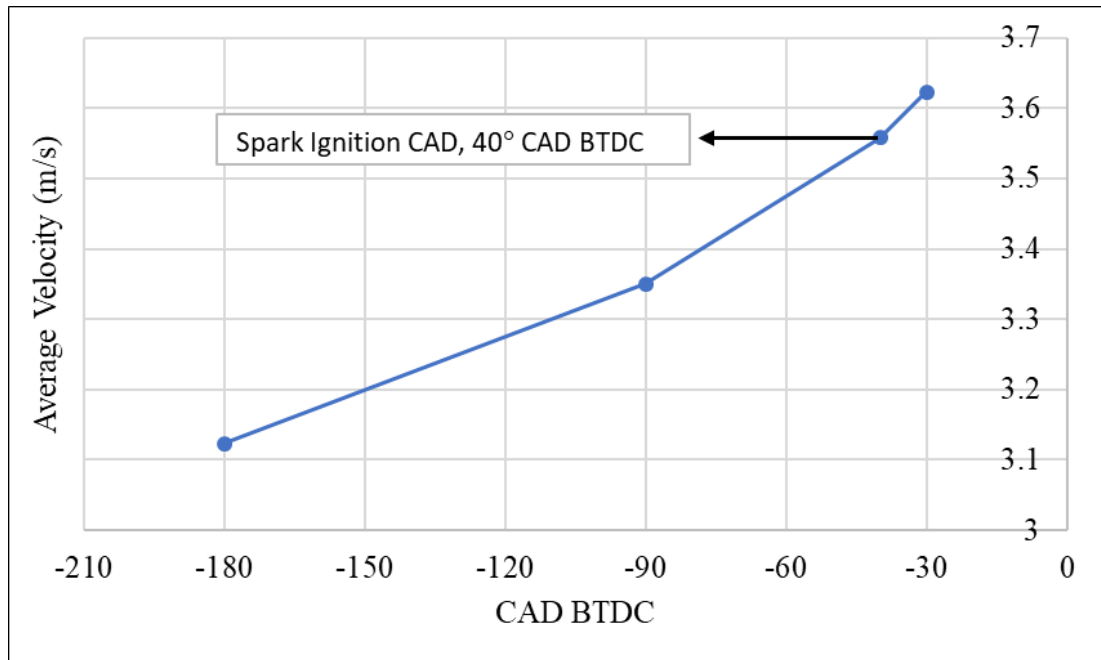


Figure 6.10. PIV measurement of the variation of average velocity against crank angle degree. Measured at 10mm below the spark plug where the laser sheet was located.

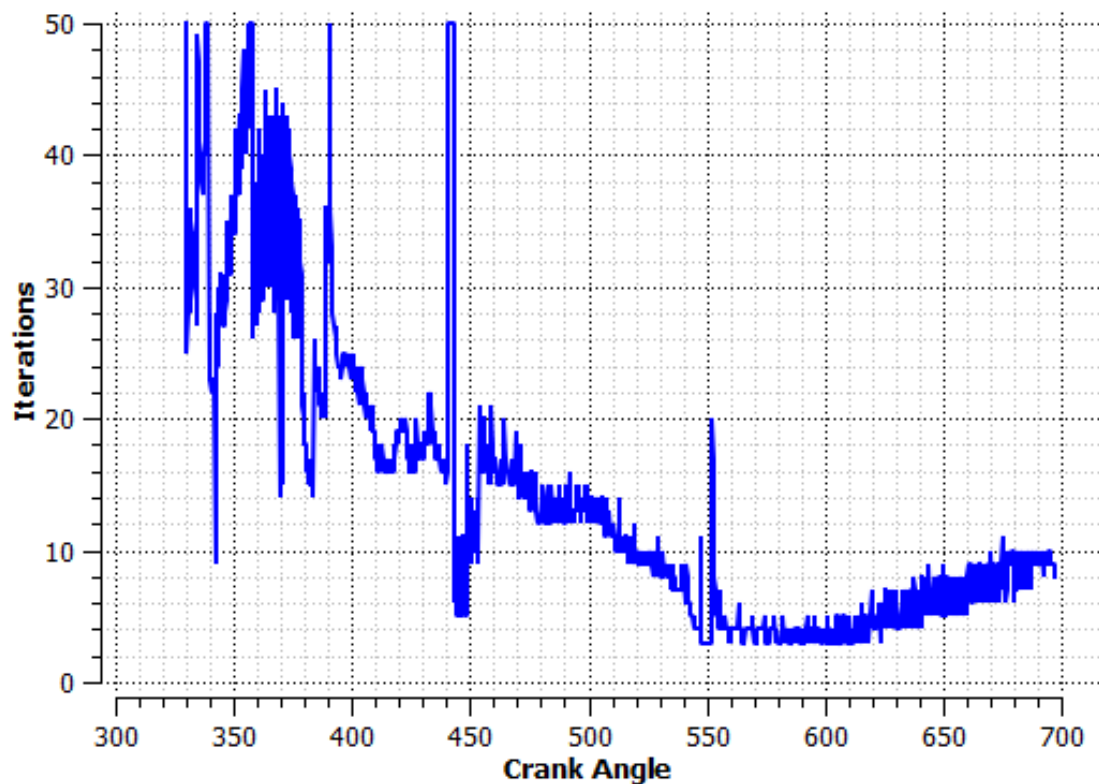


Figure 6.11. Number of iterations per time step is shown at each crank angle degrees.

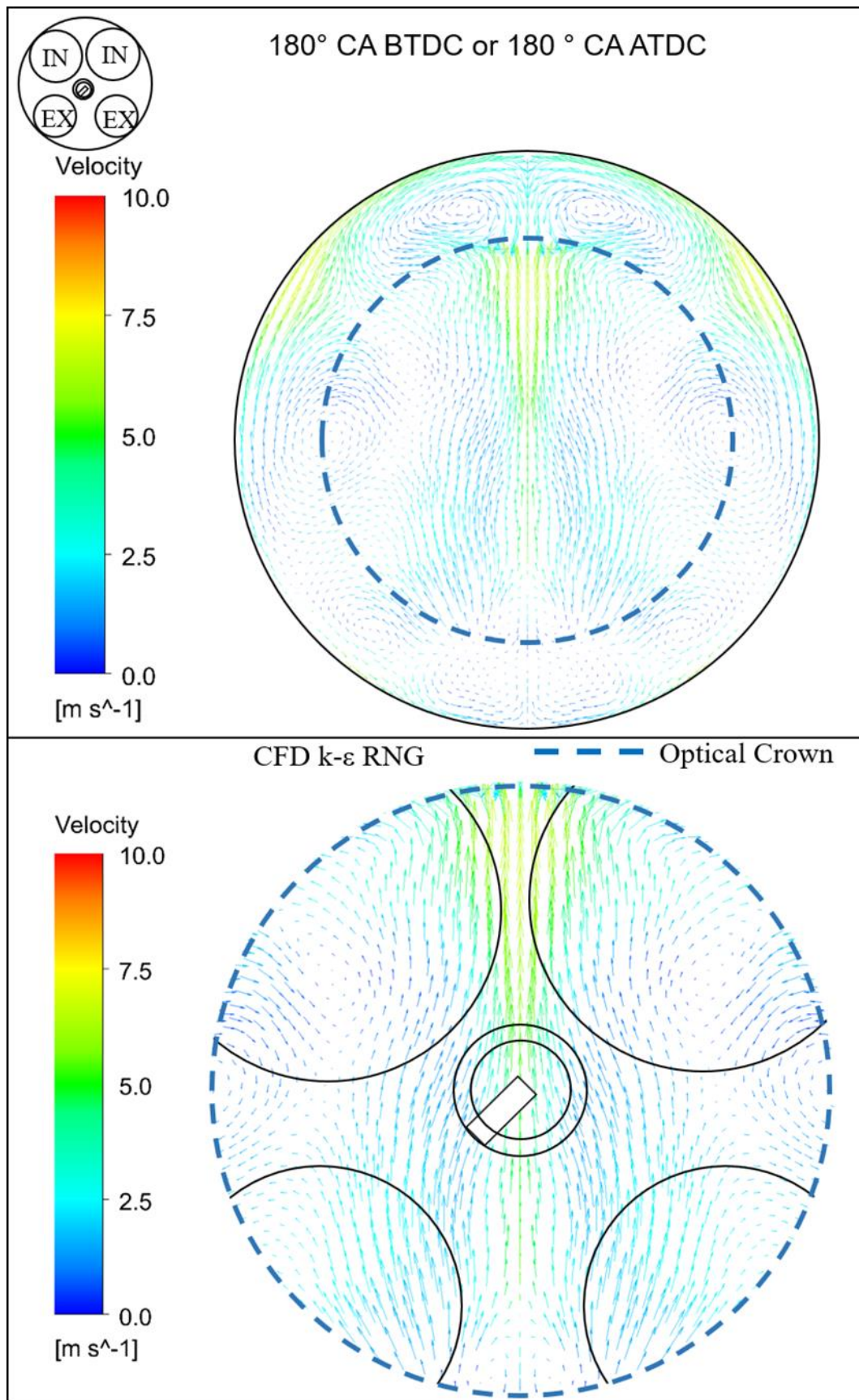


Figure 6.12. Velocity fields on the horizontal plane using $k-\epsilon$ RNG at 180° CA BTDC. Measured at 10mm below the spark plug where the laser sheet was located for PIV measurements.

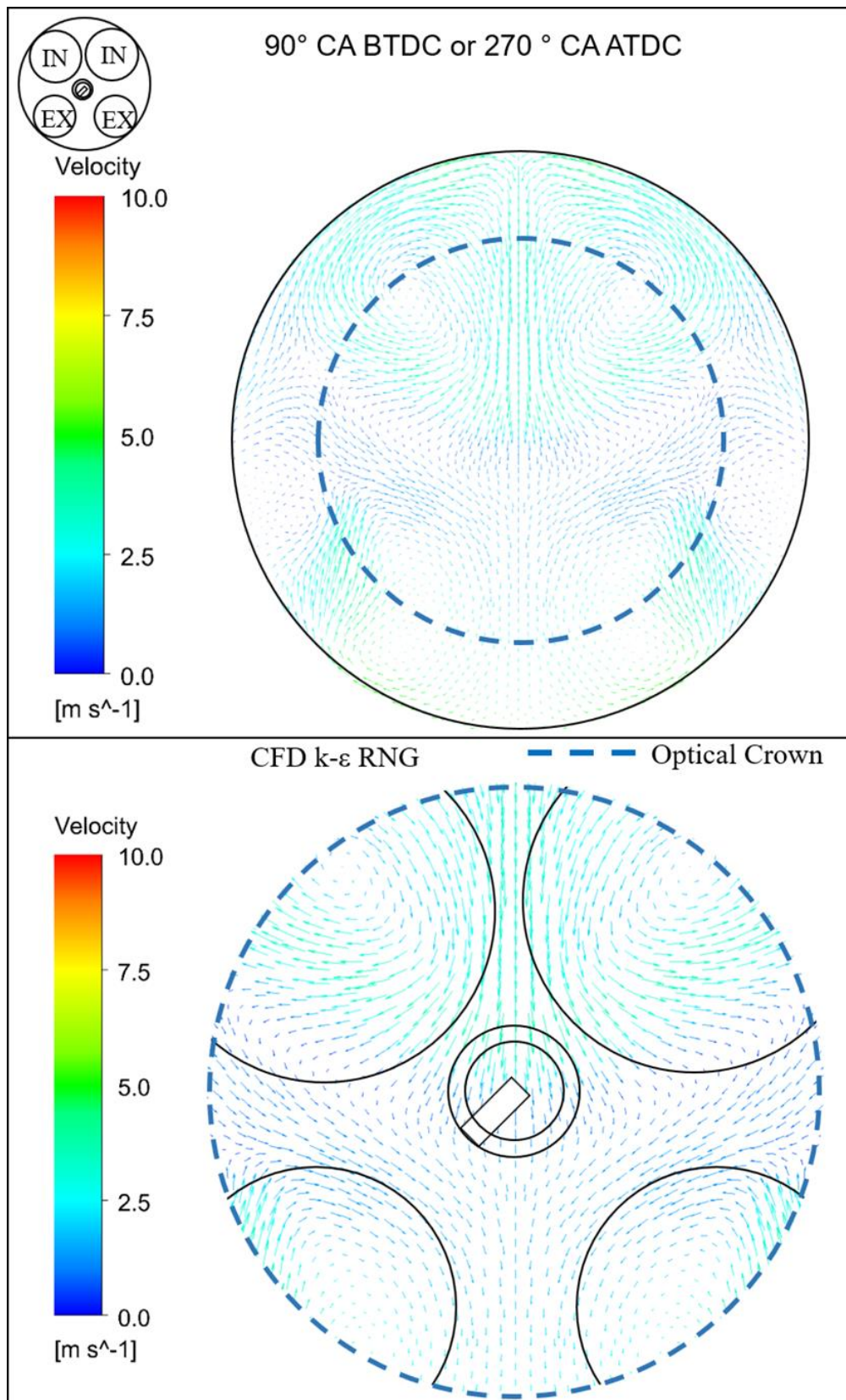


Figure 6.13. Velocity fields on the horizontal plane using $k-\epsilon$ RNG at 90° CA BTDC. Measured at 10mm below the spark plug where the laser sheet was located for PIV measurements.

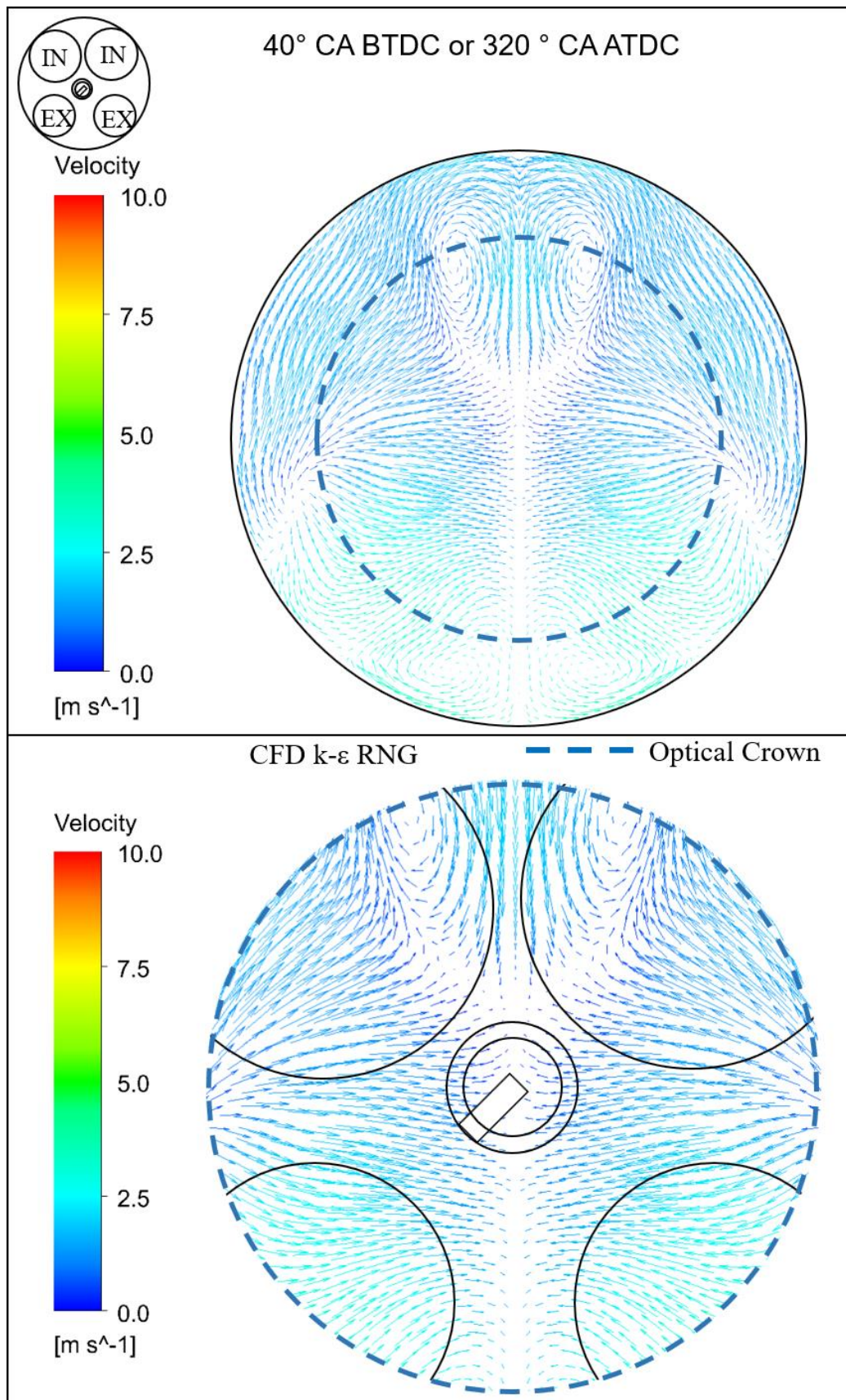


Figure 6.14. Velocity fields on the horizontal plane using $k-\epsilon$ RNG at 40° CA BTDC. Measured at 10mm below the spark plug where the laser sheet was located for PIV measurements.

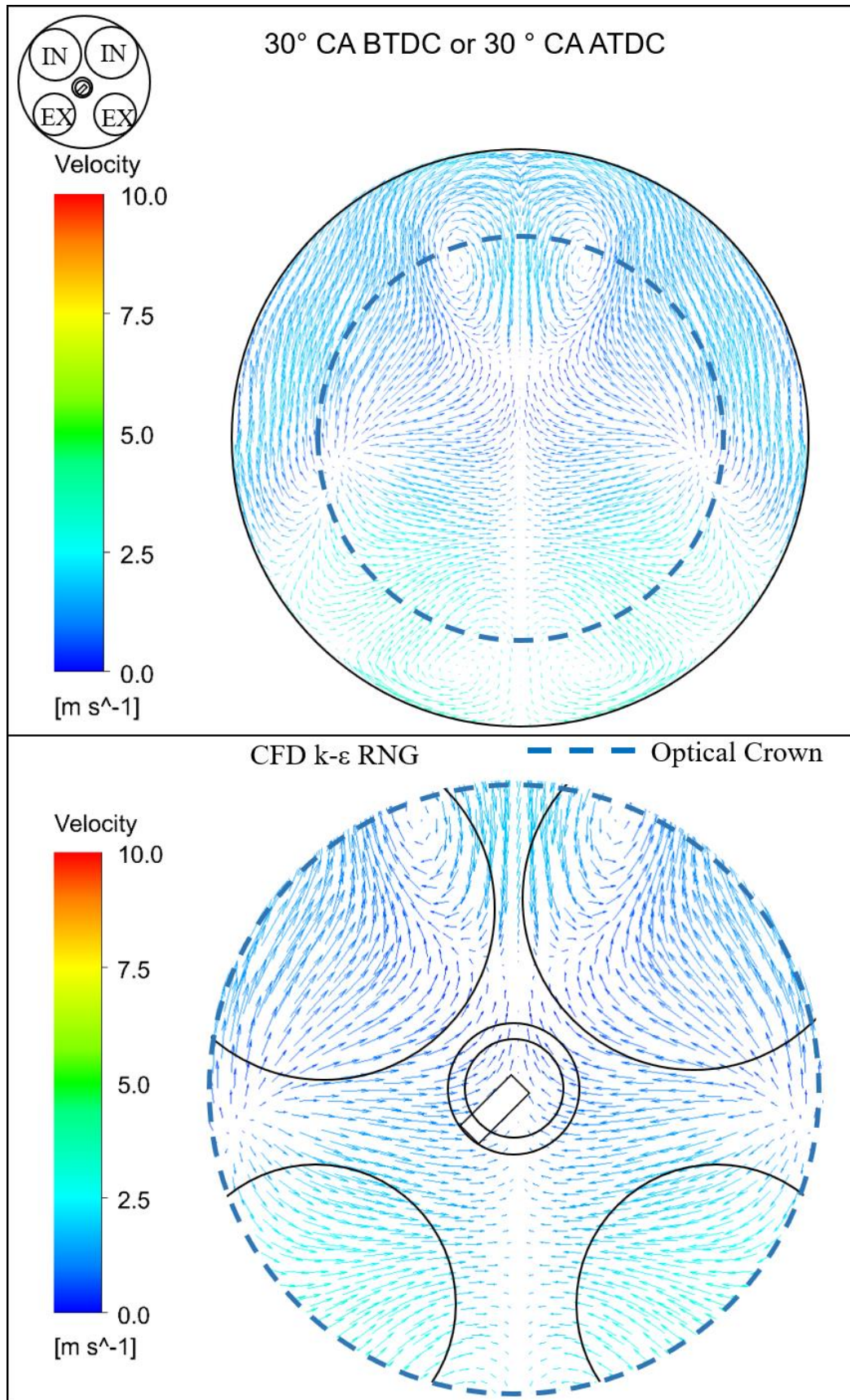


Figure 6.15. Velocity fields on the horizontal plane using $k-\epsilon$ RNG at 30° CA BTDC. Measured at 10mm below the spark plug where the laser sheet was located for PIV measurements.

6.2.4.2 K-epsilon Predictions

Shown in Figure 6.16 is Computational fluid dynamics mean velocity vectors at 180° CA BTDC produced using the k- ϵ model. It can be seen that the overall flow is toward the inlet valves with a swirl around the middle of the piston. Again, it is important to recall that the CFD model was only simulating one side of the piston. Computational fluid dynamics velocity vectors at 90° CA BTDC using the k- ϵ model are shown in Figure 6.17. The flow seems to be going toward the exhaust side of the piston with two apparent swirl flows moving toward the centre and side of the piston located near the inlet valves. The overall main visible structure appeared to have less velocity in comparison to the flow at 180° CA BTDC.

Computational fluid dynamics analysis indicates the main visible structure of the flow at 40° CA BTDC (Spark Timing) is toward centre of the piston, however, small swirl spotted around the inlet valves, pushing the flow toward spark location. It seems that for this plane in Figure 6.18, from 90° CA BTDC, the bulk flow structure is stabilized and maintained for the rest of the intake stroke, this would be expected as the mass flow rate should be stabilized around that point.

Figure 6.19 showing the flow going toward the centre of the piston with three spotted swirl flows on the top, left and bottom side of the piston. It can also be seen swirl flow at the top section of the piston where inlet valves are located are going toward the side of the piston. It is also worth noting at this point that as the piston tends towards top dead centre, with the PIV plane of interest fixed 10mm below the combustion chamber “fireface”, the PIV technique becomes impossible to implement as the side windows were covered by the piston.

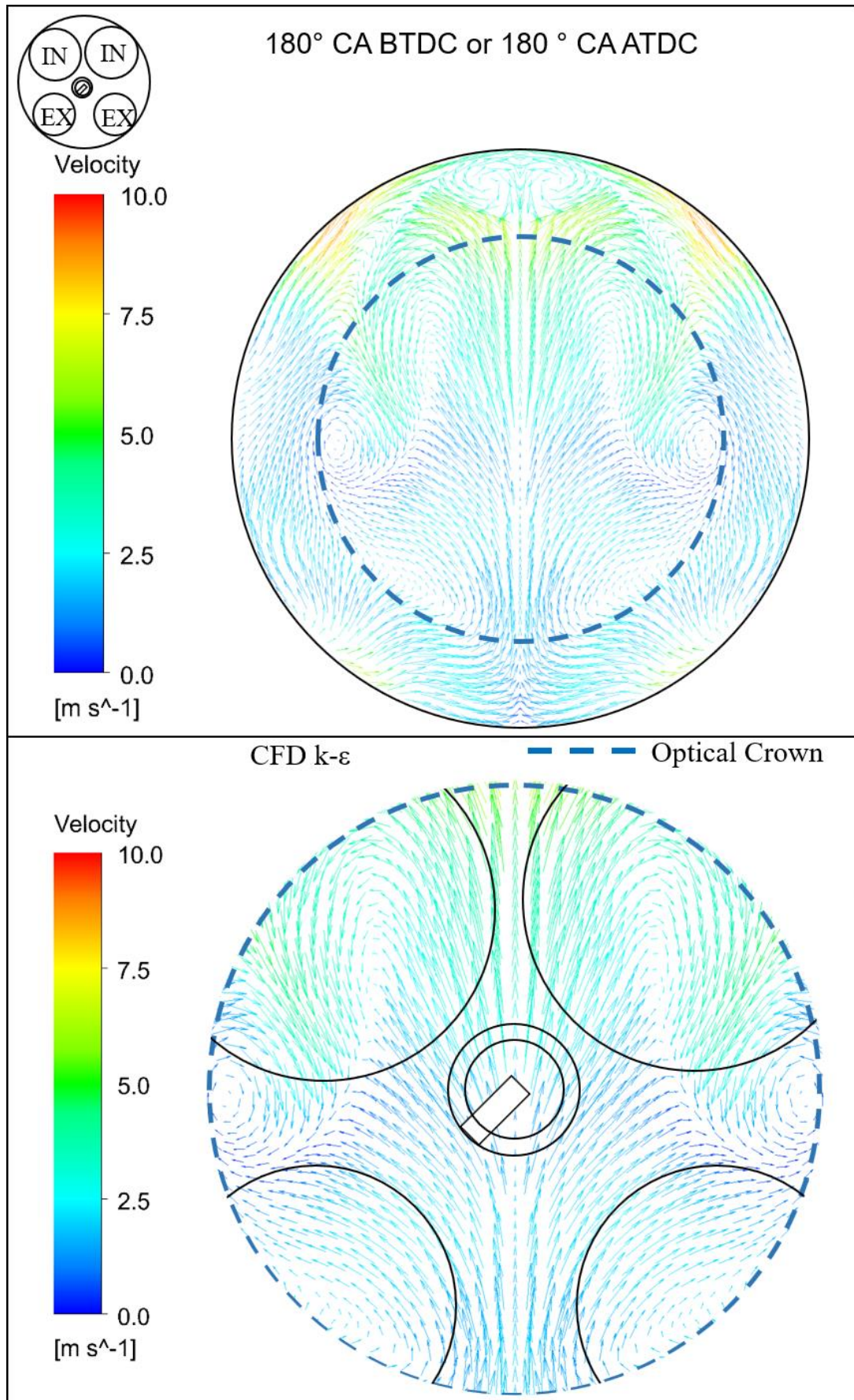


Figure 6.16. Velocity fields on the horizontal plane using k-ε at 180° CA BTDC.

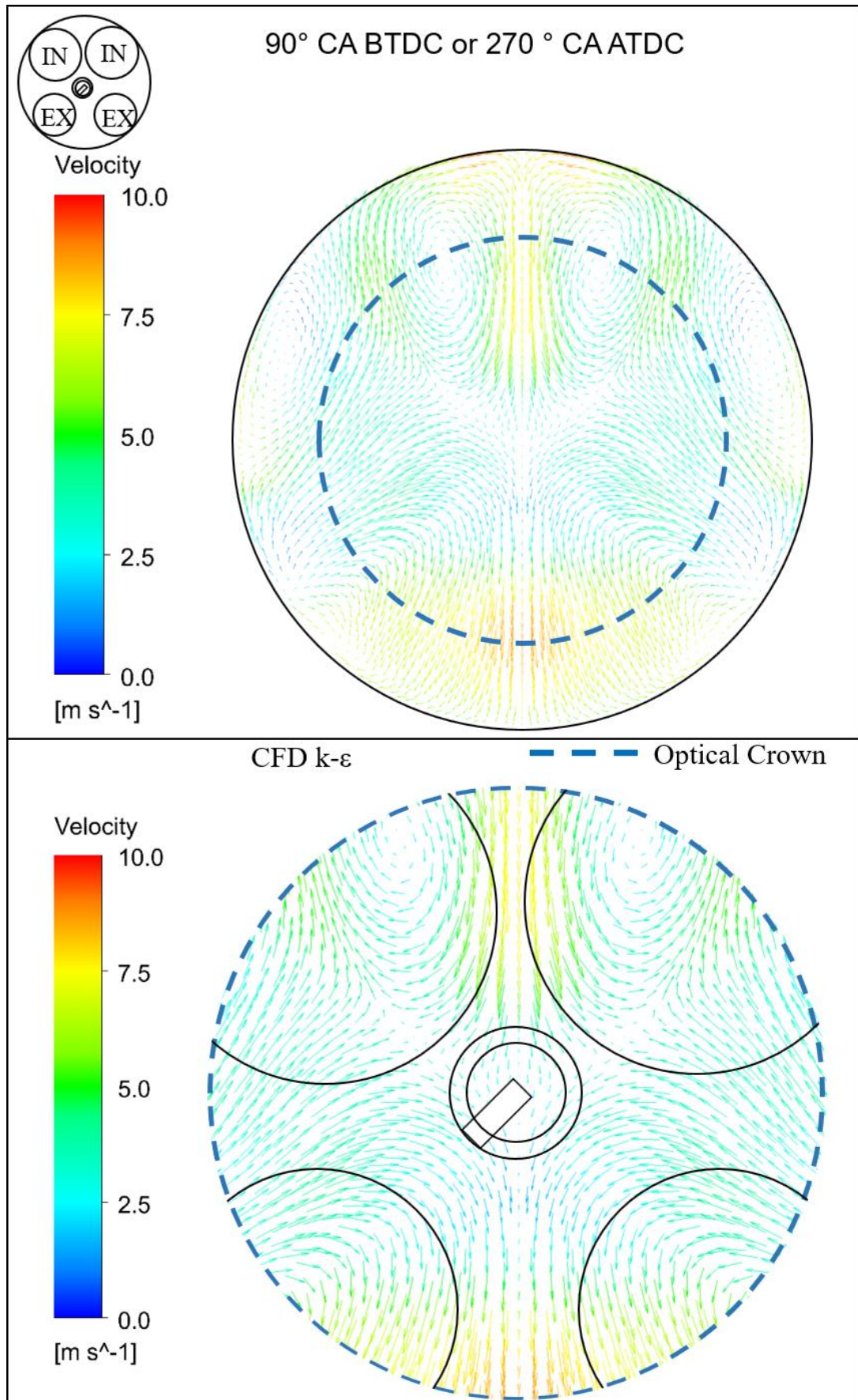


Figure 6.17. Velocity fields on the horizontal plane using k-ε at 90° CA BTDC

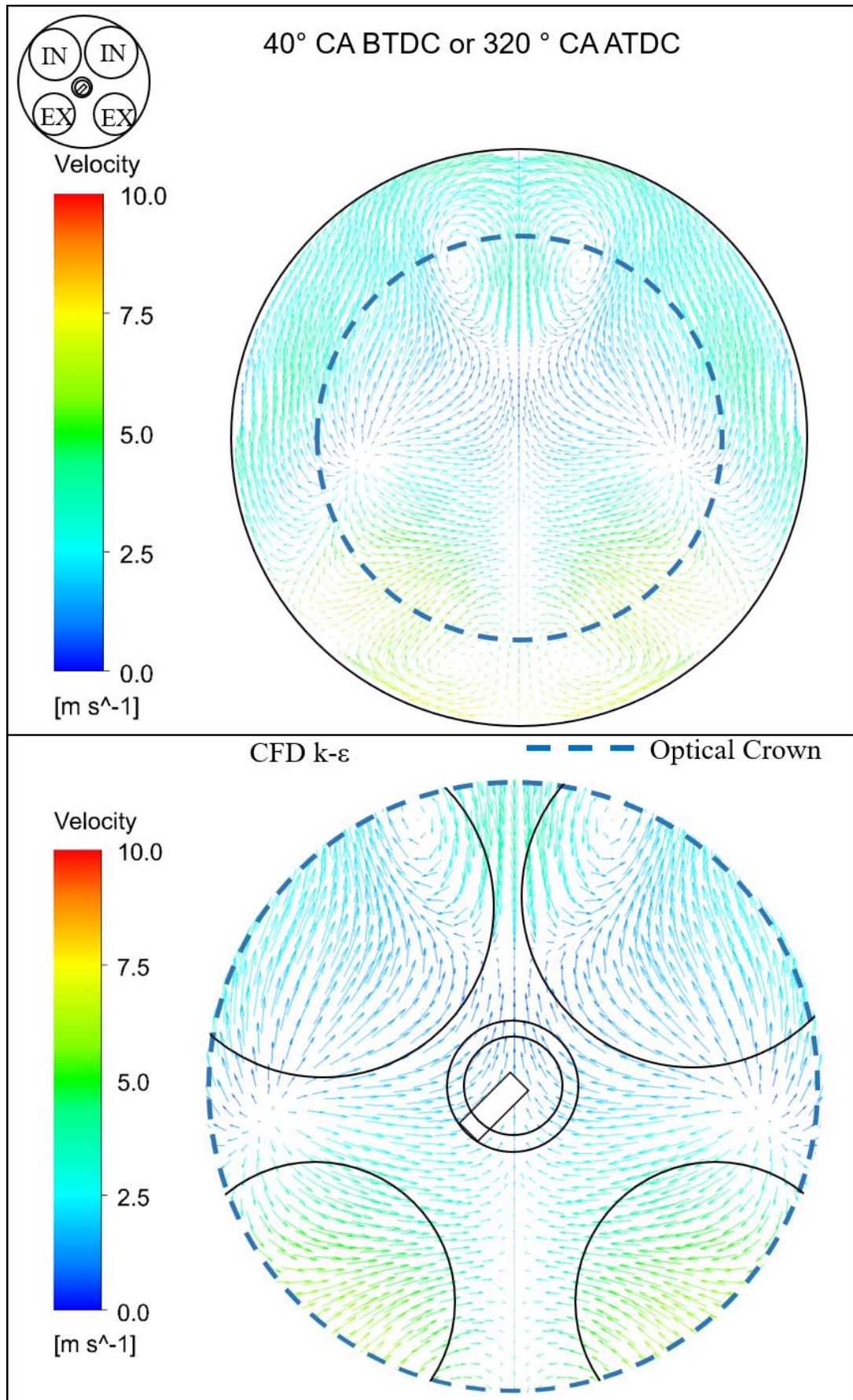


Figure 6.18. Velocity fields on the horizontal plane using k- ϵ at 40° CA BTDC.

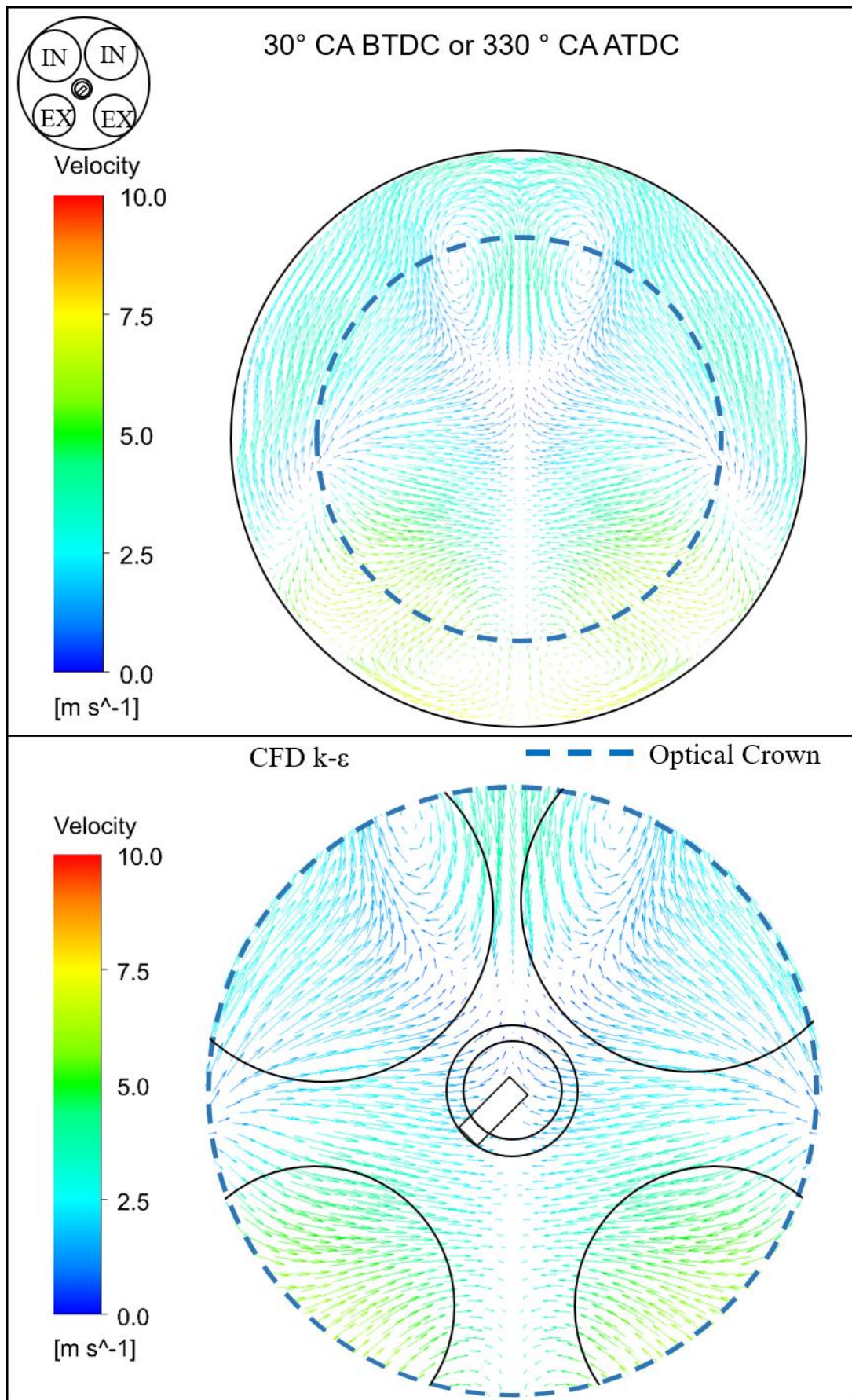


Figure 6.19. Velocity fields on the horizontal plane using k- ϵ at 30° CA BTDC.

6.2.4.3 A comparison between K- ϵ and K- ϵ RNG

Shown in Figure 6.20 to Figure 6.23 is the comparison between the computational fluid dynamics models. It can be seen that the flow structure at 180 ° CA BTDC showed very similar patterns. The two turbulence models do not reveal any major differences. Apart from the clear discrepancy in velocity magnitude, the overall average velocity magnitude of k-epsilon is about 6.24 m/s compared to 5.05 m/s for the k-epsilon RNG turbulence model. A clear discrepancy in both flow structures and velocity magnitudes can be seen in Figure 6.21 considering the flow structure at 90 ° CA BTDC. The K-epsilon turbulence model shows higher swirl in the vicinity of inlet valves also visible within the optical crown. In addition, overall average velocity magnitude was approximately 10% higher for k-epsilon turbulence model. The flow structures are very similar for both 30° and 40° CA BTDC. The only difference being flow near the exhaust valve for both crank angle degrees apparently heading towards the centre and upward in k-epsilon compared to going toward the centre in the k-epsilon RNG. Moreover, a notable average velocity magnitude of almost 7% variation was observed, the average velocity magnitude using k-epsilon is 4.81 m/s whereas k-epsilon turbulence model computed a 4.5 m/s average velocity magnitude.

In conclusion, a direct comparison between the two turbulence models does not reveal any major differences, apart from the discrepancy in both flow structures and velocity magnitudes at the earliest timing of 180° and 90° CA BTDC. K-epsilon RNG turbulence model is slightly better in agreement with the measured data from PIV as discussed in the next section. Hence it might be concluded that the Re-Normalisation Group theory was better inflow estimation and better represented the flow structure, especially very close to ignition timing around 30° and 40° CA BTDC. RNG was therefore considered the better turbulence model and was used to compare with the PIV results, as explained in the next section. The K-epsilon RNG method is considered a robust method preferred over k-epsilon by many researchers especially estimating the flow where maximum intake valve lift is located, further detail of this study can be found here [18].

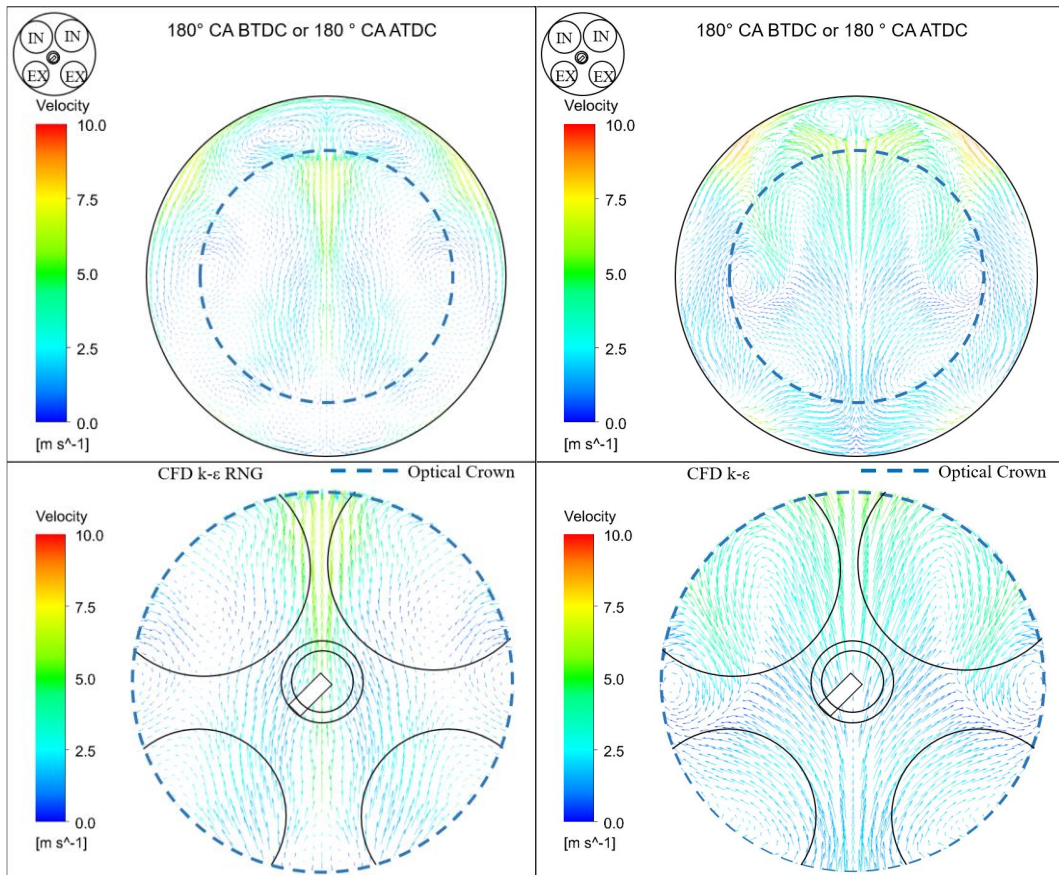


Figure 6.20. k- ϵ and k- ϵ RNG (on the left) CFD at 180° CA BTDC.

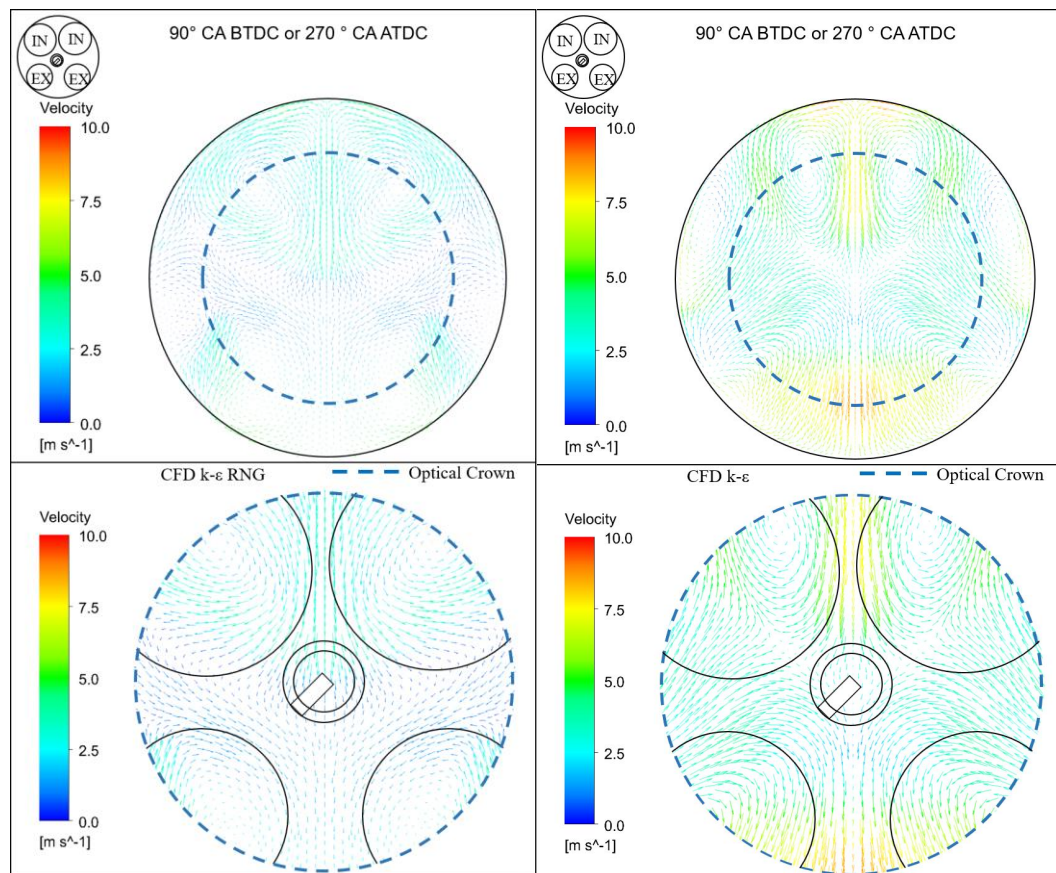


Figure 6.21. k- ϵ and k- ϵ RNG (on the left) CFD at 90° CA BTDC.

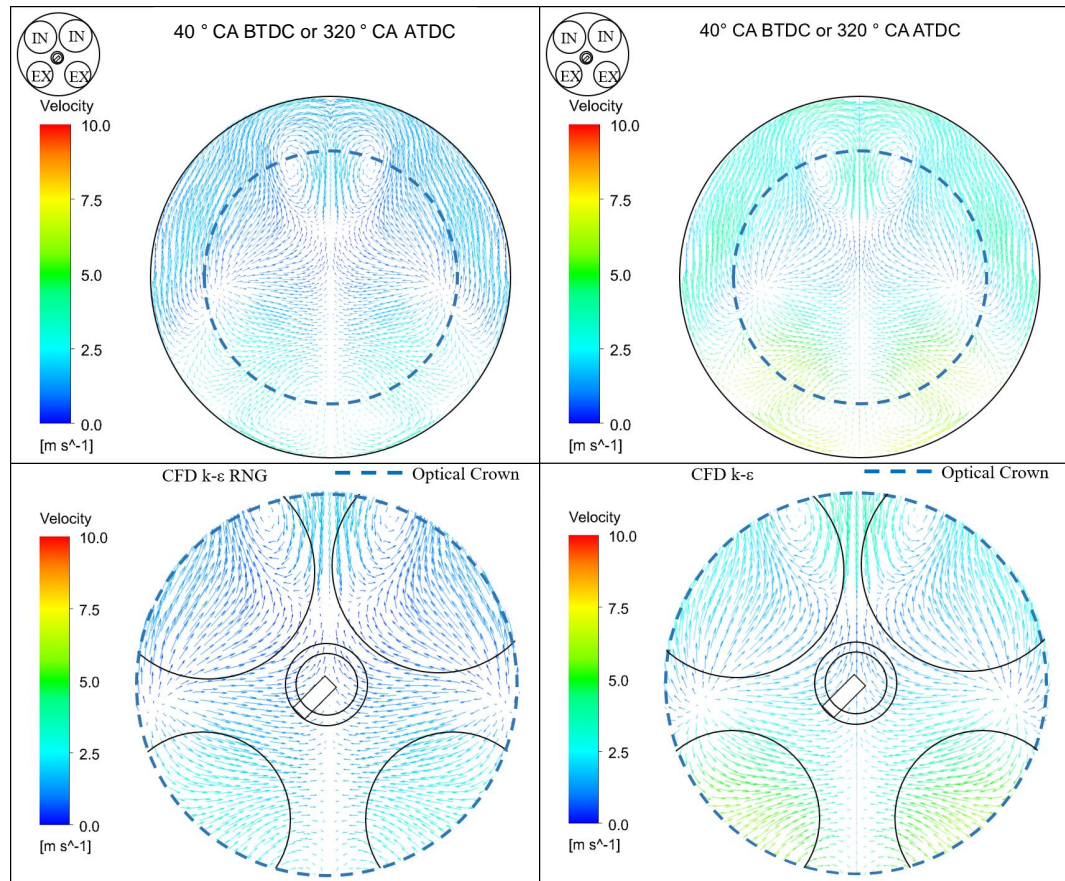


Figure 6.22. $k-\epsilon$ and $k-\epsilon$ RNG (on the left) CFD at 40° CA BTDC.

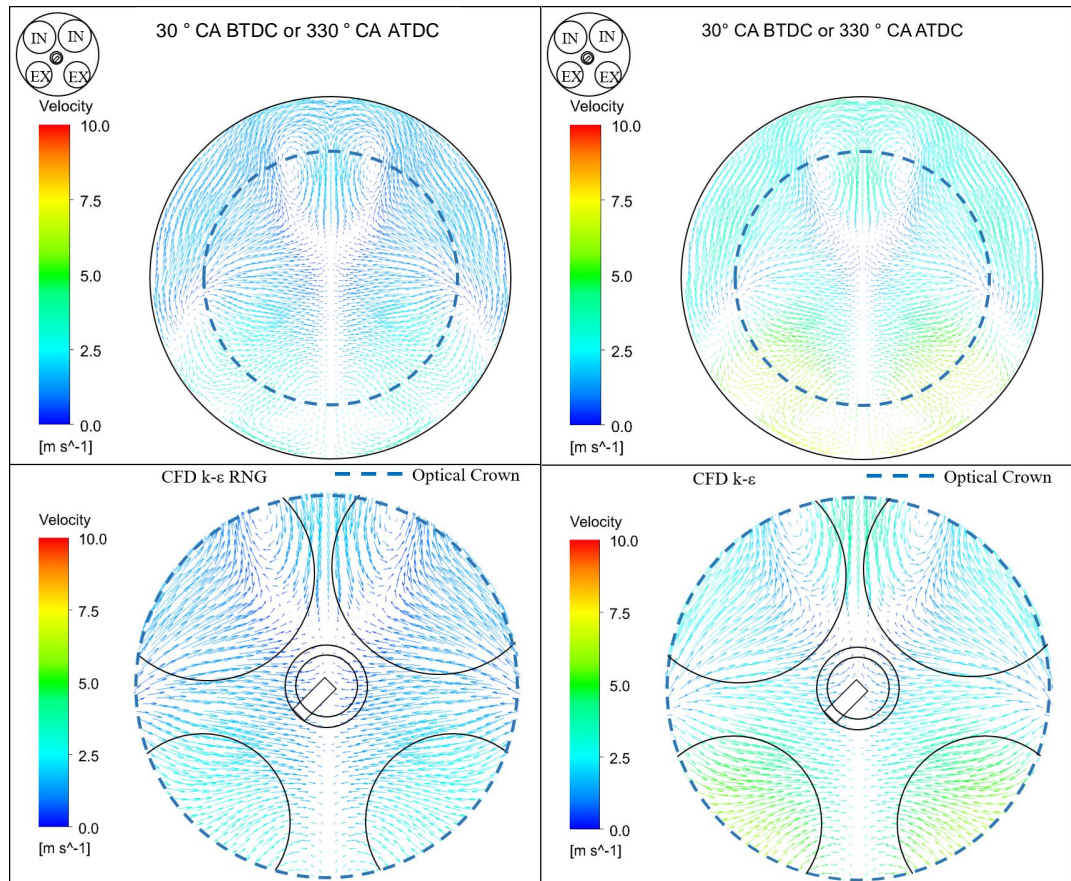


Figure 6.23. $k-\epsilon$ and $k-\epsilon$ RNG (on the left) CFD at 30° CA BTDC.

Comparison between the two turbulence models does not reveal any major differences, apart from the clear discrepancy in velocity magnitudes at spark ignition and 10° after spark ignition. Hence a vector magnitude comparison of two turbulence models for 30° and 40° bTDC is shown in Figure 6.24 where the mean velocity field divided into 5 by 5 grid (total of 25 zones). This comparison is further presented in Figure 6.25 that shows the calculated magnitude velocity of each zone for CFD (k-epsilon) on X-axis and CFD (k-epsilon RNG) on the Y-axis. It can be seen that k-epsilon turbulence model magnitude velocities are higher than Re-Normalisation Group (RNG) turbulence model data by almost 10% and are showing very similar flow.

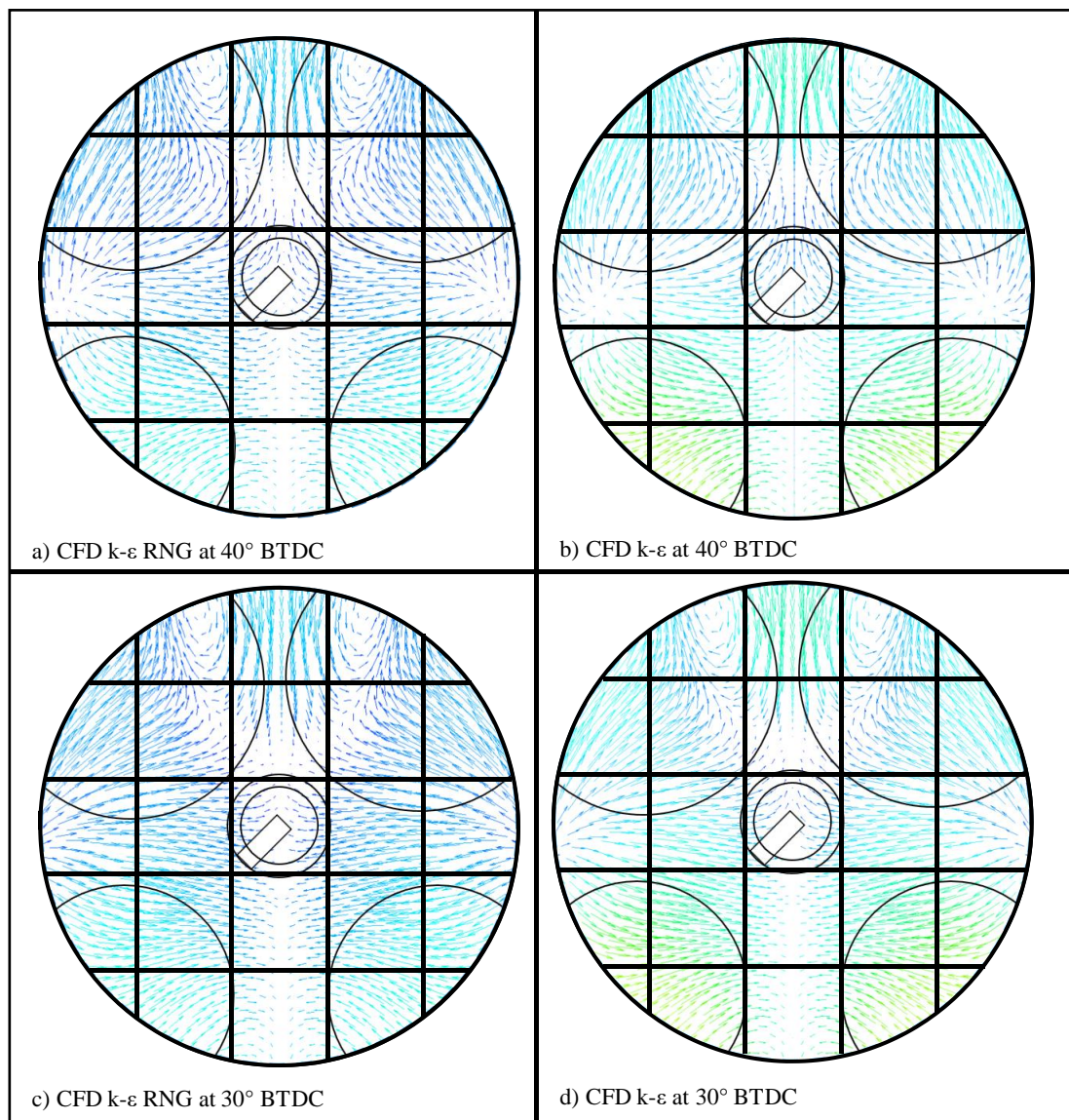


Figure 6.24. CFD k- ϵ and k- ϵ RNG mean velocity field divided into 25 zones. a) CFD k- ϵ RNG mean velocity field at 40° BTDC, b) CFD k- ϵ mean velocity field at 40° BTDC, c) CFD k- ϵ RNG mean velocity field at 30° BTDC, and d) CFD k- ϵ mean velocity field at 30° BTDC.

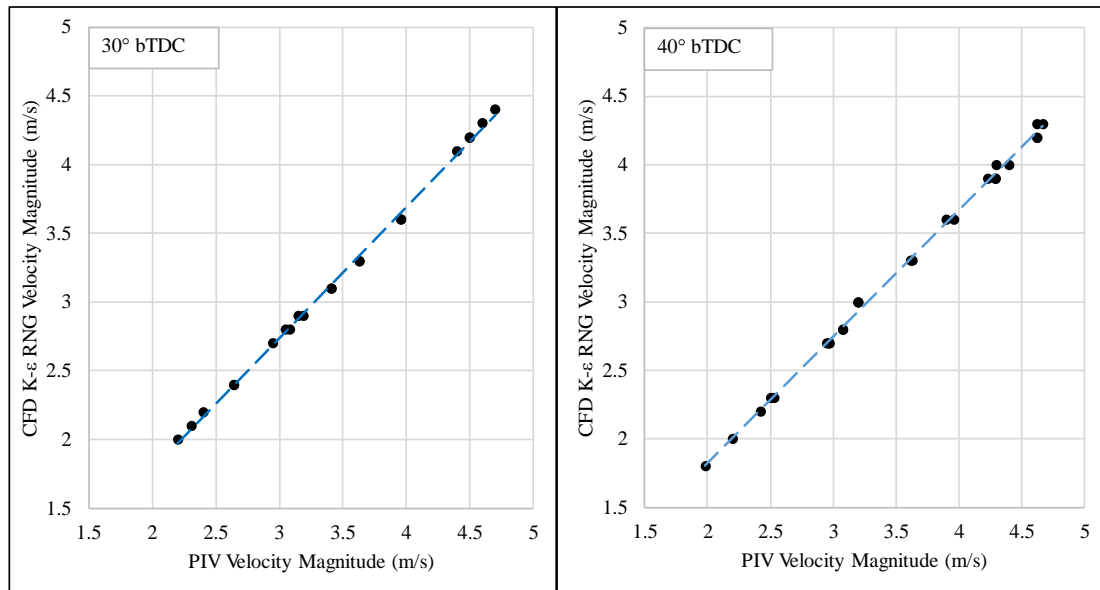


Figure 6.25. Comparison between two turbulence methods CFD (k-epsilon RNG) and CFD (k-epsilon), showing magnitude velocity for 30° (left) and 40° bTDC (right).

The 3-D CFD computations with the two different turbulence models predicted very similar in-cylinder flow motion and structure. Both models predicted higher values of maximum velocities on all measured planes in comparison to PIV. However, at specific crank angles, especially soon after BTDC and up to mid compression stroke, or even late compression stroke, the RNG model showed slightly better agreement with the measured data.

6.2.5 A Comparison between PIV and CFD

Shown in Figure 6.26 is the comparison of k-epsilon RNG computational fluid dynamics mean velocity vectors with Particle Image Velocimetry data obtained from Matlab analysis. It can be seen from the CFD data that the overall flow at 180° CA BTDC is toward the inlet valves located on the top side of the piston. Data obtained from PIV at the same crank angle degree shows an overall flow toward the top side of the piston with a marginal shift toward the piston wall. CFD data at 90° CA BTDC are in a good agreement with PIV velocity measurements with the only major difference being at the bottom side of the piston. PIV velocity data shows a flow trend toward the upper side whereas CFD data shows a flow going toward the centre and bottom side of the piston. This contradiction might be because of the nature of the modelling approach. Section c) of Figure 6.26 demonstrates a very similar flow pattern between CFD and PIV data at 40° CA BTDC (spark ignition timing). The only noticeable difference is around the top right side (zone I2) where PIV data shows the dominant flow towards the centre of the piston whereas CFD analysis shows a swirl flow pattern toward the bottom side of the centre. The mean magnitude velocity of CFD data is approximately 7% higher than PIV data.

Shown in section d) is data obtained from PIV and CFD at 30° CA BTDC. Overall the flow structure seems to be similar except the flow pattern on top right side (zone I2). Flow from PIV shows a tendency toward the upper side whereas CFD data shows a pattern toward the centre and upper side of the piston. This could be because of the nature of CFD modelling as the symmetrical piston is limited to flow simulation only on one side of the piston. In general, the air flow structure visible from the optical window of the piston crown follows coherent and discernable patterns that visually correlate reasonably well with the CFD results. Furthermore, for this plane, it can be seen that many major vortices appear, albeit the centre of these structures were at the edges of the PIV plane. It is noticeable that in each zone the values for turbulence intensities were very close as showed in Table 6.3, which emphasizes the fact that there was no bulk flow motion toward any side of the piston. This fact can also be seen within the CFD results although some caution is required given the idealized nature of the modelling approach. Further details on the CFD and PIV setup and procedures can be found in previous chapters.

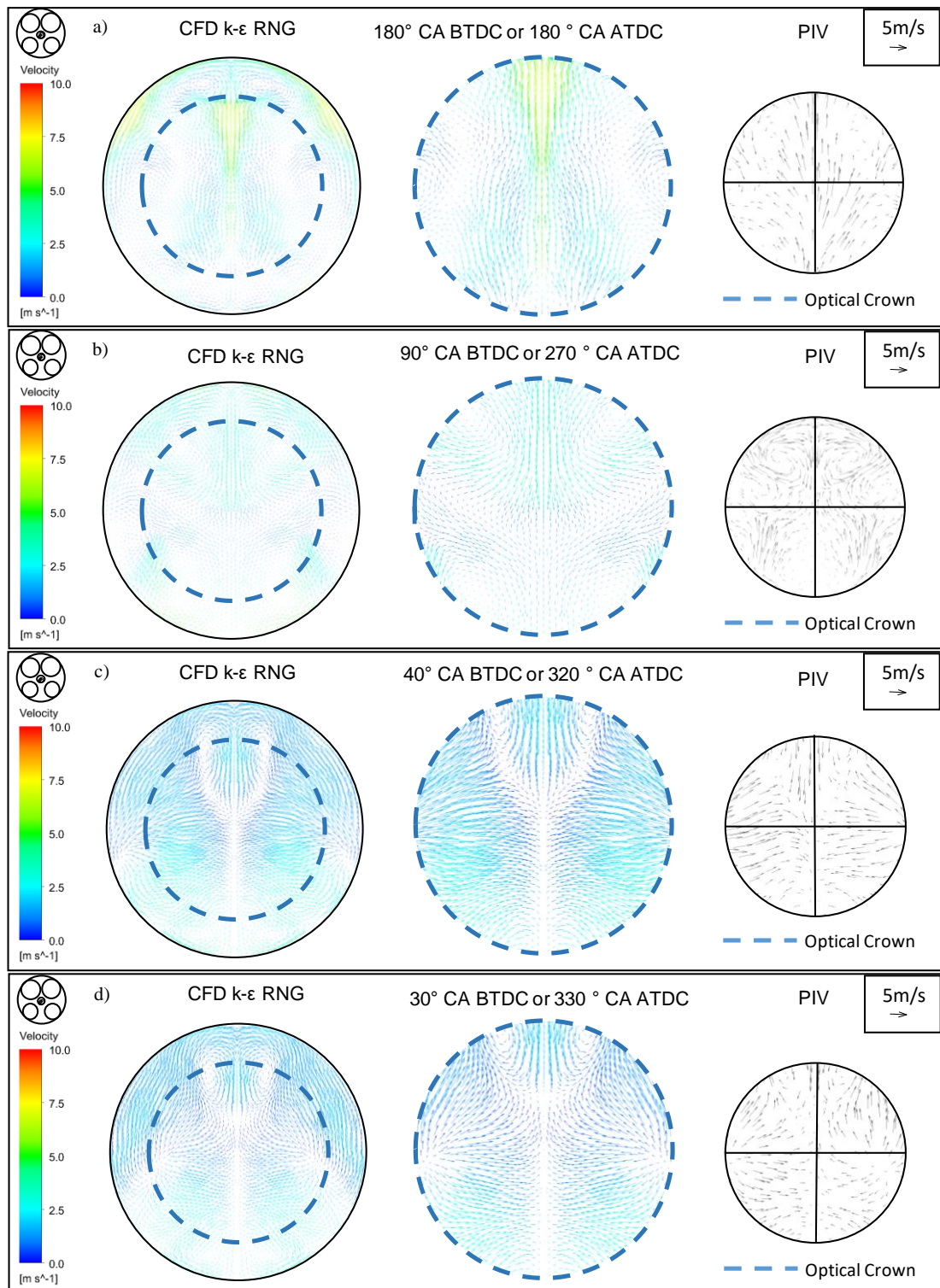


Figure 6.26. Mean velocity fields on the horizontal plane for CFD and PIV images.

It was imperative to further correlate CFD and PIV data for 40° bTDC where the ignition occurs, and 30° bTDC to validate the flow at these points. Hence an additional comparison of CFD and PIV for 30° and 40° bTDC is shown in Figure 6.27 where the mean velocity field divided into 5 by 5 grid (total of 25 zones).

This comparison is further presented in Figure 6.28 shows the calculated magnitude velocity of each zone for PIV on X-axis and CFD (k-epsilon RNG) on the Y-axis. It can be seen that CFD magnitude velocity are higher than PIV data by almost 7% and in a good agreement with each other, however at both 30° and 40° bTDC grids near the wall are showing the highest variance. It is important to note the CFD model was symmetrical so the difference between CFD and PIV cannot be fully validated. Moreover, zone 21(bottom left) and 25 (bottom right) were ignored as the velocity vectors were not available in the PIV data.

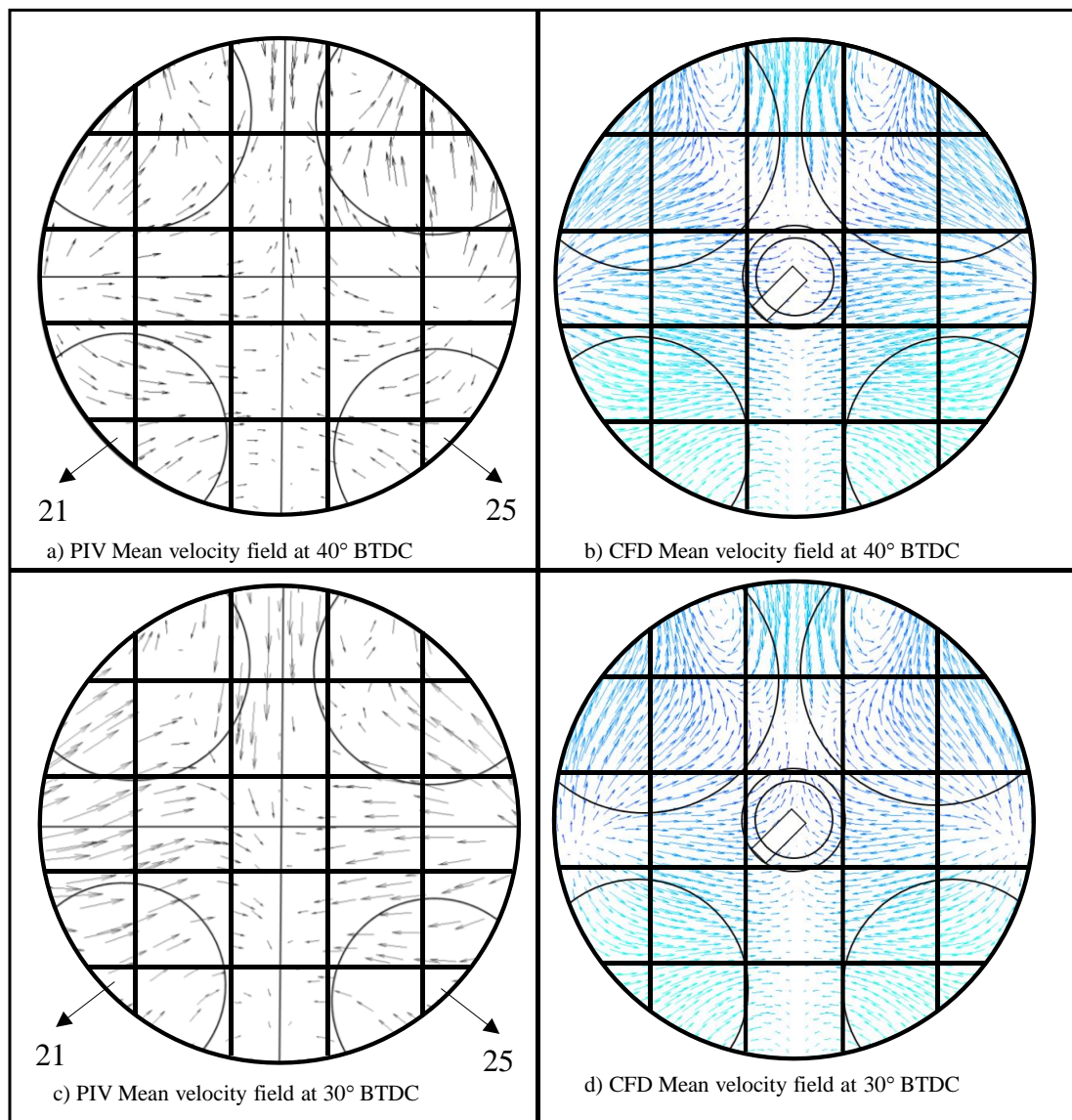


Figure 6.27. CFD and PIV mean velocity field divided into 25 zones. a) PIV Mean velocity field at 40° BTDC, b) CFD Mean velocity field at 40° BTDC, c) PIV Mean velocity field at 30° BTDC, and d) CFD Mean velocity field at 30° BTDC.

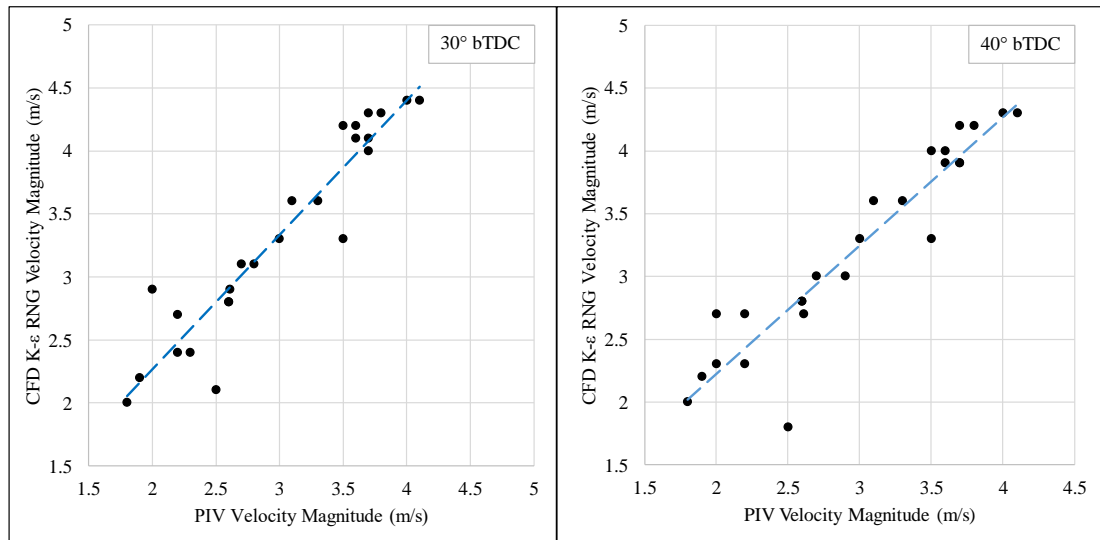


Figure 6.28. Comparison between CFD (k-epsilon RNG) and PIV, showing magnitude velocity for 30° (left) and 40° bTDC (right).

6.2.5.1 CFD on The Tumble Plane

Fuel injector was added to the CFD model to create similar piston configuration with PIV, however, it was not used to spray fuel in the cold flow run, also in PIV measurements fuel injector was not used to spray fuel on to flow. Start of fuel injection was set to 270° bTDC this was to make sure optimum air and fuel mixture homogeneity that was also showed by the previous researcher [110].

Examples of the central tumble plane flow field are shown in Figure 6.29 to Figure 6.31. From the presented data it can be observed that for most of the compression stroke some variety of tumble motion is present. As the compression stroke progresses, the dominant flow structures have velocities of ~ 2.5 m/s moving towards the centre line of the bore. Also, there seems to be a large-scale motion on the inlet side of the cylinder. The key engine geometry including the valves and spark plug are superimposed to the CFD flow field to show spark plug position in respect to the flow. These observations are in agreement with the swirl-plane measurements, as at both 90° CA and 40° CA BTDC. The main scales of motion and the higher levels of velocity magnitude were visible at the same positions.

CFD Vertical Plane at 40° CA BTDC or 320° CA ATDC

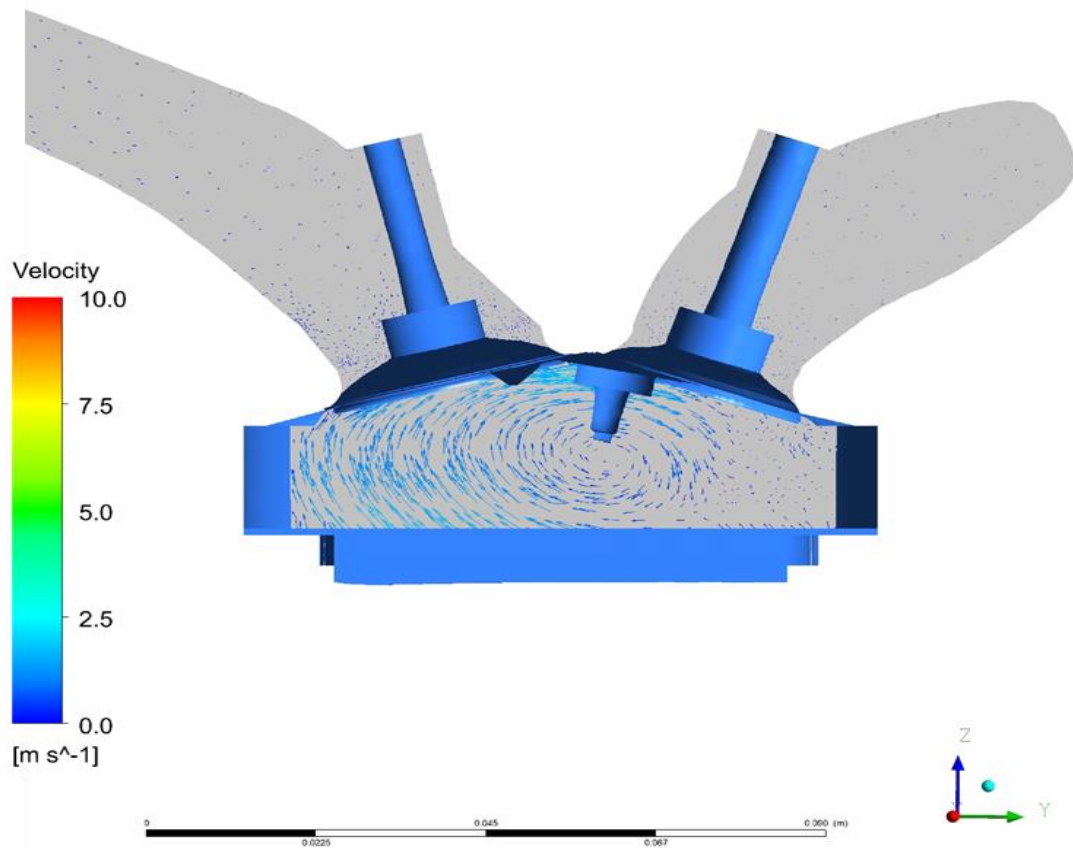


Figure 6.29. Mean Velocity Field on the Tumble Plane at 40° CA BTDC.

Presented in Figure 6.30 is the tumble plan flow field at 90° CA BTDC. The flow at the left side of the piston shows clear dominant velocity starting from the lowest point of the piston and moving towards top side where the inlet valve is located. This flow then is shifting to the exhaust side at the end of the pattern. Also, similar trend can be seen in a larger scale shown in tumble plane at 180° CA BTDC.

CFD Vertical Plane at 90° CA BTDC or 270° CA ATDC

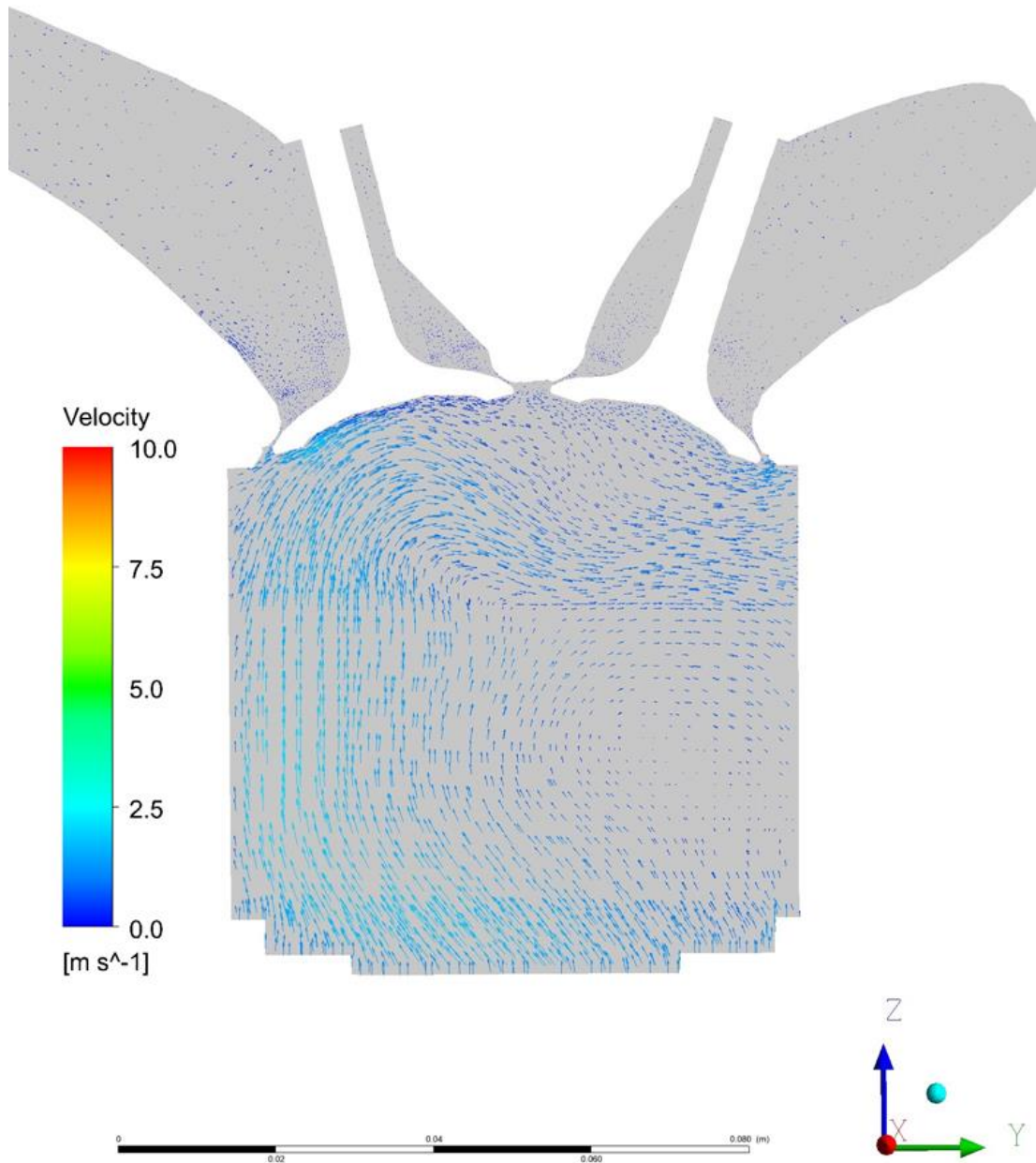
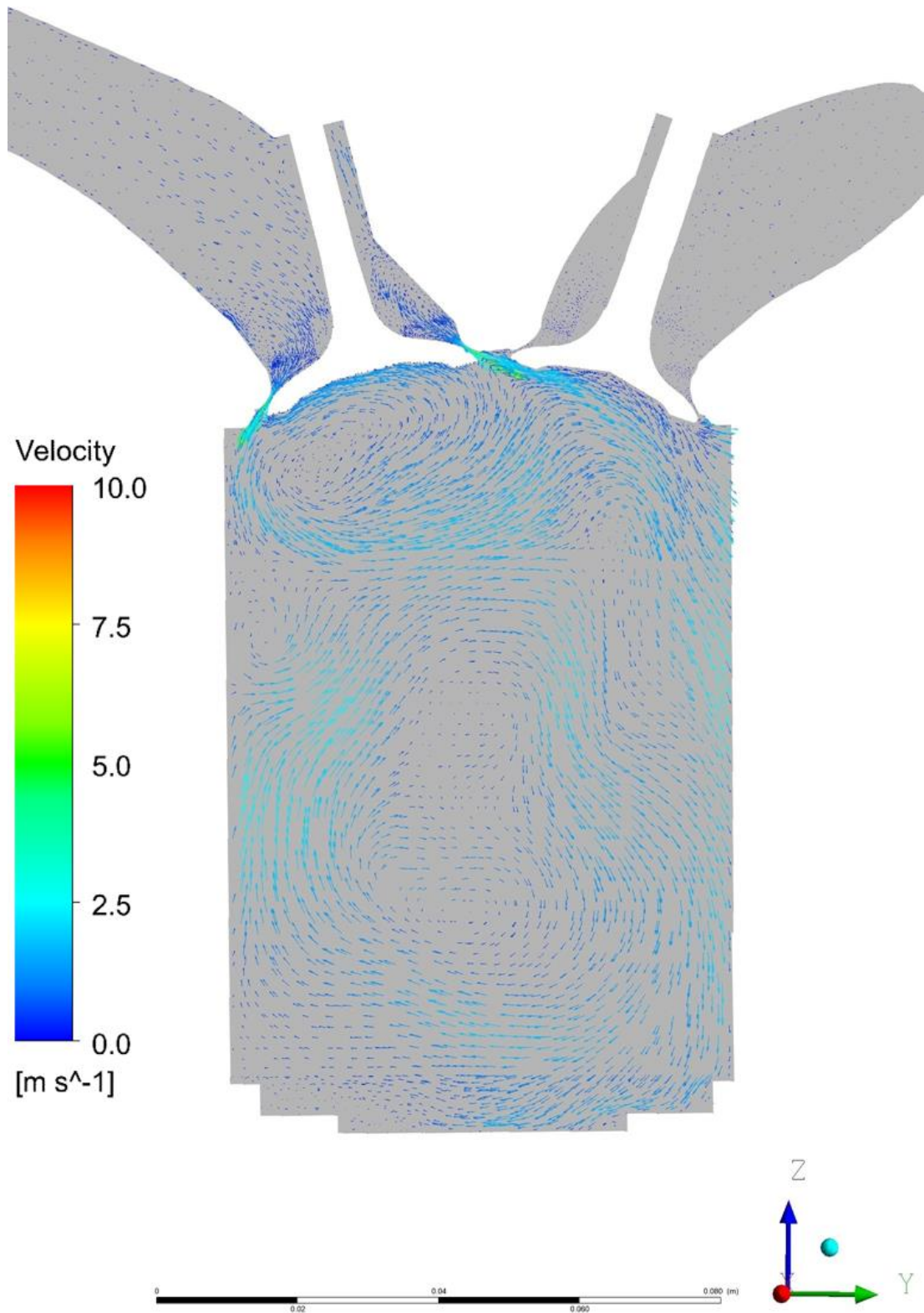


Figure 6.30. Mean Velocity Field in the Tumble Plane at 90° CA BTDC.

CFD Vertical Plane at 180° CA BTDC or 180° CA ATDCFigure 6.31. Mean Velocity Field in the Tumble Plane at 180° CA BTDC.

6.3 Combustion

Presented in this chapter is an in-depth analysis of the optical data obtained and thermodynamic analysis during this work. The main aim of this study was to improve the fundamental understanding of the combustion characteristics of the following fuels:

Two Base fuels,

1. Iso-octane
2. Ethanol

Three Anhydrous blends,

1. E10I90 (10% ethanol, 90% iso-octane)
2. B16 I84 (16% butanol, 84% iso-octane)
3. E6B9I85 (6% ethanol, 9% butanol, 85% iso-octane)

Four Hydrous blends,

1. W5E95 (5% water, 95% ethanol)
2. W12E88 (12% water, 88% ethanol),
3. W20E80 (20% water, 80% ethanol)
4. E85I10W5 (85% ethanol, 10% iso-octane, 5% water)

The aim of pressure data analysis was to obtain data such as the mass fraction burned, in-cylinder pressure and the COV of IMEP. At the same time, the flame images were processed to calculate the mean flame radius, apparent flame speed, laminar burning velocity, and the level and severity of any distortion of the flame (also called flame centre displacement). Both the thermodynamic and optical data have been used to understand the differences between the combustion characteristics of the tested fuels at fixed spark timing at 40° CA BTDC (which corresponded to MBT for the fastest burning pure ethanol fuel). Engine-out emissions measurements were not considered due to the optical setup and impact of the glass on heat transfer. The general effects of such fuels on emissions were discussed in Chapter 2.

6.3.1 Thermodynamic Data

The associated load and combustion stability for the fixed spark timing at 40°bTDC (which corresponded to MBT for the fasted burning pure ethanol fuel) are shown in Figure 6.32. Data presented is in terms of Net IMEP and combustion stability values from a cycle closest across the full 300 cycles. The spark timing was fixed at the MBT value, this was to ensure that, nominally, the same flow field conditions existed on average at ignition timing for all tests.

It can be seen from Figure 6.32 that the lowest COV of IMEP of 1.52 was recorded for ethanol fuel with the highest IMEP of 4.32 bar, as a result of faster combustion hence shorter combustion duration, fixed ethanol MBT and lower flame development angle. COV of IMEP was increased as the water content increased and slightly decreased net IMEP this was due to the slower combustion (longer combustion duration). Net IMEP over input energy was also computed because the heating value and the injected mass are not the same for the tested fuels, the net IMEP is hence normalized with the input energy. The highest COV of IMEP of 4.07 was recorded for W20E80 with 4.1 bar net IMEP, it was mainly because of slower combustion (longer combustion duration) because of added water (20%) and probable misfires in the combustion. Presented in Figure 6.33 is the Net IMEP and combustion stability values from the cycles closest to the optical mean (300 cycles) of B16I84, E10I90, E6B8I85 and E85I10W5 under MBT fix spark timing conditions. This shows the lowest COV of IMEP of 1.59 recorded for the fuel with the highest amount of ethanol blend, (E85I10W5). In the agreement, comparing net IMEP over input energy shows the highest value of 5.74 for (E85I10W5) followed by B16I84, E10I90 and E6B9I85.

Finally, all of the fuels net IMEP and combustion stability values from the cycles closest to the optical mean (300 cycles) under MBT fix spark timing condition are compared in Figure 6.34. Ethanol clearly has the highest net IMEP and net IMEP over input energy. In highest to lowest order net IMEP of W5E95, W12E88, E85I10W5, B16I84, E6B9I85, E10I90, iso-octane and W20E80 are 4.28,4.24,4.23, 4.22,4.18, 4.14,4.1 and 4.09 bar respectively.

Net IMEP/ input energy shows a different trend, with E85I10W5, is the second highest after ethanol with a value of 5.74 bar in compare to 5.88 bar of ethanol. This is because of the more injected mass of fuel to maintain stoichiometric condition. Net IMEP/input

energy of B16I84, E10I90, iso-octane, E6B9I85, W5E95, W12E88 and W20E80 are 5.46, 5.21, 5.2, 5.19, 4.57, 4.56 and 4.56 respectively, in highest to lowest order.

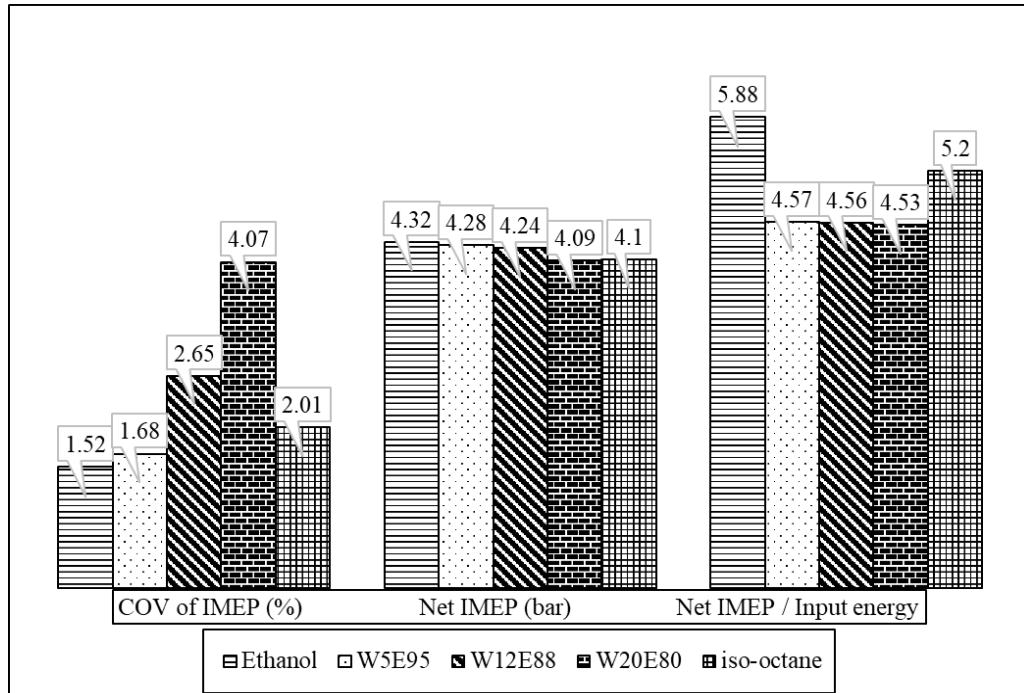


Figure 6.32. Net IMEP and combustion stability values from the cycles closest to the optical mean (300 cycles) of base fuels and wet ethanol. (1500 rpm, 0.5 bar inlet pressure, ethanol MBT).

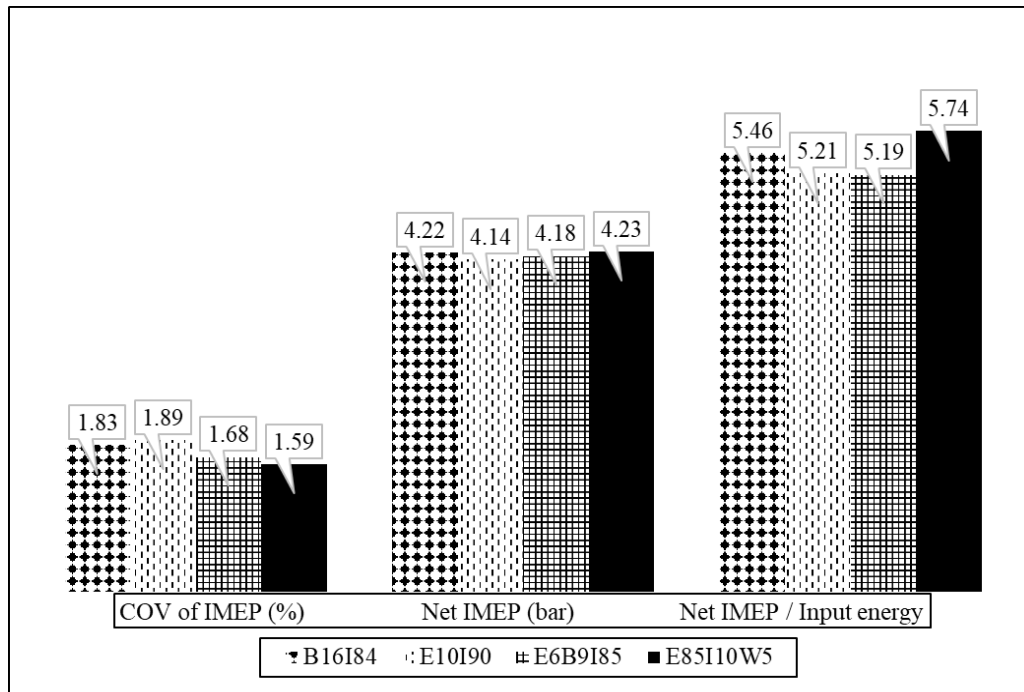


Figure 6.33. Net IMEP and combustion stability values from the cycles closest to the optical mean (300 cycles) of B16I84, E10I90, E6B8I85 and E85I10W5. (1500 rpm, 0.5 bar inlet pressure, ethanol MBT).

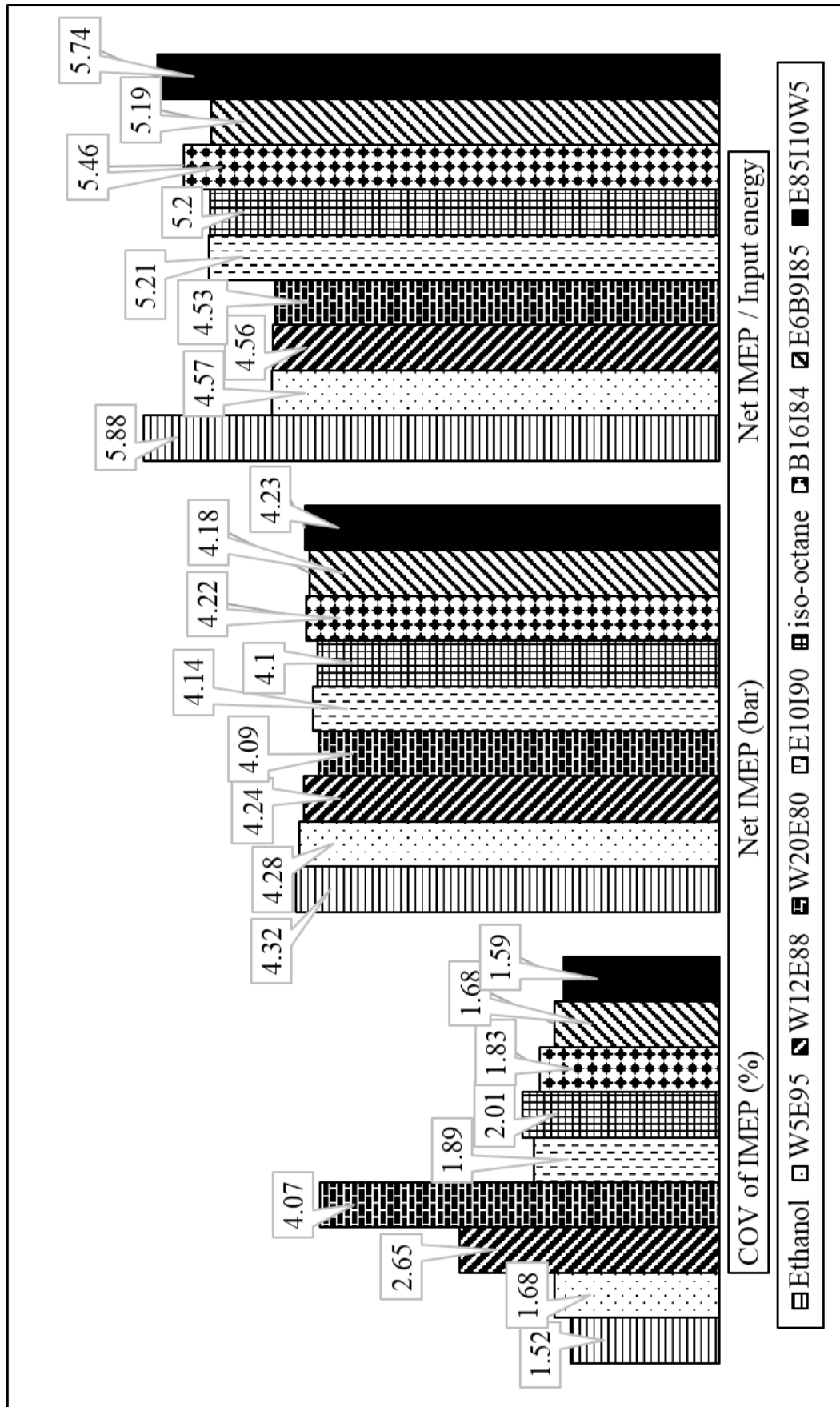


Figure 6.34. Net IMEP and combustion stability values from the cycles closest to the average cycle (1500 rpm, 0.5 bar inlet, ethanol MBT).

It can be seen from Figure 6.35 to Figure 6.37 that ethanol with the highest peak pressure of 18.11, 20.37, and 25.82 bar for the closest cycle to slow, mean and fast cycle respectively is followed by 5% water content in ethanol and W20E80 indicated the lowest peak pressure of 11.95, 16.37, and 20.09 bar for the closest cycle to slow, mean and fast cycle respectively. It is important to note the comparison were made with ethanol MBT for all the fuels. It can be seen hydrous ethanol have lower peak pressure in comparison to anhydrous ethanol, due to the faster burn rate of pure ethanol and longer combustion duration of hydrous ethanol.

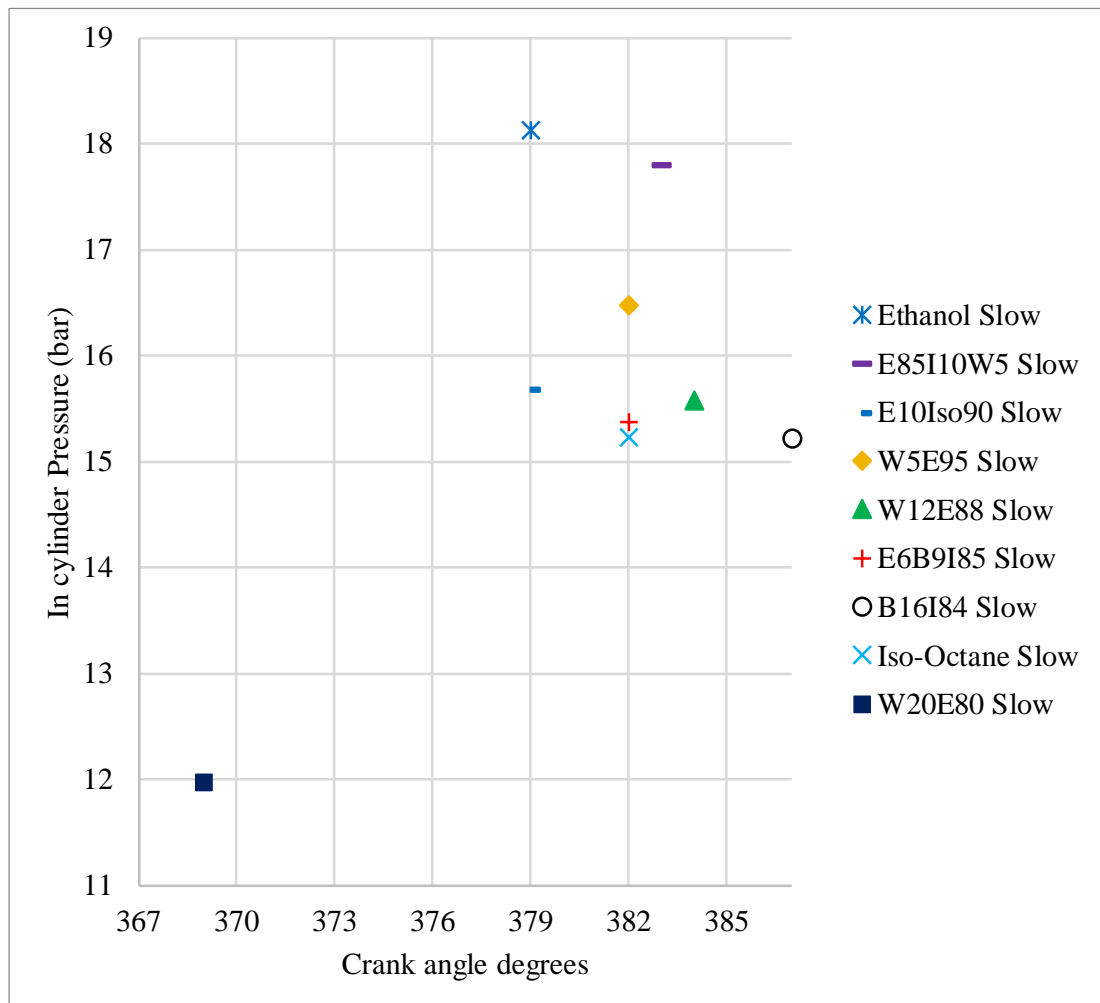


Figure 6.35. Position of maximum pressure for all the fuels. Closest cycle to the arithmetic slow cycle. (1500 rpm, 0.5 bar inlet pressure, ethanol MBT).

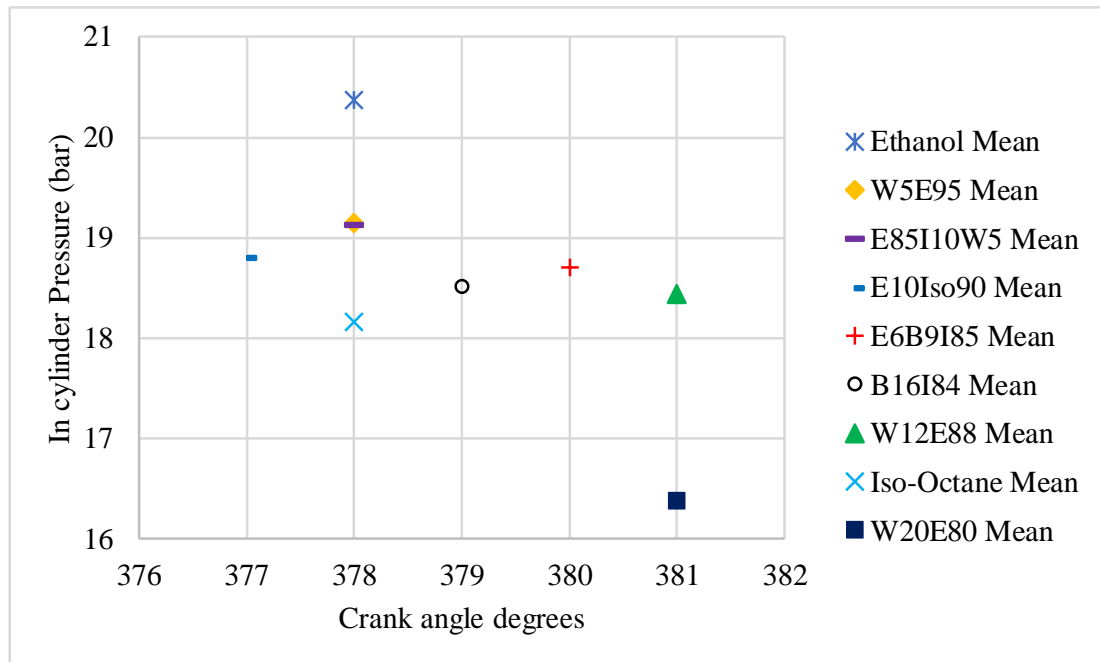


Figure 6.36. Position of maximum pressure for all the fuels. Closest cycle to arithmetic mean cycle. (1500 rpm, 0.5 bar inlet pressure, ethanol MBT).

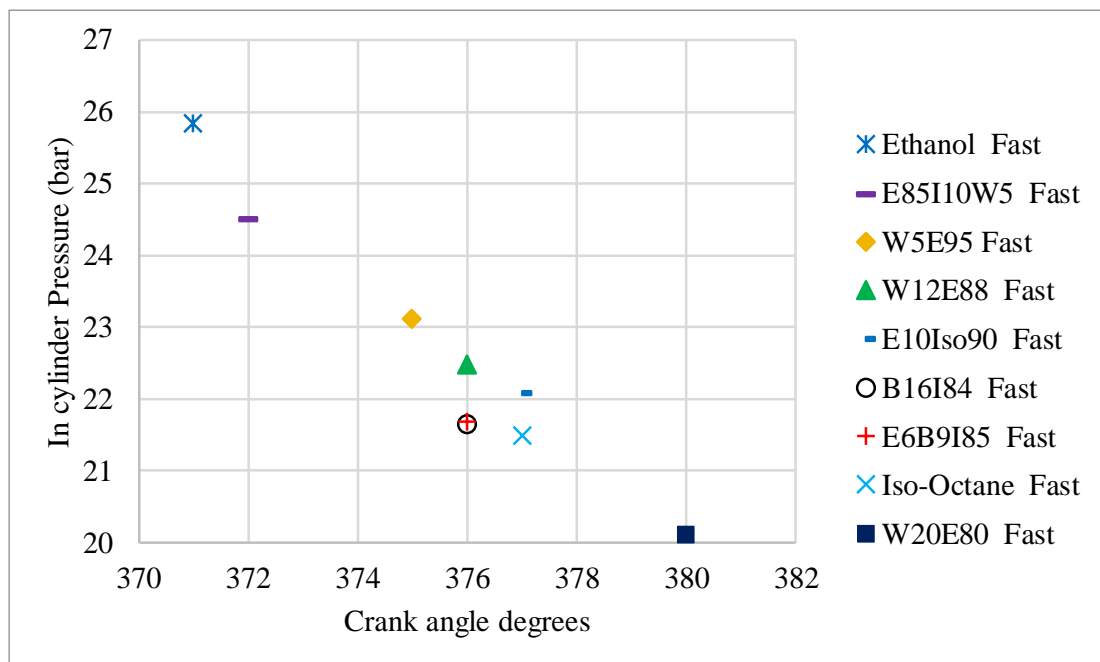


Figure 6.37. Position of maximum pressure for all the fuels. Closest cycle to arithmetic fast cycle. (1500 rpm, 0.5 bar inlet pressure, ethanol MBT).

Presented in Figure 6.38 are pressure data for mean 300 combustion cycles of base fuels and wet ethanol under fixed spark timing displayed with the cycles closest to numerical mean at 1500 rpm. Figure 6.39 shows pressure data for combustion cycles of B16I84, E10I90, E6B8I85 and E85I10W5 under the fix spark timing condition

displayed with the cycles closest to numerical mean at 1500 rpm. E85I10W5 has the highest pressure followed by the slightly lower pressure of fuel E10I90. The lowest peak pressure belongs to B16I84 that is slightly lower than 18.71 bar of E6B9I85. The comparative pressure traces for all the fuels including base fuels, hydrous and anhydrous fuels are set out in Figure 6.41. Ethanol has the highest peak pressure and the lowest peak pressure of 16.37 bar is for the W20E80 blend. The fastest and slowest cycle for each fuel under fixed spark timing of ethanol at MBT is presented in Figure 6.40. It is showing the small difference between ethanol and W5E95 (and a noticeable difference comparing ethanol to W20E80).

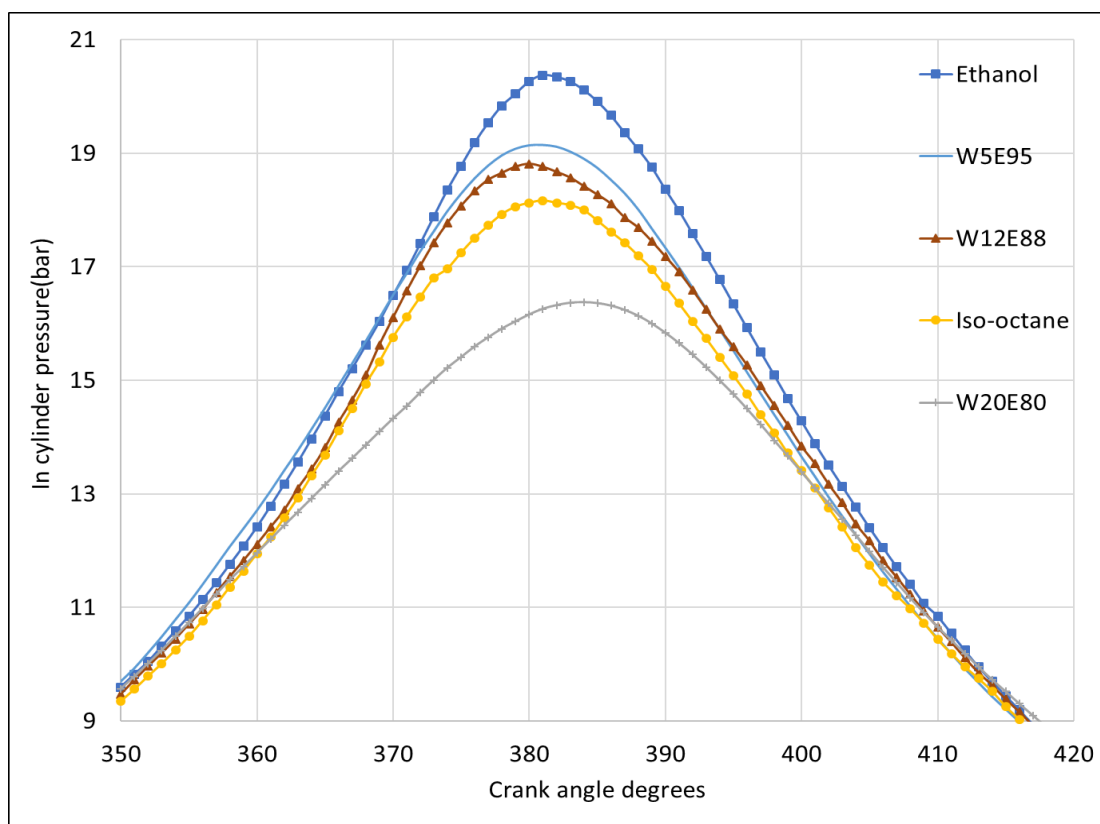


Figure 6.38. 300 combustion cycles of base fuels and wet ethanol under MBT fix spark timing displayed with the cycles closest to numerical mean (1500 rpm, 0.5 bar inlet pressure, ethanol MBT).

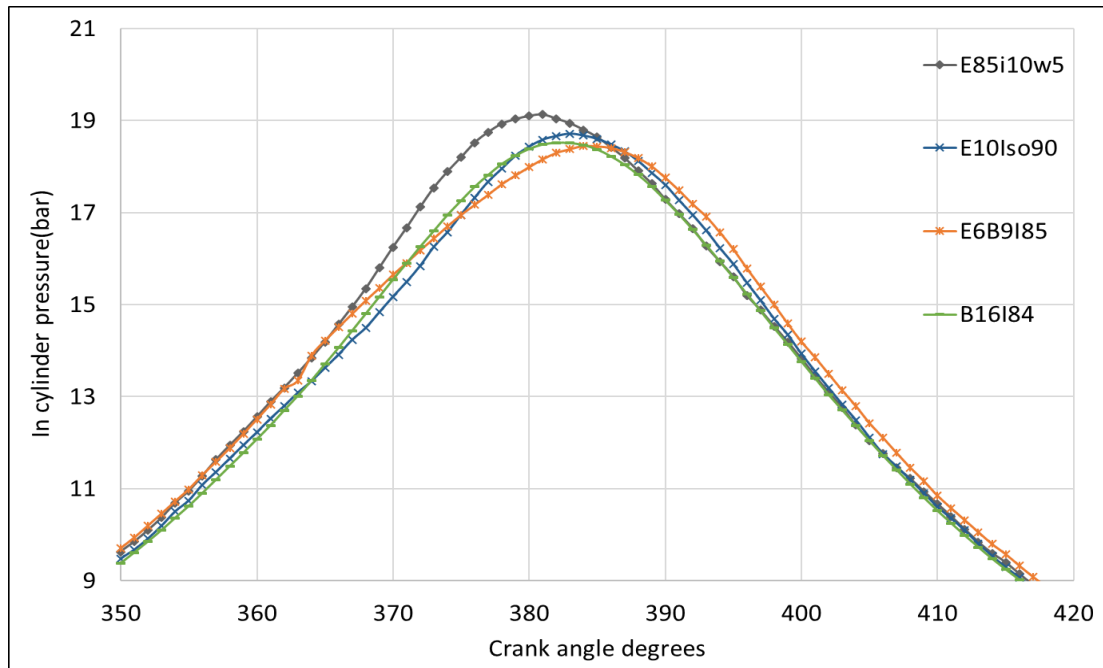


Figure 6.39. 300 combustion cycles of B16I84, E10I90, E6B8I85 and E85I10W5 under MBT fixed spark timing for ethanol condition displayed with the cycles closest to numerical mean. (1500 rpm, 0.5 bar inlet pressure, ethanol MBT).

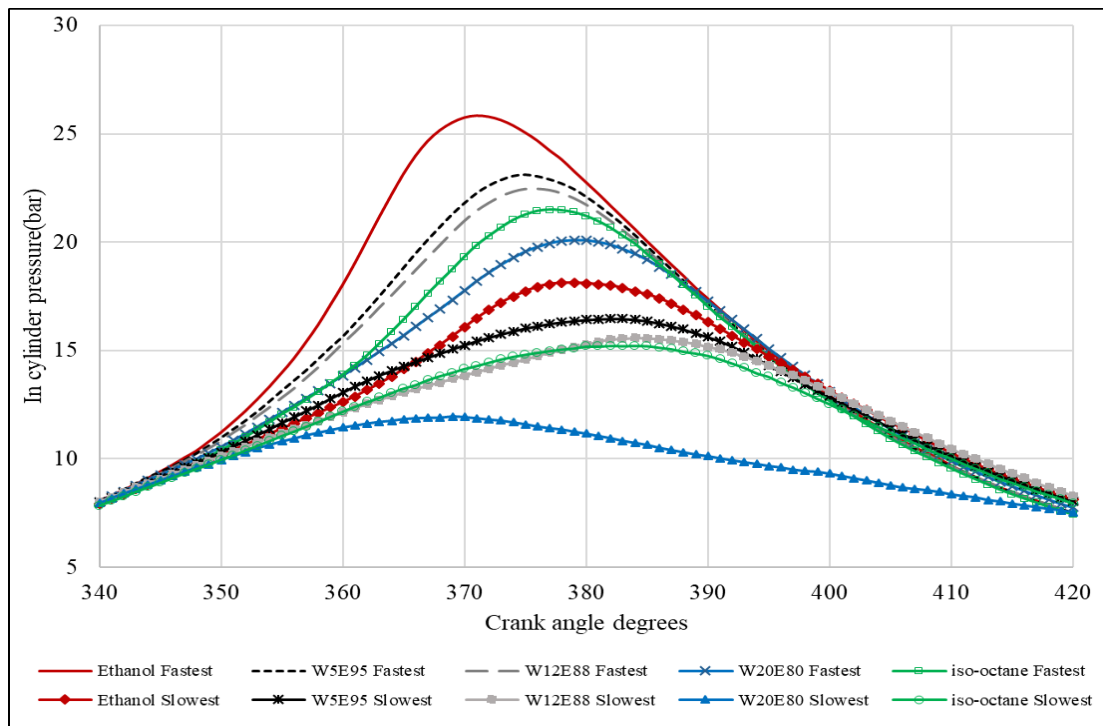


Figure 6.40. Experimental in-cylinder pressure data (60 cycles) for the relevant fastest and slowest cycles; taken from combustion under stoichiometric conditions, (1500 rpm, 0.5 bar inlet pressure, ethanol MBT).

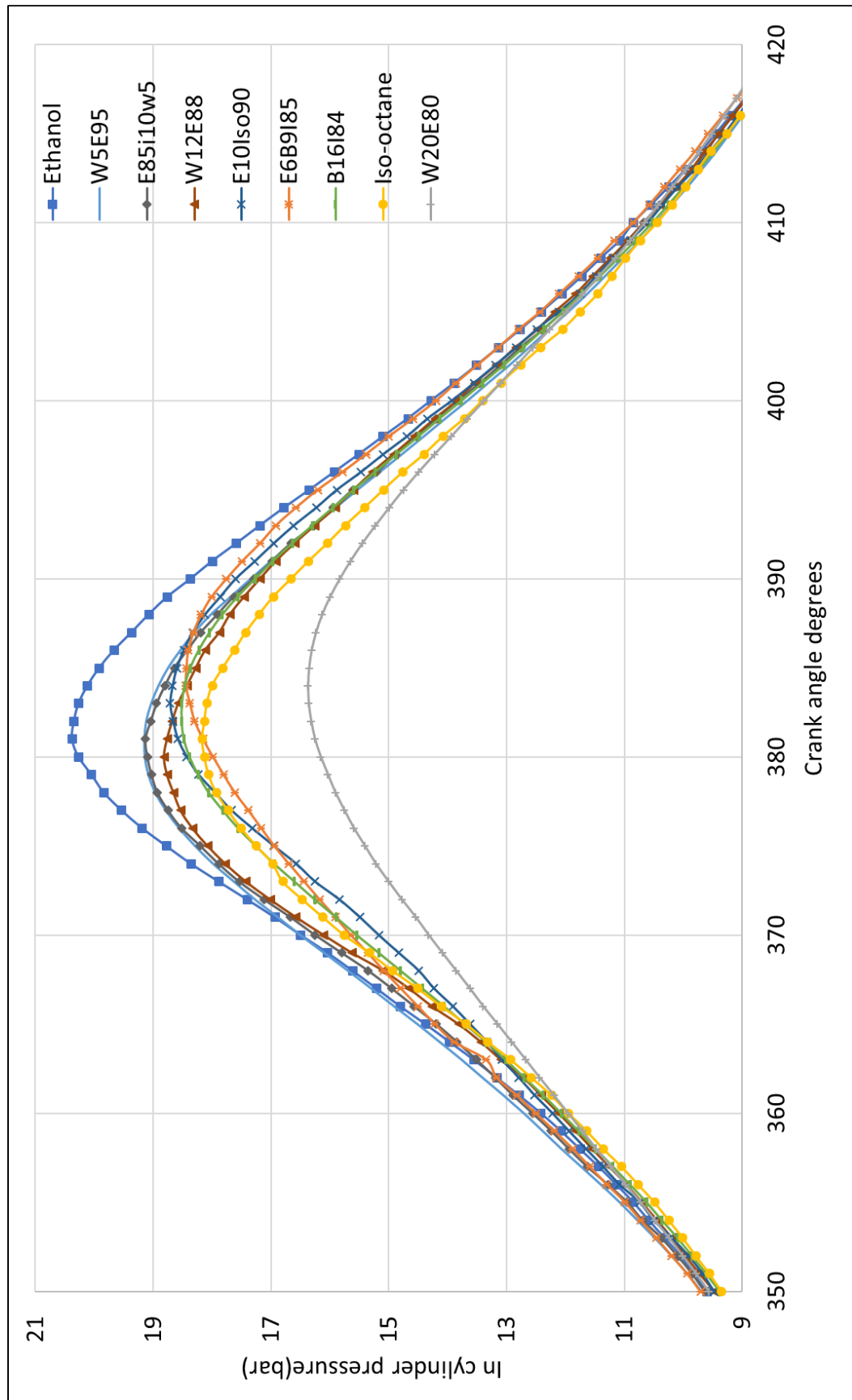


Figure 6.41. 300 combustion cycles displayed with the cycles closest to numerical mean (1500 rpm, 0.5 bar inlet pressure, ethanol MBT for all the fuels).

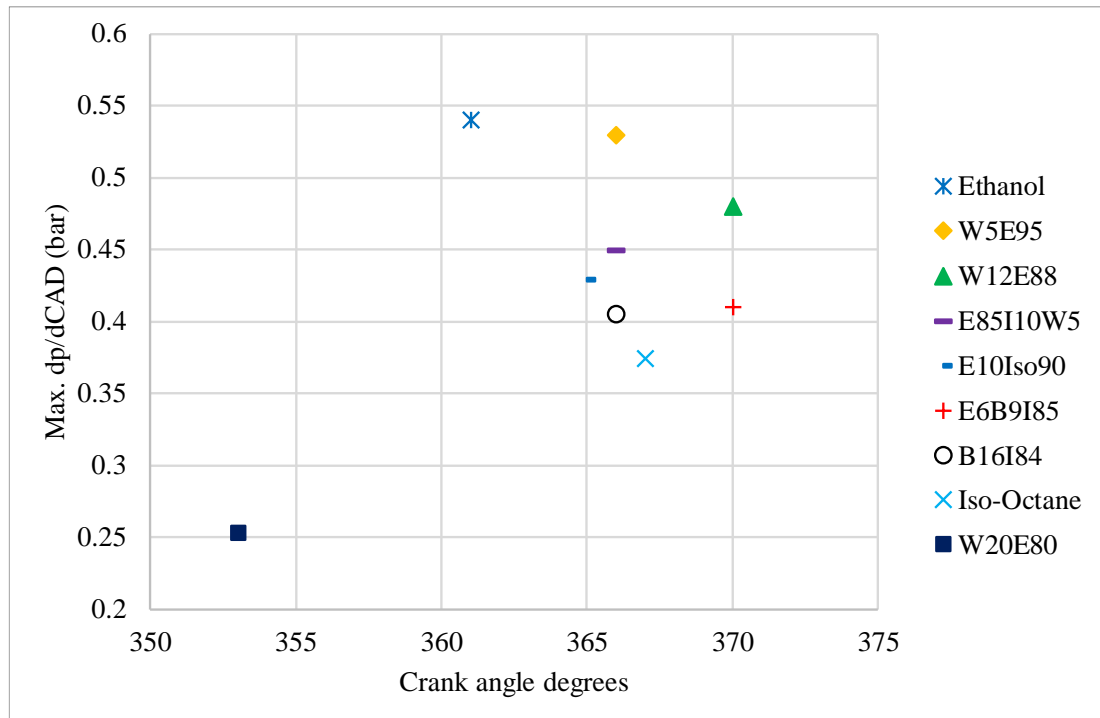


Figure 6.42. Maximum pressure rise rate for all the fuels. 1500 rpm, ethanol MBT operation. Cycle closest to the arithmetic mean.

The position of the maximum pressure rise rate for all the tested fuel at ethanol MBT are presented in Figure 6.42 with the maximum value of 0.55 bar per one crank angle degree for ethanol as the fastest fuel followed by 5% water in Ethanol and 12% water in ethanol. Maximum pressure rise rate is affected by laminar flame speed which are related with the early flame kernel development. The faster laminar flame speed means combustion occurs at smaller volume hence higher pressure rise rate.

Presented in Figure 6.43 to Figure 6.45 are the apparent heat release rate values for base fuels, wet ethanol blends, B16I84, E10I90, E6B8I85 and E85I10W5. Indicating pure ethanol as the fastest burning fuel and W20E80 as the slowest fuel. This is due to the higher in-cylinder pressure and the maximum pressure rise rate discussed in the previous section. Calorific values of the fuels, as well as the laminar flame speed which are related with the early flame kernel development are also playing an important part.

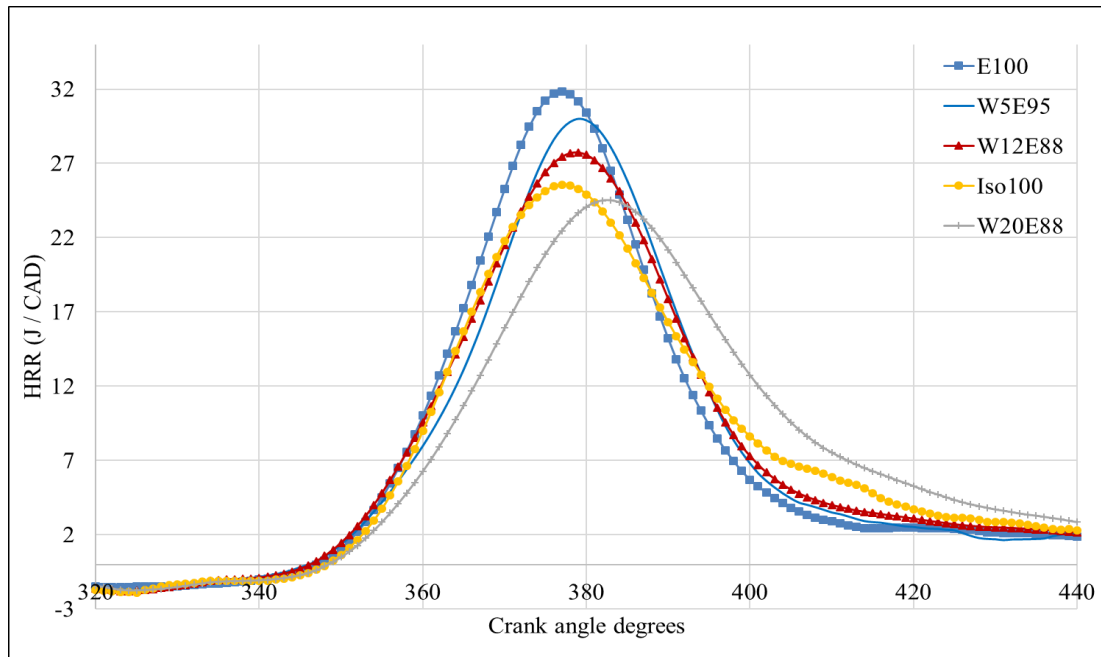


Figure 6.43. 300 cycles average apparent heat release rate for base fuels and wet ethanol fuels (1500 rpm, 0.5 bar inlet pressure, ethanol MBT for all the fuels).

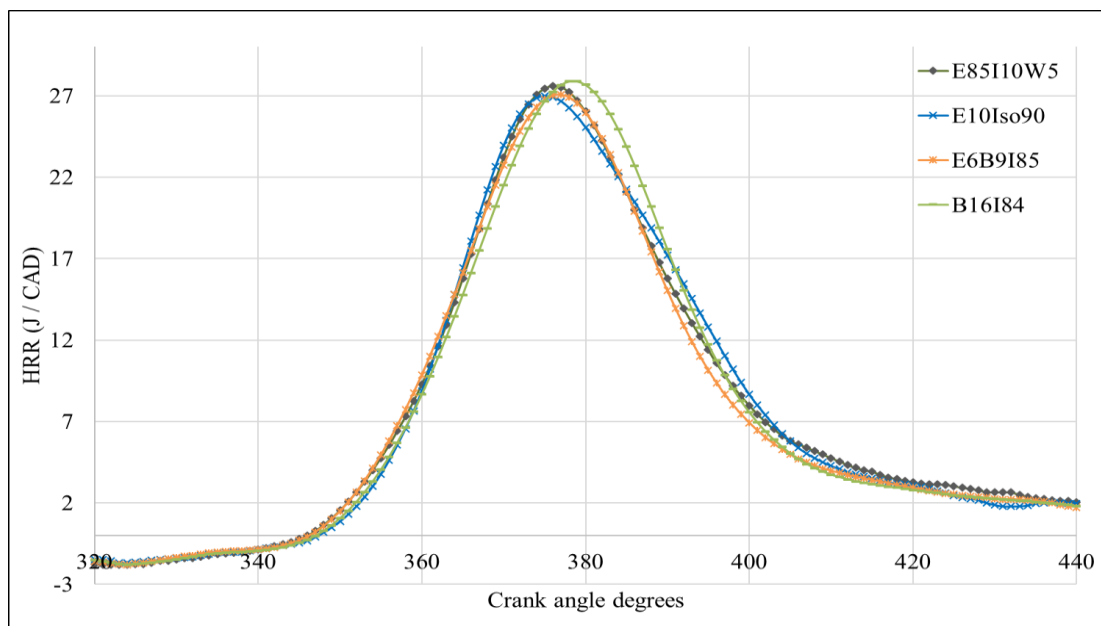


Figure 6.44. 300 cycles average apparent heat release rate for B16I84, E10I90, E6B8I85 and E85I10W5 (1500 rpm, 0.5 bar inlet pressure, ethanol MBT for all the fuels).

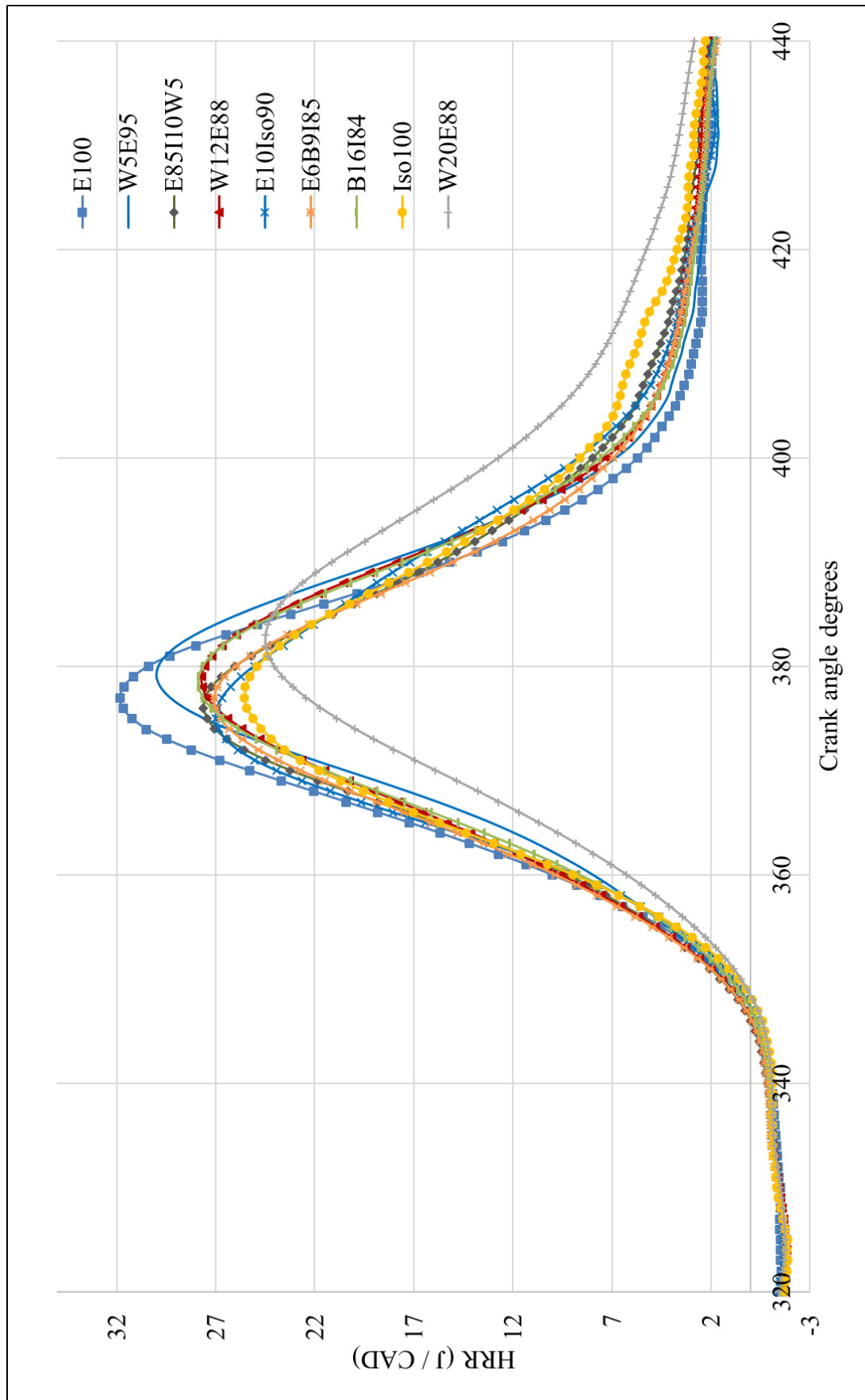


Figure 6.45. 300 cycles average apparent heat release rate for all fuels (1500 rpm, 0.5 bar inlet pressure, ethanol MBT for all the fuels).

6.3.2 Flame Imaging

6.3.2.1 Flame Radius

Shown in Figure 6.46 is the mean flame radius development for ethanol, iso-octane, W5E95, W12E88 and W20E80. The maximum limit for flame radius in this figure is the optical piston window restriction of 27.5 mm radius and by considering flame stretching due to the hotter side of the piston, the maximum flame radius was reached to 19.05 mm as the flame reached the wall (exhaust side) sooner. The flame centroid displacement towards the hotter side of the chamber should also be taken into account. The maximum flame radius reduces to 19.04, 18.20, 17.45 and 15 mm for ethanol, W5E95, W12E88 and W20E80 respectively. The flame radius development rate for the ethanol and W5E95 fuels was very similar within 5 CAD after ignition timing and exhibited a notably faster initial flame radius in the period of 0-7 CAD AIT. Overall, ethanol was the fastest propagating fuel followed by W5E95, W12E88 and W20E80. This seems to be in accordance with burning velocity correlations for ethanol and hydrous ethanol e.g. [50].

Set out in Figure 6.47 is the flame radius development for B16I84, E10I90, E6B8I85 and E85I10W5, it can be seen from cropped section the highest flame radius of 2.65 mm recorded for E85I10W5 that is comparatively a faster fuel than other blended fuels. The lowest flame radius of 2.2 mm at the same crank angle degree recorded for B16I84 that shows about 20% slower flame development.

Demonstrated in the last figure are listed all the tested fuels, showing a logical trend in pressure data. As expected, the fastest fuel ethanol has the highest flame radius development in almost every crank angle degrees and the slowest fuel W20E80 has the least flame development radius. Uncertainty level also shows faster fuel ethanol has the lowest error of 2.5% and the 20% added water increased the error to 10%. Flame development data are compared in the zoomed section at 15 crank angle degrees, it can be seen flame kernel for ethanol reached 2.93 mm in radius at this crank angle in comparison to 1.9 mm of W20E80. This indicates the difference between fastest and slowest fuel at 15 crank angle degree after ignition timing is about 1.03 mm. The maximum flame radius of 15 mm for W20E80 was achieved at 33 crank angle degrees after ignition timing, the same flame radius achieved at 28.5 CAD AIT for ethanol in comparison).

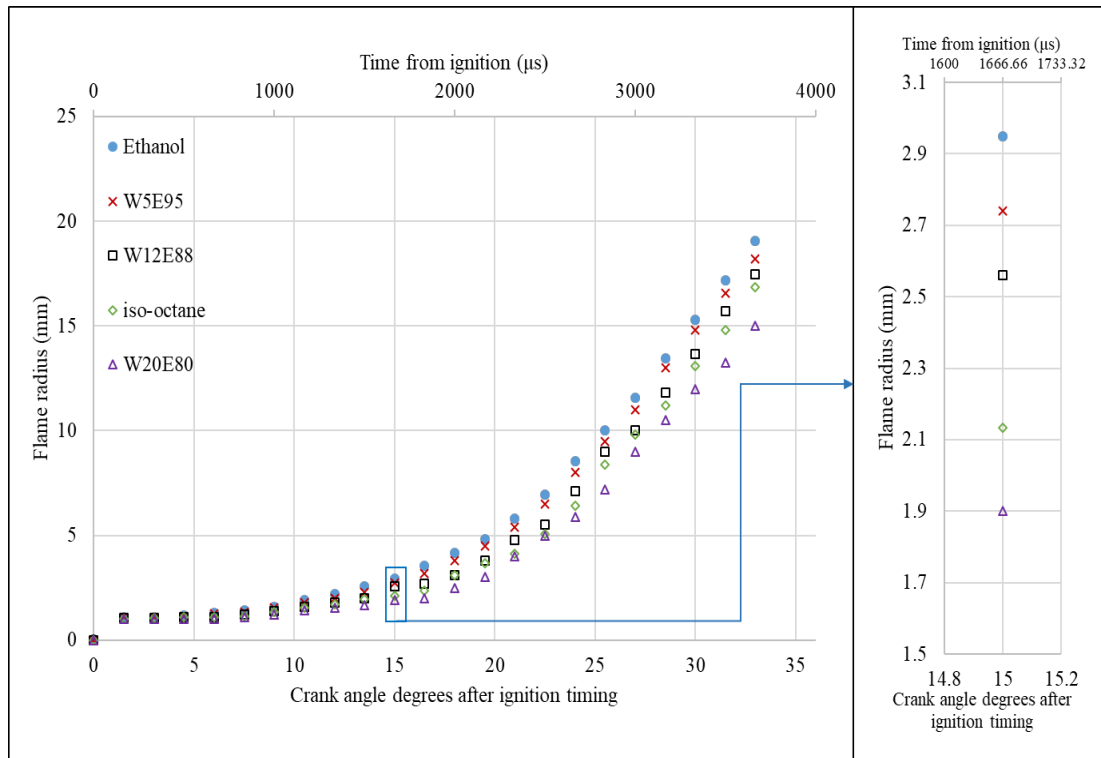


Figure 6.46. Computed flame radius closest data to 60 averaged cycles for base fuels and wet ethanol fuels (1500 rpm, 0.5 bar inlet pressure, ethanol MBT for all the fuels). Highlighted section was chosen at 15 CAD AIT to show the values in larger scales.

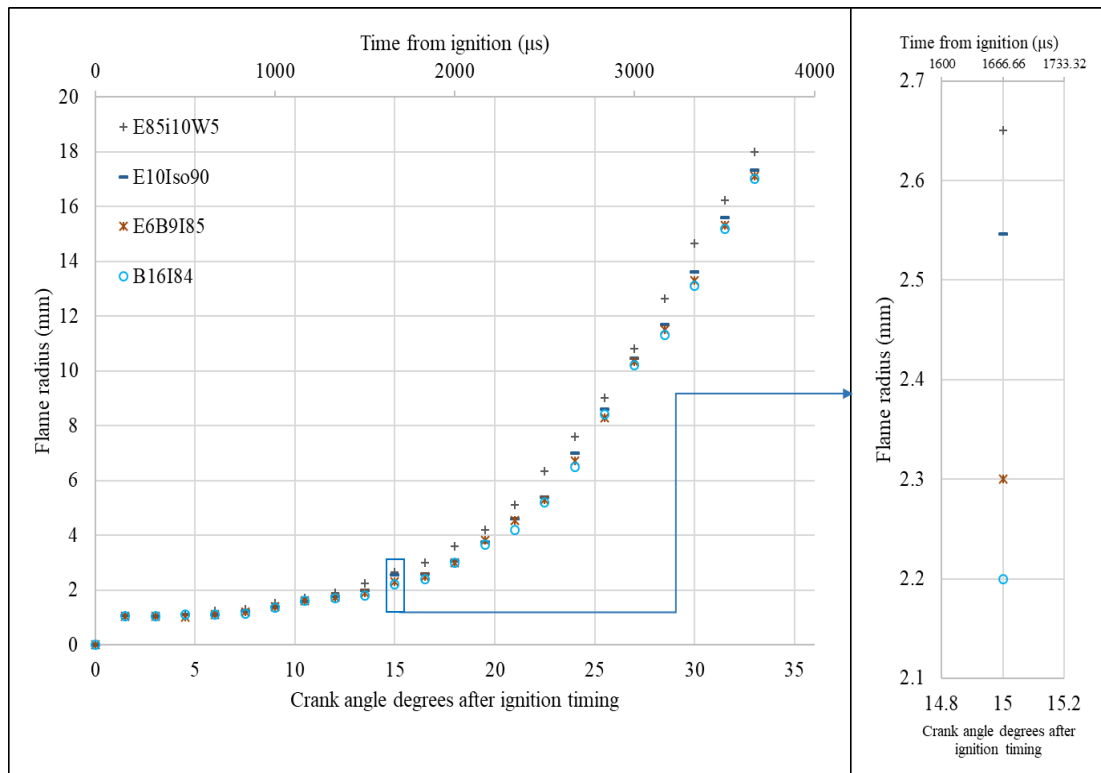


Figure 6.47. Computed flame radius closest data to 60 averaged cycles for B16I84, E10I90, E6B8I85 and E85I10W5 (1500 rpm, 0.5 bar inlet pressure, ethanol MBT for all the fuels). Highlighted section was chosen at 15 CAD AIT to show the values in larger scales.

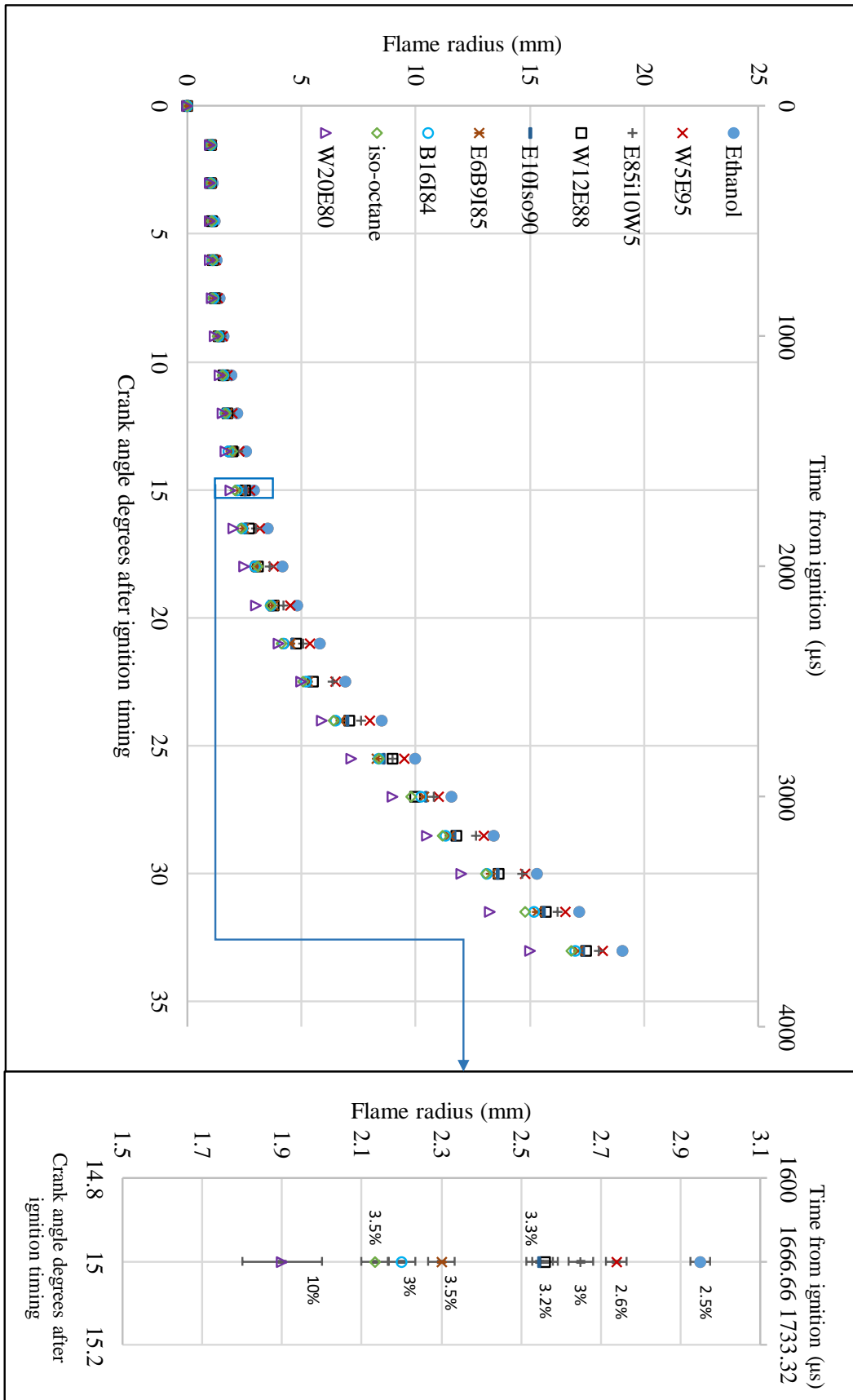


Figure 6.48. Computed flame radius closest data to 60 averaged cycles for all fuels (1500 rpm, 0.5 bar inlet pressure, ethanol MBT for all the fuels). Highlighted section was chosen at 15 CAD AIT to show the values in larger scales with the error bars.

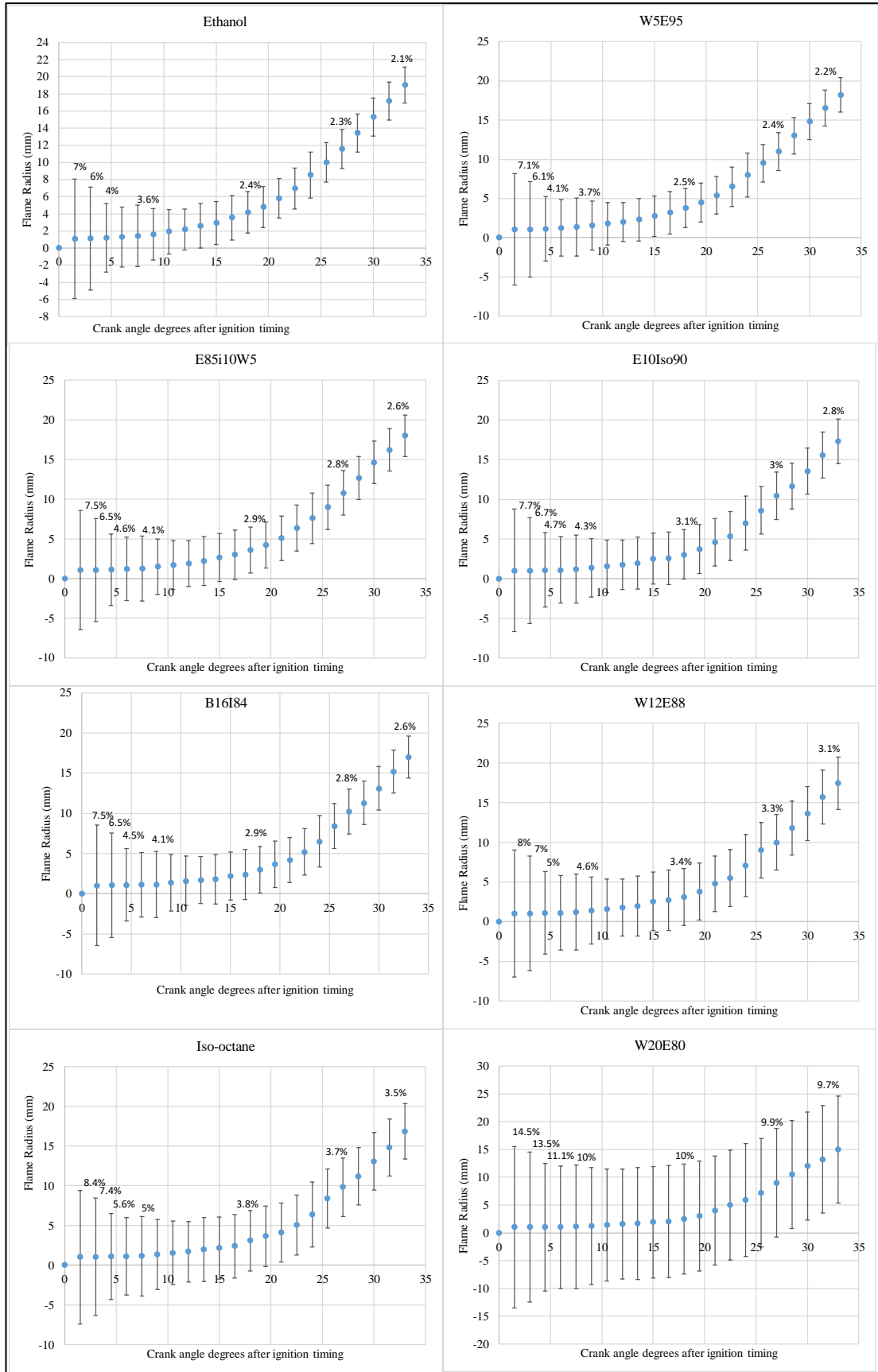


Figure 6.49 Error bars for computed flame radius closest data to 60 averaged cycles for all fuels (1500 rpm, ethanol MBT for all the fuels). The error bars are multiplied by 100 (not the error values above) in order to compare errors in the same graph.

It can be seen from Figure 6.49 that at the start of flame propagation flame radius has the highest error. It is mainly due to the fact that smaller flame can be more distorted with the turbulence, and as the flame radius increases less distortion is caused by the turbulence. It can also be seen that added 20% water to ethanol increased uncertainty, this is in a good agreement with the pressure data analysis.

6.3.2.2 Flame Speed

The apparent flame speed shown in Figure 6.50 to Figure 6.52 is also in good agreement with prior observations, indicating the highest flame speed of 10.93 m/s for ethanol and lowest (peak) speed of 8.2 m/s for W20E80. The maximum flame speed of 8.2m/s was achieved at 33 CAD AIT for W20E80 (the same flame speed achieved at 24 CAD AIT for ethanol in comparison). Apparent flame speed increases through cycles predominantly because of the expansion element and the burning of the gasses.

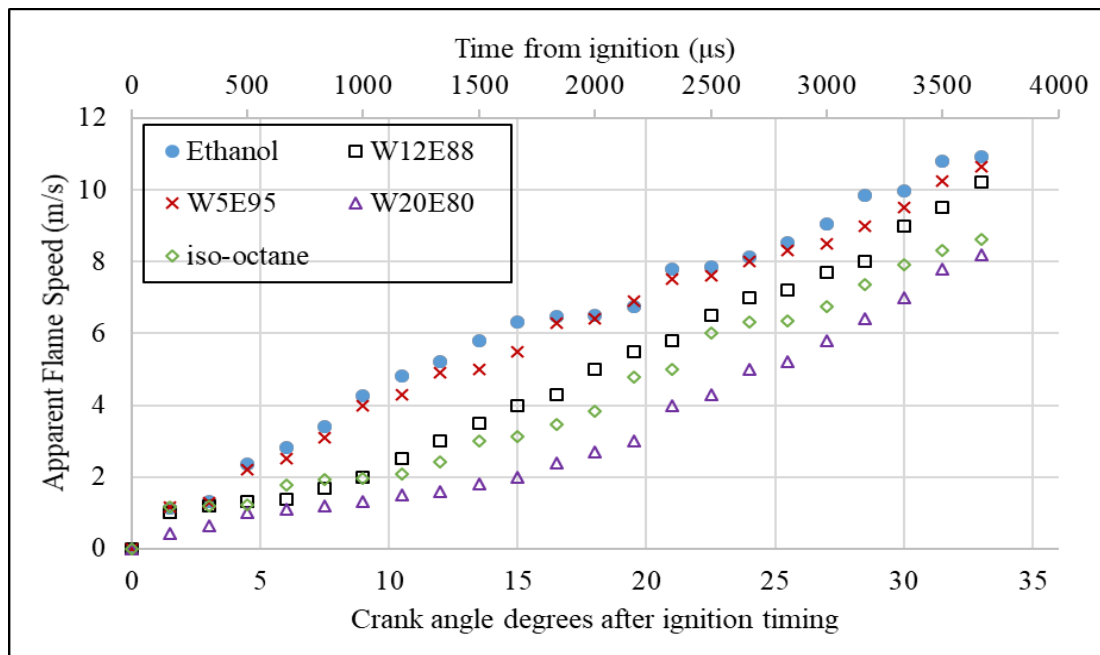


Figure 6.50. Apparent flame speed closest data to 60 averaged cycles for base fuels and wet ethanol fuels (1500 rpm, 0.5 bar inlet pressure, ethanol MBT for all the fuels).

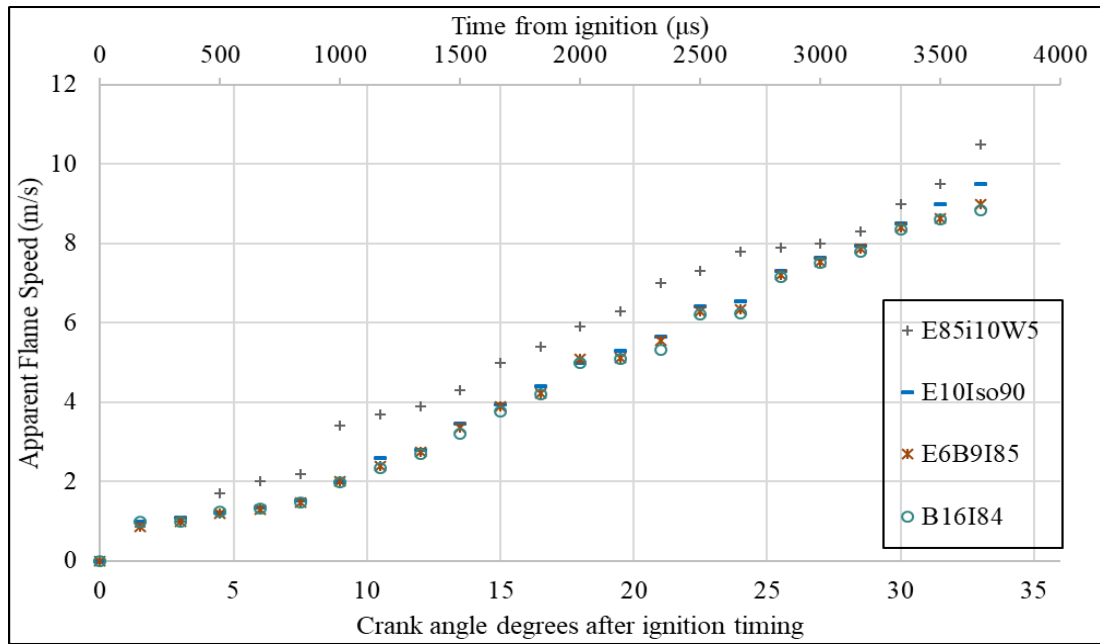


Figure 6.51. Apparent flame speed closest data to 60 averaged cycles for B16I84, E10I90, E6B8I85 and E85I10W5. (1500 rpm, 0.5 bar inlet pressure, ethanol MBT).

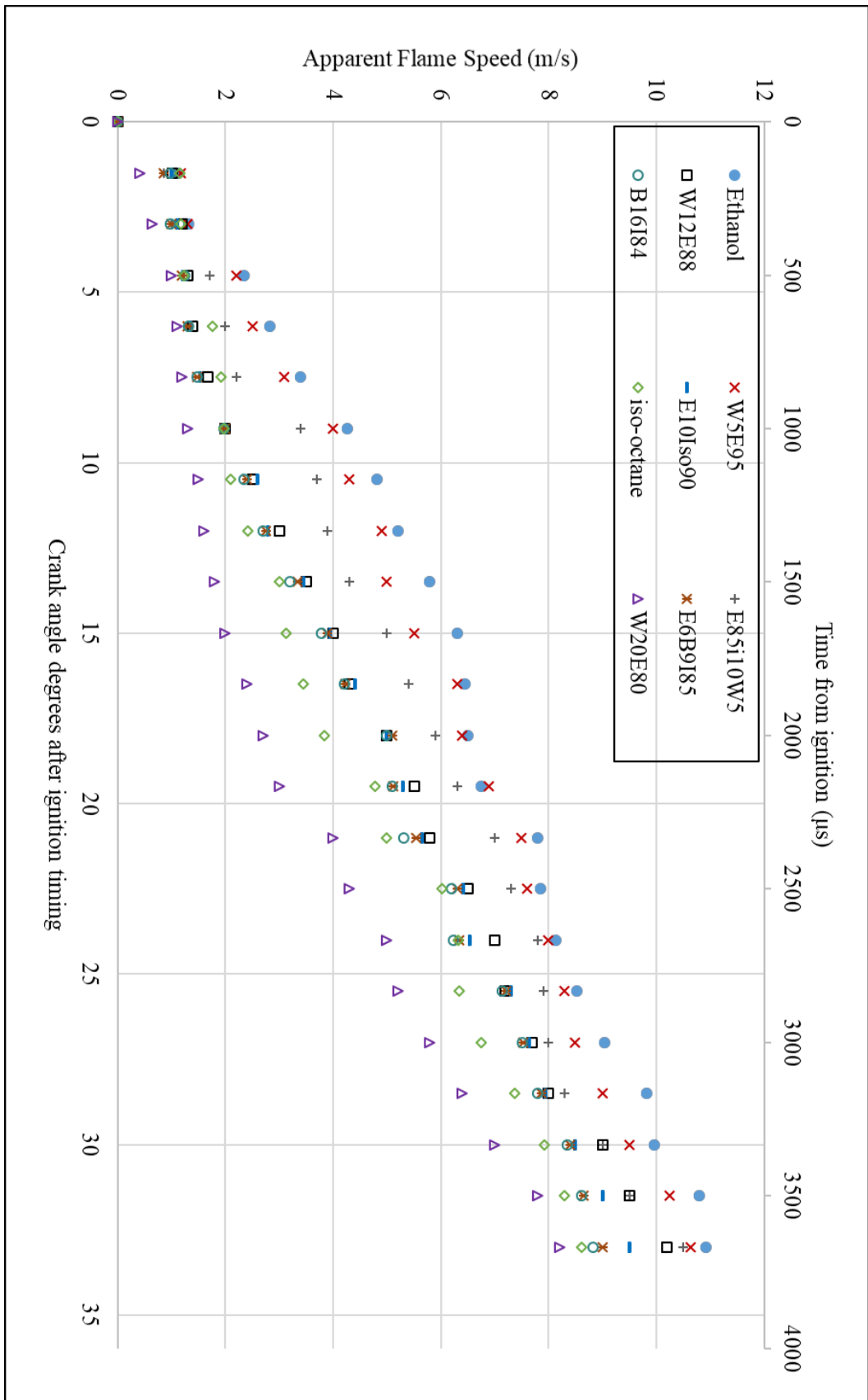


Figure 6.52. Apparent flame speed closest data to 60 averaged cycles for all the studied fuels (1500 rpm, 0.5 bar inlet pressure, ethanol MBT for all the fuels).

6.3.2.3 Centroid Displacement

Early kernel flame growth generally will be affected by two main features of the flow field: 1-large-scale convection by ‘bulk’ motion and 2-small-scale turbulence. The flame centroid displacement can be described as an indication of the movement of the flame kernel due to flows around it during its growth. It can be seen from the previous results that fuels with the higher laminar burning velocity (faster chemistry) have higher apparent flame speed and flame radius growth in comparison to fuels with lower laminar burning velocity so, there is less time to distort the flame. Hence combustion faster fuels are more resistant to flame centroid displacement. Figure 6.54 shows the average flame Euclidean distance from the spark plug until one frame (1.5 CAD) before the flame (W20E88) reaches the window periphery. The (0,0) point represents the spark-plug electrode point. This figure demonstrates a similar trend for all fuels, where the flames grew initially towards the exhaust side of the engine in agreement with previous studies [141,203]. The ethanol flame contour moved away from its centre by 6.7 mm in y and 1 mm in x-direction total of 7.7 mm, compared to W5E95 (y=6.95 mm, x=1.2 mm total of 8.15), W12E88 (y=6.88 mm, x=1.6 mm total of 8.48 mm), W20E80 (y=8 mm, x=5.5 mm total of 13.5 mm) and iso-octane (y=9.6 mm, x=1.73 mm total of 11.33).

This indicates that 5% water in ethanol (W5E95) is 5.8% less resistant to flame centroid displacement and flame stretching compared to pure ethanol. 12% (W12E88) and 20% (W20E80) water in ethanol indicated notably less resistance to flame centroid displacement and flame stretching compared to ethanol by 10.15 and 75% respectively. Iso-octane has higher flame distortion than ethanol and wet ethanol of 5% and 12% water content, which is also in a good agreement with the flame stretch analysis in previous work [203–205]. It can be seen that by adding 16% butanol to iso-octane the B16I84 flame contour moved away from its centre by 7.8 mm in y and 2.9 mm in x-direction with a total of 10.7 mm in comparison to iso-octane of 11.33 total distortion. That is approximately 6% higher resistant to flame displacement in comparison to iso-octane. Individual fast, mean and slow flame cycles were selected to understand minimum centroid displacement. As centroid displacement would compromise the comparison of fuels with partial optical access (as the flame contour reaches the piston window earlier if the centroid is going toward any side of the piston).

To verify the synchronized pressure and computed flame radius from in-house Matlab script, each individual cycle was compared to two other fuels. It can be seen from Figure 6.53 each fuel last flame contour (up to the 55mm diameter) reached the optical window periphery in 30, 31.5 and 33 CAD AIT for ethanol, iso-octane and B16I84 respectively. In the case of mean individual flame contour propagation, ethanol was the fastest with 33 CAD duration followed by 34.5 CAD duration for iso-octane and finally 36 CAD duration for slowest burning fuel B16I84 blend. The iso-octane and B16I84 blend both reached the piston window at 37.5 CAD AIT, these contours are 1 flame contour (equivalent to 1.5 CAD) before hitting the wall (optical window)

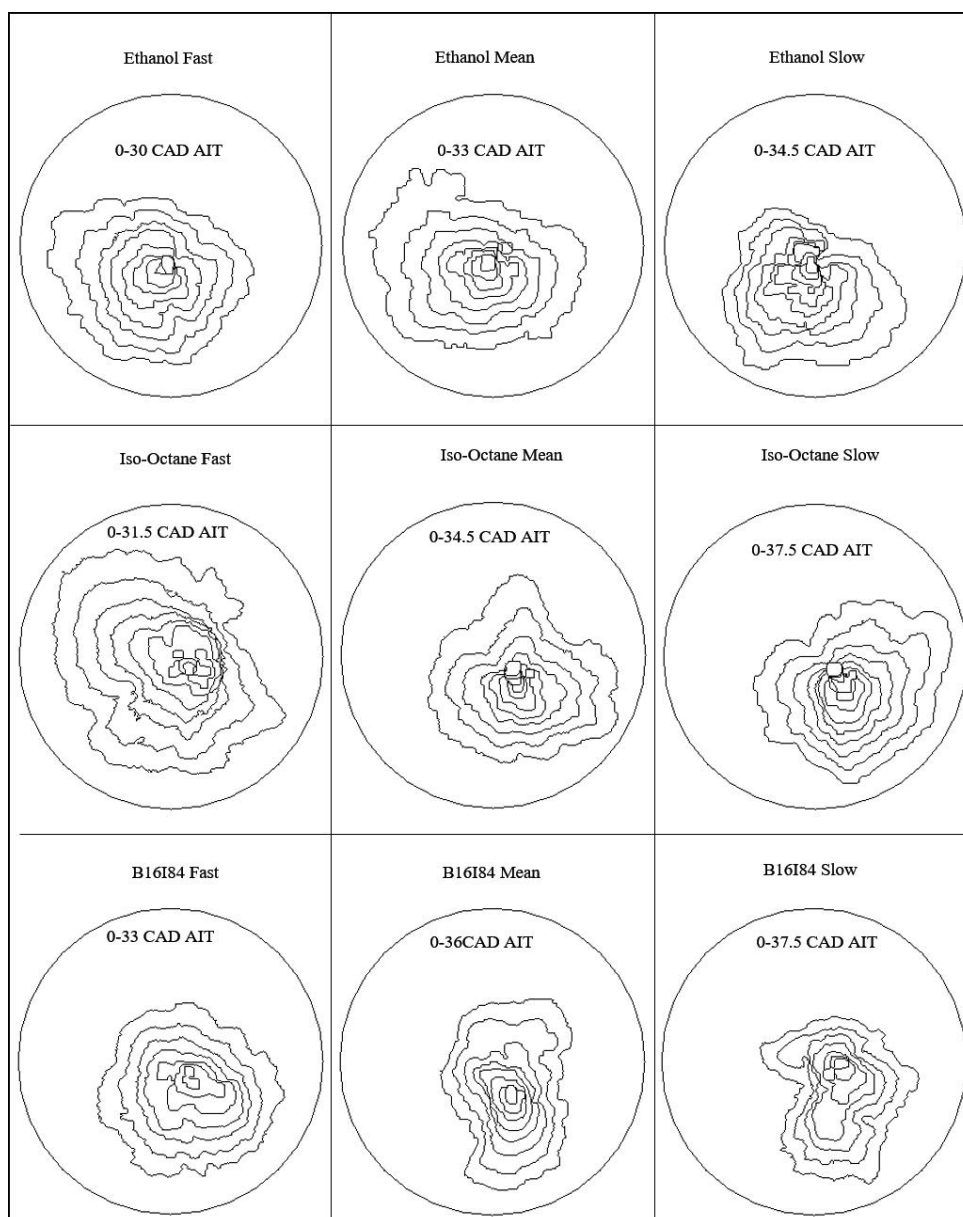


Figure 6.53. Individual Flame contours of fastest slowest and mean cycles, starting from ignition until one contour before the optical window was approached in every 3 intervals. (1500 rpm, 0.5 bar inlet pressure, ethanol MBT for all the fuels).

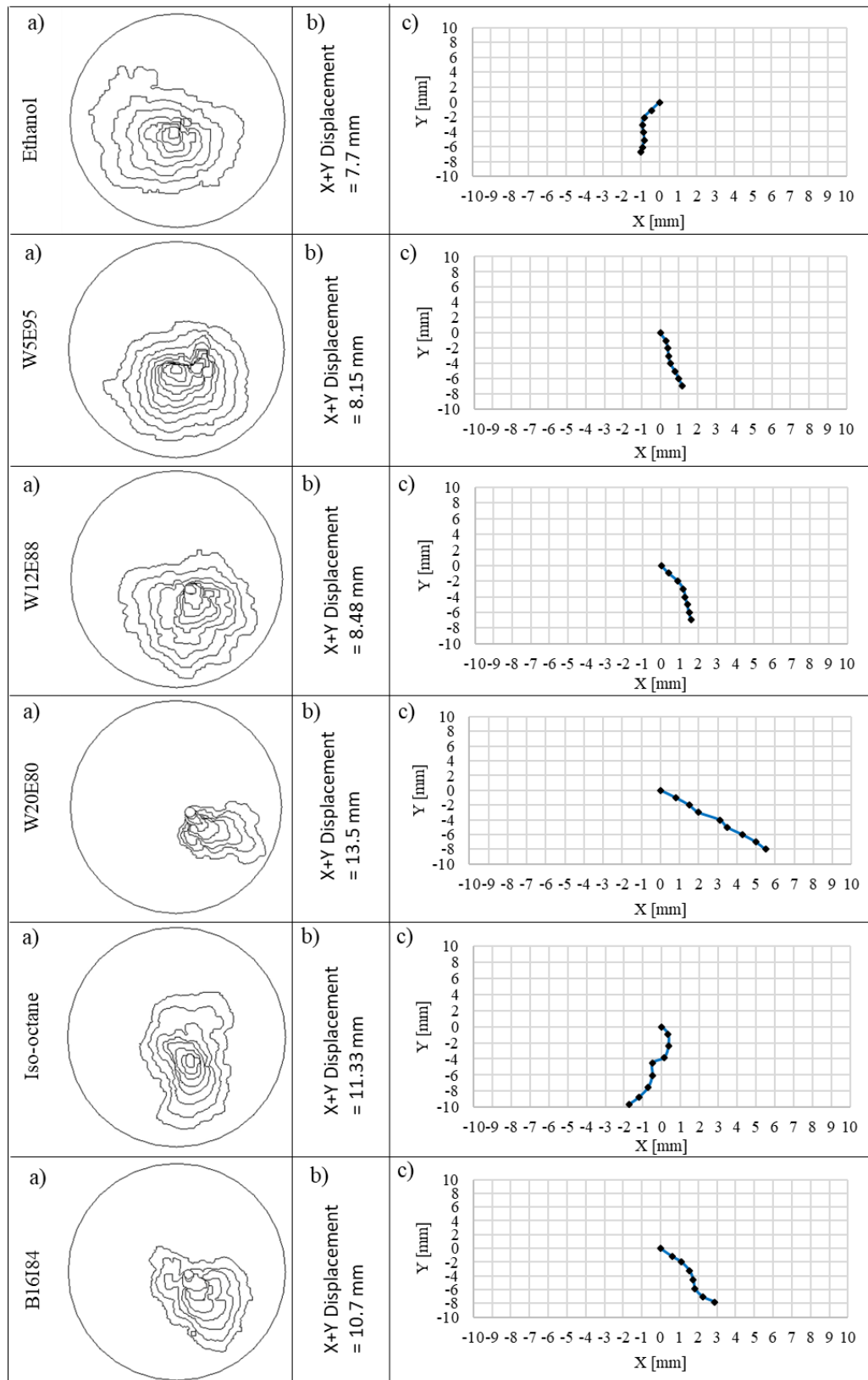


Figure 6.54. a) Flame contour for ethanol, W5E95, W12E88, W20E80, iso-octane and B16I84 closest to 60 averaged flames. b) Euclidean centroid displacement measurement for all 4 fuels closest to 60 averaged flames. (1500 rpm, 0.5 bar inlet pressure, ethanol MBT for all the fuels).

6.3.2.4 Shape Factor

Shown in Figure 6.55 to Figure 6.57 are corresponding computations of shape factor for the mean cycles, segmented in three graphs, comparing base fuels and wet ethanol blends, B16I84, E10I90, E6B8I85, E85I10W5. Finally, Figure 6.57 is representing all the fuels. The slower burning W20E80 fuel was subjected to the turbulent spectrum for a prolonged period, which resulted in increased distortion of the mean flame shape as the larger scales of turbulence were encroached towards the end of the visible propagation event. The observation of increased bulk flame distortion leading to slower burning suggests the detrimental effects of flame stretch cancel out any benefits of a larger inflamed area due to higher distortion. This may be associated with the flame tendency to migrate towards the hotter exhaust side of the engine. Recent prior PLIF and emissions measurement work [206] with iso-octane, E10 (10% ethanol in 95RON gasoline), E85 (85% ethanol in 95RON gasoline) and similar operating conditions (start of injection 270° bTDC) indicates the fuel-air charge distribution is most homogeneous at start of injection of 270° bTDC. This observation also compounds the likelihood of the hotter exhaust temperatures leading to the observed flame centroid migration. The flame can only be wrinkled by scales of turbulence smaller than the flame itself; initially, the flame is only wrinkled by the smallest scales of turbulence, larger scales merely convect and distort the flame rather than directly increasing inflamed area. As the kernel develops the larger turbulent scales wrinkle the flame until it reaches a fully developed state. where the entire turbulent spectrum can wrinkle the flame [21].

Ethanol as the fastest fuel exposed to the least flame wrinkling with the lowest average shape factor at each crank angle degrees in comparison to all tested fuels. Zoomed view section of each graph clearly shows ethanol lowest shape factor value followed by W5E95, E85I10W5, W12E88, E10I90, E6B9I85, B16I84, iso-octane. Shown at Figure 6.56 zoomed view section, it can be found at some crank angles shape factor value of B16I84 is less than E6B9I85, observing the corresponding shape factor data. Clear trend associated with this phenomenon cannot be extracted (arguably too much noise in the data due to third-dimensional flame distortion effects). In addition, this contradiction can be the reason of an error in radius of the best-fit circle calculation that could be estimated with minor error and eventually leads to this contradiction.

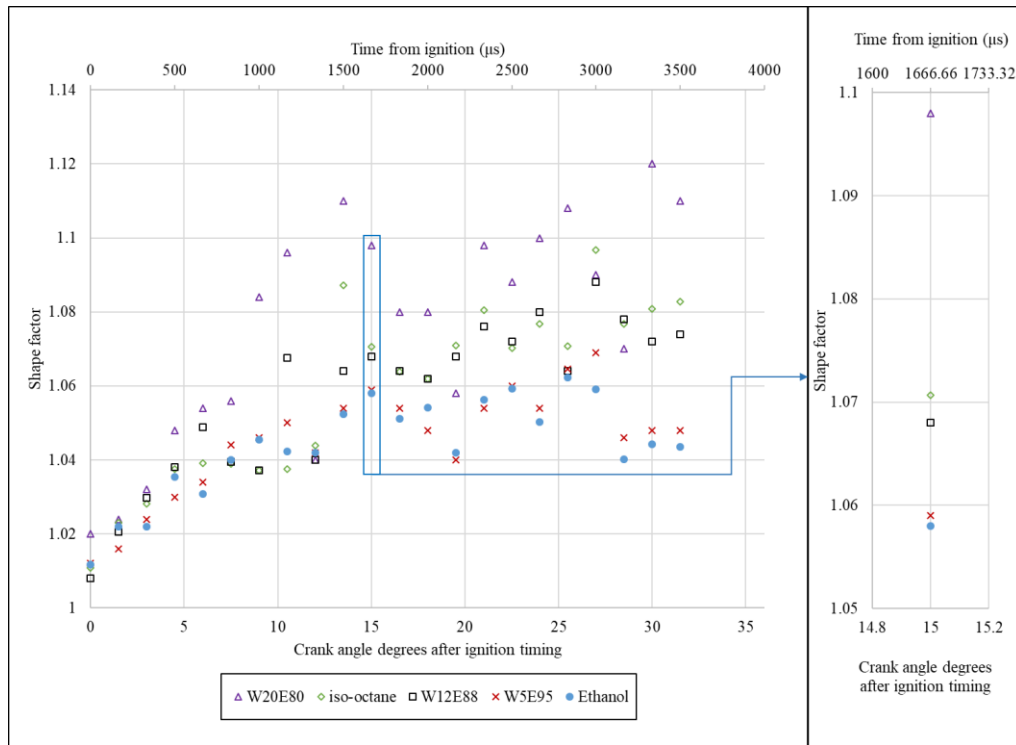


Figure 6.55. Computed shape factor speed closest data to 60 averaged cycles for base fuels and wet ethanol fuels (1500 rpm, 0.5 bar inlet pressure, ethanol MBT for all the fuels). Highlighted section was chosen at 15 CAD AIT to show the values in larger scales.

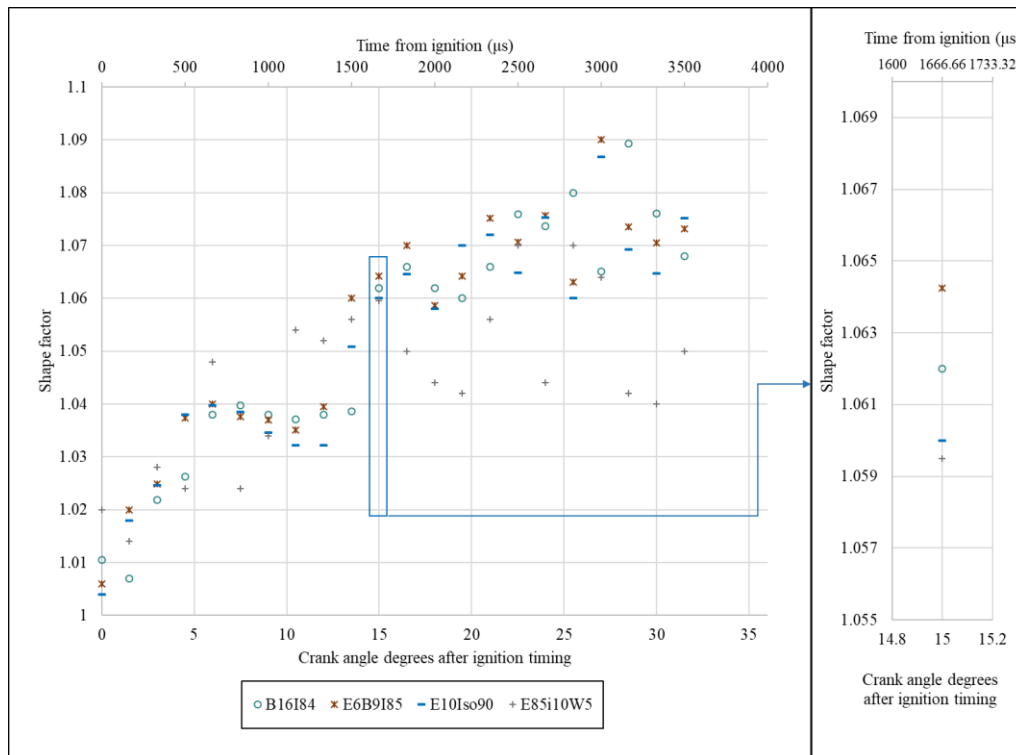


Figure 6.56. Computed shape factor closest data to 60 averaged cycles for B16I84, E10I90, E6B8I85 and E85I10W5 (1500 rpm, 0.5 bar inlet pressure, ethanol MBT for all the fuels). Highlighted section was chosen at 15 CAD AIT to show the values in larger scales.

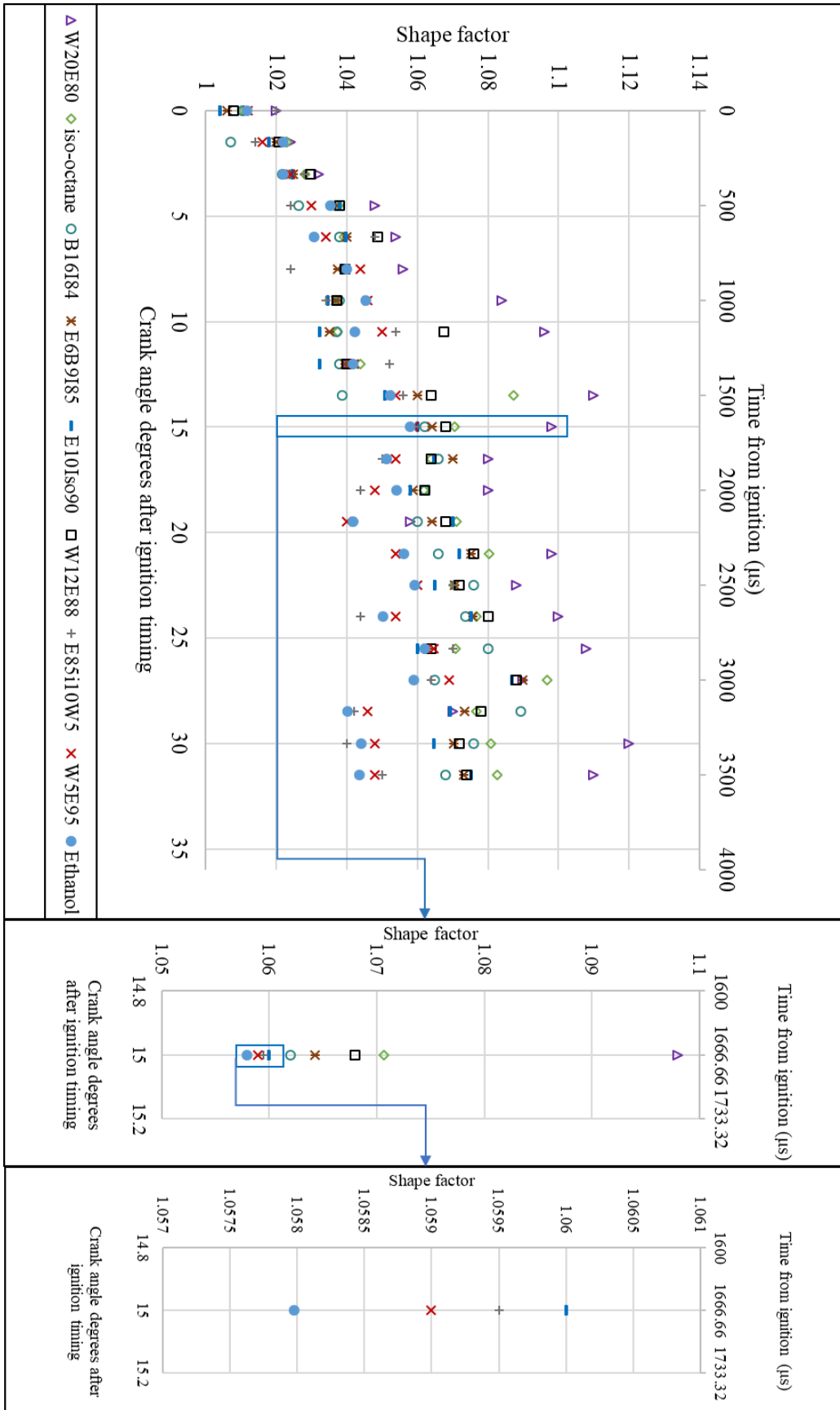


Figure 6.57. Computed shape factor closest data to 60 averaged cycles for all fuels (1500 rpm, 0.5 bar inlet pressure, ethanol MBT for all the fuels). Highlighted section was chosen at 15 CAD AIT to show the values in larger scales.

6.3.3 Burned and Unburned Gas Temperature

The predictions of unburned and burned gas temperature shown in Figure 6.58 and Figure 6.59 were produced using the two-zone heat release model explained in section 5.6.6. Subsequently, these predictions, along with the measured in-cylinder pressure data for the mean cycles, could be used to predict the laminar burning velocity for each case via equations from Heywood [31] explained in section 5.6.6.1.

Unburned gas temperature of iso-octane is the highest among all the tested fuels this is because of the higher lower heating value of iso-octane in comparison to ethanol and butanol, moreover, charge cooling effect of evaporation of ethanol is also considered to be the reason of lower temperature of ethanol. Iso-octane blends of 10% ethanol and 16% butanol reduced the unburned gas temperature in comparison to pure iso-octane. B16I84 has slightly higher unburned gas temperature in comparison to E10Iso90, due to the fact that butanol lower heating value is higher than ethanol.

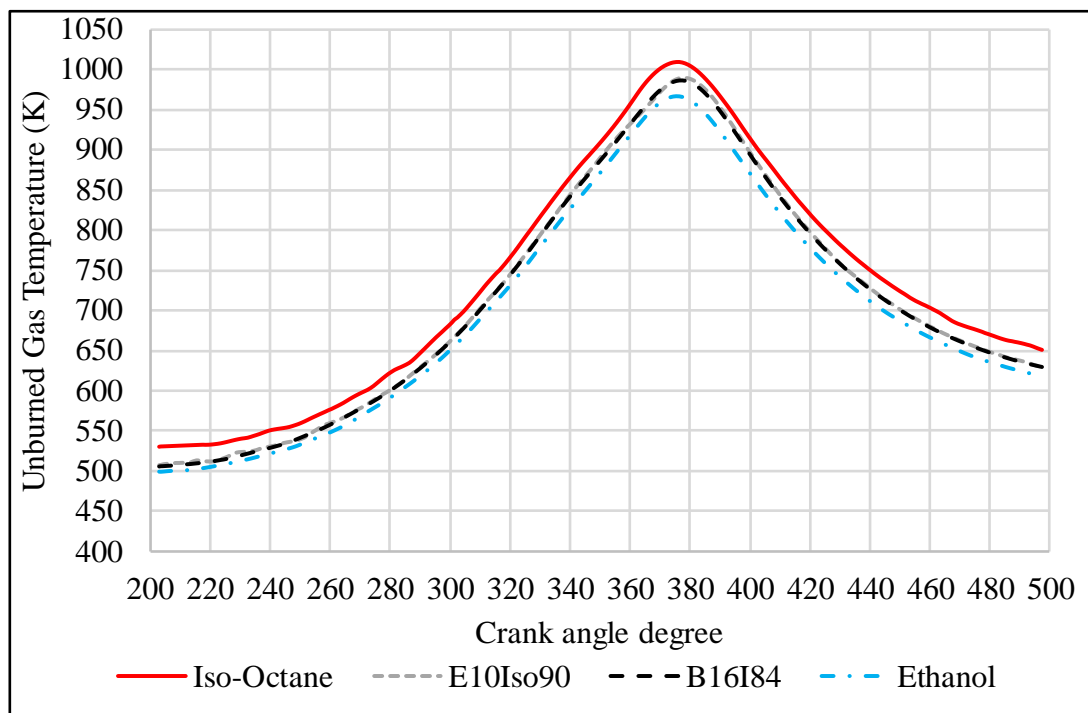


Figure 6.58. Computed values of unburnt gas temperatures for the two base fuels and iso-octane blends. Obtained from the two-zone heat release model. (1500 rpm, 0.5 bar inlet pressure, ethanol MBT for all the fuels).

Burned gas temperature of B16I84 is slightly higher than E10Iso90 and is followed closely by ethanol and iso-octane this is due to the reason that even though iso-octane

has the highest unburned gas temperature; ethanol has the highest in-cylinder pressure, this could be further explained with average gas temperature values. This calculation is scaled with mass fraction burned in a way that at the start of combustion (mass fraction burned =0) the average temperature is equal to unburned gas temperature and at the end of combustion (mass fraction burned =1) the average temperature is equal to burned gas temperature. It can be seen from the data presented in Figure 6.60 iso-octane with the highest unburned gas temperature has the lowest average burned gas temperature because of lower in-cylinder pressure in comparison to ethanol. Furthermore, E10Iso90 has the highest average gas temperature of all the fuels tested followed closely by B16I84.

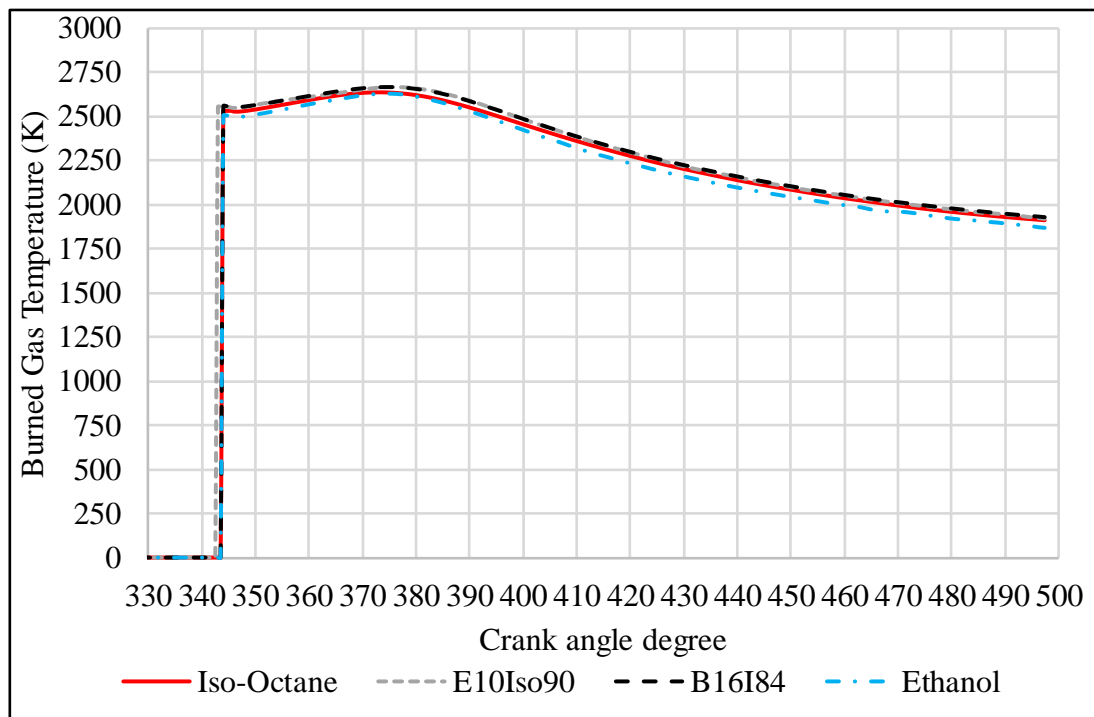


Figure 6.59. Computed values of burnt gas temperatures for the two base fuels and iso-octane blends. Obtained from the two-zone heat release model. (1500 rpm, 0.5 bar inlet pressure, ethanol MBT for all the fuels).

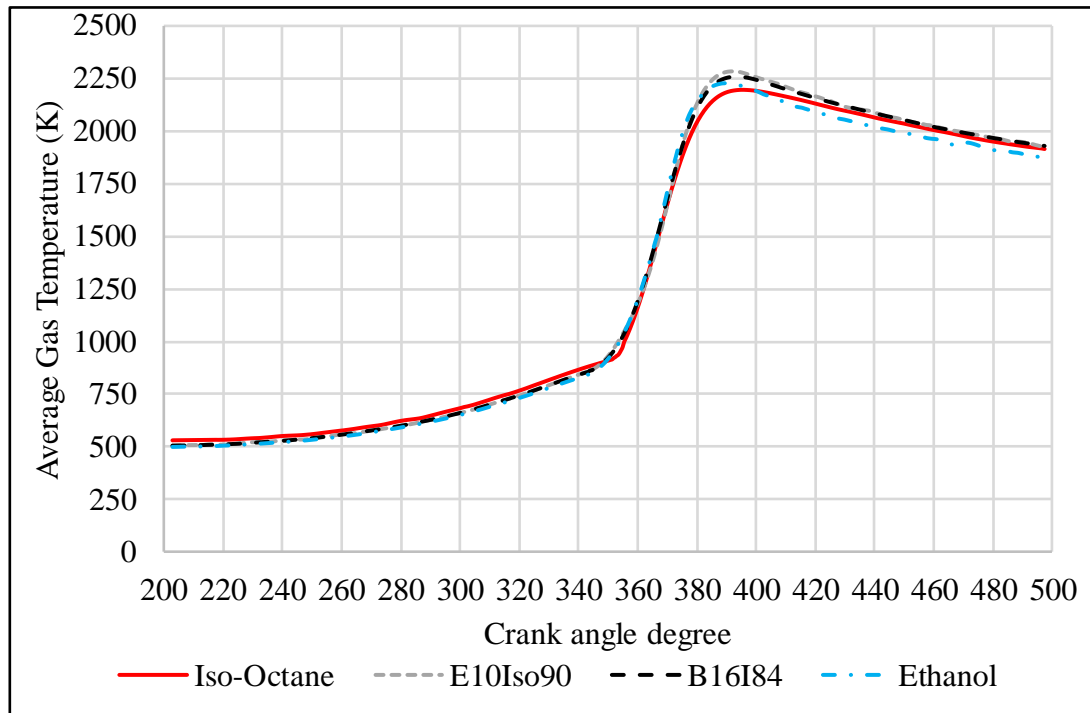


Figure 6.60. Computed values of average gas temperature scaled with mass fraction burned (at mass fraction burned=0, average temperature= unburned gas temperature and at mass fraction burned=1, average temperature= burned gas temperature), the two base fuels and iso-octane blends. Obtained from the two-zone heat release model. (1500 rpm, 0.5 bar inlet pressure, ethanol MBT for all the fuels).

Shown in Figure 6.61 is the unburned gas temperature for ethanol and hydrous ethanol blends of 5%, 12%, and 20%. It can be seen that blend of 20% water to ethanol significantly reduced unburned gas temperature almost by 15%, from 500 K to 425 K at 200 crank angle degree. This is due to the cooling effect of added water to ethanol. Similarly, 5% water in ethanol slightly reduced unburned gas temperature followed by 12% water in ethanol that reduced unburned gas by 10%, from 500 K to 450 K. Burned gas temperature of the ethanol and hydrous ethanol shows a similar trend with ethanol having the highest burned gas temperature followed by W5E95, W12E88, and W20E80 as demonstrated in Figure 6.62. Presented in Figure 6.63 the average gas temperature is also showing the highest value for ethanol with the peak temperature of approximately 2250 K, 2140 K, 2050 K, and 1825 K for ethanol, W5E85, W12E88 and W20E80 respectively. It can be seen 20% water to ethanol reduces average gas temperature by almost 20%.

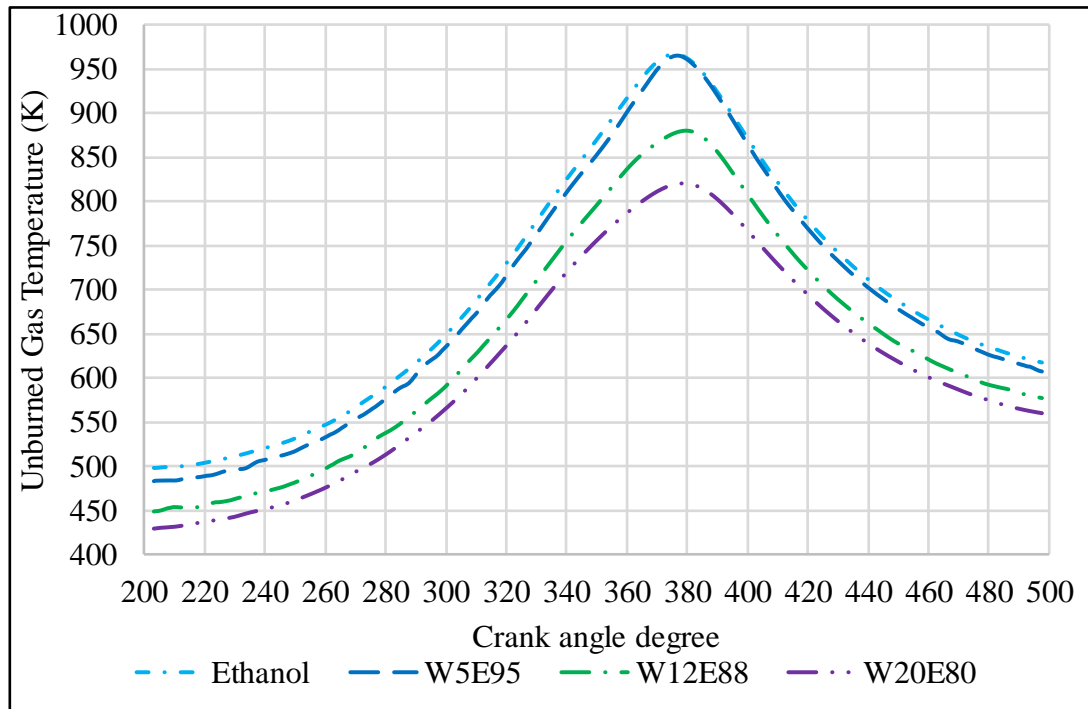


Figure 6.61. Computed values of unburnt gas temperatures for ethanol and hydrous blends. Obtained from the two-zone heat release model. (1500 rpm, 0.5 bar inlet pressure, ethanol MBT for all the fuels).

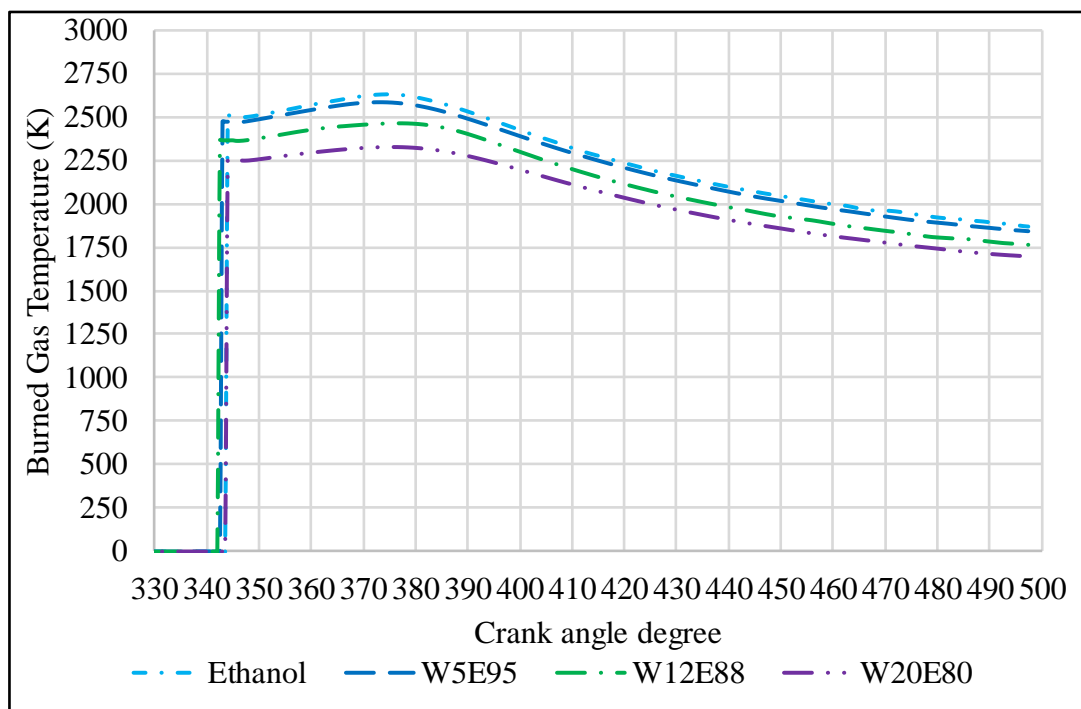


Figure 6.62. Computed values of burnt gas temperatures for ethanol and hydrous blends. Obtained from the two-zone heat release model. (1500 rpm, 0.5 bar inlet pressure, ethanol MBT for all the fuels).

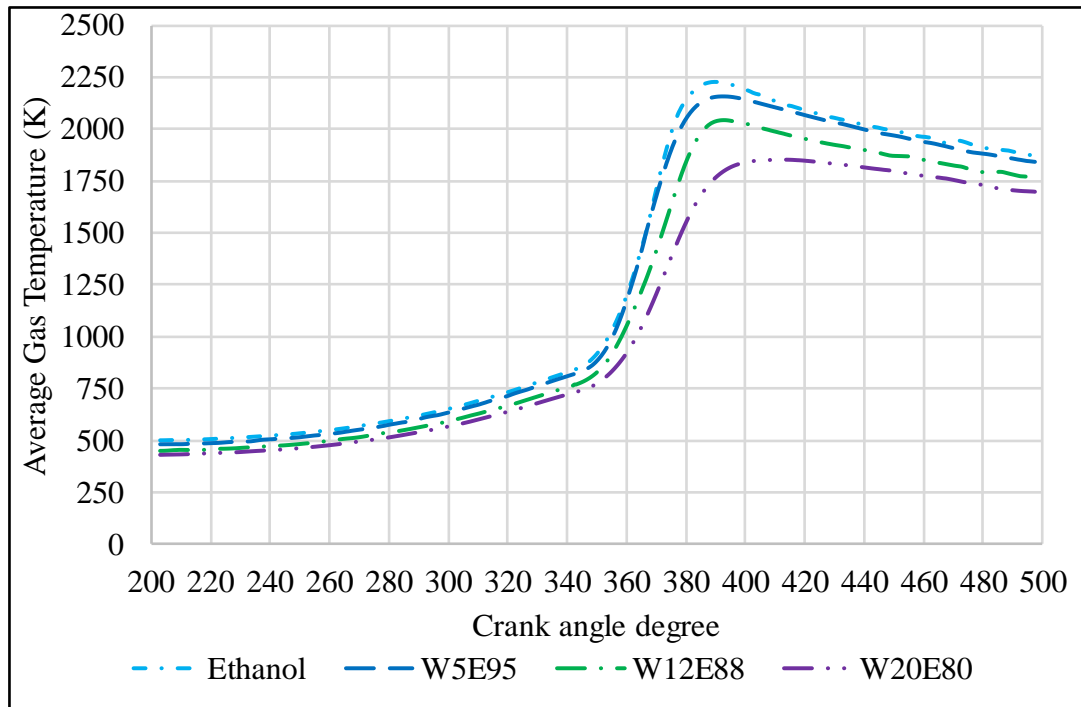


Figure 6.63. Computed values of average gas temperature scaled with mass fraction burned (at mass fraction burned=0, average temperature= unburned gas temperature and at mass fraction burned=1, average temperature= burned gas temperature), for ethanol and hydrous blends. Obtained from the two-zone heat release model. (1500 rpm, 0.5 bar inlet pressure, ethanol MBT for all the fuels).

Presented in Figure 6.64 to Figure 6.66 are the unburned, burned, and average gas temperature for all the fuels tested in one graph, it can be seen iso-octane has the highest peak unburned gas temperature of slightly above 1000K and W20E80 has the lowest peak unburned gas temperature of 825K. However, computed burned gas temperature figure shows the highest value for B16I84 and the lowest temperature for W20E80. Average gas peak temperature scaled with mass fraction burned, from highest to lowest are 2300K, 2260K, 2250K, 2200K, 2125K, 2050K, and 1800K for E10Iso90, B16I84, ethanol, iso-octane, W5E95, W12E85 and W20E80 respectively.

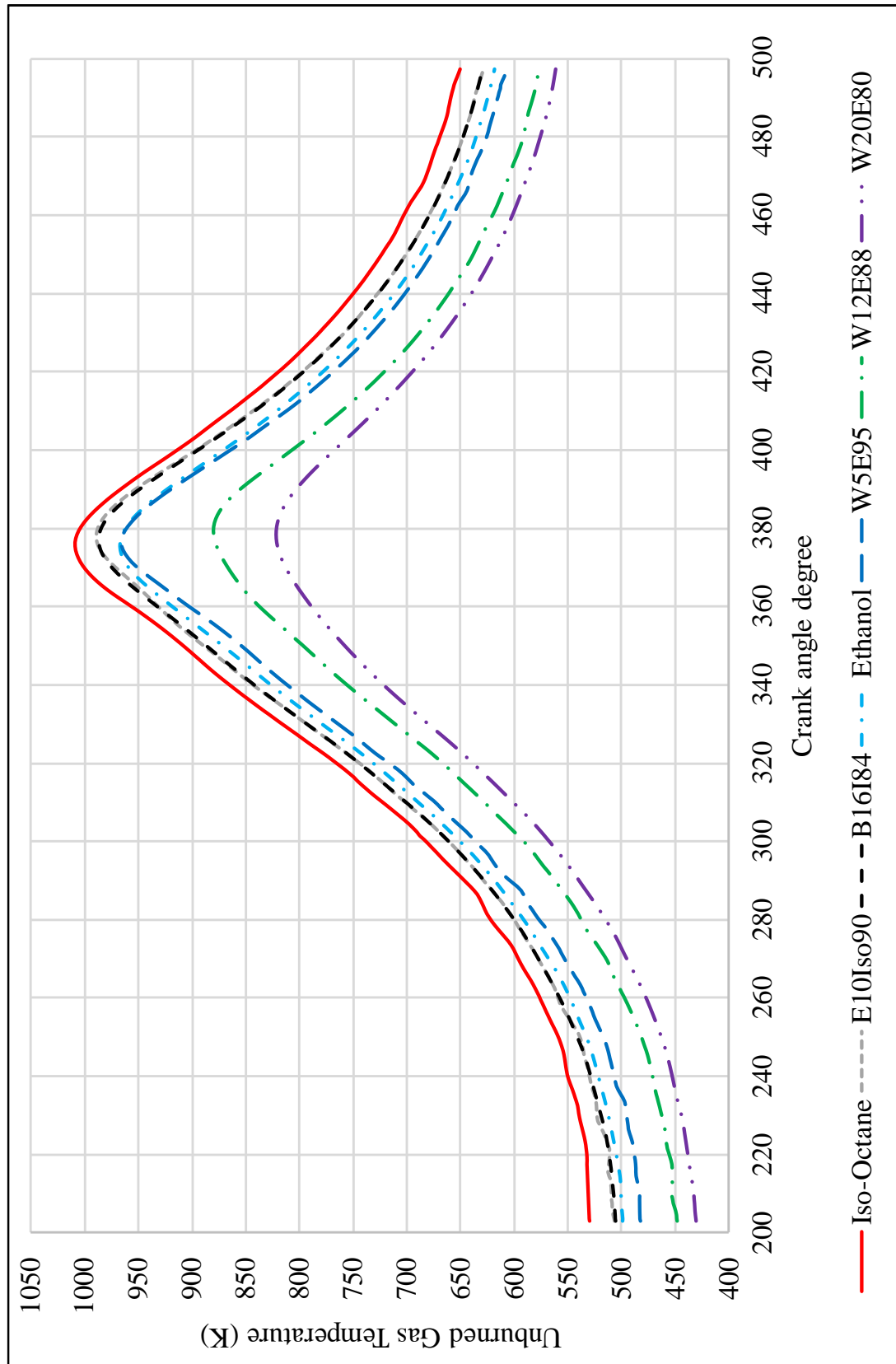


Figure 6.64. Computed values of unburnt gas temperatures for all the fuels tested. Obtained from the two-zone heat release model. (1500 rpm, 0.5 bar inlet pressure, ethanol MBT for all the fuels).

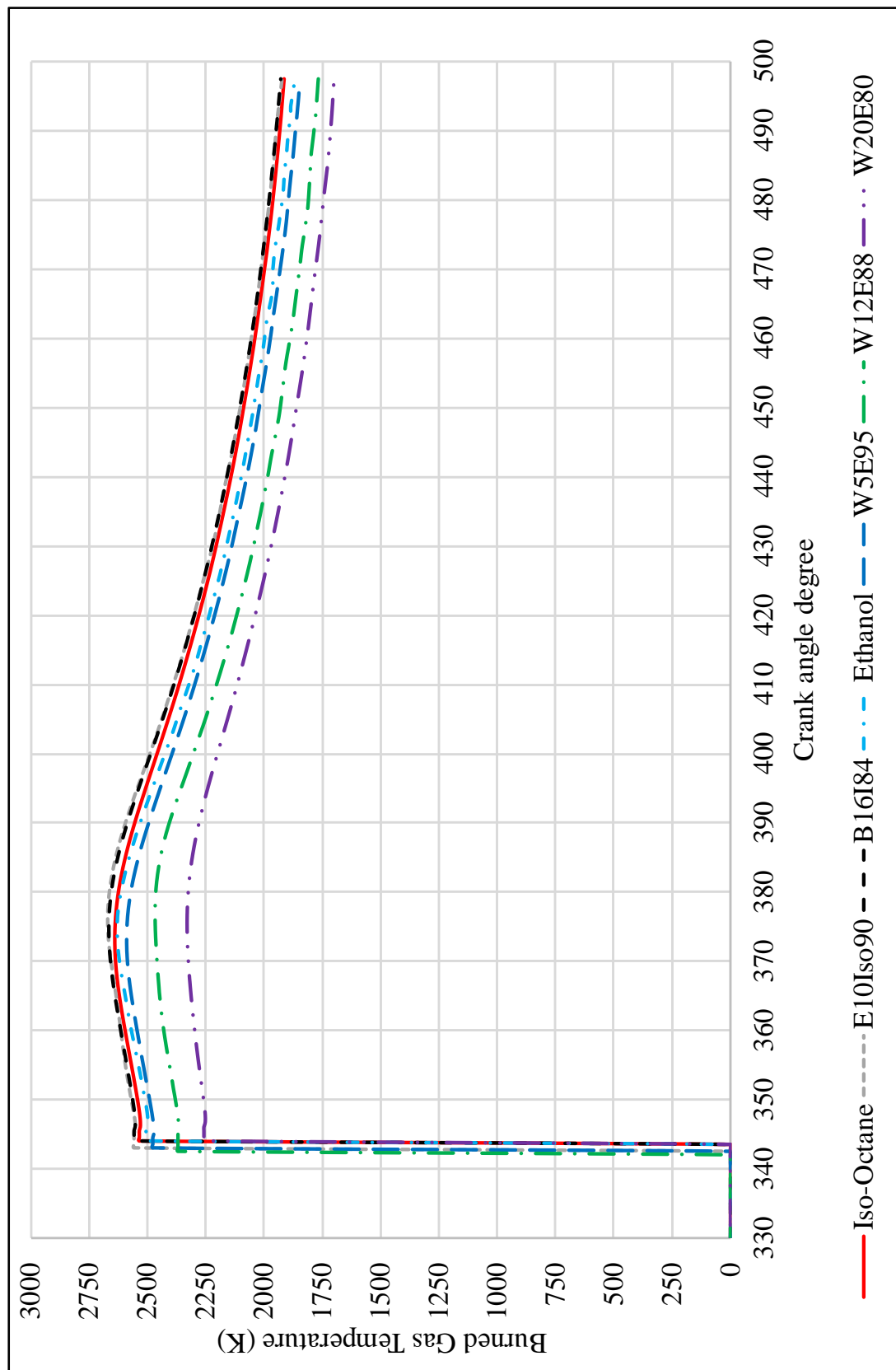


Figure 6.65. Computed values of burnt gas temperatures for all the fuels tested. Obtained from the two-zone heat release model. (1500 rpm, 0.5 bar inlet pressure, ethanol MBT for all the fuels).

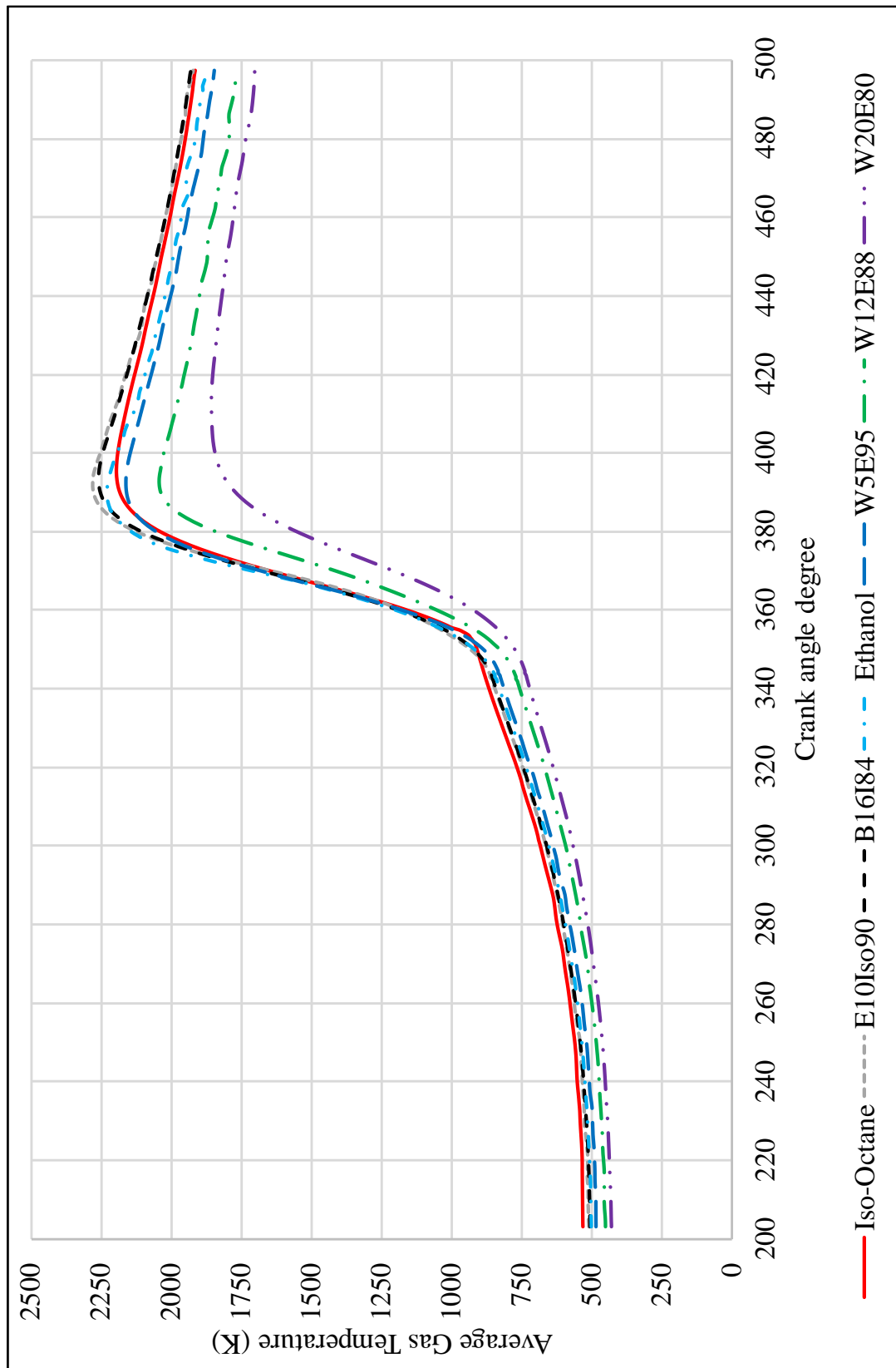


Figure 6.66. Computed values of average gas temperature scaled with mass fraction burned (at mass fraction burned=0, average temperature= unburned gas temperature and at mass fraction burned=1, average temperature= burned gas temperature), for all the fuels tested. Obtained from the two-zone heat release model. (1500 rpm, 0.5 bar inlet pressure, ethanol MBT for all the fuels).

6.3.4 Laminar Burning Velocity

Considering the predicted values shown in Figure 6.67 in a qualitative manner, it can be seen that faster burning would be expected in the pure ethanol case with the maximum value of 1.68 m/s, despite the lower initial starting temperature in the chamber due to the thermodynamic properties and charge state incurred with this fuel. The computed laminar burning velocity of E10Iso90 was slightly higher than iso-octane with the maximum value of 1.35 and 1.31 m/s respectively, this was because of added 10% ethanol and were in a good agreement with the laminar burning velocity data presented in Table 6.1.

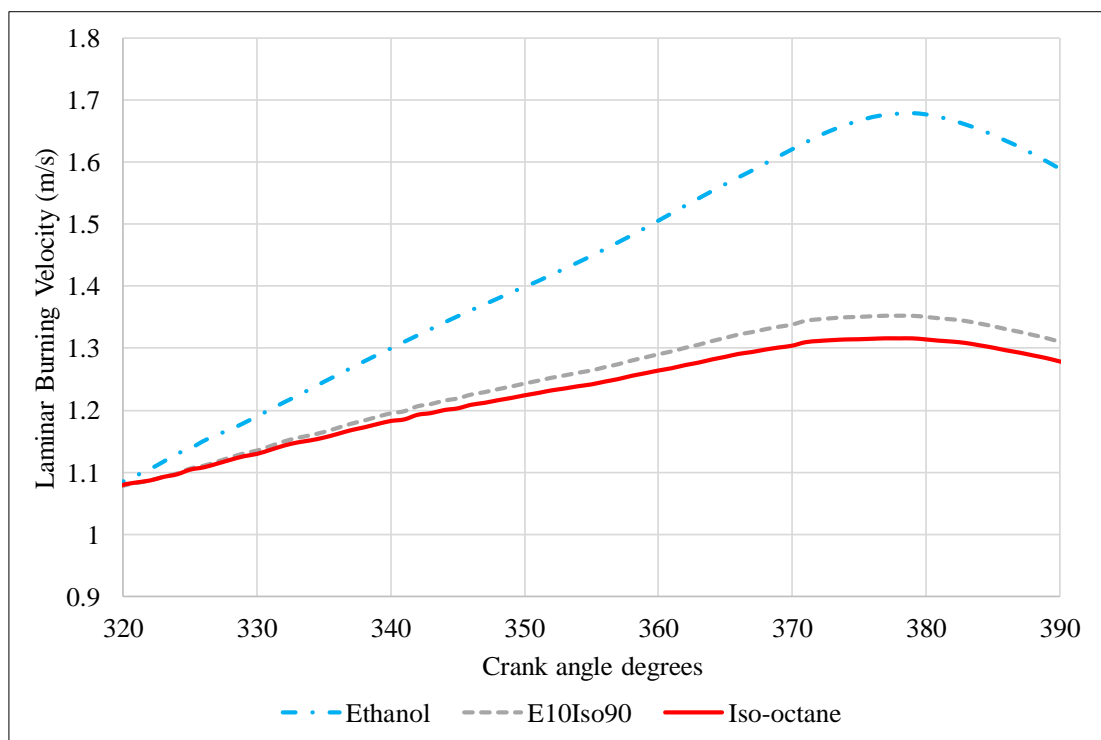


Figure 6.67. Computed values of laminar burning velocity for the ethanol, iso-octane, and E10Iso90. (1500 rpm, 0.5 bar inlet pressure, ethanol MBT for all the fuels).

7. Conclusion & Recommendations

7.1 Summary of Results

Two-dimensional Particle Image Velocimetry (PIV) and flame image analysis has been undertaken and compared to CFD k- ϵ RNG modelling to understand the interaction of the in-cylinder flow and flame with ethanol, iso-octane, B16I84, E10I90, E6B8I85, E85I10W5 and hydrous ethanol at 5%, 12% and 20% volume water fuels in a spark ignition engine with a modern direct injection combustion chamber layout. The fixed spark timing was set to equal that of the MBT timing for ethanol. In terms of combustion stability, the worst performing fuel was still operating well below the imposed limit of 5% COV of IMEP.

Initial flame development plays a significant role during the transition toward a fully developed state, the flame can only be wrinkled by scales of turbulence smaller than the flame itself; larger scales merely serve to convect and distort the flame rather than directly improving inflamed area. Because of the faster chemistry, initial flames can develop more quickly, hence more of the turbulent spectrum will become available more quickly to aid flame wrinkling and improve the rate of unburned mass entrainment into the flame. Faster initial chemical reaction rates of high ethanol content fuels in SI engines drive from such physical effects. It can also be concluded that the opposite is true for the slower burning fuels, while ethanol was aided by the knock-on effect of a faster laminar burning velocity, fuels with a slower laminar burning velocity may be negatively influenced by the flow. This is more evident in the slower fuels such as water blends and iso-octane with the lower laminar burning velocity, hence the flame kernel may be more heavily distorted by the turbulent spectrum.

Under the part-load experimental operating conditions tested, PIV experiments indicated that the mean flow-field for this engine on the swirl plane is nearly symmetrical across four divided zones of the combustion chamber at the time of combustion initiation this was previously showed at Table 6.3 and validated with

computational fluid analysis.

In addition, this work further serves to highlight the difference between a blended fuel's combustion characteristics and those of its constituent fuels. In 2010 Beeckmann, Kruse and Peters [207] conducted several studies into burning velocities for different neat alcohol fuels. It was reported that butanol has a faster laminar burning velocity than iso-octane and ethanol. Even though this data was gathered in a bomb, it demonstrated that blended fuels have vastly different laminar burning velocities when compared to their constituent fuels and even the authors stated they were unsure of the exact reasons as to why this occurred. Moreover, Beeckmann [207] mentioned that E10 was 5cm/s faster than Bu10. It is important to note these two fuels were not equal in oxygen content, this result would indicate that the two fuels are not identical in burn structure and propagation during the laminar phase, contrary to the tested fuels presented here. This emphasizes that care should be taken when consulting the literature for laminar burning velocities as they are by no means definitive nor are they indicative of standard engine operating conditions. One out of the five correlations presented from literature, only one factored in the flame stretch and instability effects and none accounted for flame centre displacement.

Symmetrical bulk air flow in the piston during the compression showed the minimal effect of the flow on the flame so high speed flame imaging was done to understand the flame. Comparing the flame radius development of 60 averaged cycles, ethanol exhibited faster flame propagation, the rate of mass burning and in-cylinder pressure development, all are in good agreement with burning velocity correlations within the literature. The maximum flame radius measured for ethanol, W5E95, W12E88 and W20E80 were 19.04, 18.20, 17.45 and 15 mm respectively. The difference between the fastest and slowest fuel at 15 crank angle degrees after ignition timing was small and about 1.03 mm. Also, the maximum flame speed of 8.2m/s was achieved at 33 CAD AIT for W20E80 (the same flame speed achieved at 24 CAD AIT for ethanol in comparison). Blending water with ethanol was done to study the effect of flame characteristics. By adding 5% water to ethanol the combustion appeared to be marginally slower. An attempt was made to validate these results with calculated burned and unburned gas temperature of hydrous ethanol, which were in good agreement.

By adding 20% water to ethanol the combustion appeared to be noticeably slower with a tremendous increase in flame shape distortion as quantified by shape factor values. This was due to the fact that the increased amount of water decreased in-cylinder pressure, burned and unburned gas temperature. Variety of different blends tested also showed the faster fuel (higher laminar burning velocity) leads to faster combustion for example by adding 16% n-butanol to iso-octane the combustion appeared to be faster than pure iso-octane. An attempt was made to compare these results with laminar burning velocity correlations shown in Table 6.1, which were clearly in a good agreement. Ethanol as the fastest fuel exposed to least flame wrinkling with the lowest average shape factor at each crank angle degrees in comparison to all tested fuels. W5E95 has the second lowest shape factor value followed by E85I10W5, W12E88, E10I90, E6B9I85, B16I84, Iso-octane and W20 E80.

The flame images obtained with all fuels showed a tendency for biased flame growth towards the exhaust valves. The PIV flow field showed no bulk motion toward the exhaust in the imaging plane. The use of pure ethanol resulted in faster combustion and higher resistance to such flame migration. This benefit diminished with the addition of water, in good agreement with recent laminar burning velocity correlations for hydrous ethanol. Temperature analysis shows the highest unburned gas temperature for iso-octane out of all the tested fuels due to the fuel properties such as a higher lower heating value in comparison to other tested fuels. However, by adding 16% n-butanol to iso-octane the average gas temperature appeared to be slightly higher than pure iso-octane, also adding 10% ethanol to iso-octane increased average gas temperature. These results were in a good agreement with the faster burning chemistry of tested fuels.

On the contrary, by adding 5% water to ethanol the combustion temperature appeared to be slightly lower. This is mainly because adding water has an influence on the cooling effect. Water has a higher latent heat of vaporization and a higher specific heat capacity than ethanol. Because the stoichiometric air quantity (L_s) decreases with higher water content, the latent heat of vaporization per kg air increases significantly and this leads to an even bigger cooling effect of the intake charge. The water vapor dilution of the air-fuel mixture yields a lower laminar burning velocity and lower adiabatic flame temperature. Because of the lower laminar burning velocity, the combustion process takes more time to complete and is less isochoric.

Also, by adding 12% and 20% water to ethanol significantly reduced both unburned and burned gas temperature, mainly because of water cooling effect and negative lower heating value of water and decreased the calorific value of the blended fuel. Out of the hydrous ethanol blends tested in this study water in ethanol content (v/v) of 12% is considered to represent a maximum tolerable limit in terms of flame distortion, with 7% slower maximum flame speed and 10% more flame distortion in comparison to pure ethanol but similar distortion to an iso-octane baseline case.

Prior research has indicated adequate charge homogeneity in this engine during such operation [206]. Larger scales of turbulence around the spark plug may have been responsible for the migration of the flame towards the exhaust, however, it is believed that any remaining large-scale tumble would still have manifested in higher velocities in the horizontal imaging plane. This phenomenon was more likely associated with the hotter wall temperatures at the exhaust side of the bore.

Similar in-cylinder flow motion and structure were predicted by the 3-D CFD computations adopting both turbulence models. However, at specific crank angles for example soon after BTDC and up to mid compression stroke, or even late compression stroke, the RNG model demonstrated slightly better agreement with the measured data. At crank angle timings close to peak intake valve lift the CFD results indicated a clear difference in behaviour from the measured values of velocity by showing a large dip in the velocity component in the direction of the piston's motion. This was identified as a result of the different tumble flow pattern detected in the CFD results at that particular crank angle.

Finally, comparisons between PIV and CFD data showed very similar velocity magnitudes as the end of compression was approached. At earlier crank angle timings (e.g. 90° CA BTDC) the CFD results showed a clear difference from the measured values of velocity (possibly associated with the persisting bulk air flow structures in the real engine). The effects of the injection event on the flow were neglected, albeit injection occurred early in the cycle at 270° bTDC.

7.2 Claims for Originality

The work was concerned with quantifying the interaction of the flow with the flame and vice versa with potential new alcohol blended fuels of reduced source to wheel energy consumption and hence lower carbon footprint. The study led to new observations of bulk flame distortion and migration effects, with potential significant consequences in future engine design.

It was concluded in-cylinder flow is symmetrical so, high speed chemiluminescence flame study was done to understand the flame characteristics in detail. This study investigated the flame cellularity and demonstrated how centre of the flame is moved through the flame propagation. In addition, several flame related parameters, such as shape factor and apparent flame speed, are discussed and compared with the flow and heat release analysis.

Fastest combustion was observed with ethanol, that was in a good agreement with laminar burning velocity correlations within the literature. The ethanol could be seen to offset the tendency of migration of the flame toward the exhaust walls. This exhaust migration phenomenon has been noted previously by others in optical pent-roofed engines but without both flow and flame imaging data being available. The results may imply that the spark plug should ideally be biased further towards the intake side of the chamber if the flame is to approach the intake and exhaust walls at similar times. Such a layout is typically not preferred due to the priority given to central fuel injector location and maximizing the size of the inlet valves for improved volumetric efficiency.

The final investigation of this thesis was concerned with the effect of water in ethanol. This investigation uncovered the degree of residual water content that can be reasonably tolerated in terms of combustion characteristics in future ethanol SI engines (with the energy required to reduce water levels then potentially reduced). Out of the hydrous ethanol blends tested in this study water in ethanol content (v/v) of 12% is considered to represent a maximum tolerable limit in terms of flame distortion, with 7% slower maximum flame speed and 10% more flame distortion in comparison to pure ethanol but similar distortion to an iso-octane baseline case.

7.3 Recommendations for Future Work

Future work should be concerned with the need for side window imaging to eliminate possible bulk flow effects in the third dimension. It would be better to have a fully optical engine design (glass liner with pent roof access). This would also solve the current limitation of PIV until 30° CA BTDC only. In the current combustion chamber, design side windows and metal clamps must be removed in order to clean the piston crown. It would be better to design optical access in a way that optical window is placed and sealed permanently inside a metal frame. This would increase experiment precision due to easier access to clean optical instruments and reduce overall maintenance. It is strongly recommended that the optical piston design is revisited, with the reasons for apparent high blow-by investigated and resolved. This may require a new piston to be designed including reduced top-land and inter-ring volumes (which would be necessary if the rings were to run on a glass liner anyway).

It would also be useful to evaluate the effects of water content under high load multi-cylinder conditions with elevated compression ratios in an attempt to understand the influence of the water on the octane appetite of the engine. In addition, variable boost pressure and exhaust back pressure should be provided to simulate the interactions between the engine and a turbocharger. Some caution is still required, as optical engines are only fired for a limited period and pressure, so this may exhibit larger variations in wall temperatures than during fully warm operation in “real” engines.

The current high speed camera was capable of recording around 30 combustion cycles and data had to be transferred to a computer to take another set of tests. High speed flame imaging of 60 cycles was considered robust enough for image analysis. So, each test had to be repeated twice, which could be a reason for some variations. Due to cyclic variations, it would be suggested to use a high speed camera capable of higher buffer size and memory storage to record a minimum of 100 cycles in a single firing test.

It would be ideal to use two-line PLIF for temperature distribution measurements, this would help to understand the combustion in more detail.

It is also suggested to use a robust CFD method to simulate both LES cold flow and combustion. However, the evaluation and calibration of the fuel injection and spray

models will be required. In addition, the combustion model needs to be developed to predict the heat release process and engine performance. Both spark ignition flame propagation and auto-ignition models should be included in the combustion modelling.

Large eddy simulation is highly suggested to be used to predict the flow inside the cylinder, however, this method is computationally expensive and requires further caution, selecting an appropriate filter function to solve large eddies and simulate smaller size eddies.

It would be suggested to implement state of the art techniques for PIV analysis such as local correlation averaging and correlation multiplication. These techniques can be used to enhance the correlation peak height and reduce the noisy peaks, hence, eliminate sparse vector generated with Dantecstudio software in this study.

8. References

- [1] Fraser N, Blaxill H, Lumsden G, Bassett M. Challenges for Increased Efficiency through Gasoline Engine Downsizing. *SAE Int J Engines* 2009;2:2009-01-1053. doi:10.4271/2009-01-1053.
- [2] Turner J, Popplewell A, Patel R, Johnson T.R, Darnton N.J, Richardson S, et al. Ultra Boost for Economy: Extending the Limits of Extreme Engine Downsizing. *SAE Int* 2014;7:387–417. doi:10.4271/2014-01-1185.
- [3] Bassett M, Hall J, Kennedy G, Cains T, Powell J, Warth M. The Development of a Range Extender Electric Vehicle Demonstrator. *SAE Tech. Pap.*, 2013. doi:10.4271/2013-01-1469.
- [4] Ricardo. Driving automotive electrification white paper. 2017.
- [5] Ladisch MR, Dyck K. Dehydration of ethanol: new approach gives positive energy balance. *Science* 1979;205:898–900. doi:10.1126/science.205.4409.898.
- [6] Flowers DL, Aceves SM, Frias JM. Improving Ethanol Life Cycle Energy Efficiency by Direct Utilization of Wet Ethanol in HCCI Engines. *SAE Tech. Pap.*, 2007, p. 1070–8. doi:10.4271/2007-01-1867.
- [7] Mack JH, Aceves SM, Dibble RW. Demonstrating direct use of wet ethanol in a homogeneous charge compression ignition (HCCI) engine. *Energy* 2009;34:782–7. doi:10.1016/j.energy.2009.02.010.
- [8] López-Plaza EL, Hernández S, Barroso-Muñoz FO, Segovia-Hernández JG, Aceves SM, Martínez-Frías J, et al. Experimental and theoretical study of the energy savings from wet ethanol production and utilization. *Energy Technol* 2014;2:440–5. doi:10.1002/ente.201300180.
- [9] Saffy H a, Northrop WF, Kittelson DB, Boies AM. Energy , carbon dioxide and water use implications of hydrous ethanol production. *Energy Convers*

- Manag 2015;105:900–7. doi:10.1016/j.enconman.2015.08.039.
- [10] Lanzasova TDM, Dalla Nora M, Zhao H. Performance and economic analysis of a direct injection spark ignition engine fueled with wet ethanol. *Appl Energy* 2016;169:230–9. doi:10.1016/j.apenergy.2016.02.016.
- [11] Brewster S, Railton D, Maisey M, Frew R. The Effect of E100 Water Content on High Load Performance of a Spray Guide Direct Injection Boosted Engine. *SAE Tech. Pap.*, 2007. doi:10.4271/2007-01-2648.
- [12] Lanzasova TDM, Vielmo HA, Sari RL, Dornelles HM, Tatsch GA, Martins MES, et al. Performance Analysis of a Spark Ignited Engine Running on Different Water-in-Ethanol Mixtures. *SAE Tech. Pap.*, 2013. doi:10.4271/2013-36-0202.
- [13] Chu, S., & Majumdar A. Opportunities and challenges for a sustainable energy future. *Nature* 2012. doi:10.1038/nature11475.
- [14] Munsin R, Laonual Y, Jugjai S, Imai Y. An experimental study on performance and emissions of a small SI engine generator set fuelled by hydrous ethanol with high water contents up to 40%. *Fuel* 2013;106:586–92. doi:10.1016/j.fuel.2012.12.079.
- [15] Morganti K, Almansour M, Khan A, Kalghatgi G, Przesmitzki S. Leveraging the benefits of ethanol in advanced engine-fuel systems. *Energy Convers Manag* 2018;157:480–97. doi:10.1016/j.enconman.2017.11.086.
- [16] Siewert RM, Groff EG. Unassisted Cold Starts to –29 C and Steady-State Tests of a Direct-Injection Stratified-Charge (DISC) Engine Operated on Heat Alcohols. *SAE Technical Paper*; 1987. doi:10.4271/872066.
- [17] Davis GW, Bouboulis J, Heil ET. The effect of a multiple spark discharge ignition system and spark plug electrode configuration on cold starting of a dedicated E85-fueled vehicle. *34th Intersoc Energy Convers Eng Conf* 1999. doi:10.4271/1999-01-2664.
- [18] Malcolm J, Behringer M, Aleiferis P, Mital J, OudeNijeweme D. Characterisation of Flow Structures in a Direct-Injection Spark-Ignition Engine using PIV, LDV and CFD. *SAE Tech Pap* 2011-01-1290 2011.

- doi:10.4271/2011-01-1290.
- [19] Suyabodha A, Pennycott A, Brace CJ. A preliminary approach to simulating cyclic variability in a port fuel injection spark ignition engine. *Proc Inst Mech Eng Part D J Automob Eng* 2013;227:665–74.
doi:10.1177/0954407012455972.
- [20] Gillespie L, Lawes M, Sheppard CGW, Woolley R. Aspects of Laminar and Turbulent Burning Velocity Relevant to SI Engines. *Sae Tech Pap Ser* 2000.
doi:10.4271/2000-01-0192.
- [21] Moxey BG, Cairns A, Zhao H. A Study of Turbulent Flame Development with Ethanol Fuels in an Optical Spark Ignition Engine. *SAE Pap* 2014.
doi:10.4271/2014-01-2622.
- [22] Cairns A, Sheppard CGW. Cyclically Resolved Simultaneous Flame and Flow Imaging in a SI Engine. *SAE Tech. Pap.*, 2000. doi:10.4271/2000-01-2832.
- [23] Reuss D, Bardsley M, Felton P. Velocity, vorticity, and strain-rate ahead of a flame measured in an engine using particle image velocimetry. *SAE Trans* 1990. doi:10.4271/900053.
- [24] US EPA Climate Change Division. Greenhouse Gases Overview. *Greenh Gas Emiss* 2014. <http://www.epa.gov/climatechange/ghgemissions/gases.html>.
- [25] UNFCCC. Adoption of the Paris Agreement. Report No. FCCC/CP/2015/L.9/Rev.1.,. 2015.
- [26] The Society of Motor Manufacturers and Traders Limited. *New Car CO2 Report 2015 The 14th report*. 2015.
- [27] U.S. Energy Information Administration. *International Energy Outlook 2016*. vol. 0484(2016). 2016. doi:www.eia.gov/forecasts/ieo/pdf/0484(2016).pdf.
- [28] European Commission. *Reducing CO2 emissions from passenger cars - European Commission*. *EC Clim Policy* 2016:28–30.
- [29] Mock P. EU CO2 standards for passenger cars and light-commercial vehicles. *Int Counc Clean Transp* 2014:1–9.
- [30] Stone R, 1955- RS. *Introduction to internal combustion engines*. 2012.

doi:10.1017/CBO9781107415324.004.

- [31] Heywood JB. *Internal Combustion Engine Fundamentals*. vol. 21. 1988.
- [32] Heywood JB. Pollutant formation and control in spark-ignition engines. *Prog Energy Combust Sci* 1976;1:135–64. doi:10.1016/0360-1285(76)90012-5.
- [33] Vafamehr H, Cairns A, Sampson O, Koupaie MM. The competing chemical and physical effects of transient fuel enrichment on heavy knock in an optical spark ignition engine. *Appl Energy* 2016;179:687–97. doi:10.1016/j.apenergy.2016.07.038.
- [34] Hattrell T, Sheppard CGW, Burluka a. a., Neumeister J, Cairns a. Burn Rate Implications of Alternative Knock Reduction Strategies for Turbocharged SI Engines. *SAE Tech Pap* 2006-01-1110 2006. doi:2006-01-1110.
- [35] Wang Z, Liu H, Reitz RD. Knocking combustion in spark-ignition engines. *Prog Energy Combust Sci* 2017;61:78–112. doi:10.1016/j.pecs.2017.03.004.
- [36] Taylor J, Fraser N, Wieske P. Water Cooled Exhaust Manifold and Full Load EGR Technology Applied to a Downsized Direct Injection Spark Ignition Engine. *SAE Int J Engines* 2010;3:225–40. doi:10.4271/2010-01-0356.
- [37] Turner JWG, Pearson RJ, Curtis R, Holland B. Improving Fuel Economy in a Turbocharged DISI Engine Already Employing Integrated Exhaust Manifold Technology and Variable Valve Timing 2008. doi:10.4271/2008-01-2449.
- [38] Hires SD, Tabaczynski RJ, Novak JM. The Prediction of Ignition Delay and Combustion Intervals for a Homogeneous Charge, Spark Ignition Engine 1978. doi:10.4271/780232.
- [39] Kulzer A, Christ A, Rauscher M, Sauer C, Würfel G, Blank T. Thermodynamic Analysis and Benchmark of Various Gasoline Combustion Concepts 2006. doi:https://doi.org/10.4271/2006-01-0231.
- [40] Osborne RJ, Li G, Sapsford SM, Stokes J, Lake TH, Heikal MR. Evaluation of HCCI for Future Gasoline Powertrains 2003. doi:https://doi.org/10.4271/2003-01-0750.
- [41] Atkins MJ, Koch CR. A Well-to-Wheel Comparison of Several Powertrain

- Technologies 2003. doi:<https://doi.org/10.4271/2003-01-0081>.
- [42] Cairns A, Blaxill H. Lean Boost and External Exhaust Gas Recirculation for High Load Controlled Auto-Ignition. SAE Tech Pap 2005;2005013744. doi:10.4271/2005-01-3744.
- [43] King J, Schmidt L, Stokes J, Seabrook J, Nor F, Sahadan S. Multiple injection and boosting benefits for improved fuel consumption on a spray guided direct injection gasoline engine. Intern. Combust. Engines Improv. Performance, Fuel Econ. Emiss., 2011, p. 13–26. doi:10.1533/9780857095060.
- [44] Stephenson M. Engine Downsizing—An Analysis Perspective. SIMULIA Cust. Conf., 2009.
- [45] Bandel W, Fraidl GK, Kapus PE, Sikinger H, Cowland CN. The turbocharged GDI engine: boosted synergies for high fuel economy plus ultra-low emission. SAE Technical Paper; 2006. doi:10.4271/2006-01-1266.
- [46] Zhao H. Advanced direct injection combustion engine technologies and development. 2010. doi:10.1533/9781845697457.
- [47] Pulkrabek WW. Engineering Fundamentals of the Internal Combustion Engine, 2nd Ed. J Eng Gas Turbines Power 2004;126:198. doi:10.1115/1.1669459.
- [48] Cairns A. Turbulent Flame Development in a spark ignition engine. Ph.D. thesis, University of Leeds, 2001.
- [49] Metghalchi M, Keck JC. Laminar burning velocity of propane-air mixtures at high temperature and pressure. Combust Flame 1980;38:143–54. doi:10.1016/0010-2180(80)90046-2.
- [50] Metghalchi M, Keck JC. Burning velocities of mixtures of air with methanol, isooctane, and indolene at high pressure and temperature. Combust Flame 1982;48:191–210. doi:10.1016/0010-2180(82)90127-4.
- [51] Gatowski JA, Heywood JB, Deleplace C. Flame photographs in a spark-ignition engine. Combust Flame 1984;56:71–81. doi:10.1016/0010-2180(84)90006-3.

- [52] Tabaczynski RJ. Turbulence and turbulent combustion in spark-ignition engines. *Prog Energy Combust Sci* 1976;2:143–65. doi:10.1016/0360-1285(76)90010-1.
- [53] Nagayama I, Araki Y, Iioka Y. Effects of swirl and squish on SI engine combustion and emission. *SAE Technical Paper*; 770217,1977. doi:10.4271/770217.
- [54] Fujimoto M, Tabata M. Effect of swirl rate on mixture formation in a spark ignition engine based on laser 2-D visualization techniques. *SAE Technical Paper*; 1993. doi:10.4271/770217.
- [55] Hua Zhao. *Laser Diagnostics and Optical Measurement Techniques in Internal Combustion Engines*. 2012.
- [56] Nordgren H, Hildingsson L, Johansson B, Dahlén L, Konstanzer D. Comparison between in-cylinder PIV measurements, CFD simulations and steady-flow impulse torque swirl meter measurements. *SAE Technical Paper*; 2003. doi:10.4271/2003-01-3147.
- [57] Bradley D, Lung F.-K. Spark ignition and the early stages of turbulent flame propagation. *Combust Flame* 1987;69:71–93. doi:10.1016/0010-2180(87)90022-8.
- [58] Amann CA. Cylinder-pressure measurement and its use in engine research. *SAE Technical paper*; 1985. doi:10.4271/852067.
- [59] Gülder ÖL. Laminar burning velocities of methanol, ethanol and isoctane-air mixtures. *Symp Combust* 1982;19:275–81. doi:10.1016/S0082-0784(82)80198-7.
- [60] Harper CM. *Turbulence and Combustion Instabilities in Engines*. Ph.D. thesis, University of Leeds, 1989.
- [61] Abraham J, Williams FA, Bracco F V. A Discussion of Turbulent Flame Structure in Premixed Charges. *Soc Automot Eng* 1985:128–43. doi:10.4271/850345.
- [62] Bradley D, Lau AKC, Lawes M. Flame Stretch Rate as a Determinant of Turbulent Burning Velocity. *Philos Trans R Soc A Math Phys Eng Sci*

- 1992;338:359–87. doi:10.1098/rsta.1992.0012.
- [63] Peters N. Laminar flamelet concepts in turbulent combustion. *Symp Combust* 1988;21:1231–50. doi:10.1016/S0082-0784(88)80355-2.
- [64] Borghi R. Turbulent combustion modelling. *Prog Energy Combust Sci* 1988;14:245–92.
- [65] Turner JWG, Pearson RJ, Holland B, Peck R. Alcohol-Based Fuels in High Performance Engines. *Fuels Emiss Conf 2007*:776–90. doi:10.4271/2007-01-0056.
- [66] Cairns A, Stansfield P, Fraser N, Blaxill H, Gold M, Rogerson J, et al. A Study of Gasoline-Alcohol Blended Fuels in an Advanced Turbocharged DISI Engine. *SAE Int J Fuels Lubr 2009*;2:2009-01–0138. doi:10.4271/2009-01-0138.
- [67] Kar K, Last T, Haywood C, Raine R. Measurement of Vapor Pressures and Enthalpies of Vaporization of Gasoline and Ethanol Blends and Their Effects on Mixture Preparation in an SI Engine. *SAE Int J Fuels Lubr 2008*;1:2008-01–0317. doi:10.4271/2008-01-0317.
- [68] Nakajima S, Saiki R, Goryozono Y. Development of an engine for flexible fuel vehicles (FFV). *SAE Technical Paper*; 2007. doi:10.4271/2007-01-3616.
- [69] Kameoka A, Nagai K, Sugiyama G, Seko T. Effect of Alcohol fuels on Fuel-line materials of Gasoline vehicles. *SAE Technical Paper*; 2005. doi:10.4271/2005-01-3708.
- [70] Bergström K, Nordin H, Königstein A, Marriott CD, Wiles MA. ABC—Alcohol based combustion engines—challenges and opportunities. 16th Aachener Kolloquium Fahrzeug-und Mot. Aachen, 8th-10th Oct., 2007.
- [71] Taniguchi S, Yoshida K, Tsukasaki Y. Feasibility study of ethanol applications to a direct injection gasoline engine. *SAE Technical Paper*; 2007. doi:10.4271/2007-01-2037.
- [72] Galante-Fox J, Von Bacho P, Notaro C, Zizelman J. E-85 Fuel Corrosivity: Effects on Port Fuel Injector Durability Performance. *SAE Technical Paper*; 2007. doi:10.4271/2007-01-4072.

- [73] Yacoub Y, Bata R, Gautam M, Bata R, Yacoub Y, Bata R, et al. The performance and emission characteristics of C₁-C₅ alcohol-gasoline blends with matched oxygen content in a single-cylinder spark ignition engine. *Proc Inst Mech Eng Part A J Power Energy* 1998;212:363–79. doi:10.1243/0957650981536934.
- [74] Malcolm JS, Aleiferis PG, Todd AR, Cairns A, Hume A, Blaxill H, et al. A Study of Alcohol Blended Fuels in a New Optical Spark Ignition Engine. *IMEchE Performance, Fuel Econ. Emiss. Conf.*, London: 2007.
- [75] Bata RM, Elrod C, Ewandowski TP. Butanol as a Blending Agent for I.C. Engines, (1989). *SAE Pap* 1989. doi:10.4271/890434.
- [76] Li Y, Zhao H, Brouzos N. CAI combustion with methanol and ethanol in an air-assisted direct injection SI engine. *SAE Technical Paper*; 2008. doi:10.4271/2008-01-1673.
- [77] Dai D, Hu Z, Pu G, Li H, Wang C. Energy efficiency and potentials of cassava fuel ethanol in Guangxi region of China. *Energy Convers Manag* 2006;47:1686–99.
- [78] Rosillo-Calle F, Cortez LAB. Towards ProAlcool II—a review of the Brazilian bioethanol programme. *Biomass and Bioenergy* 1998;14:115–24.
- [79] Bentivoglio D, Finco A, Bacchi MRP. Interdependencies between biofuel, fuel and food prices: The case of the Brazilian ethanol market. *Energies* 2016;9:464.
- [80] Machado GB, de Melo TCC, de Mendonça Soares LA. Flex Fuel Engine- Influence of Fuel Composition on the CA50 at Maximum Brake Torque Condition. *SAE Technical Paper*; 2015. doi:10.4271/2015-36-0215.
- [81] Duffield Ja, Xiarchos Im, Halbrosk sa. Ethanol policy. past, present, and future. *SdL Rev* 2008;53:425.
- [82] Stephen JD, Mabee WE, Saddler JN. Will second-generation ethanol be able to compete with first-generation ethanol? Opportunities for cost reduction. *Biofuels, Bioprod Biorefining* 2012;6:159–76.
- [83] M. Henderson, N. Koehler, J. Seurer and BD. 2017 ETHANOL INDUSTRY

- OUTLOOK. 2017.
- [84] Union E. Directive 2009/28/EC of the European Parliament and of the Council of 23 April 2009 on the promotion of the use of energy from renewable sources and amending and subsequently repealing Directives 2001/77/EC and 2003/30/EC. *Off J Eur Union* 2009;5:2009.
- [85] Renewable Fuels Association. 2013 Ethanol Industry Outlook - Battling for the Barrel. *Ethanol Ind Outlook* 2013:29.
- [86] Hill J. Environmental costs and benefits of transportation biofuel production from food-and lignocellulose-based energy crops. A review. *Agron Sustain Dev* 2007;27:1–12.
- [87] Walter A, Dolzan P, Quilodrán O, de Oliveira JG, da Silva C, Piacente F, et al. Sustainability assessment of bio-ethanol production in Brazil considering land use change, GHG emissions and socio-economic aspects. *Energy Policy* 2011;39:5703–16.
- [88] Hill J, Nelson E, Tilman D, Polasky S, Tiffany D. Environmental, economic, and energetic costs and benefits of biodiesel and ethanol biofuels. *Proc Natl Acad Sci* 2006;103:11206–10.
- [89] Group UNEPBW, Management UNEPIP for SR. Towards sustainable production and use of resources: assessing biofuels. UNEP/Earthprint; 2009.
- [90] Elbehri A, Segerstedt A, Liu P. Biofuels and the sustainability challenge: a global assessment of sustainability issues, trends and policies for biofuels and related feedstocks. Food and Agriculture Organization of the United Nations (FAO); 2013.
- [91] MOVE DG. State of the Art on Alternative Fuels Transport Systems in the European Union–Final Report 2015.
- [92] Louis JJJ. Well-to-Wheel Energy Use and Greenhouse Gas Emissions for Various Vehicle Technologies 2001. doi:<https://doi.org/10.4271/2001-01-1343>.
- [93] Özçimen D, İnan B. An overview of bioethanol production from algae. *Biofuels-Status Perspect.*, InTech; 2015.

- [94] Quintero JA, Montoya MI, Sánchez OJ, Giraldo OH, Cardona CA. Fuel ethanol production from sugarcane and corn: comparative analysis for a Colombian case. *Energy* 2008;33:385–99.
- [95] Huang H-J, Ramaswamy S, Tschirner UW, Ramarao B V. A review of separation technologies in current and future biorefineries. *Sep Purif Technol* 2008;62:1–21.
- [96] Chen W-C, Sheng C-T, Liu Y-C, Chen W-J, Huang W-L, Chang S-H, et al. Optimizing the efficiency of anhydrous ethanol purification via regenerable molecular sieve. *Appl Energy* 2014;135:483–9.
- [97] Fagundez JLS, Martins MES, Salau NPG. Study of Wet Ethanol Energy Balance: From Production to Fuel. SAE Technical Paper; 2015. doi:10.4271/2015-36-0485.
- [98] Fagundez JLS, Sari RL, Mayer FD, Martins MES, Salau NPG. Determination of optimal wet ethanol composition as a fuel in spark ignition engine. *Appl Therm Eng* 2017;112:317–25.
- [99] Wiebe R, Porter JC. Alcohol-water injection for spark-ignition engines. Northern Regional Research Laboratory, Peoria; 1949.
- [100] Rotz A, Cruz M, Wilkinson R, Stout B. Utilization of alcohol in spark-ignition and diesel engines. *Ext Bull E-Cooperative Ext Serv Michigan State Univ* 1980. doi:10.4271/800262.
- [101] Taraba JL, Turner GM, Razor R. The Use of Ethanol as an Unmixed Fuel for internal combustion engines. Citeseer; 1981. doi:10.1.1.381.5954.
- [102] Cordon D, Clarke E, Beyerlein S, Steciak J, Cherry M. Catalytic Igniter to Support Combustion of Ethanol-Water/Air Mixtures in Internal Combustion Engines. SAE Technical Paper; 2002. doi:10.4271/2002-01-2863.
- [103] Olberding J, Beyerlein DCS, Steciak J, Cherry M. Dynamometer testing of an ethanol-water fueled transit van. SAE Technical Paper; 2005. doi:10.4271/2005-01-3706.
- [104] Bem AD. Performance analysis of an Otto cycle engine powered with alcohol of 75 INPM. Universidade de São Paulo, 2008.

- [105] Munsin R, Laoonual Y, Bavornsethanan S, Jugjai S. An experimental study on aldehyde emissions of a hydrous ethanol fuelled small SI engine generator set. *Ratio* 2010;20:22.
- [106] Augoye A, Aleiferis P. Characterization of Flame Development with Hydrous and Anhydrous Ethanol Fuels in a Spark-Ignition Engine with Direct Injection and Port Injection Systems. *SAE Tech. Pap.*, 2014. doi:10.4271/2014-01-2623.
- [107] Manida Tongroon. Combustion characteristics and in-cylinder process of CAI combustion with alcohol fuels. Ph.D. thesis, Brunel University London, 2010.
- [108] Anbari Attar. Development and optimisation of two-line planar laser induced fluorescence technique for combustion measurements. Ph.D. thesis, Brunel University London, 2012.
- [109] Ma J. Numerical and Experimental Study of a Boosted Uniflow 2-Stroke Engine. Ph.D. thesis, Brunel University London, 2014.
- [110] Liu Q. Planar Laser Induced Fluorescence Imaging and Analysis with Ethanol Blended Fuels in a Direct Injection Spark Ignition Engine. Ph.D. thesis, Brunel University London, 2017.
- [111] Coates B. Investigation of Engine Design Parameters on the Efficiency and Performance of the High Specific Power Downsized Si Engine. Ph.D. thesis, Brunel University London, 2012.
- [112] Skogsberg M, Dahlander P, Denbratt I. Spray shape and atomization quality of an outward-opening piezo gasoline DI injector. *SAE Technical Paper*; 2007. doi:10.4271/2007-01-1409.
- [113] Schulz C, Sick V, Wolfrum J, Drewes V, Zahn M, Maly R. Quantitative 2D single-shot imaging of no concentrations and temperatures in a transparent SI engine. *Symp Combust* 1996;26:2597–604. doi:10.1016/S0082-0784(96)80093-2.
- [114] The Ricardo/Cussons Standard Hydra Engine and Test Bed Manual. 1986.
- [115] Movva V.S. Simulation of fluid flow in internal combustion engines using wave action simulation. Texas Tech University, 2004.

- [116] Wiebe II. Semi-empirical expression for combustion rate in engines. Proc. Conf. Pist. engines, 1956, p. 185–91.
- [117] Ghojel JI. Review of the development and applications of the Wiebe function: A tribute to the contribution of Ivan Wiebe to engine research. *Int J Engine Res* 2010;11:297–312. doi:10.1243/14680874JER06510.
- [118] Agnew WG. Fifty years of combustion research at General Motors. *Prog Energy Combust Sci* 1978;4:115–55. doi:10.1016/0360-1285(78)90007-2.
- [119] Hiroyasu H, Kadota T. Models for Combustion and Formation of Nitric Oxide and Soot in Direct Injection Diesel Engines. *SAE Int* 1976:513–26. doi:10.4271/760129.
- [120] Kong S-C, Marriott CD, Reitz RD, Christensen M. Modeling and experiments of HCCI engine combustion using detailed chemical kinetics with multidimensional CFD. SAE Technical paper; 2001. doi:10.4271/2001-01-1026.
- [121] Shi Y, Hai-Wen G, Reitz RD. Computational Optimization of Internal Combustion Engines. 2014. doi:10.1007/s13398-014-0173-7.2.
- [122] Ferziger JH, Peric M. *Computational Methods for Fluid Dynamics*. 2002. doi:10.1016/S0898-1221(03)90046-0.
- [123] Argyropoulos CD, Markatos NC. Recent advances on the numerical modelling of turbulent flows. *Appl Math Model* 2014;39:693–732. doi:10.1016/j.apm.2014.07.001.
- [124] Moin P, Mahesh K. Direct Numerical Simulation: A Tool in Turbulence Research. *Annu Rev Fluid Mech* 1998;30:539–78. doi:10.1146/annurev.fluid.30.1.539.
- [125] Markatos NC. Modelling of two-phase transient flow and combustion of granular propellants. *Int J Multiph Flow* 1986;12:913–33. doi:10.1016/0301-9322(86)90035-2.
- [126] Lecordier B, Demare D, Vervisch LMJ, Réveillon J, Trinité M. Estimation of the accuracy of PIV treatments for turbulent flow studies by direct numerical simulation of multi-phase flow. *Meas Sci Technol* 2001;12:1382–91.

doi:10.1088/0957-0233/12/9/302.

- [127] Markatos NC. The mathematical modelling of turbulent flows. *Appl Math Model* 1986;10:190–220. doi:10.1016/0307-904X(86)90045-4.
- [128] Sandham ND. *Introduction to direct numerical simulation 2002*. Cambridge, UK. Cambridge University Press, pp. 248-266. (doi:10.2277/0521792088).
- [129] Coleman GN, Sandberg RD. A primer on direct numerical simulation of turbulence - methods, procedures and guidelines. *Tech Rep* 2010:1–21.
- [130] Reynolds O. On the Dynamical Theory of Incompressible Viscous Fluids and the Determination of the Criterion. *Philos Trans R Soc A Math Phys Eng Sci* 1895;186:123–64. doi:10.1098/rsta.1895.0004.
- [131] Frost W, Bitte J. Statistical concepts of turbulence. *Handb. Turbul.*, Springer; 1977, p. 53–83.
- [132] Bradshaw P. An introduction to turbulence and its measurement. The Commonwealth and International Library of Science and Technology Engineering and Liberal Studies, Thermodynamics and Fluid Mechanics Division 1971.
- [133] Tennekes H. *A First Course in Turbulence*. 1972. doi:10.1017/S002211207321251X.
- [134] Vassilicos JC, Hunt JCR. *Turbulence Structure and Vortex Dynamics*. Cambridge University Press; 2000.
- [135] Frost W. Spectral Theory of Turbulence. In: Frost W, Moulden TH, editors. *Handb. Turbul. Vol. 1 Fundam. Appl.*, Boston, MA: Springer US; 1977, p. 85–125. doi:10.1007/978-1-4684-2322-8_4.
- [136] Hanjalic K. Will RANS Survive LES? A View of Perspectives. *J Fluids Eng* 2005;127:831. doi:10.1115/1.2037084.
- [137] Launder BE, Sharma BI. Application of the energy-dissipation model of turbulence to the calculation of flow near a spinning disc. *Lett Heat Mass Transf* 1974;1:131–7. doi:10.1016/0094-4548(74)90150-7.
- [138] Wilcox DC. *Turbulence Modeling for CFD (Third Edition)*. DCW Ind

- 2006:2006. doi:0963605151.
- [139] Gatski TB. Constitutive equations for turbulent flows. *Theor Comput Fluid Dyn* 2004;18:345–69. doi:10.1007/s00162-004-0119-3.
- [140] Yakhot V, Orszag S a., Thangam S, Gatski TB, Speziale CG. Development of turbulence models for shear flows by a double expansion technique. *Phys Fluids A* 1992;4:1510–20. doi:10.1063/1.858424.
- [141] Aleiferis PG, Serras-Pereira J, Richardson D. Characterisation of flame development with ethanol, butanol, iso-octane, gasoline and methane in a direct-injection spark-ignition engine. *Fuel* 2013;109:256–78. doi:10.1016/j.fuel.2012.12.088.
- [142] Karabelas SJ, Koumroglou BC, Argyropoulos CD, Markatos NC. High Reynolds number turbulent flow past a rotating cylinder. *Appl Math Model* 2012;36:379–98. doi:10.1016/j.apm.2011.07.032.
- [143] Tennekes H, Lumley JL. Chapter 3 The Dynamics of Turbulence. *A First Course Turbul* 1972.
- [144] Launder BE, Spalding DB. Mathematical Models of Turbulence. *J Appl Math Mech* 1973;53:424. doi:10.1002/zamm.19730530619.
- [145] WILCOX DC. Reassessment of the scale-determining equation for advanced turbulence models. *AIAA J* 1988;26:1299–310. doi:10.2514/3.10041.
- [146] Froehlich J, Rodi W. Introduction to Large Eddy Simulation of Turbulent Flows. *Clos. Strateg. Turbul. Transitional Flows*, 2002, p. 267–98.
- [147] Deardorff JW. A numerical study of three-dimensional turbulent channel flow at large Reynolds numbers. *J Fluid Mech* 1970;41:453–80. doi:10.1017/S0022112070000691.
- [148] Leonard A. Energy cascade in large-eddy simulations of turbulent fluid flows. *Adv Geophys* 1974;18:237–48. doi:10.1016/S0065-2687(08)60464-1.
- [149] Piomelli U. Large-eddy simulation: achievements and challenges. *Prog Aerosp Sci* 1999;35:335–62. doi:10.1016/S0376-0421(98)00014-1.
- [150] Aldama AA. Turbulence Modeling. *Filter. Tech. Turbul. Flow Simul.*, Berlin,

- Heidelberg: Springer Berlin Heidelberg; 1990, p. 7–41. doi:10.1007/978-3-642-84091-3_2.
- [151] Pope SB. Turbulent Flows. vol. 1. 2000. doi:10.1088/0957-0233/12/11/705.
- [152] Sagaut P, Meneveau C. Large Eddy Simulation for Incompressible Flows. Springer 2006:558. doi:10.1007/b137536.
- [153] Buran D. Turbulent flame propagation in a methane fuelled spark ignition engine. Ph.D. thesis, University of Leeds, 1998.
- [154] Rassweiler GM, Withrow L. Motion Pictures of Engine Flames Correlated with Pressure Cards. SAE J Trans 1938;42:185–204. doi:10.4271/380139.
- [155] Keck JC. Turbulent Flame Structure and Speed in Spark-Ignition Engines. Ninet Symp Combust Combust Inst 1982:1451–66. doi:10.1016/S0082-0784(82)80322-6.
- [156] Smith JR. Turbulent Flame Structure in a Homogeneous-Charge Engine 1982. doi:10.4271/820043.
- [157] Nye D., Lee J., Lee T-W, Santavicca D. Flame stretch measurements during the interaction of premixed flames and Kármán vortex streets using PIV. Combust Flame 1996;105:167–79. doi:10.1016/0010-2180(95)00186-7.
- [158] Zur Loye AO, Bracco F V. Two-dimensional visualization of ignition kernels in an IC engine. Combust Flame 1987;69:59–69. doi:10.1016/0010-2180(87)90021-6.
- [159] Ziegler GFW, Zettlitz A, Meinhardt P, Herweg R, Maly R, Pfister W. Cycle-Resolved Two-Dimensional Flame Visualization in a Spark-Ignition Engine 1988. doi:10.4271/881634.
- [160] North GI, Santavicca da. The fractal nature of premixed turbulent flames. Combust Sci Technol 1990;72:215–32. doi:10.1080/00102209008951648.
- [161] Bhattacharjee S. DLS and zeta potential—What they are and what they are not? J Control Release 2016;235:337–51.
- [162] Reuss DL, Kuo T-W, Khalighi B, Haworth D, Rosalik M. Particle Image Velocimetry Measurements in a High-Swirl Engine Used for Evaluation of

- Computational Fluid Dynamics Calculations. *Fuels Lubr.*, 1995.
doi:10.4271/952381.
- [163] Reeves M, Garner CP, Dent JC, Halliwell NA. Particle image velocimetry measurements of in-cylinder flow in a multi-valve internal combustion engine. *Proc Inst Mech Eng Part D-Journal Automob Eng* 1996;210:63–70. doi:Doi 10.1243/Pime_Proc_1996_210_245_02.
- [164] Keane RD, Adrian RJ. Theory of cross-correlation analysis of PIV images. *Appl Sci Res* 1992;49:191–215. doi:10.1007/BF00384623.
- [165] Morsi SA, Alexander AJ. An investigation of particle trajectories in two-phase flow systems. *J Fluid Mech* 1972;55:193. doi:10.1017/S0022112072001806.
- [166] Raffel M, Willert CE, Wereley ST, Kompenhans J. *Particle Image Velocimetry: A Practical Guide*. vol. 2nd. 2007.
doi:10.1097/JTO.0b013e3182370e69.
- [167] Weng W, Jaw S, Chen J, Hwang RR. Optimization of particle image distortion for PIV measurements. *J Hydrodyn Ser B* 2010;22:296–306.
- [168] Prasad AK, Adrian RJ, Landreth CC, Offutt PW. Effect of resolution on the speed and accuracy of particle image velocimetry interrogation. *Exp Fluids* 1992;13:105–16.
- [169] Christensen KT. The influence of peak-locking errors on turbulence statistics computed from PIV ensembles. *Exp Fluids* 2004;36:484–97.
- [170] Scarano F. Iterative image deformation methods in PIV. *Meas Sci Technol* 2001;13:R1.
- [171] Westerweel J, Dabiri D, Gharib M. The effect of a discrete window offset on the accuracy of cross-correlation analysis of digital PIV recordings. *Exp Fluids* 1997;23:20–8.
- [172] Tropea C, Yarin AL. *Springer handbook of experimental fluid mechanics*. vol. 1. Springer Science & Business Media; 2007.
- [173] Delnoij E, Westerweel J, Deen NG, Kuipers JAM, van Swaaij WPM. Ensemble correlation PIV applied to bubble plumes rising in a bubble column.

- Chem Eng Sci 1999;54:5159–71.
- [174] Meinhart CD, Wereley ST, Santiago JG. A PIV algorithm for estimating time-averaged velocity fields. *J Fluids Eng* 2000;122:285–9.
- [175] Hart DP. PIV error correction. *Exp Fluids* 2000;29:13–22.
- [176] Chomiak J. Application of chemiluminescence measurement to the study of turbulent flame structure. *Combust Flame* 1972;18:429–34.
doi:[https://doi.org/10.1016/S0010-2180\(72\)80194-9](https://doi.org/10.1016/S0010-2180(72)80194-9).
- [177] SRINIVASAN CA, Saravanan CG. Emission Reduction on Ethanol–Gasoline Blends using 1, 4 Dioxan. *Proc. World Congr. Eng.*, vol. 2, 2010.
- [178] Moxey BG. A Study of Flame Development with Isooctane- alcohol blended Fuels in an Optical Spark Ignition Engine. Ph.D. thesis, Brunel University London, 2014.
- [179] Murad. Flow and Combustion in disc and pent-roof SI engines. Ph.D. thesis, Leeds University, 2006.
- [180] Zhao H, Ladommatos N. Engine Combustion Instrumentation and Diagnostics. Society of Automotive Engineers; 2001. ISBN: 0768006651.
- [181] Nori V, Seitzman J. 1ee Evaluation of Chemiluminescence as a Combustion Diagnostic under Varying Operating Conditions. 46th AIAA Aerosp Sci Meet Exhib 2008:1–14. doi:10.2514/6.2008-953.
- [182] The MathWorks. MATLAB: "MATLAB 2015a, Brunel University London License, 2015.
- [183] Beretta GP, Rashidi M, Keck JC. Turbulent flame propagation and combustion in spark ignition engines. *Combust Flame* 1983;52:217–45.
doi:10.1016/0010-2180(83)90135-9.
- [184] Gander W, Strebel R, Golub GH. Fitting of circles and ellipses least squares solution. *SVD Signal Process. III*, Elsevier; 1995, p. 349–56.
- [185] Brown R. FITCIRCLE 2007. Least-squares fitting of circles and ellipses", W. Gander, G. Golub, R. Strebel - BIT Numerical Mathematics, 1994, Springer.

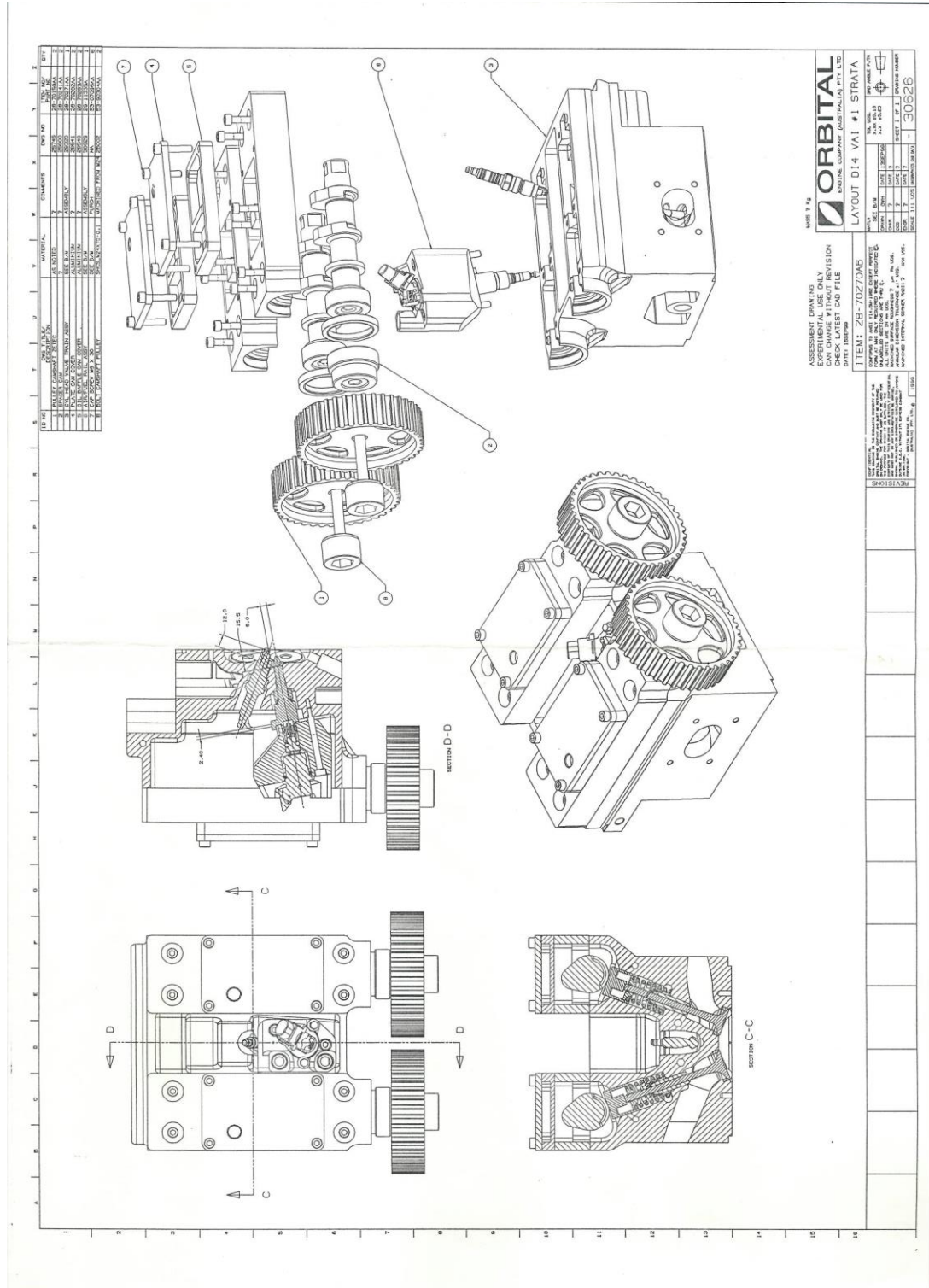
- [186] Gillespie L. Imaging and Analysis of Turbulent Flame Development in Spark Ignition Engines. Ph.D. thesis, University of Leeds, 1998.
- [187] Lancaster DR, Krieger RB, Lienesch JH. Measurement and Analysis of Engine Pressure Data. SAE Tech Pap 1975. doi:10.4271/750026.
- [188] Young MB. Cyclic Dispersion in the Homogeneous -Charge Spark Ignition Engine – A Literature Survey. SAE Tech. Pap 1981. doi:10.4271/810020.
- [189] Lyon D. Knock and cyclic dispersion in a spark ignition engine. Internatiol Conf. Pet. Based Fuels Automot. Appl., 1986, p. 105–15.
- [190] Ma F, Shen H, Liu C, Wu D, Li G, Jiang D. The Importance of Turbulence and Initial Flame Kernel Center Position on the Cyclic Combustion Variations for Spark-Ignition Engine. SAE Pap. No. 961969, 1996. doi:10.4271/961969.
- [191] Brunt MFJ, Emtage AL. Evaluation of IMEP Routines and Analysis Errors. SAE Tech Pap 1996. doi:10.4271/960609.
- [192] Brunt MFJ, Pond CR. Evaluation of Techniques for Absolute Cylinder Pressure Correction. Int. Congr. Expo., SAE International; 1997. doi:<https://doi.org/10.4271/970036>.
- [193] Chun KM, Heywood JB. Estimating heat-release and mass-of-mixture burned from spark-ignition engine pressure data. Combust Sci Technol 1987;54:133–43.
- [194] Guezennec YG, Hamama W. Two-zone heat release analysis of combustion data and calibration of heat transfer correlation in an IC engine. SAE Technical Paper; 1999.
- [195] Ortiz-Soto EA, Lavoie GA, Martz JB, Wooldridge MS, Assanis DN. Enhanced heat release analysis for advanced multi-mode combustion engine experiments. Appl Energy 2014;136:465–79.
- [196] Ferguson CR, Kirkpatrick AT. Internal combustion engines: applied thermosciences. John Wiley & Sons; 2015.
- [197] Olikara C, Borman GL. A computer program for calculating properties of equilibrium combustion products with some applications to IC engines. SAE

- Technical Paper; 1975.
- [198] Group T and FM, Annand WJD. Heat transfer in the cylinders of reciprocating internal combustion engines. *Proc Inst Mech Eng* 1963;177:973–96.
- [199] Rakopoulos CD, Michos CN. Development and validation of a multi-zone combustion model for performance and nitric oxide formation in syngas fueled spark ignition engine. *Energy Convers Manag* 2008;49:2924–38.
- [200] Gülder ÖL. Burning velocities of ethanol-isoctane blends. *Combust Flame* 1984. doi:10.1016/0010-2180(84)90060-9.
- [201] Moslemin Koupaie M, Cairns A, vafamehr H, Lanzasova T. Cyclically Resolved Flame and Flow Imaging in an SI Engine Operating with Future Ethanol Fuels. WCX™ 17 SAE World Congr. Exp., vol. 2017–March, SAE International; 2017. doi:https://doi.org/10.4271/2017-01-0655.
- [202] Stanislas M, Okamoto K, Kähler CJ, Westerweel J. Main results of the second international PIV challenge. *Exp Fluids* 2005;39:170–91.
- [203] Brequigny P, Mounaïm-Rousselle C, Halter F, Moreau B, Dubois T. Impact of Fuel Properties and Flame Stretch on the Turbulent Flame Speed in Spark-Ignition Engines. SAE Tech Pap 2013. doi:10.4271/2013-24-0054.
- [204] Parag S, Raghavan V. Experimental investigation of burning rates of pure ethanol and ethanol blended fuels. *Combust Flame* 2009;156:997–1005. doi:10.1016/j.combustflame.2008.10.011.
- [205] Eisazadeh-Far K, Moghaddas A, Al-Mulki J, Metghalchi H. Laminar burning speeds of ethanol/air/diluent mixtures. *Proc Combust Inst* 2011;33:1021–7. doi:10.1016/j.proci.2010.05.105.
- [206] Liu Q, Cairns A, Zhao H, Anbari Attar M, Cruff L, Blaxill H. The Effects of Charge Homogeneity and Repeatability on Particulates Using the PLIF Technique in an Optical DISI Engine. *SAE Int J Engines* 2014;7:500–18. doi:10.4271/2014-01-1207.
- [207] Beeckmann J, Kruse S, Peters N. Effect of Ethanol and n-Butanol on Standard Gasoline Regarding Laminar Burning Velocities. *Int Powertrains, Fuels Lubr Meet* 2010. doi:10.4271/2010-01-1452.

Appendices

Appendix A

Orbital Cylinder Head



Appendix B**PIV MATLAB Code**

```

clc
clear
tic
format long
files= dir('C:\Users\mohse\Desktop\35\*.csv');
num_files = length(files);
data_length = cell(1,num_files);
for(i=1:1:num_files);
    %import all data from Column E to K
    data_length{i} = xlsread(files(i).name,'E:K');
end

A = cell2mat(data_length);
i = 3:7:(num_files-1)*7+3;
j = 4:7:(num_files-1)*7+4;
k = sort([i j]);
%Remove two columns G and H
A(:,k)=[];
% defining mask area
r = 55/2;
p = r+2;
i = 1:5:(num_files-1)*5+1;
j = 2:5:(num_files-1)*5+2;
x = A(:,i);
y = A(:,j);
R = (x-p).^2+(y-p).^2<=r^2;
k = 5:5:(num_files-1)*5+5;
Le = A(:,k).*R;
Le(Le==0) = [];

```

```

x=A(:,i).*R;
x(x==0) = [];
y=A(:,j).*R;
y(y==0) = [];
standard_deviation_Le=std(Le);

k = 4:5:(num_files-1)*5+4;
velocity_v=A(:,k).*R;
velocity_v(velocity_v==0) = [];
positive_velocity_v=abs(velocity_v);
standard_deviation_v=std(positive_velocity_v);

k = 3:5:(num_files-1)*5+3;
velocity_u=A(:,k).*R;
velocity_u(velocity_u==0) = [];
positive_velocity_u=abs(velocity_u);
standard_deviation_u=std(positive_velocity_u);

TKE=0.5*(standard_deviation_u^2+standard_deviation_v^2+((standard_deviation_u+stand
ard_deviation_v)/2)^2);
number=numel(x)/num_files;

%Averaging Velocity u
E=reshape(velocity_u,number,num_files);
E=E';
E=var(E);
%Averaging Velocity v
W=reshape(velocity_v,number,num_files);
W=W';
W=var(W);
%Averaging x
X=reshape(x,number,num_files);

```

```
X=X';  
X=mean(X);  
%Averaging y  
Y=reshape(y,number,num_files);  
Y=Y';  
Y=mean(Y);  
scale_factor = 0.1;  
figure  
quiver(X,Y,E*scale_factor,W*scale_factor,'AutoScale','off')
```

Appendix C**Gasketing**

Sealing Section	Gasket/Sealant	Thickness
Camshaft Lobes Covers	Gaskoid Joining	0.25 mm
Camshaft Covers	Hylomar PL32 Medium Non-sticky Instant Gasket	-
Sandwich plate optical window and metal window dummy	Hermetite SDSHM202 Instant Rubber Silicon Gasket	-
Sandwich plate window clamp	Gaskoid Joining	0.25 mm
Cylinder head-sandwich plate contact surface	Chieftain Gasket Jointing	1 mm
Sandwich plate-cylinder block contact surface	Chieftain Gasket Jointing	1 mm
Piston quartz window-piston crown	Klingersill C-4400	1.5 mm
Piston quartz window-piston crown	Klinger TSM-AS graphite gasket	2 mm